

The isolation, structure, and membrane interactions of biologically active peptides

A thesis submitted for the degree of doctor of philosophy

By

Patrick James Sherman
B. Sc. (Hons.)

from the

Department of Chemistry

The University of Adelaide



June, 2012

Contents

Acknowledgements	viii
Statement of originality	x
Abstract	xi
Abbreviations	xiii
Chapter 1	
Biologically active peptides	1
1.1 Synopsis	1
1.2 Peptide Biosynthesis	2
1.3 Anuran secretions	4
1.3.1 Collection of anuran secretion	5
1.3.2 Australian anuran peptides	7
1.4 Scorpion venoms	13
1.4.1 Collection of scorpion venom	14
1.4.2 Scorpion peptides	15
Chapter 2	
Methodology I – Mass Spectrometry	20
2.1 Mass Spectrometry	20
2.2 The Q-TOF2 Mass Spectrometer	21
2.2.1 The Quadrupole analyser	22
2.2.2 The Hexapole Collision Cell	23
2.2.3 The Time of Flight Sector	24
2.3 Electrospray ionisation	25
2.4 Peptide sequence determination	26
2.4.1 High Performance Liquid Chromatography	27
2.4.2 Positive ion fragmentation	27
2.4.3 Negative ion fragmentation	28
2.4.4 Edman Sequencing	31

Chapter 3

Methodology II – Nuclear Magnetic Resonance Spectroscopy	33
3.1 Nuclear magnetic resonance spectroscopy of peptides in solution	33
3.1.1 Principles of nuclear magnetic resonance spectroscopy	34
3.1.2 One-dimensional NMR spectroscopy	36
3.1.3 Two-dimensional NMR spectroscopy	40
3.1.3.1 Correlation NMR spectroscopy	41
3.1.3.2 Total correlation NMR spectroscopy	44
3.1.3.3 Nuclear Overhauser effect NMR spectroscopy	45
3.1.4 Chemical shift Assignment	46
3.1.5 NOE Connectivities	48
3.1.6 Secondary shifts	50
3.1.7 Coupling constants	51
3.1.8 Peptide structure calculations	54
3.1.8.1 NOE derived structural restraints	54
3.1.8.2 Ambiguous NOEs	56
3.1.8.3 Stereo-specific assignment	58
3.1.8.4 Restrained molecular dynamics and simulated annealing	58
3.1.9 Structure quality	61
3.1.10 Solvent selection	64
3.2 Solid-state NMR spectroscopy	66
3.2.1 Chemical shift anisotropy	66
3.2.2 Quadrupolar interactions	68
3.2.2 Dipolar interactions	72
3.2.4 Solid-state NMR of phospholipid membranes	73
3.2.4.1 ³¹ P NMR of phospholipid membranes	76
3.2.4.2 ² H NMR of phospholipid membranes	78

Chapter 4

The Peptide profiles of the Australian brown tree frog <i>Litoria ewingii</i>	82
4.1 Introduction	82

4.1.1	The Australian brown tree frog <i>Litoria ewingii</i>	82
4.1.2	Peptide profiles of Australian frogs	83
4.1.3	Populations and taxonomy of <i>Litoria ewingii</i>	85
4.2	Results and Discussion	87
4.2.1	Isolation of <i>Litoria ewingii</i> skin peptides	87
4.2.2	Sequence determination of <i>Litoria ewingii</i> peptides	89
4.2.3	Biological activities of <i>Litoria ewingii</i> skin peptides	100
4.2.4	Morphological differences in <i>Litoria ewingii</i> populations	100
4.3	Summary and Conclusions	101
4.4	Experimental	103
4.4.1	Collection and preparation of frog skin secretions	103
4.4.2	HPLC separation of granular secretion	103
4.4.3	Sequence determination of peptides by mass spectrometry	103
4.4.4	Automated Edman sequencing	104
4.4.5	Synthesis of peptides from <i>Litoria ewingii</i>	104
4.4.6	Biological activity testing	104
4.4.6.1	Smooth muscle activity testing	104
4.4.6.2	Opioid activity studies	105

Chapter 5

Solution structures of two antimicrobial peptides from the scorpion *Mesobuthus eupeus mongolicus*

		107
5.1	Introduction	107
5.1.1	<i>Mesobuthus eupeus mongolicus</i>	107
5.1.2	The venom composition of <i>Mesobuthus eupeus</i>	108
5.1.3	Antimicrobial meucin peptides	111
5.2	Results	114
5.2.1	Chemical shift assignment	114
5.2.2	Secondary Chemical Shifts	119
5.2.3	NOE Connectivities	122
5.2.4	Coupling constants	124

5.2.5	Structure calculations	124
5.3	Discussion	130
5.4	Experimental	133
5.4.1	Cross-peak assignment and structure calculations	133

Chapter 6

Solid-state NMR studies of the antimicrobial peptide, fallaxidin 4.1a **134**

6.1	Introduction	134
6.1.1	Membrane active antimicrobial peptides	134
6.1.2	Bacterial and cytoplasmic membranes	136
6.1.3	Structure and biological activity of fallaxidin 4.1a	137
6.2	Results	141
6.2.1	³¹ P solid-state NMR spectroscopy	141
6.2.2	² H solid-state NMR spectroscopy	143
6.2.3	Quartz Crystal Microbalance	146
6.3	Discussion	149
6.3.1	Solid-state NMR spectroscopy and QCM	150
6.3.2	Mechanism of antimicrobial activity	151
6.4	Experimental	153
6.4.1	Sample preparation	153
6.4.2	³¹ P solid-state NMR	153
6.4.3	² H solid-state NMR	154
6.4.4	Quartz Crystal Microbalance	154

Chapter 7

NMR studies of CCK2 agonists **153**

7.1	Introduction	153
7.1.1	Biological activities of amphibian neuropeptides	153
7.1.2	Membrane mediated receptor binding of hormone peptides	155
7.1.3	Cholecystokinin receptor ligands	157
7.2	Results	161

7.2.1	Solution structures of rothein 1.3 and rothein 1.4	161
7.2.1.1	Chemical shift assignment	161
7.2.1.2	Secondary chemical shifts	165
7.2.1.3	NOE connectivities	167
7.2.1.4	Coupling constants	169
7.2.1.5	Structure calculations	169
7.2.2	Solid-state NMR of amphibian neuropeptides with membranes	174
7.2.2.1	³¹ P solid-state NMR	174
7.2.2.2	² H solid-state NMR	175
7.3	Discussion	179
7.3.1	Structure analysis of rothein analogues	179
7.3.2	Solid-state NMR	182
7.3.3	Additional remarks	186
7.4	Experimental	188
7.4.1	Preparation of synthetic rothein 1 peptides	188
7.4.2	NMR Spectroscopy	188
7.4.3	Cross-peak assignment and structure calculations	189
7.4.4	Sample Preparation of MLV suspensions	189
7.4.5	³¹ P solid-state NMR	190
7.4.6	² H solid-state NMR	190

Chapter 8

Summary	191	
8.1	The peptide profiles of two <i>Litoria ewingii</i> populations	191
8.2	The solution structures meucin-13 and meucin-18	192
8.3	Membrane interactions of the antimicrobial peptide fallaxidin 4.1a	193
8.4	The solutions structures of two analogues of rothein 1 and the membrane interactions of CCK2 active amphibian neuropeptides	193
8.5	Conclusion	196

References	197
Appendices	237
Publications	242

Acknowledgements

First and foremost I would like to thank my supervisor Prof. John Bowie for allowing me to undertake a variety of challenging and exiting research projects. I cherish his wisdom, encouragement, patience and guidance over the past few years.

Secondly I would like to thank previous and current members of the Bowie research group, Dr. Tara Pukala, Dr. Daniel Bilusich, Dr. Margit Sorrel, Dr. Rebecca Beumer, Dr. Tianfang Wang, Dr. Peter Eichinger for generously donating their time toward teaching me the techniques of 2D NMR, HPLC, and mass spectrometry. It has been a great experience to work with people who are so approachable, open, and happy to pass on their knowledge to guide myself, and others within the research team. I would also like to thank fellow Ph. D. students in the Bowie group Hayley Andrezza, Antonio Calabrese, and Micheal Maclean, for helping me through the challenging times, and for all of the fun we've had through the years at various events. It has been great to work with such a group of people who take pride in their work, have a great sense of humour, and know how to have a good time.

I would like to thank the technical and academic staff members from the University of Adelaide. From the Department of Chemistry, Phil Clements for his great assistance with NMR and mass spectrometry, also Gino Farese and Graham Bull for their help and advice with HPLC. From the school of Molecular Biosciences I would like to thank Chris Cursaro for operating the Edman sequencer and Cvetan Stojkoski for his assistance with molecular dynamics. I would also like to thank Associate professor Mike J. Tyler from the Department of Environmental Biology for providing the frogs for milking amphibian skin secretions. I greatly enjoyed the monthly visits and sharing in his vast knowledge of amphibians.

Another group of people I would like to thank is those I have worked with in collaborative research projects. Firstly, I want to thank Prof. Frances Separovic and Dr.

John Gheman from the the University of Melbourne for assisting with solid-state NMR experiments. Also Prof. Mibel Aguilar, Dr. John Lee, Assoc. Prof. Lisa Martin, George McCubbin, Slavica Praporski and Adam Mechler from Monash University for conducting real time experments with lipid films (QCM and DPI). Additional thanks to Professor Shunyi Zhu and Bin Gao from the Chinese academy of sciences, for providing the NMR data of the meucin peptides. I would also like to thanks Assoc. Prof. Jenny Beck and Dr. Thitima Urathamakul from the University of Wollongong for their assistance with mass spectrometry of peptide complexes.

I would like to thank all of the great friends I've made during the Ph. D. largely made up of fellow students, Scott Buckley, Alex Gentleman, Danielle Williams, Megan Garvy, Marcus Pietsche, David Thorn, Chris Brockwell, Tom Koudelka, Peter Valente, just to name a few. I cherish the friendships made, the good times, and most of all the laughter.

I would like to thank members of family for there support throughout the Ph. D. journey. Thank you to my parents, Brian and Janemarie Sherman for encouragment, support and repeatedly asking 'when are you going to hand in that thesis'. I would also like to thank my brothers and sisters (too many to mention) for their support over the years.

Lastly I would like to thank my lovely girlfriend Jennifer Barter for putting up with me throughout this journey, and her parents Chris and Laurie Barter for keeping me well fed during the final stages of writing up the thesis.

Thanks everyone.

Statement of originality

This thesis contains no material that has been accepted for the award of any other degree or diploma in any university or tertiary institution and, to the best of my knowledge and belief, contains no material previously published or written by another person, except where due reference has been made in the text.

I give consent to this copy of my thesis, when deposited to the University Library, being made available for loan and photocopying, subject to the provisions of the Copyright Act 1968.

I also give permission for the digital version of my thesis to be made available on the web, via the University's digital research repository, the Library catalogue, the Australian Digital Theses Program (ATDP) and also through the web search engines, unless permission has been granted by the University to restrict access for a period of time.

Patrick James Sherman

____/____/____

Date

Abstract

The host-defence secretions of amphibians and the venoms of arachnids are an abundant source of biologically active peptides with a great potential for use in therapeutic pharmacology. Over millions of years of evolution, the chemical arsenals of a multitude of species have produced a vast collection of peptides that have potent and selective activities. The research presented in this thesis details the isolation, structure determination and mechanistic pathways of a selection of biologically active peptides.

The southern brown tree frog *Litoria ewingi* occupies areas of the southeastern coast of Australia and Tasmania. Over a twelve month period, the peptide skin profile of a population of *L. ewingii* from Penola (South Australia) was determined using a combination of chromatography, tandem mass spectrometry and Edman degradation techniques. The peptide profiles of a *L. ewingi* from Penola show surprising differences relative to a population previously studied from the Adelaide hills, despite appearing to be morphologically identical. A total of six skin peptides were identified, four of which were unique; showing peptide sequence homology with peptides from Adelaide hills population. The evidence showed how a species can evolve separately after long periods of geographical isolation, how peptide profiling can be used to trace the migration of a species, and how new peptides can be discovered from different populations of a species. The antimicrobial meucin peptides were first identified using cDNA cloning of DNA from the venom gland of the 'Lesser Asian scorpion' *Mesobuthus eupus mongolicus*. These peptides exhibit cytolytic effects against a number of eukaryotic and prokaryotic cells at micromolar concentrations, and their peptide sequences share similarities with other antimicrobial peptides from scorpions, arthropods and amphibian species. The secondary structures of the meucin peptides were determined using 2-D NMR and molecular dynamics calculations. Both meucin peptides exhibit α -helical structure, and are amphipathic in nature. The study further shows how the length of the α -helical structure can as an antibiotic affect the cytolytic activity of the peptide, since meucin-18 is more potent than meucin-13.

The C-terminal amide analogue of the peptide fallaxidin 4.1 (fallaxidin 4.1a) isolated from the dermal secretions of *Litoria fallax*, is partially α -helical in nature, and shows potent activity against a wide range of yeast and bacteria (both Gram-positive and Gram-negative). This thesis uses solid-state NMR to detail the dynamic interactions of fallaxidin 4.1a with artificial lipid bilayers, and to explore the surface interactions of the peptides with eukaryotic (neutral) and prokaryotic (anionic) membranes. The solid state NMR and analysis using a quartz crystal microbalance indicated that the peptide acts via a surface interaction with neutral membranes and forms pores within anionic membranes at micromolar concentrations, indicating the specific pore forming mechanism by which the peptide interacts with anionic (prokaryotic) membranes.

Rothein 1, an 11 residue neuropeptide from the dermal secretions of *Litoria rothii*, and two alanine substituted analogues, rothein 1.4 and 1.5; show differing activities via binding to CCK2 receptors. The structures of rothein 1.4 and 1.5 were determined using 2-D NMR and molecular dynamics calculations. Each peptide has a largely extended structure, with similarities to the structure of rothein 1. Two 10 residue, disulfide-containing neuropeptides signiferin 1 and riparin 1 from dermal secretions of frogs of the *Crinia* genus, show potent smooth muscle and splenocyte activities. The dynamics of the interaction of signiferin 1, riparin1 and rothein 1 with artificial eukaryotic (neutral) lipid bilayer suspensions were probed using solid-state NMR, to emulate how a neuropeptide interacts with a cellular membrane surface prior to receptor binding. Solid-state NMR showed that rothein 1 had little effect on the mobility and orientation of the lipids, signiferin 1 interacted largely at the surface of the bilayers, and riparin 1 was partially inserted into the membrane. Rothein 1 is significantly less active than the disulphide peptides and more hydrophilic in nature; this is reflected in the interactions with bilayers. The disulphide peptides are more hydrophobic in character and the solid-state NMR indicated that they adhere to membranes.

Abbreviations

1D	One-dimensional
2D	Two-dimensional
3D	Three-dimensional
ARIA	Ambiguous Restraints for Iterative Assignment
CCK	Cholecystokinin
CCK1R	Type I cholecystokinin receptor
CCK2R	Type II cholecystokinin receptor
CID	Collision induced dissociation
C _L	Lethal concentration
CNS	Crystallography and NMR system
COSY	Correlation spectroscopy
CSA	Chemical shift anisotropy
DC	Direct current
DMPC	Dimyristoyl phosphatidylcholine
DMPG	Dimyristoyl phosphatidylglycerole
DNA	Deoxyribonucleic acid
DPC	Dodecylphosphotydylcholine
DPI	Dual polarisation interferometry
DQF	Double quantum filtered
ESI	Electrospray ionisation
ESMS	Electrospray mass spectrometry
ETD	Electron transfer dissociation
GUV	Giant unilamellar vesicle
HPLC	High performance liquid chromatography
HSQC	Heteronuclear single quantum coherence
HV	High volume
IC ₅₀	Half maximal (50%) inhibitory concentration
IRMPD	Infrared multiphoton dissociation
L _α	Lamellar phase
L-NNA	L-N-nitroarginine
MCP	Microchannel Plate
MIC	Minimum inhibitory concentration
MLV	Multi-lamellar vesicle
MOPS	3-(<i>N</i> -morpholino)propanesulfonic acid
MPA	3-mercaptopropionic acid

mRNA	Mature ribonucleic acid
MS	Mass spectrometry
MS/MS	Tandem mass spectrometry
NMR	Nuclear magnetic resonance
nNOS	Neuronal nitric oxide synthase
NOE	Nuclear overhauser effect
NOESY	Nuclear overhauser effect spectroscopy
PC	Phosphatidylcholine
PG	Phosphatidylglycerole
QCM	Quartz crystal microbalance
QCM-D	Quartz crystal microbalance with dissipation monitoring
RF	Radiofrequency
RMD	Restrained molecular dynamics
RMSD	Route mean standard deviation
RNA	Ribonucleic acid
SA	Simulated annealing
S _{CD}	Carbon-deuterium order parameter
SES	Surface electrical stimulation
SLB	Supported lipid bilayer
TFE	Trifluoroethanol
TMS	tetramethylsilane
TOCSY	Total correlation spectroscopy
TOF	Time of flight
TQF	Triple quantum filtered
VMD	Visual molecular dynamics
YM022	(R)-1-[2,3-dihydro-1-(2'-methyl-phenacyl)-2-oxo-5-phenyl-1H-1,4-benzodiazepin-3-yl]-3-(3-methylphenyl)urea

Chapter 1

Biologically active peptides

1.1 Synopsis

The evolution of life on earth has generated many competing means of survival amongst a vast array of species. This has led to a chemical arms race for species to defend from predators, infectious microbial organisms, viruses and other organisms competing for nutrients and habitat. There are many chemicals used for biological defence such as catechols produced from poison ivy and poison oak (*Toxicodendron spp*) species [1], to tetrodotoxin isolated from many sea creatures such as the infamous blue-ringed octopus (*Hapalochlaena spp*) and puffer fish (*Tetraodontidae spp*) [2, 3]. Alternatively some organisms are armed with chemicals for offense, such as the neurotoxins produced by many snakes, spiders and scorpions used to immobilize their prey [4-6].

To this present day chemists have isolated an extensive body of biologically active chemicals produced in nature for a wide variety of pharmaceutical applications. The predominant methods involve screening for compounds using predictive structure activity relationships of biologically active, lead compounds from natural sources. Usually these screenings have been tested for small biologically active molecules, however in recent times there is a growing interest toward the use of peptides and proteins for pharmaceutical applications [7, 8].

The use of peptides and proteins in the pharmaceutical industry poses many dilemmas. Many peptides and proteins lack the physicochemical properties to perform a desired biological action. They may not have correct hydrophobicity for transport around the body, can be rapidly broken down by proteolytic enzymes, and many negative side effects may arise from immune responses [8-10]. Despite these obstacles, developments in the fields of biochemistry, genetics and molecular biology provide new and innovative methodologies for molecular drug design. An increase in the use of peptides and proteins as pharmaceuticals in the modern market would be predicted in years to come.

This thesis details a study of the biological action, molecular structure, and membrane interactions of a range of peptides isolated from anurans and a species of scorpion. The purpose of this study is to further explore the biological activity of these peptides, their evolutionary origins, cell selectivity, and pharmaceutical applications.

1.2 Peptide Biosynthesis

A peptide is made up of a series of α -amino acids joined together via amide bonds between the α -carbonyl and α -amino groups of adjacent amino acids (figure 1.1). Proteins are made up of linked amino acids in the same way, though they differ from peptides as they are larger. There is a great deal of debate on how to define a peptide from a protein; in general peptides are made up of 50 or less amino acids [8]. The molecular weights and structures of the 20 most commonly occurring amino acids are tabulated in Appendix A.

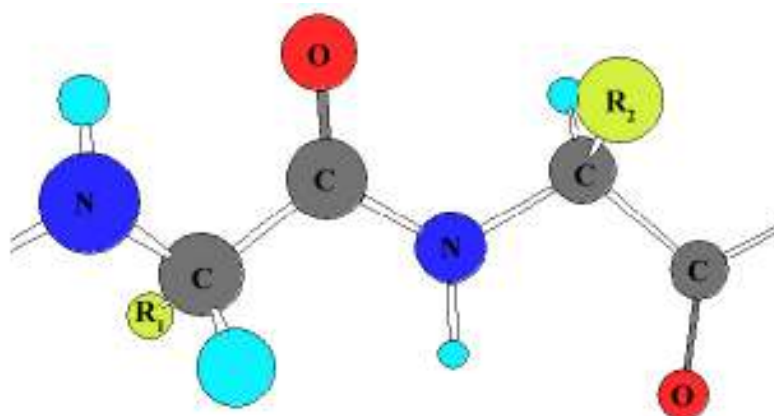


Figure 1.1 Partial structure of a peptide, amino acid sidechain groups are labelled as R₁ and R₂, hydrogen atoms are represented as light blue spheres.

Peptides are biosynthesised starting from the genes encoding the peptide within the deoxyribonucleic acid (DNA). When the gene encoding a peptide is transcribed, ribonucleic acids (RNA) are processed (to form mRNA) and translated within ribosomes

to generate a peptide precursor, known as a prepropeptide. A prepropeptide is made up of a signal segment, a spacer, and one or more active peptides.

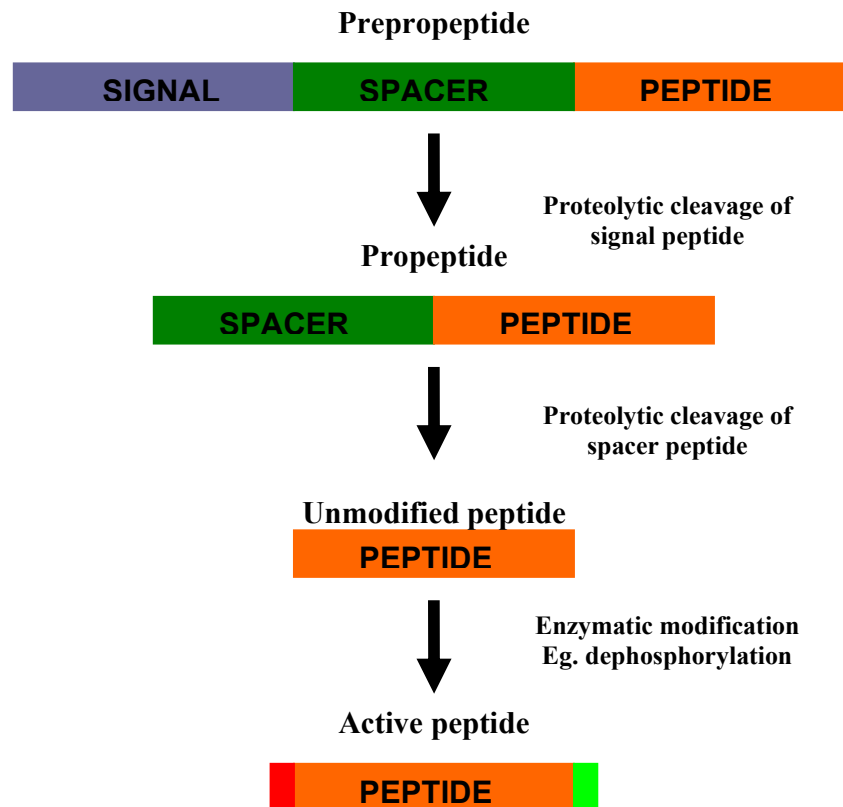


Figure 1.2 Biological synthesis of a peptide from the prepropeptide precursor.

The signal segment of the prepropeptide allows for transport through biological membranes and the endoplasmic reticulum. Once the prepropeptide reaches a certain destination proteolytic enzymes cleave the signal sequence to yield the propeptide. The propeptide moves to the Golgi complex, where proteolytic cleavage of the spacer segment may occur and any other post-translational modifications. These include phosphorylation, C-terminal amidation, acetylation, glycosylation, disulfide bond formation and the conversion of N-terminal glutamate residue to a pyroglutamate [11, 12]. The peptide is stored in the active form as granules within the endocrine system ready to be released. In some cases the peptide may be stored as the propeptide and enzymatically cleaved shortly before release [11-14].

1.3 Anuran secretions

Anurans are fascinating amphibians with a vast variety of biologically active compounds within their secretions. For thousands of years, anuran secretions have been used for hunting by natives of South America, and as ancient Chinese medicine [15-17]. Tribes in Central and South America coated spears and hunting tools with the secretions of the poison dart anuran, which contain highly neurotoxic alkaloids [18]. Peruvian Indians utilized the stimulant effects of anuran secretions to improve alertness and stamina whilst hunting [19, 20]. In Chinese medicine, a product prepared from the parotid secretions of *Bufo bufo gargarizans* or *Bufo melanostictus* toads known as ‘Chan Su’, was utilised as a topical anaesthetic, and to stimulate myocardial contraction. The effects are due to the presence of ‘steroid like’ bufadienolyde compounds within the toad secretions [16, 17, 21].

The stagnant water of ponds and streams is an ideal breeding ground for infectious microbes; in order to survive anurans have evolved various protective strategies to remain immune. Anurans secrete a diverse mixture of chemicals on their skin in response to environmental stresses such as pathogenic microbes. In the 1960’s, the work of Vittorio Erspamer and co-workers were the first to isolate and characterize components of anuran secretions [22, 23]. For the following five decades, many bioactive compounds have been identified from anuran secretions, including biogenic amines [24], steroids [25], alkaloids [26] and peptides [27, 28].

A number of bioactive compounds from amphibians have been developed to treat a range of infections, pain and cancer [29-31]. Caerulein, a peptide isolated from the Australian tree frog *Litoria caerulea*, has potential therapeutic use as it causes contraction of smooth muscle within the gastrointestinal tract and stimulates the gall bladder. This is the result of a hormone-receptor interaction, analogous to the human hormone peptides, cholecystokinin and gastrin [32, 33]. Another important discovery was that of epibatidine, an analgesic alkaloid isolated from the skin of an Ecuadorian poison dart frog *Epipedobates tricolour*, which is 200 times more potent than morphine [34]. A large

collection of antibiotic peptides have been isolated from anurans, the earliest of which were the magainins isolated from the secretions of the African clawed frog *Xenopus laevis*. The magainins and their synthetic analogues exhibit broad spectrum of antibiotic activity [35, 36]. In addition to antibiotic activities, many anuran peptides exhibit antiviral, antifungal and anticancer activities [28, 37, 38]. These peptides play a vital role in the development of new antibiotics as bacteria may not evolve resistance as rapidly with respect to current antibiotics [39]. Only a small portion of the world's anuran species have been studied to this date, hence there still remains a large reservoir of anuran bioactive compounds for future research.

1.3.1 Collection of anuran secretion

NOTE:
This figure/table/image has been removed
to comply with copyright regulations.
It is included in the print copy of the thesis
held by the University of Adelaide Library.

Figure 1.3 Schematic representation of a granular gland in *X. laevis*. Adapted from [40].

The dermal layer on frogs contains a mixture of secretions to protect, thermoregulate, regulate pH, maintain moisture and allow for respiration through the skin. Two principle secretory glands exist within the dermal layer, namely the mucal and granular glands. The mucal glands are abundant and produce an aqueous mixture of mucins and mucopolysaccharides. The granular glands are slightly larger; they produce the active alkaloids, enzymes and peptides involved in response to natural stress. The granular glands are syncytia which lie just below the epidermis, and are comprised of compacted secretor granules surrounded by multiple nuclei (within a network of complex

endoplasmic reticulum and Golgi complexes) and outer myoepithelial cells (figure 1.3). In a stress response, the myoepithelial cells contract and force the secretory granules through ducts and onto the dermal surface [40, 41].

The original means of collecting anuran secretion involved killing the frogs, followed by removal and drying of the skin. The skin secretions were then extracted from the dried skin using solvents [33, 42, 43]. Another method of collecting secretion is to inject solution containing adrenalin and noradrenalin to induce a stress response [40]. A less invasive method was developed in 1992, surface electrical stimulation (SES), by which a small voltage is applied across the dorsal surface of the animal, inducing glandular secretion, similar to a natural stress response (figure 1.4). Activation of the granular glands via the SES method does cause them to become almost depleted of secretion. However, it is replenished over a number of days or weeks [13, 40].



Figure 1.4 The surface electrical stimulation (SES) method for milking anuran secretion [44].

The SES method firstly involves holding a frog specimen by its hind legs and applying an electrical stimulus until a secretion can be observed on its dorsal surface. Some of the peptides secreted are cytotoxic to the anuran itself, and they are deactivated by enzymes that cleave the peptides [45]. For this reason, the skin secretion is washed off of the anuran with deionised water, and an equal volume of methanol is added to denature and precipitate any enzymes which may cleave a peptide of interest [46]. The SES can be performed on as little as one anuran and repeated on a monthly basis to monitor any seasonal changes in the peptide profiles. The SES method is ideal for analysing peptide profiles as it does not kill the frogs or require hormone injections.

1.3.2 Australian anuran peptides

There are 5891 described anuran species worldwide to this date, 228 (4%) which are Australian [47]. Hence, Australian anurans are an abundant resource for the study of biologically active peptides. Vittoria Erspamer pioneered the research of peptides from Australian anurans by surveying dried anuran skins from one hundred specimens of Australia and Papua New Guinea in the period 1964-1978 [43]. The peptides were assayed for their smooth muscle activities and effect on systemic blood pressure, and the most abundant peptides were of the caerulein, bombesin and tachykinin peptide families.

For the past two decades, the Bowie research group has isolated a significant collection of peptides from Australian anurans. The majority study has been performed on anuran species within the *Litoria* genus; though species from the *Lymnodynastes*, *Crinia* and *Uperoleia* genera have also been investigated. The peptides have shown a wide array of biological activities; such as antimicrobial, anticancer, antifungal, antimalarial, and smooth muscle activities, as well as inhibitors of neuronal nitric oxide synthase [28, 48-50]. Many species of anurans, in particular of the *Litoria* genus; contain a neuropeptide and a potent wide spectrum antimicrobial peptide within their secretion. In addition to host-defence peptides, a sex pheromone has also been isolated from an anuran secretion [48, 51]. The array of biological activities show anuran peptides are a significant resource for research and development of pharmaceuticals. A selection of peptides isolated from Australian anurans is summarized in table 1.1.

Table 1.1: Selected peptides isolated from Australian anuran skin secretions. Adapted from [48].

Peptide	Sequence	Species ¹	Activity ²
Aurein 1.1	GLFDI IKKIAESI-NH ₂	a	1, 2
Aurein 1.2	GLFDI IKKIAESF-NH ₂	a	1, 2
Aurein 2.1	GLLDIVKKVVGAFGSL-NH ₂	a, b	1, 2
Aurein 2.2	GLFDIVKKVVGALGSL-NH ₂	b	1-3
Aurein 3.1	GLFDIVKKIAGHIAGSI-NH ₂	a, b	1, 2
Aurein 4.1	GLIQTIKEKELKELAGGLVTGIQS-OH	b	1, 2
Aurein 5.2	GLMSSIGKALGGLIVDVLKPKTPAS-OH	a, b	1, 2
Caeridin 1.1	GLL α DGLLGTGL-NH ₂	c, d, e, f, g	
Caeridin 1.2	GLL β DGLLGTGL-NH ₂	e	
Caeridin 2	GLLDVVGNNLLGGLGL-NH ₂	d, e	
Caeridin 3	GLFDAIGNLLGGLGL-NH ₂	d, e	
Caeridin 4	GLLDVVGNNVLHSGL-NH ₂	d	
Caerin 1.1	GLLSVLGSAVAKHVLPHVVPVIAEHL-NH ₂	c, d, e	1-5
Caerin 1.3	GLLSVLGSAVQHVLPHVVPVIAEHL-NH ₂	d	1, 2
Caerin 1.4	GLLSSLGSAVAKHVLPHVVPVIAEHL-NH ₂	d, e	1
Caerin 1.8	GLFKVLGSAVAKHLLPHVVPVIAEKL-NH ₂	g	1-3, 5
Caerin 1.9	GLFGVLGSAIAKHVLPHVVPVIAEKL-NH ₂	g	1-5
Caerin 2.1	GLVSSIGRALGGLLADVVKSKGQPA-OH	c	1, 5
Caerin 2.2	GLVSSIGRALGGLLADVVKSEKQPA-OH	d	1, 5
Caerin 3.1	GLWQKIKDKASELVSGIVEQVK-NH ₂	c, d	1
Caerin 3.2	GLWEKIKEKASELVSGIVEGVK-NH ₂	d	1
Caerin 4.1	GLWQKIKSAAGDLASGIVEGIKS-NH ₂	d	1
Caerin 4.2	GLWQKIKSAAGDLASGIVEAIKS-NH ₂	d	1
Caerulein 1.1	pEQDY (SO ₃) TGWMDF-NH ₂	h	6
Caerulein 1.2	pEQDY (SO ₃) TGWFDF-NH ₂	c, i	6
Citropin 1.1	GLFDVIKKVASVIGGL-NH ₂	i	1-3, 5
Citropin 1.2	GLFDI IKKVASVVGGL-NH ₂	i	1-3, 5
Citropin 1.3	GLFDI IKKVASVIGGL-NH ₂	i	1-3, 5
Dahlein 1.1	GLFDI IKNIVSTL-NH ₂	j	1
Dahlein 1.2	GLFDI IKNIFSGL-NH ₂	j	1
Dahlein 4.1	GLWQLIKDKIKDAATGLVTGIQS-NH ₂	j	
Dahlein 5.1	GLLSIGNAIGAFIANKLKP-OH	j	5
Ewingiin 1	GWFDVVKIASAV-NH ₂	k	
Ewingiin 1.1	FDVVKHIASAV-NH ₂	k	
Ewingiin 2.1	GLLDMVTGLLGNL-NH ₂	k	
Ewingiin 2.2	GLLDMVTGLLGGL-NH ₂	k	
Ewingiin 2.3	GLLDVVTSLLGNL-NH ₂	k	
Ewingiin 2.4	GLLDVVTAVLGNLGL-NH ₂	k	

Table 1.1 Continued

Peptide	Sequence	Species ¹	Activity ²
Frenatin 1	GLLDALSGILGL-NH ₂	m	
Frenatin 2	GLLGTGNLLNGLGL-NH ₂	m	
Frenatin 3	GLMSVLGHA VGNVLGGLFKPKS-OH	m	5
Maculatin 1.1	GLFGVLAKVAAHVVP AIAEHF-NH ₂	s	1-3, 5
Maculatin 1.3	GLLGLLGSVVSHVVP AIVGHF-NH ₂	t	1, 2
Maculatin 2.1	GFVDFLKKVAGTIANVVT-NH ₂	t	1, 2
Maculatin 3.1	GLLQTIKEKLESLAKGIVSGIQA-NH ₂	s	
Riparin 1.1	RLCIPVIFPC-OH	u	6
Riparin 2.1	IIIEKLVNTALGLLSGL-NH ₂	u	1
Rothein 1	SVSNIPESIGF-OH	v	6
Rothein 2.1	AGGLDDLLLEPVLNSADNLVHGL-NH ₂	v	
Rothein 3.1	ASAAGAVRAGGLDDLLLEPVLNSADNLVHGL-NH ₂	v	
Rubellidin 4.1	GLGDILGLLGL-NH ₂	w	
Rubellidin 4.2	AGLLDILGL-NH ₂	w	
Signiferin 1	RLCIPYIIPC-OH	x	6
Signiferin 2.1	IIIGHLIK TALGMLGL-NH ₂	x	1
Signiferin 3.1	GIAEFLNYIKSKA-NH ₂	u, x	5
Splendipherin	GLVSSIGKALGGLLADVVKSKGQPA-OH	c, d	7
Tryptophyllin L 1.1	PWL-NH ₂	w	
Tryptophyllin L 1.2	FPWL-NH ₂	k, w	
Tryptophyllin L 1.3	pEFPWL-NH ₂	w	6
Tryptophyllin L 1.4	FPPFWL-NH ₂	w	
Tryptophyllin 6.1	LFFWG-NH ₂	l	
Tryptophyllin 6.2	IFFFP-NH ₂	l	
Tryptophyllin 6.3	IVFFP-NH ₂	l	

¹**Species:** *a.* *Litoria raniformis* [52]; *b.* *Litoria aurea* [52]; *c.* *Litoria splendida* [53]; *d.* *Litoria caerulea* [54]; *e.* *Litoria gilleni* [55]; *f.* *Litoria xanthomera* [56]; *g.* *Litoria chloris* [57]; *h.* various species from genus *Litoria*, *Xenopus laevis* [33, 58], *Leptodactylus labyrinthicus*; *i.* *Litoria citropa* [46]; *j.* *Litoria dahlia* [59]; *k.* *Litoria ewingi* [60]; *l.* *Limnodynastes fletcheri* [61]; *m.* *Litoria infrafrenata* [62], *n.* *Litoria lesueuri* [63]; *s.* *Litoria genimaculata* [64]; *t.* *Litoria eucnemis* [65]; *u.* *Crinia riparia* [66]; *v.* *Litoria rothii* [67]; *w.* *Litoria rubella* [68]; *x.* *Crinia signifera* [69]; *y.* *Uperoleia inundata* [70].

²**Activity:** 1. antimicrobial agent; 2. anticancer agent; 3. fungicide; 4. antiviral; 5. nNOS inhibitor; 6. neuropeptide (displaying activities such as smooth muscle contraction, immunomodulation, hormone, neurotransmitter and opioid activity); 7. pheromone.

To this day, bacterial strains continue to emerge which are resistant to therapeutic antibiotics such as penicillin, streptomycin, and vancomycin. Antimicrobial peptides are of great importance as they provide an alternative to modern antibiotics to which bacteria have evolved resistance. Some good examples of antibiotic peptides isolated from Australian anurans are aurein 1.2, caerin 1.1 and maculatin 1.1 [54, 64, 71].

To this date, many anuran antimicrobial peptides have been described and tested against a range of microbes, but few have undergone clinical trials for human use. A synthetic derivative of the frog skin peptide magainin II (from *Xenopus laevis*), known as pexiganan acetate (MSI 98), reached stage III clinical trials for therapeutic use against impetigo, a polymicrobial skin infection. However, these trials ended as it was shown that simply washing the site tended to clear the infection in 75% of cases [72-74]. Further clinical trials of pexiganan acetate for the treatment of infected foot ulcers in diabetic patients showed that when a cream containing the peptide was applied, the foot ulcers closed in 18-30 % of the cases. However, the Food and Drug administration had informed Magainin Pharmaceuticals Inc. that their non-disclosure agreement had been deemed not approvable, and no further trials have been undertaken since [73].

Many anuran antimicrobial peptides adopt a linear α -helical structure and exert their action via two proposed mechanisms leading to the disruption of bacterial membranes (figure 1.5). The barrel-stave model, where peptides aggregate, insert themselves into the bacterial cell membrane and form transmembrane pores that cause leaking of cellular contents, and cell death [75, 76]. The carpet model, where peptides aggregate and coat the bacterial membrane parallel to the surface in a carpet like manner. Once a threshold concentration is reached, curvature of the membrane occurs followed by destruction of the membrane via mixed micelle formation [77, 78]. An additional model exists, the toroidal pore model, which is similar to the barrel stave model, where phospholipid headgroups, as well as the peptides line the inner lumen of a transmembrane pore [79]. These mechanisms of membrane disruption appear to be non-specific with respect to

bacterial species, and consequently bacteria may not evolve resistance as rapidly compared to the current antibiotics [80]. Many antimicrobial peptides show additional antiviral and anticancer activities. This is likely due the same mechanism of membrane destruction, upon interaction with cancerous cells and lipid enveloped viruses.

NOTE:

This figure/table/image has been removed to comply with copyright regulations. It is included in the print copy of the thesis held by the University of Adelaide Library.

Figure 1.5 (a) Barrel-stave model: the helical peptides aggregate on the membrane surface prior to forming transmembrane pores, and **(b)** carpet model: the peptides align parallel to the membrane surface, when a threshold concentration is reached membrane dissociation and mixed micelle formation occurs. The peptides are represented by cylinders with hydrophilic and hydrophobic regions shown in blue and red respectively. Based on a figure from [81].

An antimicrobial peptide is often membrane selective, in that it is destructive to bacterial cell membranes whilst leaving eukaryotic (mammalian) cell membranes intact. The investigation of an amide modified antimicrobial peptide, fallaxidin 4.1a, isolated from *Litoria fallax*, with bacterial and eukaryotic model membranes is detailed in Chapter 6.

The chapter details the dynamics of the peptide-membrane interaction using ^{31}P and ^2H solid-state NMR. The NMR derived solution structure of fallaxidin 4.1a (performed by Rebecca Jackway) and a Quartz Crystal Microbalance (QCM) experiments (performed by Dr. Lisa Martin's research group) are also included as part of the study [82].

Anuran excretions have been found to contain a number of hormones and neuropeptides. Studies have led to the discovery of many peptides which effect smooth muscle contraction [27, 33, 50] and inhibit the enzyme neuronal nitric oxide (nNOS) synthase [49]. Two disulfide peptides isolated from *Crinia* species, riparin 1 and signiferin 1, and a linear peptide isolated from *Litoria rothii*, rothein 1; bind to type 2 cholecystokinin (CCK) receptors [50, 83]. CCK receptors are G-protein coupled receptors that exist as two subtypes, CCK1R and CCK2R; which differ in their biological action and locality within the body. In the ileum CCK1R acts directly on smooth muscle, whilst CCK2R acts by binding to cholinergic nerves in the myenteric plexus, resulting in the release of acetylcholine. Acetylcholine binds to muscarinic receptors inducing smooth muscle contraction. Conversely, the proliferation of lymphocytes is known to initiate exclusively via peptide binding to CCK2R [84]. Riparin 1, signiferin 1 and rothein 1 have been shown to initiate lymphocyte proliferation, yet only the disulfide peptides induce muscle contraction [50, 83]. Both types of tissue contain the same receptor, which brings into question why a peptide would show one activity with one type of tissue, yet no activity for another.

One model for the mode of action of a hormone peptide depicts: (i) a direct peptide-receptor association, and (ii) a conformational change of the peptide-receptor complex required for activation of the receptor [9]. However, riparin 1, signiferin 1 and rothein 1 appear to bind to CCK2R on lymphocytes and smooth muscle cells with differing affinities. One distinct difference between the cell types is the lipid composition of the cellular membranes. Also, hormone receptors only make up a small percentage of a cell surface, so it is more probable that a peptide would associate with lipids on a membrane surface prior to receptor binding, rather than directly from the extracellular fluid. It is for these reasons that an alternative model should be considered: (i) an association of the

hormone peptide and the cellular membrane, (ii) binding of the membrane associated peptide to the receptor and, (iii) a conformational change of the peptide-receptor complex required for activation of the receptor. This proposed model, which has been the subject of many studies, is known as membrane mediated peptide-receptor binding [85-90].

It is important to study the structure of a hormone peptide in a solvent system which mimics a membrane surface. The solution structures of the hormone peptides, rothein 1, rothein 1.3 and rothein 1.4 in 1:1 TFE/H₂O, are discussed in Chapter 7. Also an investigation of the peptide-membrane interactions of the hormone peptides riparin 1, signiferin 1 and rothein 1 using solid-state NMR is discussed in Chapter 7.

Each species possesses a unique spectrum of skin peptides (the peptide profile) within their skin secretions. Differences in peptide profiles are useful in classification and studying evolutionary traits of anurans. The method is so sensitive that it may also be used to differentiate different geographic populations of the same species of anuran. This has previously been shown with closely related *Litoria caerulea* and *Litoria gilleni*; each species exhibited a unique peptide profile, confirming that they are different species; putting an end to any further dispute [54, 55]. Further studies of major *L. caerulea* populations from the Northern Territory, Queensland and Melville Island also show differences in their peptide profiles, presumably a result of geographical isolation [55, 91, 92]. A detailed comparison of the peptide profiles of Australian Brown Tree frog *Litoria ewingi*; taken from populations in the Adelaide hills and Penola regions of South Australia, is discussed in Chapter 4.

1.4 Scorpion venoms

There are approximately 2000 described species of scorpion distributed throughout the world, which are divided into 14 families (that are found alive today) [93]. They inhabit all parts of the world except New Zealand and Antarctica, and tend to occupy warmer regions with temperature ranges of 20-37°C. Scorpions are ancient arachnids and have fossil records dating back the beginning of the paleozoic era over 400 million years ago. They are descendants of *Eurypteryds*, more commonly known as sea scorpions, the

largest of known arthropods ever recorded. One ancient species, *Jaekelopterus rhenaniae* was estimated to be an impressive 2.5m in body length [94]. It is believed that scorpion ancestors existed as marine arthropods, which later evolved into aquatic arthropods, which later became terrestrial. After the carboniferous period, as oxygen levels in the air decreased, scorpions evolved into much smaller land arthropods. Little change in their morphological traits have occurred over the past 300 million years [6].

Scorpions are nocturnal animals, which hibernate from predators during the day and come out at night to feed predominantly on spiders, insects and other scorpions. Scorpions are renowned for their venom, though only a small number of species carry venom which is toxic to humans [6]. The majority of potentially fatal scorpions are from the genera *Androctonus*, *Centruroides*, *Hottentotta*, *Leiurus*, *Parabuthus* and *Tityus*, all within the *Buthidae* family, the largest of the described scorpion families [93].

Scorpion venom is rich in neurotoxins which it uses to subdue its prey and defend from predation. Scorpion venom is composed of a mixture of alkaloids, steroidal compounds, proteolytic enzymes, lipolytic enzymes, proteins and peptides [6]. The key neurotoxins within scorpion venom are low molecular weight (1-4 kDa) disulfide rich peptides which interact with ion channels on cell membranes. The lipolytic and proteolytic enzymes aid in digestion of prey and may amplify the effectiveness of the neurotoxins [6].

1.4.1 Collection of scorpion venom

Scorpion venom is biologically synthesised within a pair of venom glands in the telson (stinger), situated at the anterior end of the tail (figure 1.4). The venom glands are surrounded by compressor muscles, and when they contract, the venom is compressed against the surrounding cuticle and forced out a pair of exit ducts which allow the venom to be expelled through the aculeus. The interior of the venom gland has a folded network of secretory epithelia, the extent of folding of this epithelia differs greatly between different families of scorpions [6]. Scorpions within the *Chactidae* family have very little folding in their secretor epithelia, scorpions from the *Buthidae* family have a high degree of folding.

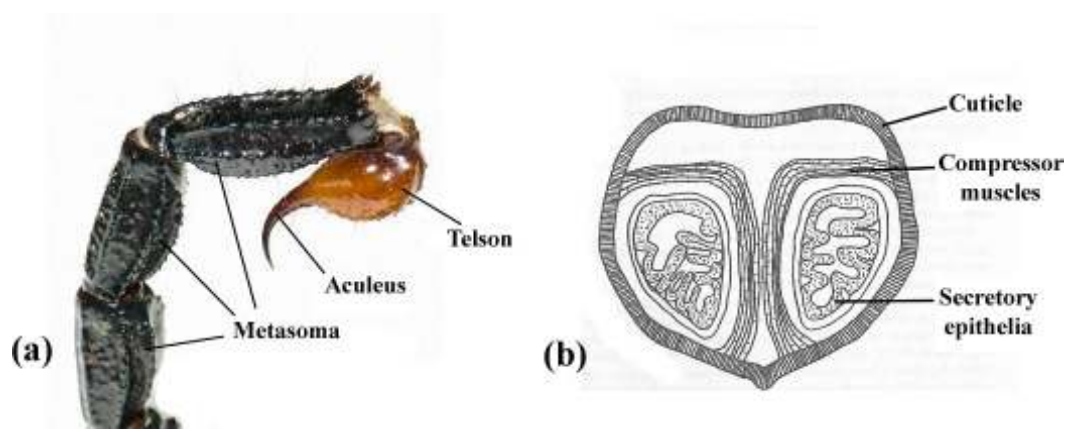


Figure 1.6 (a) The tail of an emperor scorpion, the venom is stored in the telson and injected through a thin hollow tube in the aculeus (sting). (b) A cross section of the venom gland of a scorpion, the venom is stored within the folds of the secretory epithelia. Figure adapted from [95].

The collection of scorpion venom is generally performed by one of two methods, the telson (stinger) of the scorpion tail pierces a vessel containing a thin membrane, or the secretion is collected via low voltage electrical stimulation of the telson. Scorpions are subdued via putting them above a bed of dry ice prior to extracting the venom. Once collected, the venom sample is usually lyophilised and stored for further analysis [96].

1.4.2 Scorpion peptides

The earliest studies of scorpion peptides were by Lissitzki and Co-workers in the 1950s. They isolated the neurotoxic components of two north African scorpions *Androctonus australis Hector* and *Buthus occitanus* [97-100]. After chromatographic separation, it was determined that each scorpion appeared to have two neurotoxic peptide (or protein) fractions. The precise biological actions and sequences of the peptides were not determined until some years later, and advances in chromatography techniques allowed for the isolation and identification of additional peptides within the venoms [101-104].

As years progressed a growing number of neurotoxic scorpion peptides from many scorpion species were isolated. They typically contain 1-5 disulfide bridges, with a high degree of specificity for sodium, potassium, calcium and chloride ion channels on cellular

membranes [105, 106]. Some show specificity for insect ion channels, and others for vertebrate ion channels; in some cases they bind to the channels depending on the membrane composition of the cell. One peptide, *Androctonus australis* insect selective toxin (AaIT1), has potential for use as an insecticide [107]. Generally these peptides either block activation or slow the inactivation of ion channels [106]. The venom mixtures tend to contain peptides that target multiple ion channels simultaneously, enhancing their overall neurotoxicity. In addition to neurotoxic peptides, a new class of scorpion peptides has emerged and gained interest over recent years. These peptides do not contain disulfide bridges. Selected peptides isolated from scorpion venoms are summarised in table 1.2.

To this date, very few non-disulfide bridged peptides from scorpion venoms have been characterised. These peptides show immune-modulating, haemolytic and antimicrobial activities [108]. Many of these peptides are cationic and exhibit helical secondary structures, similar to many anuran, bee and spider antimicrobial peptides [109-112]. Zhu and his colleagues previously found the antimicrobial peptide, BmKb1, isolated from the scorpion *Buthus martensi Karsch* was up regulated in response to exposure of the venom gland to bacteria [96]. This demonstrated that the venom gland itself produces antimicrobial peptides to inhibit infection. Chapter 5 of this study includes the solution structure determination of two novel antimicrobial peptides from the ‘Lesser Asian Scorpion’ *Methobuthus eupus mongolicus*, using 2D-NMR. The chapter details the analysis of the 2D NMR spectra, the sample preparation, acquisition of the NMR spectra, and antimicrobial tests were performed by Professor Shunyi Zhu’s research group [113].

Table 1.2 Selected peptides from scorpion venoms. Table adapted from [106, 108].

<i>Peptide</i>	<i>Sequence</i> ¹	<i>Disulfide motif</i>	<i>Species</i> ²	<i>Activity</i> ³
AaHI	KRDGYIVYPNNCVYHCVPPCDGLCKKNGSSGSCSF LVPSGLACWCKDLPDNPVIKDTSRKCT-NH ₂	12-61, 16-34, 20-44, 24-46	<i>a</i>	<i>l</i>
AaHII	VKDGYIVDDVNCTYFCGRNAYCNEECTKLKGESGYC QWASPYGNACYCYKLPDHPVRTKGPGRCH-NH ₂	12-62, 16-36, 22-46, 26-48	<i>a</i>	<i>l</i>
AaHIII	VRDGYIVNSKNCVYHCVPPCDGLCKKNGAKSGSCGF LIPSGLACWCVALPDNPVIKDPSTYKCHS-NH ₂	12-61, 16-34, 20-44, 24-46	<i>a</i>	<i>l</i>
Be12	ADGVKKGSGCKISCFDNDLNCADCKYYGGKNLSWC IPDKSGYCWCPNKGWNSIKSETNTC-OH	10-60, 14-36, 21-44, 25-46	<i>b</i>	<i>l</i>
BeM9	ARDAYIAKPHNCVYECYNPKGSYCNDLCTENGAESG YCQILGKYGNACWCIQLPDNPVIRIPGKCH-OH	12-64, 16-38, 24-48, 28-50	<i>b</i>	<i>l</i>
BeM10	VRDGYIADDDKCAVFCGRNAYCDEECKKGAESGKCW YAGQYGNACWCYKLPDWPVIKQKVS GKCN-OH	12-63, 16-35, 22-45, 26-47	<i>b</i>	<i>l</i>
BmKI	VRDAYIAKPHNCVYECARNEYCNDLCTKDGA KSGYC QWVGKYGNGCWCIELPDNPVIRVPGKCH-NH ₂	12-62, 16-36, 22-46, 26-48	<i>c</i>	<i>l</i>
BmKII	VRDAYIAKPHNCVYECARNEYCNDLCTKDGA KSGYC QWVGKYGNGCWCIELPDNPVIRIPGNCH-NH ₂	12-62, 16-36, 22-46, 26-48	<i>c</i>	<i>l</i>
BomIII	GRDGYIAQPENCVYHCFPGSSGCDTLCTKEKGATSG HCGFLPGSGVACWCNDLNPVKVIVVGGEEKCHF-NH ₂	12-65, 16-38, 23-48, 27-50	<i>d</i>	<i>l</i>
BomIV	GRDAYIAQPENCVYECAKNSYCNDLCTKNGAKSGYC QWLKGYGNACWCEDLPDNPVIRIPGKCHF-NH ₂	12-62, 16-36, 22-46, 26-48	<i>d</i>	<i>l</i>
BotI	GRDAYIAQPENCVYECAQNSYCNDLCTKNGATSGYC QWLKGYGNACWCKDLPDNPVIRIPGKCHF-NH ₂	12-62, 16-36, 22-46, 26-48	<i>e</i>	<i>l</i>
BotII	GRDAYIAQPENCVYECAKSSYCNDLCTKNGAKSGYC QWLGRWGNACYCIDLPDKVPIRIEGKCHF-NH ₂	12-62, 16-36, 22-46, 26-48	<i>e</i>	<i>l</i>
Bukatoxin	VRDGYIADDDKCAVFCGRNAYCDEECIINGAESGYC QQAGVYGNACWCYKLPDKVPIRVSGECQQ-OH	12-62, 16-36, 22-46, 26-48	<i>c</i>	<i>l</i>
Kurtoxin	KIDGYPVDYWNCKRICWYNNKYCNDLCKGLKADSGY CWGWTLSYCYQGLPDNARIKRSGRCRA-NH ₂	12-60, 16-37, 23-44, 27-46	<i>f</i>	<i>l,3</i>
LqhII	IKDGYIVDDVNCTYFCGRNAYCNEECTKLKGESGYC QWASPYGNACYCYKLPDHPVRTKGPGRCR-NH ₂	12-62, 16-36, 22-46, 26-48	<i>g</i>	<i>l</i>
LqhIII	VRDGYIAQPENCVYHCFPGSSGCDTLCKEKGATSGH CGFKVGHGLACWCNALPDVGIIVEGEEKCHS-NH ₂	12-63, 16-37, 23-47, 27-49	<i>g</i>	<i>l</i>
Ts1	KKDGYPVEYDNCAYICWNYDNAYCDKLCCKKADSG YCYWVHILCYCYGLPDSEPTKTNGKCKS-OH	12-60, 16-38, 24-45, 28-47	<i>h</i>	<i>l</i>
Ts2	GREGYPADSKGCKITCFLTAAGYCNTECTLKKGSSG YCAWPACYCYGLPESVKIWTSETNKC-OH	12-60, 16-38, 24-43, 28-45	<i>h</i>	<i>l</i>

Table 1.2 continued

<i>Peptide</i>	<i>Sequence¹</i>	<i>Disulfide motif</i>	<i>Species²</i>	<i>Activity³</i>
Agitotoxin 1	GVPINVKCTGSPQCLKPKCKDAGMRFGKCINGKCHCT PK-OH	8-28, 14-33, 18-35	<i>g</i>	2
Agitotoxin 2	GVPINVSTGSPQCIKPKCKDAGMRFGKCMNRKCHCT PK-OH	8-28, 14-33, 18-35	<i>g</i>	2
BmTx1	QFTDVKCTGSKQCWPVCKQMFVKPNGKCMNGKCRCY S-OH	7-28, 13-33, 17-35	<i>c</i>	2
BmTx2	QFTNVSCSASSQCWPVCKKLFQTYRGKCMNSKCRCY S-OH	7-28, 13-33, 17-35	<i>c</i>	2
Kaliotoxin	GVEINVKCSGSPQCLKPKCKDAGMRFGKCMNRKCHCT P-NH ₂	8-28, 14-33, 18-35	<i>i</i>	2
Kaliotoxin 2	VRIPVSCKHSGQCLKPKCKDAGMRFGKCMNGKCDCTP K-OH	7-27, 13-32, 17-34	<i>a</i>	2
Margatoxin	TIINVKCTSPKQCLPPCKAQFGQSAGAKCMNGKCKC YPH-OH	7-29, 13-34, 17-36	<i>j</i>	2
Noxiustoxin	TIINVKCTSPKQCSKPKELTGSSAGAKCMNGKCK CYNN-NH ₂	7-30, 13-35, 17-37	<i>k</i>	2
OsK1	GVIINVKCKISRQCLEPCKKAGMRFGKCMNGKCHCT PK-OH	8-28, 14-33, 18-35	<i>l</i>	2
Tc1	ACGSCRKKCKGSGKCINGRCKCY-OH	2-15, 5-20, 9- 22	<i>m</i>	2
BmCa1	GCNRLNKKCNDSGDCCRYGERCIISTGVNYYCRPDFG P-OH	2-16, 9-22, 15-31	<i>c</i>	3
ImperatoxinA	GDCLPHLKRCADNDCCGKKCKRRGTNAEKRCR-OH	3-17, 10-21, 16-32	<i>n</i>	3
Maurocalcine	GDCLPHLKLCKENKDCCSKKCKRRGTNIEKRCR-OH	3-17, 10-21, 16-32	<i>o</i>	3
Opicalcine1	GDCLPHLKRCKENNDCCSKKCKRRGTNPEKRCR-OH	3-17, 10-21, 16-32	<i>p</i>	3
Opicalcine2	GDCLPHLKRCKENNDCCSKKCKRRGANPEKRCR-OH	3-17, 10-21, 16-32	<i>p</i>	3
Chlorotoxin	MCMPCFTTDHQMARKCDDCCGGKGRGKCYGPQCLCR -OH	2-35, 5-20, 16-28, 19-33	<i>g</i>	4
Meucin-13	IFGAIAGLLKNIF-NH ₂	-	<i>q</i>	5
Meucin-18	FFGHFLKLATKIIPSLFQ-NH ₂	-	<i>q</i>	5
BmKb1	FLFSLIPSAISGLISAFK-NH ₂	-	<i>c</i>	5
BmKn2	FIGAIANLLSKIF-NH ₂	-	<i>c</i>	5

Table 1.2 continued

<i>Peptide</i>	<i>Sequence¹</i>	<i>Disulfide motif</i>	<i>Species²</i>	<i>Activity³</i>
Imcroporin	<u>MKFQYLLAVFLIVLVVTDHCQAFFSLLPSLIGGLVS</u> AIKGR-OH	-	<i>r</i>	5
IsCT1	<u>ILGKIWEGIKSLF-NH₂</u>	-	<i>s</i>	5, 6
IsCT2	<u>IFGAIWNGIKSLF-NH₂</u>	-	<i>s</i>	5, 6
Pandanin1	<u>GKVVDWIKSTAKKIWSSEPVSQKLGQVLNAAKNYVA</u> EKIGATPT-OH	-	<i>n</i>	5, 6
Pandanin2	<u>FWGALAKGALKLIPSLFSSFSKGD-OH</u>	-	<i>n</i>	5, 6
Opistoporin 1	<u>GKVVDWIKSTAKKLWNSEPVKELKNTALNAAKNLVA</u> EKIGATPS-OH	-	<i>p</i>	5, 6, 7
Opistoporin 2	<u>GKVVDWIKSTAKKLWNSEPVKELKNTALNAAKNFVA</u> EKIGATPS-OH	-	<i>p</i>	5
Hadrurin	<u>GILGTIKSIASKVWNSKTVQDLKRKGINWVANKLGV</u> SPQAA-OH	-	<i>t</i>	5,6

¹Disulfide bridging cystine residues are underlined, and the disulfide bridging motif defined.

²**Species:** *a. Adroctonus australis Hector* [101-103, 114]; *b. Mesobuthus eupeus eupeus* [115, 116]; *c. Mesobuthus martensi karsch* [117-121]; *d. Mesobuthus occitanus mardochei* [122, 123]; *e. Mesobuthus occitanus tunetanus* [104]; *f. Parabuthus transvaalicus* [124]; *g. Leiurus quinquestriatus hebraeus* [125-129]; *h. Tityus serrulatus* [130, 131]; *i. Androctonus mauretanicus mauretanicus* [132]; *j. Centruroides margaritatus* [133]; *k. Centruroides noxius* [134, 135]; *l. Orthochirus scrobiculosus* [136]; *m. Tityus cambridgei* [137, 138]; *n. Pandinus imperator* [139, 140]; *o. Scorpio maurus* [141]; *p. Opisththalmus carinatus* [142, 143]; *q. Mesobuthus eupeus mongolicus* [113]; *r. Opisthacanthus madagascariensis* [144]; *s. Isometrus maculatus* [145]; *t. Hadrurus aztecus* [146].

³**Activity:** **1.** Na⁺ channel binding; **2.** K⁺ channel binding; **3.** Ca²⁺ channel binding; **4.** Cl channel binding; **5.** Antimicrobial agent; **6.** Haemolytic activity; **7.** Immunomodular activity.

Of the approximate 2000 described species of scorpions, it is estimated that they produce 100 000 unique peptides. Only some 30 scorpions species have been studied to this date, hence scorpion venoms could be one of the most abundant resources for the discovery of biologically active peptides [147].

Chapter 2

Methodology I – Mass Spectrometry

2.1 Mass Spectrometry

One of the first of the pioneers for mass spectrometry was physicist J.J. Thomson, who in 1913, published his studies of canal rays (beams of positive ions) deflected a beam of ionised neon through a magnetic field onto a photographic plate under low pressure; discovering two patches of light. He concluded these were isotopes of neon ^{20}Ne and ^{22}Ne based on their mass to charge ratio [148]. This provided a template for early mass spectrometers which consisted of a single magnetic sector to separate ions [149, 150]. Such instruments were superseded by tandem mass spectrometers which contained both electric and magnetic sectors: these greatly improved the sensitivity and resolution of mass spectra [149, 151].

Since then many advances have been made in the field of mass spectrometry. Time of flight [152-154], quadrupole and ion trap mass spectrometers emerged in the mid to late 20th century [155, 156]. These mass spectrometers are much smaller and cheaper than the magnetic deflection instruments and are among the most commonly used today for protein and peptide studies. Many alternative methods to generate ions are available, such as electron impact ionization [150, 157, 158] and chemical ionization [159, 160]. More temperate ‘soft ionization’ methods such as matrix assisted laser desorption ionization [161-163] and electrospray ionization [164-166] (See section 2.3) methods have allowed great advances in the field of biomolecules: these are ideal for the analysis of larger, thermally unstable biological molecules such as peptides, proteins and DNA.

Advances in tandem mass spectrometry (MS/MS) and the emergence of hybrid mass spectrometers allow for the selection and fragmentation of ions with a specific m/z value from a mixture. Selection of the ion, usually by a quadrupole analyser (section 2.2.2) and further ion fragmentation via collision induced dissociation (CID) [167-169], electron transfer dissociation (ETD) [170, 171], or infrared multiphoton dissociation (IRMPD) [172] yields ‘daughter ions’ (section 2.2.2). Further analysis of daughter ions is

commonly undertaken using a time of flight sector; yielding accurate characteristic MS/MS spectra of a parent ion and/or daughter ions of interest.

Mass spectrometry allows for highly sensitive, rapid analysis of a wide range of compounds such as peptides, proteins and DNA. It remains a prevalent tool in chemistry and molecular biology for the analysis of biological media.

2.2 The Q-TOF2 Mass Spectrometer

The mass spectrometry component of this research was primarily performed on a Q-TOF 2 hybrid quadrupole time of flight mass spectrometer fitted with an electrospray source. A schematic diagram of the key components of the Q-TOF 2 instrument is shown in figure 2.1.

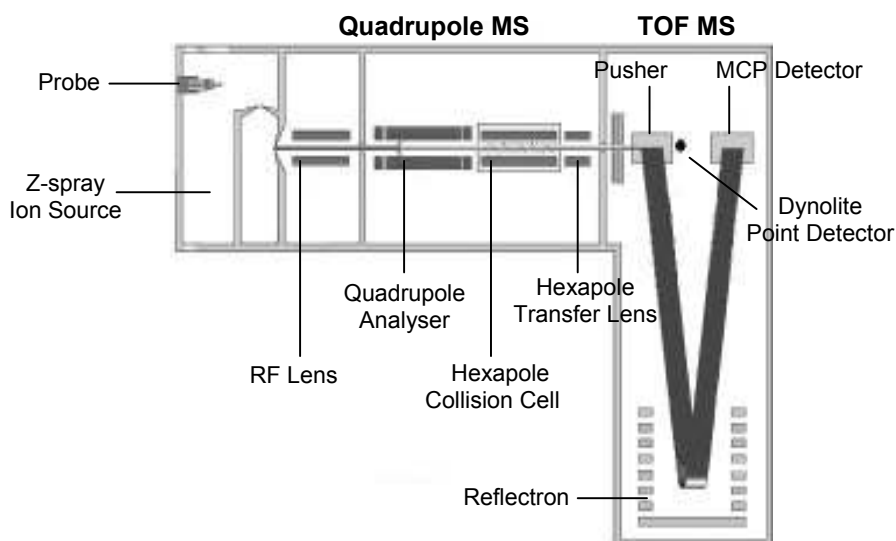


Figure 2.2 Schematic diagram of the Q-TOF 2 mass spectrometer [173].

The ionisation method accomplished within the Z-spray ion source is electrospray ionisation (Section 2.3). Once injected into the Z-spray ion source; desolvation occurs and the residual charged particles move through a sample cone aperture due to an applied electric potential (cone voltage). The electric potential applied can be adjusted for a particular ion within a range of mass to charge ratios (m/z). Generally a higher voltage is

applied for larger ions such as proteins [174]. Then the ions are analysed using a quadrupole mass analyser and an orthogonal reflectron TOF sector, separated by a hexapole collision cell.

2.2.1 The Quadrupole Analyser

The quadrupole analyser is comprised of four fixed parallel rods. An electric field is created via applying a fixed direct current (DC) and variable radiofrequency (RF) potentials (figure 2.2).

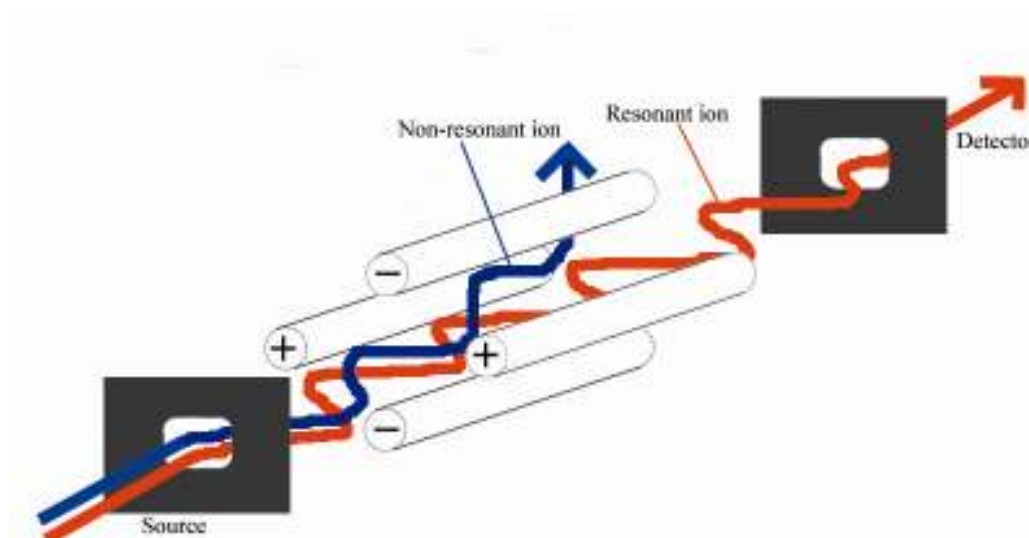


Figure 2.2 Mass selection by a linear quadrupole analyser. Four parallel rods labelled in blue, adjacent rods are alternating in charge. The ions are transmitted along the axis of the rods in the RF field, ions with an unstable trajectory are ejected from the quadrupole.

The ions are introduced into the quadrupole in a continuous beam about the central axis of the rods. The trajectory of an ion through the quadrupole analyser will depend on the applied electric field: only ions of a specific m/z will have a stable trajectory and thus pass through to the detector [155, 175, 176]. Ions outside the range of the specified m/z are deflected and do not pass through the analyser. By altering the applied DC and RF potentials between the adjacent rod pairs, ions of different specified m/z are focused on to the detector, creating a mass spectrum [176]. When the instrument is in MS mode, all ions are able to pass through the quadrupole analyser. In tandem (MS/MS) mode, ion(s)

with a discrete selected m/z are able to pass through the quadrupole analyser and through to the hexapole collision cell and TOF sector [177, 178].

2.2.2 The Hexapole Collision Cell

Within the hexapole collision cell ions are energised via collisions with a noble gas such as He or Ar. These collisions induce fragmentation of the parent ion, producing daughter ions which retain partial characteristics of the parent ion [167, 169, 179]. The daughter ions can undergo additional fragmentation producing further generations of daughter ions (figure 2.3).

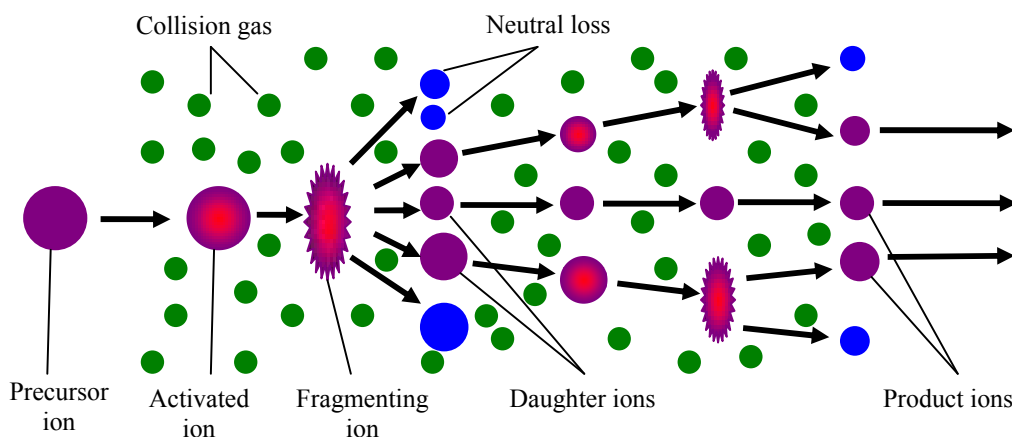


Figure 2.3 A schematic diagram of CID fragmentation. Precursor ions (purple) enter the collision cell, become activated via colliding with an inert gas (green) followed by fragmentation, producing daughter ions and neutral particles (blue). The product ions proceed to a detector.

In MS mode, all of the ions are able to pass through the quadrupole analyser, hexapole collision cell and onto a pusher, which applies translational energy to other ions prior to entering the time of flight sector. In tandem mass spectrometry (MS/MS) the quadrupole selects for a particular m/z , which then passes through the hexapole collision cell. In the collision cell, the ion(s) selected come into contact with a noble gas, in this case argon, which transfers energy to the ions leading to fragmentation. This process, known as collision induced dissociation (CID), leads to the formation of daughter ions, which retain partial structural characteristics of the parent ion [167-169, 179, 180]. As ions exit the

hexapole collision cell, they are accelerated via the pusher into the TOF sector for subsequent mass determination.

2.2.3 The Time of Flight Sector

When ions of charge z enter the TOF sector they are accelerated by an applied electric potential V , such that their kinetic energy zV is given by

$$zV = \frac{mv^2}{2}$$

where m and v are the mass and velocity of the ion, respectively. The velocity of the ion is given as the distance travelled d , per unit time t , and thus the m/z of an ion is defined as

$$m/z = \frac{2Vt^2}{d^2}$$

The ions travel a fixed distance to the detector, and the larger m/z have a longer time of flight prior to reaching the detector. Hence the detector measures the array of time of flight durations and this is interpreted as a mass spectrum [152, 154]. Ions are accelerated in the TOF tube via an applied electric field toward a reflectron, where they are reflected back toward the detector. The reflectron enhances the resolution of TOF mass spectra by correcting the distribution of velocities (kinetic energies) of the ions prior to detection [181, 182].

Ions are detected by a Microchannel Plate (MCP) which can record a spectrum (scan) at 50 μ s intervals. A possible 20,000 scans can be taken per second and combined to give the resultant spectrum for analysis [183]. The Q-TOF instrument can record an m/z range up to 4000 Da and detect ions at nanomolar concentrations.

2.3 Electrospray ionisation

Techniques such as chemical ionisation and electron impact ionisation are not ideal for mass spectrometry of peptides, as they place a limit on the size of the analyte and are often restricted to analysis of volatile analytes. The advent of electrospray ionisation allowed for great advances in the mass spectrometry of biological molecules as it allowed for the analysis of non-volatile compounds directly from solution by evaporating them into the gas phase. The first ESI experiments reported were by Dole *et al.* in 1968 involving detection of macroions produced from polystyrene. ESI techniques used for the analysis of biological molecules emerged in the 1980's largely due to the development of the technique by Fenn and his colleagues [164, 184, 185].

Electrospray ionisation involves injecting a dissolved analyte through a capillary needle at high pressure into a Z-spray ion source. In solution, the analyte forms both positive and negative ions to an extent. The dissolved ions are passed through a heated capillary tube at a flow rate within the $\mu\text{L}/\text{min}$ to nL/min range and are subjected to a potential difference from the capillary tip to the electrode. As the liquid reaches the capillary tip the electric field causes a distortion at the surface of the liquid as it leaves the capillary, forming a cone like shape known as a 'Taylor cone' [186] (figure 2.4).

NOTE:
This figure/table/image has been removed
to comply with copyright regulations.
It is included in the print copy of the thesis
held by the University of Adelaide Library.

Figure 2.4: The formation of a Taylor cone in the presence of an electric field [186].

The tip of the Taylor cone forms an elongated liquid jet. Once the surface charge density reaches past the threshold maintaining the liquid jet, charged droplets are formed. Once

the analyte solution is injected into the Z-spray source the liquid forms a fine spray, consisting of highly charged liquid droplets. Evaporation of the solvent from sample molecules occurs by passing a dry gas across the spray at high temperatures $\approx 100\text{-}200^\circ\text{C}$. As the solvent is evaporated, the droplets shrink to a critical size where repulsive Coulombic forces overcome the cohesive forces of the droplet, resulting in the generation of gas phase molecular ions (figure 1.9) which pass through the source for further mass determination [184].

NOTE:
This figure/table/image has been removed
to comply with copyright regulations.
It is included in the print copy of the thesis
held by the University of Adelaide Library.

Figure 2.5: Schematic representation of the production of positive ions in electrospray mass spectrometry [184].

The polarity of the applied potential difference between the capillary and sample cone can be altered to select for positive or negative ions. The advantage of ESMS is that MnH^+ and $(M+nH^+)^+$ ions be generated, where n is a given number of protons. This allows for the measurement of high molecular weight compounds as they can form multiply charged ions resulting in a lower m/z value, hence are more likely to be within the m/z range of the spectrometer [187]. $(M-H^+)^-$ and $(M-mH^+)^{m-}$ can also be produced and studied in negative ion mode.

2.4 Peptide sequence determination

Mass spectrometry is an advantageous method for peptide sequence determination, often from very small quantities of peptide. The peptide samples need not be pure since tandem mass spectrometry (eg. the MS/MS method) allows for the selection and analysis of an ion of interest. In cases where the peptide sample is complex, high performance liquid chromatography (HPLC) can also be employed to achieve further separation of components. In circumstances where mass spectrometry cannot distinguish between

amino acids of equal mass within a peptide sequence, Edman sequencing is used (Section 2.4.4).

2.4.1 High Performance Liquid Chromatography

In complex peptide mixtures, many peptide analytes contend for charge during the ESI process. This can produce many ions simultaneously with varying intensities depending on how ionisable each analyte is. This often produces mass spectra with a high degree of complexity where only most ionisable analytes are observed [174, 188]. To allow for easier elucidation of peptide sequence from a biological mixture, prior separation via methods such as high performance liquid chromatography HPLC is often required. HPLC provides rapid, high-resolution separations using high pressure to force the solvent through narrow columns packed with fine particles. Reversed phase HPLC is a commonly used method for separation of biological peptide mixtures. Using this technique the peptides exist in equilibrium between a hydrophobic stationary phase and a hydrophilic mobile phase. When a gradient elution profile is applied, the percentage of organic solvent is altered over time. Elution of a component occurs when the percentage of the organic solvent is enough to shift the equilibrium to the mobile phase. The equilibria between the two phases is dependent on the hydrophobicity and conformation of the analyte, hence the rate at which a peptide moves through a HPLC column is predominantly dependant the amino acid sequence [174, 189-192].

2.4.2 Positive ion fragmentation

Positive ion mass spectrometry has been the predominant method used to elucidate peptide primary structure. In positive mode, peptides fragment at the amide bonds yielding *b* and *y* fragment ions. This allows sequence determination from the mass of the fragments (figure 2.6).

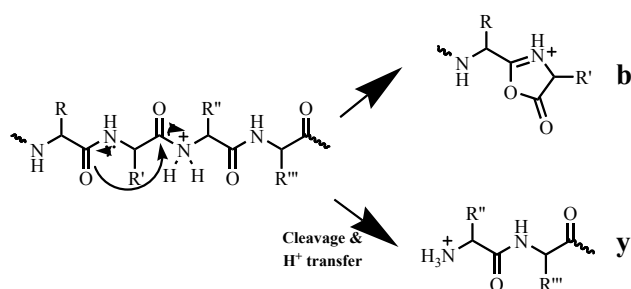


Figure 2.6: Cleavage of the amide bond of peptides yielding *b* and *y* fragment ions in the positive ion mode [193-196].

The *b* fragmentations provide the peptide sequence from the C-terminus of the peptide, whilst the *y* fragmentations provide the peptide sequence from the N-terminus. An example of the use of *b* and *y* fragmentation to sequence a peptide (caerin 1.7) is shown in figure 2.7.

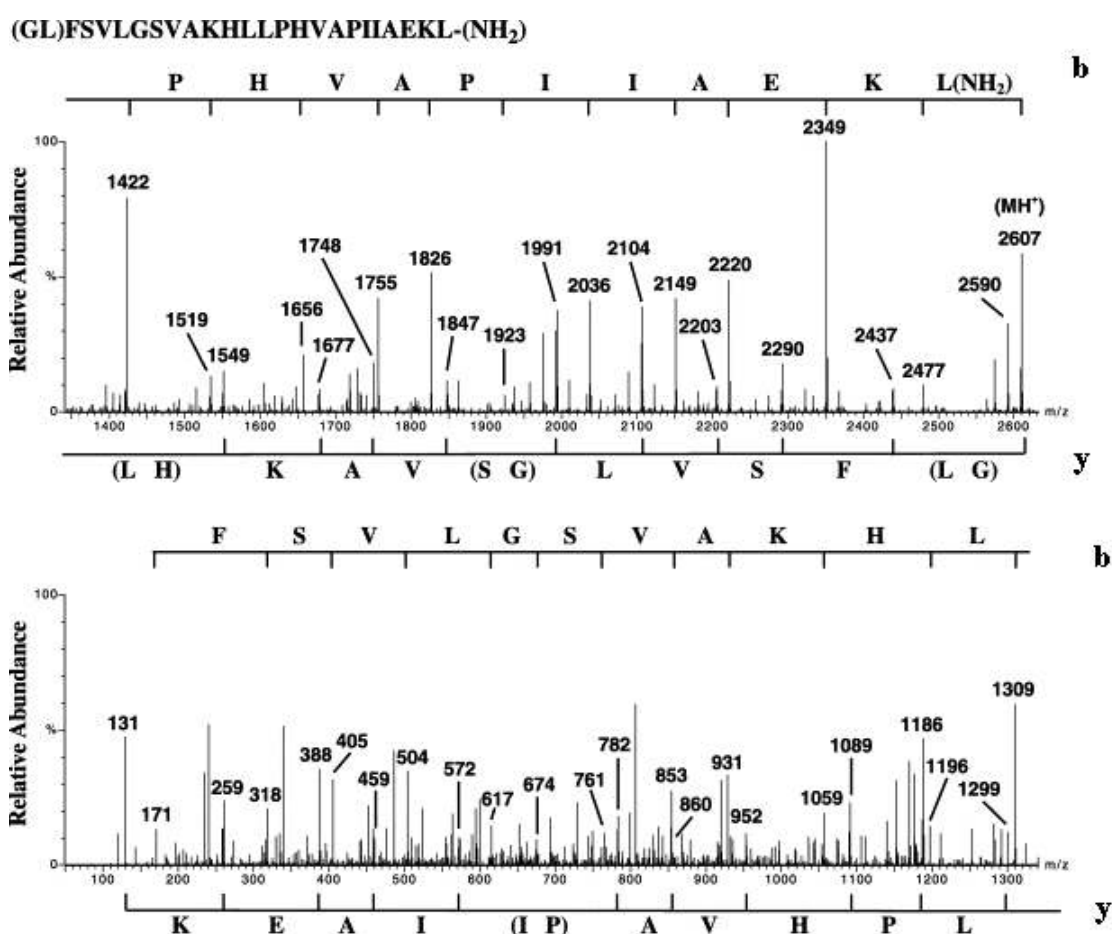


Figure 2.7: Electrospray positive ion MS/MS data for the (MH)⁺ ion from caerin 1.17 [197]. *b* and *y* cleavages are shown above and below the spectrum respectively.

2.4.3 Negative ion fragmentation

Mass spectrometry of peptides in the negative mode is performed less often than in positive mode because of the complexity of the spectra produced, and the MS/MS of peptides is seldom observed directly from the (M-H)⁻ ion. In negative ion mode, peptides

fragment at the amide bonds yielding α and β fragment ions, which are analogous to the b and y ions observed in the positive ion mode [198, 199].

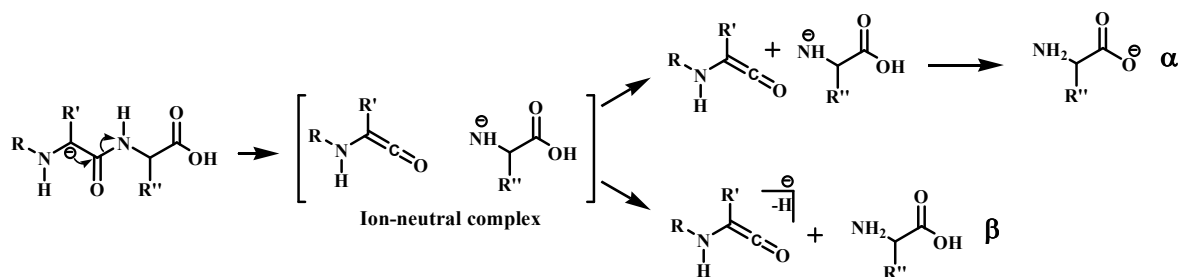


Figure 2.8: Proposed mechanism of amide bond cleavage of peptides yielding α and β fragment ions in the negative ion mode [198].

The α fragmentations provide sequence information from the N-terminal end of the peptide, β fragmentations from the C-terminal end. This provides sequence information, which is complementary to the positive ion fragmentations, as shown in negative ion ESMS of a peptide (caerin 1.7) in figure 2.9.

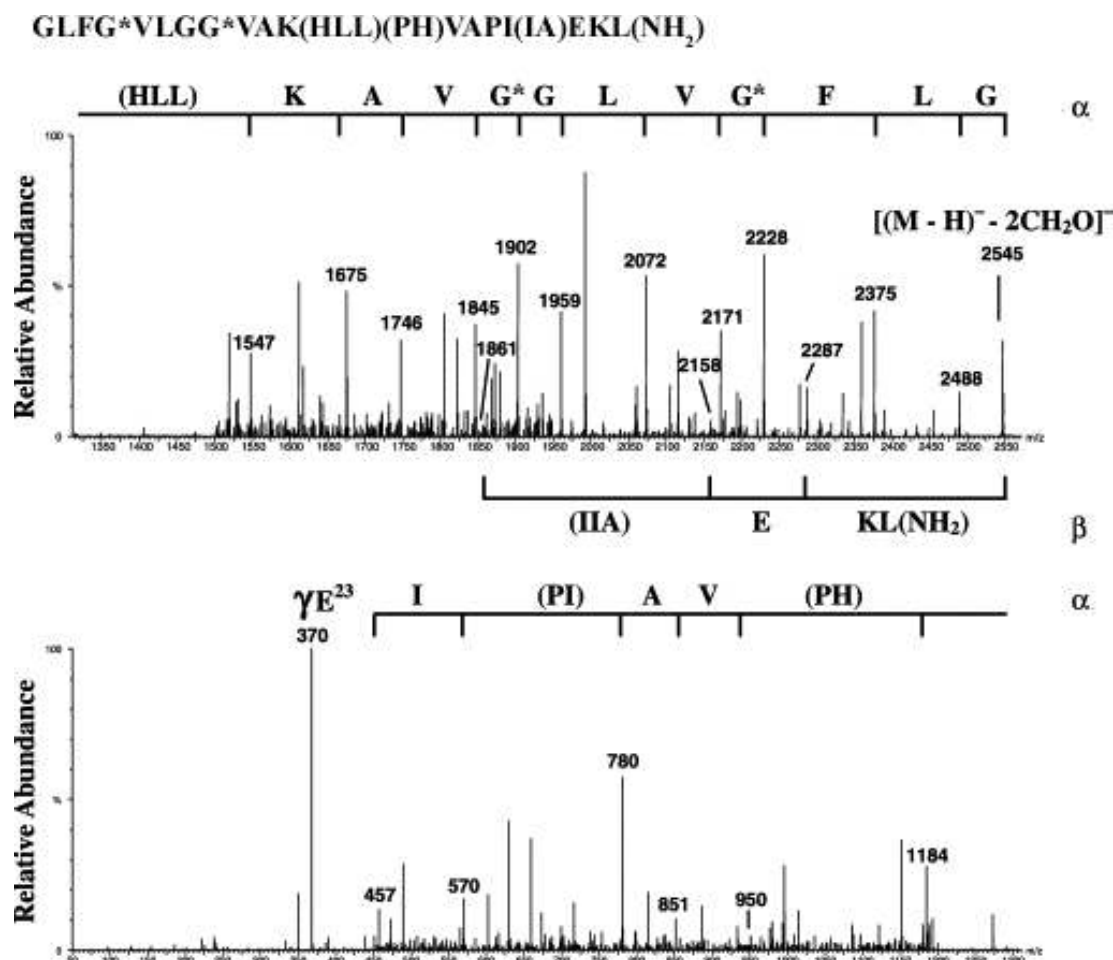


Figure 2.9: Electrospray negative ion MS/MS data for the $[(M-H)-2CH_2O]^-$ ion from caerin 1.17 [197]. α and β cleavages are shown above and below the spectrum respectively. G^* refers to Serine converted to a glycine via the facile side chain loss of CH_2O . The γE^{23} refers to the γ backbone cleavage ion produced by the sidechain induced cleavage of the glutamic acid residue.

Negative ion mass spectra can occasionally provide additional sequence data as some backbone cleavages may be observed at parts of the peptide which are not observed in the positive ion mode. In addition to the backbone cleavages, side chain cleavages (such as the loss of CH_2O from serine residues) and side chain induced backbone cleavages (producing γ and δ ions) can occur, and are often observed at a much greater intensity than the α and β backbone cleavages [68, 200, 201].

2.4.4 Edman Sequencing

Sequencing peptides from amide cleavages using mass spectrometry can be limited where the amino acid residues are isobaric: namely Leucine and Isoleucine (113 Da) or Lysine and Glutamine (128 Da). These isobaric amino acids can, however, be differentiated by instruments that can perform high resolution MS/MS analysis [202, 203]. Alternatively, Edman sequencing provides complementary peptide sequential information to support the mass spectrometry data and identify any isobaric residues. The technique uses cycles of reactions between phenylisothiocyanate and a free terminal amine group on a peptide bound to a solid support. This causes the formation of a phenylthiocarbamoyl peptide derivative, further treatment with strong acid affords the phenylthiohydantoin derivative of the N-terminal amino acid which is loaded onto a HPLC column. The amino acid is subsequently identified from its known HPLC retention time. The free terminal amine of the remaining peptide undergoes further reactions with phenylisothiocyanate in a stepwise cycle (figure 2.10); removal and identification of amino acids occurs sequentially from the N-terminus [204-206].

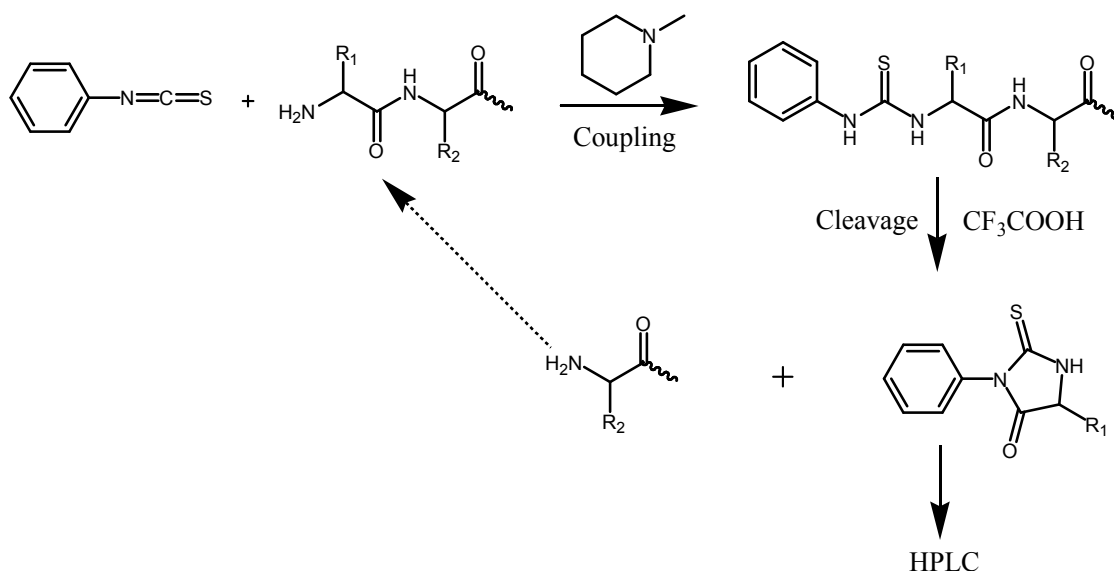


Figure 2.10: Schematic representation of Edman degradation of a peptide.

Edman sequencing is a very sensitive technique (samples can be as low as the picomolar concentrations) which can be ran in an automated fashion to afford efficient elucidation

of the primary structure of a peptide. Edman sequencing however is seldom solely used to sequence peptides, as for each cycle the reaction may not run to completion and contaminants are produced in each cycle. The HPLC traces produced can sometimes be difficult to conclusively identify the amino acid removed in each step. Also, Edman sequencing cannot be utilised when the N-terminal amide is blocked or derivatised (such as when the N-terminal residue is pyroglutamate) [199, 207].

Chapter 3

Methodology II – Nuclear Magnetic Resonance Spectroscopy

3.1 Nuclear magnetic resonance spectroscopy of peptides in solution

To understand the biological function of peptides, it is often necessary to identify their three-dimensional (3D) structures. X-ray crystallography is a principle technique of determining the 3D structure of a peptide or protein, with atomic resolution [208, 209]. This requires the sample of interest to be crystallized, which in many cases is arduous or not feasible. Also, X-ray structures may not insure a correct representation of the molecule in physiological conditions, due to crystal packing. NMR Spectroscopy is an alternative technique used to determine peptide structure in solution at an atomic level. It is a highly successful technique and is favourable to X-ray crystallography as it can provide a better representation of peptide structures in their native state, that is, where they are biologically active in solution.

Nuclear Magnetic Resonance (NMR) spectroscopy was first described by Isabel Rabi in 1938, when measuring the resonance of a gaseous lithium chloride beam placed in a variable magnetic field [210]. The technique was later refined and described by Felix Bloch and Edward Mills Purcell in 1946, for solution and solid state samples [211, 212]. They shared the Nobel prize in Physics in 1952 for their work. The first report of NMR spectroscopy of biological media was in 1954 by Jacobson et al. [213], measuring the hydration levels of deoxyribonucleic acid (DNA) in water using ^1H NMR. Three years later Masatami Takeda and Oleg Jardetzky performed NMR studies of amino acids and simple peptides [214]. Further NMR studies by Francis Bovey and Kurt Wüthrich in the late 1950's through to the 1970's pioneered the progression of biological NMR studies; from simple amino acids, to peptides and proteins [215, 216]. Advances in NMR techniques and technology, such as high field spectrometers, Fourier transform NMR, multidimensional NMR experiments, and high performance computing facilities has lead to great advances in the structural studies of proteins and peptides [217-220].

In recent years NMR has become an effective technique for determining peptide and protein molecular structure. The technique can also be used to probe the dynamics, molecular folding, conformational equilibria, as well as intra- and intermolecular interactions [221]. Additionally solid-state NMR techniques provide information on peptide structure and orientation in biological media such as phospholipid membranes (see Chapters 6 and 8). This chapter outlines the fundamentals of NMR spectroscopy, and how it is utilized in conjunction with computational techniques to elucidate peptide structure.

3.1.1 Principles of nuclear magnetic resonance spectroscopy

The principles of NMR are based on the fact that nucleons (protons and neutrons) possess an intrinsic angular momentum, referred to as ‘spin’, and are represented by a spin quantum number, I . In many nuclei (such as ^{12}C , ^{16}O and ^{24}Mg) each proton is paired with another proton, and likewise for neutrons; the total given I for these nuclei is zero. Only nuclei with unpaired nucleons (such as ^1H , ^2H and ^{13}C), where $I \neq 0$, are said to be NMR active. A list of nuclei commonly used in biological NMR is given in Table 3.1.

Table 3.1: Nuclei commonly used in biological NMR.

Nucleus	Unpaired Protons	Unpaired Neutrons	Nuclear spin (I)
^1H	1	0	$\frac{1}{2}$
^2H	1	1	1
^{13}C	0	1	$\frac{1}{2}$
^{15}N	1	0	$\frac{1}{2}$
^{19}F	1	0	$\frac{1}{2}$
^{31}P	1	0	$\frac{1}{2}$

In the absence of an external magnetic field, all nuclei are equivalent in energy. However, in the presence of an external field, nuclei can exist in $(2I + 1)$ orientations (figure 3.1). Thus a nucleus such as ^1H ($I = \frac{1}{2}$) can exist in two spin states: a low spin state (N_α – parallel to the external magnetic field), or a high spin state (N_β – antiparallel to the

external magnetic field). The small amount of energy between the two states is given by the equation;

$$\Delta E = \frac{h\gamma B_0}{2\pi}$$

where h is Planck's constant, γ is the gyromagnetic ratio (the ratio of the magnetic moment to the intrinsic angular momentum of a spinning particle, unique for each type of nucleus) and B_0 is the strength of the applied magnetic field in Tesla.

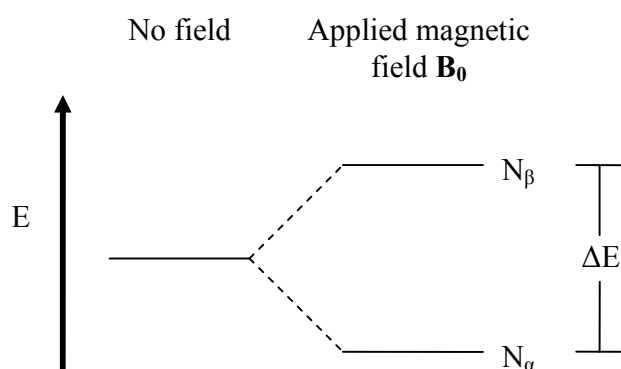


Figure 3.1 The energy states of populations of nuclei with spin ($I = 1/2$) in the presence of an applied magnetic field B_0 .

The primary populations of energy levels of nuclei such as ^1H ($I = 1/2$) in the presence of an external magnetic field are described by the Boltzmann distribution [187]:

$$\frac{N_\alpha}{N_\beta} = e^{\frac{-\Delta E}{kT}}$$

where k is the Boltzmann constant and T is the absolute temperature. A slightly greater population of nuclei will be in the N_α state relative to the N_β state, though the difference

is very minute at 298 K (~0.01 %), even when a strong magnetic field is applied. Hence NMR is a relatively insensitive technique [187, 222].

The difference in energy between spin states is quite small, corresponding to energies within the radio frequency (*rf*) range. The application of electromagnetic radiation can promote populations of nuclei with spins aligned with the external magnetic field \mathbf{B}_0 (lower energy spin state, N_α) to spins opposed the external magnetic field (a higher energy spin state, N_β) altering the total magnetic moment of the nuclei. The energy between spin states is equivalent to the frequency at which the nuclei precess in the applied magnetic field. This frequency is known as the Larmor frequency ν , which is defined as:

$$\nu = \frac{\gamma \mathbf{B}_0}{2\pi}$$

For a magnetic field of 14.1 Tesla, the Larmor frequency corresponds to 600 MHz for ^1H nuclei [187].

3.1.2 One-dimensional NMR spectroscopy

To understand how an NMR spectrum is acquired, firstly one should understand the schematics of an NMR probe, as illustrated in figure 3.2. Two magnetic poles create a strong magnetic field \mathbf{B}_0 (z-axis) orthogonal to the axis of a spinning sample tube (y-axis). The strength of the magnetic field is moderated by sweep coils in order to scan over a small range of magnetic field strengths. A radiofrequency transmitter emits the *rf* pulses to excite the nuclei of interest, and the precession of these nuclei is detected by a receiver coil mounted around the sample tube [222, 223].

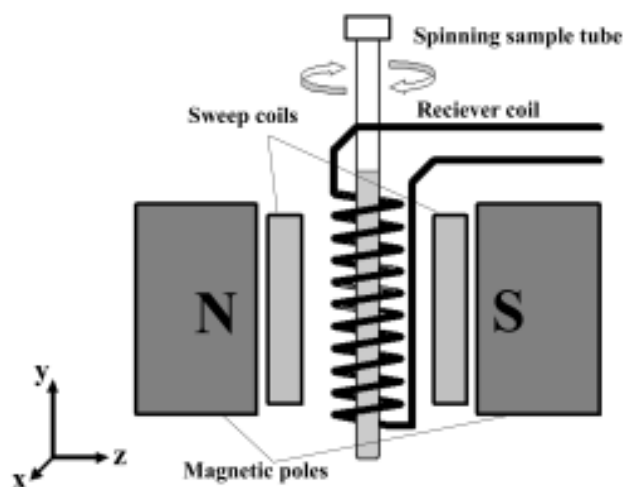


Figure 3.2 General schematic of NMR probe. The north and south magnetic poles are represented by N and S, respectively. Based on figures from [222, 223].

The effect of applying an rf pulse on nuclei precessing in a magnetic field \mathbf{B}_0 is best represented using vectors, as illustrated in figure 3.3. The rotational axis about which nuclei precess in a magnetic field \mathbf{B}_0 (z-axis) has a slightly higher population aligned parallel to the field \mathbf{B}_0 . The result is a bulk magnetisation in the direction of the applied magnetic field, represented by the vector \mathbf{M}_0 .

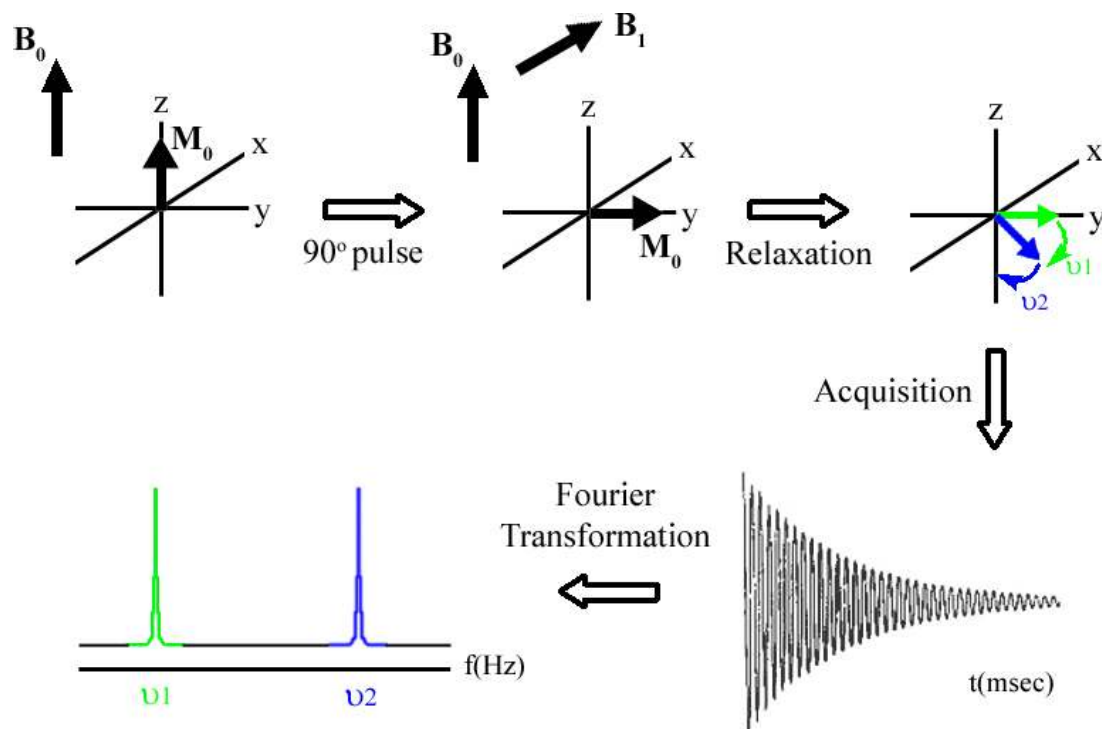


Figure 3.3 Vector Representation of the 1D NMR experiment. The vector diagrams representing the precession of nuclear resonances following the application of a 90° *rf* pulse. The acquired FID signal is converted to a 1D NMR spectrum via a Fourier transformation. Adapted from [224].

Acquisition of an NMR spectrum, occurs as follows: a strong *rf* pulse is applied, for a short duration of time t_p (usually in the order of microseconds). The *rf* pulse does not need to be monochromatic and can cover a range of frequencies, depending on the nuclei of interest. As the nuclei precess, an oscillating magnetic field B_1 is produced in the x-axis. The resultant net magnetisation M_0 is rotated into the xy-plane through some angle θ ; in most NMR experiments, t_p is selected such that θ is 90° . Once M_0 is in the xy-plane, it precesses about the applied magnetic field B_0 . As M_0 relaxes back to the equilibrium state, an induced electrical current is detected by a receiver coil mounted orthogonal to the magnetic field, that is affected by oscillations of the y-axial component of M_0 [187, 222, 225]. The induced oscillating current reduces with time, as an exponentially decaying cosine signal. The signal produced by the relaxation of M_0 is called free induction decay (FID). The FID signal can be acquired over a number of cycles to

improve signal to noise ratio. Following acquisition, the FID is converted from the time domain to the frequency domain via applying a Fourier transform function. The resultant 1D NMR spectrum displays the given Larmor frequencies of the nuclei of interest [221, 222, 225].

If all of the nuclei observed in a NMR spectrum were identical, the energy difference between their spin states and the corresponding Larmor frequencies would be the same. This would result in an NMR spectrum with one peak. However, in most instances, this is not the case. Fortunately in an NMR experiment, small magnetic fields induced by moving electrons perturb the magnetic field experienced by each nucleus. This localised electronic effect is known as nuclear shielding [226].

Nuclear shielding alters the energy difference between the high and low spin states of a given nucleus, altering the Larmor frequency as it precesses in the xy-plane. The magnitude of a magnetic field generated from moving electrons about a nucleus, is dependent on the local chemical structure and geometry. Hence upon Fourier transformation of an acquired FID, unique peaks will be observed for each nucleus in a distinct chemical environment [226]. This phenomenon is commonly employed by chemists to differentiate molecular constituents using NMR.

In order to eliminate the effect of an external magnetic field on the range of Larmor frequencies observed in an NMR spectrum, they are normalised to a given standard compound, and converted to the chemical shift scale as follows:

$$\delta = \frac{\nu_{sample} - \nu_{reference}}{\text{operating frequency}} \times 10^6$$

where δ is the chemical shift in parts per million (ppm) and the operating frequency is in MHz. Larmor frequencies are dependent on the operating frequency (and the applied magnetic field strength). The chemical shift scale is advantageous as it normalizes NMR signals, producing a chemical shift value that is independent of the operating frequency

[227]. The most common reference compound used in ^1H and ^{13}C NMR is tetramethylsilane (TMS), $(\text{CH}_3)_4\text{Si}$.

3.1.3 Two-dimensional NMR spectroscopy

Biopolymers such as peptides contain a large number of magnetically inequivalent nuclei, though many have close chemical shift values. This makes assigning a conventional 1-dimensional NMR spectrum very difficult due to the sheer number of resonances and a high degree of signal overlap. The addition of a second dimension is of a great advantage as additional correlations between nuclei can be observed on a 2-dimensional contour spectrum, and the chemical shifts of nuclei can be assigned that would otherwise be unresolved in a 1-dimensional NMR spectrum. A large portion of this study involves the assignment of peptide resonances and solution structure determination using a combination of 2-dimensional NMR methods.

The pulse sequences of all 2-dimensional NMR experiments share a characteristic series of steps: a preparation period, where the net magnetisation \mathbf{M}_0 is altered from the equilibrium state; an evolution period (t_1), an incremental delay of time where the nuclear spins are allowed to precess freely without any *rf* pulses; a mixing period (τ_m), where spins are correlated to one another; and a detection period (t_2) [224, 227]. The preparation period works in a similar way to a 1D NMR experiment, where nuclear spins are established such that the nuclei can be labelled by their chemical shifts. 2D NMR experiments are generally recorded using variable increments of the evolution period t_1 [228]. A Fourier transformation of both t_1 and t_2 into the frequency domain, followed by normalization, yields a 2D chemical shift spectrum $S(\delta_1, \delta_2)$ [229]. A visual representation of a generalized 2D NMR experiment is shown in figure 3.4.

The assignment of resonances of a peptide is possible through a combination of 2D experiments, as detailed in further sections. The information derived from the NMR data provides the foundation for peptide secondary structure determination.

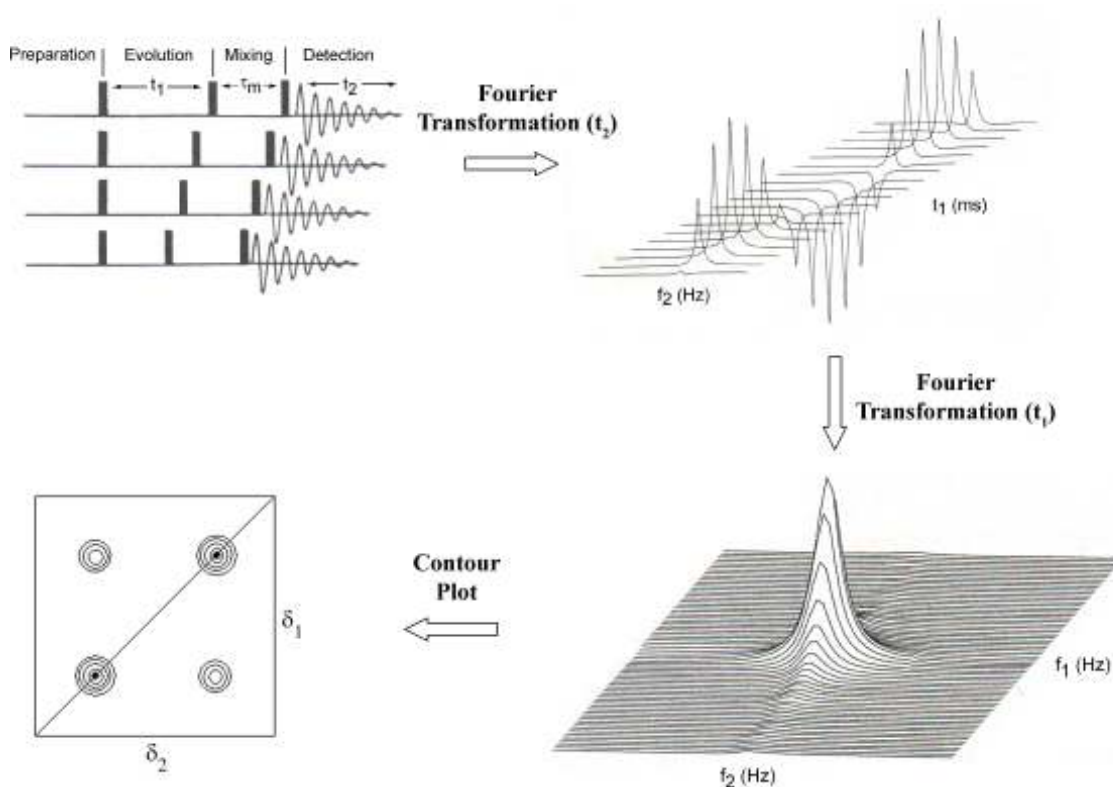


Figure 3.4 The 2-dimensional NMR experiment. Generalised pulse sequence, and separate Fourier transformations of t_1 and t_2 produces a 2-dimensional contour plot. Figure adapted from [230].

3.1.3.1 Correlation NMR spectroscopy

The simplest of the homonuclear 2D NMR methods is the Correlation spectroscopy (COSY) experiment. ^1H COSY NMR spectra indicate protons which are spin-spin coupled to one another; that is, connected by up to three covalent bonds. This is very useful in identifying closely connected protons within a peptide. The experiment involves two applied 90° *rf* pulses, separated by a variable duration t_1 , followed by acquisition of the FID signal during t_2 [224] (figure 3.5).

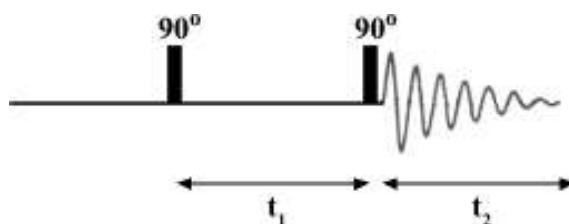


Figure 3.5 The pulse sequence of a COSY experiment.

The initial 90° pulse pushes magnetisation into the xy -plane which evolves over the t_1 period. The second 90° pulse rotates the y -axis magnetic constituent into the z -axis, this magnetic constituent cannot be observed by the receiver coil. However, the redistribution of the magnetisation through scalar spin-spin coupled (correlated) nuclei via coherence transfer, produces an observable effect [224, 231, 232]. Following Fourier transformation in each dimension, the resultant spectrum displays cross-peaks that are symmetrical about the diagonal, revealing spin-spin coupled protons, two or three bonds apart. Hence COSY spectra are used to indicate couplings between resonances of the same amino acid residue within a peptide.

One limitation within COSY spectra is the presence of peaks with the same chemical shift in both dimensions: the result of spins which are unaffected by the second 90° pulse [224]. These spins appear on the diagonal of the spectrum, are in phase, and yield the same information as the 1D NMR spectrum. The accumulation of signal intensity (and line-broadening) on the diagonal results in a much larger intensity than that of other significant cross-peaks, which appear as antiphase multiplets. The antiphase multiplets can have complex contour shapes as a result of (i) same phase coupling causing absorptive intensities and (ii) mixed phase (positive and negative) intensities cancelling each other out. Many cross-peaks can be obscured by the diagonal when phasing a COSY spectrum, or they may not be observable due to lack of sensitivity [224, 233].

Numerous alterations to the COSY experiment have been developed to improve assignment of proton resonances. For example, double quantum filtered COSY (DQF-COSY) experiments involve use of an additional 90 degree pulse after t_1 within the pulse sequence. Quantum filtration involves selecting for specific coherence transfer pathways. These coherences of magnetisation are denoted by the coherence order p , which is an integer, where zero quantum coherence is denoted by $p = 0$, single quantum coherence $p = \pm 1$, double quantum coherence $p = \pm 2$, and so forth. For all coherence transfer pathways, initially $p = 0$, where \mathbf{M}_0 is in the z -axis and the only observable signal is where $p = \pm 1$, and the net magnetisation \mathbf{M}_0 is $\pm y$ (see figure 3.3). In the conventional

cosy experiment pulse sequence is set up such that all coherences where $p = \pm 1$ are observed in the FID. In the case of DQF-COSY, the pulse sequence is set up such an additional 90 degree pulse after t_1 and phase switching delay is inserted into the sequence to select for all coherence transfer pathways where $p = -1$, and M_0 is $-y$, as illustrated in figure 3.6.

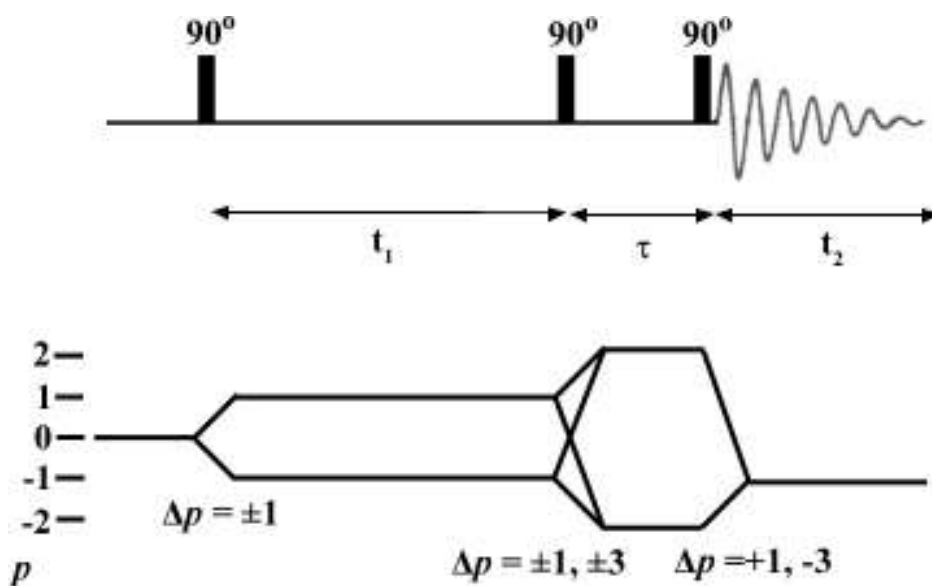


Figure 3.6 The pulse sequence of a DQF-COSY experiment (upper), and the coherence transfer pathway (lower). The given coherence orders are denoted by the black lines and Δp for each 90° pulse are also shown. Based on a figure from [234].

This technique halves the total amount of observable magnetisation that is in phase prior to FID detection (t_2), as the observable signal is where $p = \pm 1$. Also, by selecting for $p = -1$, the resultant cross-peaks in the 2-dimensional spectrum are purely absorptive. This makes the technique less sensitive relative to the conventional COSY experiment. However, the decrease in line broadening and signal overlap and allows for enhanced resolution, and lowers the intensity of the cross-peaks along the diagonal of the 2-dimensional NMR spectrum relative to a conventional COSY spectrum [224, 233]. Additional pulses and phase switching delays can be inserted into the pulse sequence: e.g.

in triple quantum filtered COSY (TQF-COSY) [224]. DQF-COSY is predominantly used for the purposes of this NMR study.

3.1.3.2 Total correlation NMR spectroscopy

Since COSY spectra only indicate couplings within two to three bonds of one another, this can make assignment difficult for nuclei with similar chemical shifts. Total correlation spectroscopy (TOCSY) extends the information possible by indicating resonances within a spin system across many bonds and relies on cross-polarization rather than spin-spin coupling [235, 236]. TOCSY is a very advantageous technique for the NMR of peptides as cross-coupling does not traverse an amide bond. Thus each amino acid residue can be analysed as a separate spin system.

The TOCSY pulse sequence involves the application of a single coherent *rf* field during the mixing time τ_m ; this is known as a spin-lock field (figure 3.7). When the *rf* field is applied, two spins become momentarily equivalent and exchange magnetisation in an oscillatory fashion. The exchange of magnetisation between scalar coupled spins is relayed connectively across all coupled spins (cross-polarisation). Thus cross-peaks can be observed due to coupling of all resonances within a spin system. In a two spin system, an entire transfer of magnetisation occurs when τ_m corresponds to $\frac{1}{2} J$, where J is the scalar coupling constant between the spins. For larger and more complex molecules, a number of spectra with different τ_m times can be applied to observe scalar coupling throughout an entire spin system.

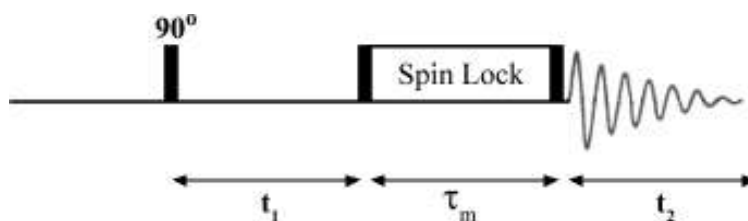


Figure 3.7 The pulse sequence of a TOCSY experiment.

As discussed, all amino acid residues can be assigned as separate spin systems within a TOCSY spectrum as cross polarization does not transfer through an amide bond. The random coil proton chemical shifts of the twenty commonly occurring amino acids have

been published [237]. These in turn can be used to derive a cross-peak motif for any given amino acid residue. In many cases, amino acid residues are initially assigned via labelling amide proton resonances correlated to sidechain proton resonances [238].

All of the peaks within a TOCSY spectrum (including the diagonal) are in phase and absorptive. Thus TOCSY spectra tend to have better resolution and sensitivity relative to COSY spectra. TOCSY spectra can, however, produce negative peaks as a result of cross-relaxation because of nuclear Overhauser effects (see section 3.1.3.3). This problem generally does not occur when short mixing times are used, as is the case for most TOCSY experiments involving peptides [224].

3.1.3.3 Nuclear Overhauser effect NMR spectroscopy

The nuclear Overhauser effect arises from the transfer of magnetisation between irradiated nuclei and nearby nuclei via cross-relaxation. Nuclear Overhauser effect spectroscopy (NOESY) experiments differ from COSY and TOCSY experiments as it involves a transfer of magnetism through space, not through bonds. Thus NOESY spectra indicate couplings of nuclei that are close in spatial proximity. The information from NOESY spectra are used to sequentially assign amino acid residues, and to determine distances between pairs of nuclei. These derived distances are used to determine the secondary structure of a peptide.

The pulse sequence of a NOESY experiment is quite similar to that of a TOCSY experiment (see figure 3.8). An initial 90° pulse forces the net magnetisation into the xy -plane, where spins evolve over a variable time t_1 . The second 90° pulse is orthogonal to the first rotates a portion of the net magnetisation into the z -axis. During the mixing period τ_m , spins which are not in equilibrium transfer their magnetisation through space via dipolar coupling. The third 90° pulse pushes any remaining magnetic component from the z -axis into the xy -plane and the FID is detected in t_2 [239]. Mixing times τ_m for NOESY experiments are usually longer in comparison to those of TOCSY experiments, and also lack the applied coherent (spin-lock) rf field in the pulse sequence.

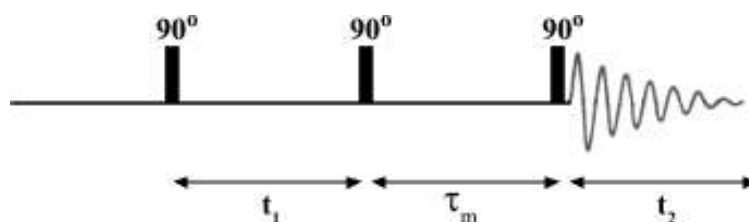


Figure 3.8 The pulse sequence of a NOESY experiment.

Depending on the internuclear distance, cross-peaks can be detected in NOESY spectra as a result of inter- or intramolecularly coupled nuclei. The relative intensity of a NOE signal is inversely proportional to the sixth power of the internuclear distance ($I \propto r^{-6}$). As a result, NOE cross-peaks can be detected from dipolar coupling of nuclei up to an approximate internuclear distance of 5 Å [187, 240].

The internuclear distances determined from NOESY spectra are not entirely accurate due to a number of contributing factors. (i) The peptides are in solution and subject to molecular vibration and conformational changes, thus the observed NOE signals are representative of the average internuclear distances. (ii) Overlap of cross-peaks that are very close to their observed chemical shifts in both dimensions can result in more intense, broader cross-peaks. (iii) Spin diffusion, as a result of the cross-relaxation spreading among many nuclei can also affect cross-peak intensities. In general, these factors are only a problem with larger molecules >10 kDa and the experimental parameters can be altered to minimise these effects. It is also possible that coherence transfer can also be observed in NOESY spectra, however, this effect can be minimised by pulsed field gradients (the use of nonuniform magnetic fields \mathbf{B}_0 over short durations of time) and phase cycling (repeating pulse sequences over a number of cycles prior to FID detection). To minimise the effects of these inaccuracies, NOE intensities are grouped into higher and lower intensities prior to distance restraint conversion (section 3.1.5).

3.1.4 Chemical shift Assignment

The first step toward chemical shift assignment of peptides, involves the use of correlation spectroscopic methods, namely TOCSY and COSY. Initially the TOCSY spectrum is analysed using the amide (NH) protons on the backbone of the peptide. Each

of the cross sections corresponding to the amide protons show correlations with protons at the α , β , γ , δ , and ϵ positions (where appropriate) of the amino acid residues. The characteristic pattern of cross-peaks for each type of amino acid can be determined from previously published chemical shifts [224, 237]. In many cases, particularly with larger peptides, there is a high degree of cross-peak overlap in the TOCSY spectrum. The COSY spectra can be used to resolve some overlapping cross-peaks from the TOCSY spectrum in where correlations are observed between protons 2-3 bonds apart. The COSY spectra can also be employed to ensure each chemically distinct proton of an amino acid residue is correctly assigned, from correlations between the amide and α protons, α and β protons, and so on. So, each resonance is assigned in a stepwise fashion, along the amino acid side chain.

Once the amino acid resonances are assigned based on their TOCSY and COSY cross-peak patterns, the NOESY spectrum is used to ensure the correct ordering of the amino acid residues within the peptide sequence. This is done by assigning correlations between protons of neighbouring amino acid residues that are close in space, this is known as 'sequential assignment'. The most useful correlations used are NH_i to NH_{i+1} , αH_i to NH_{i+1} and βH_i to NH_{i+1} [241]. The intensities of these NOESY cross-peaks are largely dependent on the conformation and local secondary structure of the peptide. However, all allowed peptide backbone conformations show at least 1 interproton distance within 3Å between neighbouring amino acids, therefore producing observable correlations in the NOESY spectrum [229]. Breaks in the sequential assignment using amide proton cross-peaks occurs where prolines are present in the sequence, as prolines are cyclic and contain no amide proton. In those cases, sequential assignment can be made upon observing correlations between protons of the previous amino acid, and the α or δ protons of the proline residue.

Additional problems can arise in the sequential assignment of peptides, largely from cross-peak overlap, due to correlations between pairs of nuclei with similar chemical shifts. This factor increases with the length of the peptide. Other problems can arise where α proton chemical shifts are obscured by large water peaks, when the experiment is

performed in aqueous media. In some cases, α proton and α carbon correlations, can be assigned from Heteronuclear single quantum coherence (HSQC) NMR spectra.

3.1.5 NOE Connectivities

Once the sequential and intraresidual signals have been assigned, the remaining NOE signals can be assigned and converted to interproton distances (NOE connectivities). NOE connectivities are the result of interproton distances within 5Å, and are highly dependant on peptide folding and secondary structure [242]. They are grouped into short (one residue), medium (two to four residues) and long range (greater than five residues) NOE connectivities. The NOE connectivities are described by the standard notation, as $d_{AB(i,i+N)}$, where two protons A and B are on residues i and $(i + N)$ respectively, and N is the number of residues from residue i (ie. $N = 1$, for sequential NOEs). All connective distances are defined across the entire peptide, and the residue indices are often omitted from the standard notation of sequential NOE connectivities (i.e. $d_{AB} \equiv d_{AB(i,i+1)}$) [229].

Different secondary structure types such as α -helices, β -strands and turns show a characteristic pattern of observed NOE connectivities (see figure 3.9). The spiral secondary structure of an α -helix is characterised by strong d_{NN} , medium $d_{\alpha N}$, $d_{\alpha N(i, i+3)}$, and $d_{\alpha\beta(i, i+3)}$ NOE connectivities. In addition, sometimes weak $d_{NN(i, i+2)}$ and $d_{\alpha N(i, i+4)}$ NOE connectivities can also be observed. In contrast, β -strands are characterised by stronger $d_{\alpha N}$ and weaker d_{NN} NOE connectivities, as a result of low curvature in the backbone structure. Also, a lack of sequential $d_{N\alpha}$ NOE connectivities, is a common characteristic of β -strand structures [243, 244].

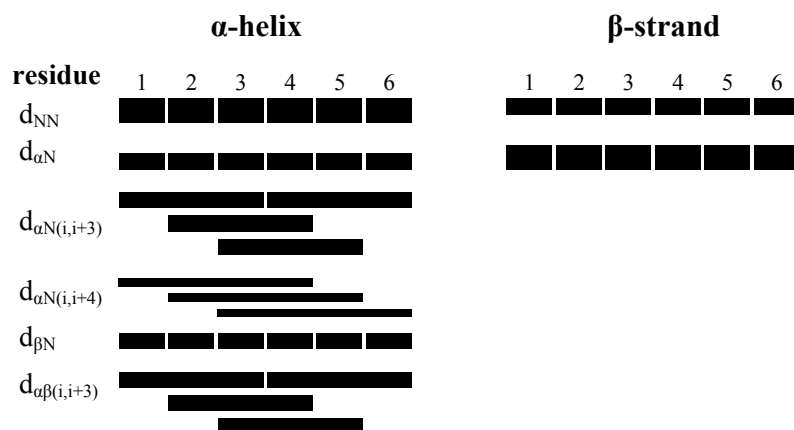


Figure 3.9 Characteristic patterns of short-range NOEs seen for ideal α -helices and β -strands. The relative intensities of NOE connectivities are indicated by the thickness of the bars [229].

Proline can undergo *cis-trans* isomerisation about the imide bond between proline and the preceding residue. NOE connectivities between the α proton of the preceding residue with the δ and α protons of the proline are used to indicate which isomer is present. In the *cis* form there is a stronger $d_{\alpha\alpha}$ NOE interaction, and in the *trans* form there is a stronger $d_{\alpha\delta}$ interaction (figure 3.10). In most cases, the *trans* isomer predominates [245].

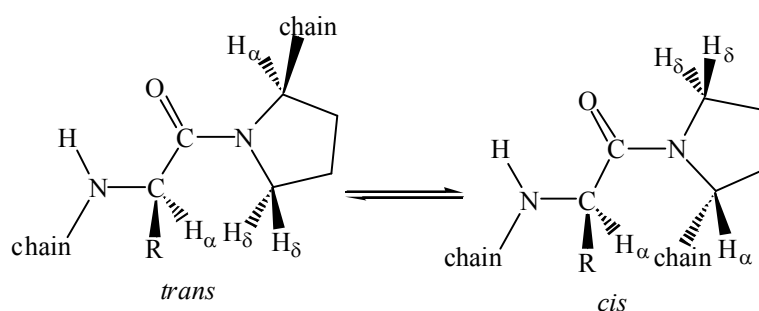


Figure 3.10 The *cis-trans* isomerisation of the imide peptide bond between proline and the preceding residue.

In many cases, not all of the NOE connectivities can be determined from the NOESY spectrum. Some signals can be obscured by the diagonal, α proton signals can be obscured by the water signal, and signals can overlap where chemical shifts are coincidental [224].

3.1.6 Secondary shifts

The chemical shift of a given nucleus is affected by the chemical environment and molecular geometry, and this can be used in the NMR study of peptides to indicate secondary structure. In ^1H NMR, the observed chemical shifts of the amide protons and α protons along the peptide backbone is highly dependent on the local secondary structure. Previously determined random coil chemical shifts ($\delta_{\text{random coil}}$) [237] are compared to the observed chemical shifts (δ_{observed}) of a given peptide, and described by a secondary chemical shift value ($\Delta\delta$), that is equal to:

$$\Delta\delta = \delta_{\text{observed}} - \delta_{\text{random coil}}$$

Plotting $\Delta\delta$ against the amino acid sequence provides an indication of regions of consistent secondary structure throughout the peptide. In many cases the $\Delta\delta$ value is smoothed over ± 2 residues. This reduces the possibility of misinterpretations, due to the local external effects on chemical shifts from proximal polar and aromatic groups.

Studies based on statistical analysis of NMR structures and further theoretical calculations show that on average, α proton secondary chemical shifts are approximately -0.39 ppm within an α -helix, and +0.37 ppm within a β -strand or extended structure [246, 247]. Amide proton chemical shifts are a lot more sensitive to pH and temperature, though some degree of interdependence between the secondary chemical shift and the secondary structure has been established [247].

In the case of amphipathic α -helices, where one face of the helix is hydrophobic and the other hydrophilic, amide proton secondary shifts often show an evident pattern of varying $\Delta\delta$ across 3-4 residues. Generally, $\Delta\delta$ values are positive about the hydrophobic face, and negative about the hydrophilic face [248, 249]. This is considered to be due to intermolecular hydrogen bonding effects between amide protons and carbonyl groups of the peptide backbone. The shorter the hydrogen bond, the more shielded an amide proton is, causing a downfield shift. Within hydrophobic regions of an α -helix, the intramolecular hydrogen bonds are stronger and shorter, and access to polar solvents (such as water) is limited, resulting in a positive $\Delta\delta$. In hydrophilic regions, the intermolecular hydrogen bonds are weakened and lengthened, and the hydrogen bonds are effectively shared with polar solvents and polar amino acid sidechains, resulting in a negative $\Delta\delta$ [248, 250].

3.1.7 Coupling constants

In NMR, characteristic spin-spin coupling constants can be observed between nuclei a few covalent bonds apart. The coupling effect is dependent on the spin pairing of each nucleus and the electrons of the covalent bonds connecting the nuclei. In this way, the coupling is sensitive to the bonding network and spin orientations of the nuclei [224]. The coupling causes observed peaks to appear as multiplets, with $2I + 1$ number of lines, where I represents the spin quantum number of the nearest nucleus, and the spacing of the lines is represented by a coupling constant, J [216, 251].

Coupling across three covalent bonds is denoted by the coupling constant 3J and is useful in identifying the secondary structure across the backbone of a peptide. 3J coupling to the α proton is observed from the splitting of amide proton shifts in the 1D NMR spectrum or the δ_2 dimension of the COSY spectrum. The coupling constant across three covalent bonds can be described by the Karplus equation:

$${}^3J = A + B\cos^2\theta + C\cos\theta$$

where A, B, and C are empirically-derived parameters whose values depend on the atoms and substituents involved and θ is the dihedral angle. In peptide structure, the amide to α proton coupling constant (${}^3J_{\text{NH}\alpha\text{H}}$) gives an indication of the range of possible dihedral angles, ϕ . The peptide backbone dihedral angle ϕ lies across the atoms C'_i , N_{i+1} , αC_{i+1} and C'_{i+1} , as illustrated in figure 3.11.

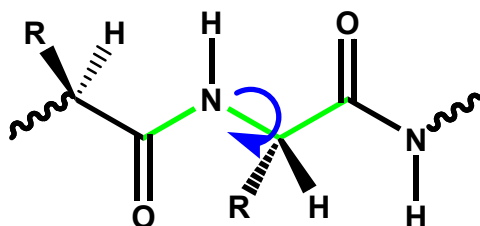


Figure 3.11 The peptide backbone dihedral angle ϕ , represented in green. ϕ is 180° in this representation.

Though the dihedral angle ϕ cannot be measured directly from the ${}^3J_{\text{NH}\alpha\text{H}}$ coupling constant, a range of structurally allowed dihedral angles can be determined. This is equated by substituting ($\theta = \phi - 60^\circ$) into the Karplus equation [252].

$${}^3J_{\text{NH}\alpha\text{H}} = 6.4\cos^2(\phi - 60^\circ) - 1.4\cos(\phi - 60^\circ) + 1.9$$

The equation gives up to four ϕ values for any given ${}^3J_{\text{NH}\alpha\text{H}}$ value, as shown in figure 3.12. ${}^3J_{\text{NH}\alpha\text{H}}$ values cannot be determined where prolines (no amide proton) or glycines (2 α protons) are present in the sequence.

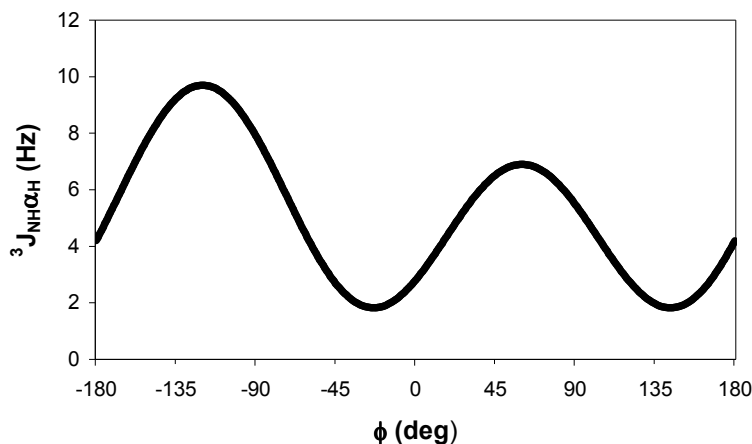


Figure 3.12 The Karplus curve illustrating the relationship between the backbone dihedral angle ϕ and the coupling constant $^3J_{\text{NH}\alpha\text{H}}$. Figure adapted from [253].

In all peptides, the usual allowed ϕ angles range from -30° to -180° . For an average α -helix the dihedral angle ϕ is -57° , for a parallel β -sheet it is -119° , and for an antiparallel β -sheet it is -139° . These have corresponding $^3J_{\text{NH}\alpha\text{H}}$ values of 3.9 Hz, 8.9 Hz and 9.7 Hz respectively. The $^3J_{\text{NH}\alpha\text{H}}$ values do not always correspond to the true dihedral angle ϕ , due to the molecular motion about the peptide backbone. The observed $^3J_{\text{NH}\alpha\text{H}}$ coupling constant is effectively the time-averaged value for all conformations, hence for a given $^3J_{\text{NH}\alpha\text{H}}$ value; a range of ϕ values are generated. In general, any $^3J_{\text{NH}\alpha\text{H}}$ below 6 Hz is considered to indicate α -helical secondary structure and any $^3J_{\text{NH}\alpha\text{H}}$ above 8 Hz considered to indicate β -sheet or β -strand secondary structure [229].

The $^3J_{\text{NH}\alpha\text{H}}$ coupling constants can be measured directly from a high resolution 1D NMR spectrum or from the antiphase multiplets in the second dimension (δ_2) of a COSY spectrum [254]. This becomes increasingly difficult with increasing peptide length, due to the increased probability of cross-peak overlap. Additionally some overestimations can be made where the spacing is smaller than the line width of the spectrum or where cross-peak overlap is observed. This also holds true for 1D NMR spectra, especially when neighbouring amide peaks are close in chemical shift [224, 229].

3.1.8 Peptide structure calculations

Peptide structure calculations are required to correctly represent the solution structure of a peptide and they provide a simplified means of collating all of the structural data from NOE connectivities, secondary chemical shifts, and $^3J_{\text{NH}\alpha\text{H}}$ coupling constants. The initial step in peptide structural calculations is to input the peptide chemical shift assignments, NOE connectivities and $^3J_{\text{NH}\alpha\text{H}}$ coupling constants. From these data sets, a series of proton-proton distance and dihedral angle restraints are generated. The next steps involve a series of computational Restrained Molecular Dynamics (RMD) and Simulated Annealing (SA) calculations. The end result is an array of 3D peptide structures, consistent with the NMR derived data.

The structure calculations used for these peptide studies were accomplished using the program ARIA (Ambiguous Restraints for Iterative Assignment) [255]. This program collates the NMR derived input data and converts it to distance restraints. It also specifies the calculation protocol for RMD and SA calculations and interfaces with a second program CNS-Solve (Crystallography and NMR System, version 1.2) [256], that essentially performs all of the 3D structure calculations. In this section, the stages of 3D peptide structure generation are discussed in detail.

3.1.8.1 NOE derived structural restraints

Within a NOESY spectrum, the intensity of NOE signals increase with increased mixing time, until it reaches a maximum and decreases to zero [257]. So, where the maximum signal is observed for a given mixing time, the longest couplings can be detected. Several other factors such as molecular tumbling time and localised molecular rotation rates can also affect NOE intensities. The rate of molecular tumbling is best described by the correlation time of the molecule, τ_c , which in turn affects the rate of NOE build-up. Parts of a molecule that rotate and vibrate at a faster rate, such as long sidechains, will exhibit greater NOE intensities [224]. Spin diffusion, as a result of the propagation of magnetisation across a molecule can also affect NOE cross-peak intensity. These factors mean that an exact calibration of NOE derived distance restraints is not possible. In the case of peptide NMR, NOE mixing times have been optimised to reflect the expected

correlation times (150-250 ms) to allow for sufficient interproton distance approximations [238].

A range of methods exist for the conversion of NOE intensities to distance restraints. In one such method, the interproton distance ranges are classified based on NOE cross-peak volumes as strong (1.8-2.8 Å), medium (2.8-3.8 Å) and weak (3.8-5.0 Å). To minimise inaccuracies, conservative upper and lower bound distance restraints are applied, whereby the lower bound restraints are set to a value determined by the sum of the van der Waals radii (1.8 Å) [241, 258]. The interproton distance (r_{ij}) between protons i and j is then calculated using the following equation [255]:

$$r_{ij} = \left[\frac{A(I)}{I_{ij}} \right]^{1/6}$$

where I_{ij} is the observed peak intensity for the coupling between the protons and $A(I)$ is an intensity proportionality factor, calculated using the following equation:

$$A(I) = \left[\frac{I - I_s}{I_w - I_s} \right] [A(I_w) - A(I_s)] + A(I_s)$$

where the average of the 10 weakest NOE intensities $A(I_w)$ is equal to:

$$A(I_w) = (5.0 \text{ \AA})^6 I_w$$

and the average of the 10 strongest NOE intensities $A(I_s)$ is equal to:

$$A(I_s) = (1.8 \text{ \AA})^6 I_s$$

These calculations calibrate the weakest NOE intensities to a corresponding distance of 5.0 Å, and strongest to 1.8 Å, in order to determine intensity-dependent proportionality factors for the remaining peaks.

When employing ARIA methodology, an additional error estimate (Δ_r) is used to determine the upper (U) and lower (L) bounds for the distances [255, 259]:

$$U = r_{ij} + \Delta_r$$

$$L = r_{ij} - \Delta_r$$

Rather than using a percentage of the distance r_{ij} , Δ_r is best determined from the square of the calibrated distances, as the error dependence of distance restraints is not linear. The error estimate is hence expressed using a second order polynomial [259]:

$$\Delta_r = 0.12 \times r_{ij}^2$$

This is only one of many functional methods available when using ARIA [259, 260]. In most cases altering the restrictiveness of the bound of r_{ij} does not greatly affect the outcome of the peptide structures [255, 261].

3.1.8.2 Ambiguous NOEs

The probability of NOE cross-peak overlap in a NOESY spectrum increases with molecular size, as does the probability of coincidental chemical shifts. In peptide NMR, this leads to a degree of ambiguity when assigning NOE resonances. In such cases where one cross-peak could be due to a number of possible correlations, the signal intensity cannot be directly converted into a distance restraint. Though all of the proton chemical shifts may be assigned, all possible cross couplings must be taken into account to ensure a complete derivation of the 3D peptide structure [262].

Generally, the majority of the assigned cross-peaks in the NOESY spectrum are unambiguous. So, when structural calculations are performed in an iterative process, only the unambiguous distance restraints are used in the first iteration. These initial structures give an indication of interproton distances throughout the entire peptide structure. Depending on the range of conformations produced, some ambiguity may be resolved as only 1 ambiguous interproton distance may be structurally allowed. With each iteration, the structures can be continuously refined in this way, improving the resultant structures [262, 263]. In some cases, violations of distance restraints may result depending on the initial assignment of the NOESY spectrum. Additionally, entirely different structures can result depending on the validity of the NOEs assigned. In these instances, violations to distance restraints or incorrect assignment of resonances require reassignment of the NOESY spectrum [259, 264].

Ambiguous NOEs may not need to be assigned to one proton pair in cases where cross-peak volumes are the result of multiple contributing NOE interactions, the sum averaging method can be employed [262, 265]. Given the NOE distance dependence and the isolated spin pairs approximation are both established [255], an ambiguous NOE intensity (I_{xy}) is dependent on the sum of the inverse sixth power of each contributing interproton distance:

$$I_{xy} \propto \sum_{a=1}^{N_{\delta}} r_a^{-6}$$

where a runs through all N_{δ} contributions to NOE cross-peak intensity, at frequencies x and y , and r_a is the distance between two protons to the a^{th} contribution. This means the NOE cross-peak corresponds to a summed distance (D), relative to the negative inverse sixth power of the NOE cross-peak intensity:

$$D \propto \left(\sum_{a=1}^{N_{\delta}} r_a^{-6} \right)^{-1/6}$$

So, the sum of the volumes of each contributing peak is summed to give the total intensity of the ambiguous cross-peak. This results in a number of constrained r_a values so that the equation is fulfilled. This method of ambiguous NOE assignment generally is less accurate, though it allows all possible interproton distances from NOEs to be expressed in the final structures [255, 262].

3.1.8.3 Stereo-specific assignment

The methylene protons of many amino acid sidechains exhibit unique chemical shifts. For this reason it is necessary to allow for stereo-specific assignment, to ensure distance restraints are correctly assigned [261, 266, 267]. This can often be achieved by assessing the relative NOE intensities of couplings with nearby protons, such as β -methylene protons with amide and α proton signals. This method is also utilised to stereo-assign methyl groups on valine, leucine and isoleucine sidechains [268]. Though this method can be successful, it is often quite difficult to assign, hence alternative automated methods are often used to achieve correct stereo-specific assignment. Also in regions where a high degree of molecular motion is present, the chemical shifts of methylene protons can become degenerate.

When using the program ARIA, stereo-specific assignment can be achieved by the ‘floating chirality’ method [269]. This method involves assigning stereo-specific resonances as pro-S or pro-R chirality, and allowing them to swap their assigned chirality. The ‘floating’ between chirality types has an associated ‘improper dihedral’ energy term. The chirality is usually resolved as the structures are refined over several iteration cycles, to achieve the minimal improper dihedral energy [241, 270]. In this way, stereo-assignment is achieved in an automated fashion, without specific assignment of the resonances.

3.1.8.4 Restrained molecular dynamics and simulated annealing

Molecular dynamics uses the known physical properties of molecules to calculate the minimal potential energies of the molecular structures. In the case of restrained molecular

dynamics (RMD), restraints obtained from NMR or X-ray crystallographic data are incorporated into the calculations [243, 261, 262]. Many types of RMD methodologies exist, all of which use a molecular dynamics force field to calculate molecular potential energies [264, 271-273].

The fundamental laws of physics involving the motions of particles form the basis of RMD calculations. The particles, in this case atoms, begin with an array of random Cartesian coordinates and subsequent velocities. The relative positions of the atoms are allowed to evolve with each calculation step, each with an intrinsic force calculated using Newton's second law of motion:

$$F_i = m_i a_i$$

where F_i is the force on the atom i , m_i is the mass of the atom and a_i is the acceleration. Both force and acceleration are expressed as vectors quantities. The force F_i on the atom can alternatively be calculated from the derivative of its potential energy (E) [224]. Also, the atomic acceleration a_i with respect to time t_i , can be expressed as the second derivative of the atomic coordinate r_i :

$$\frac{dE}{dr_i} = m_i \frac{d^2 r_i}{dt_i^2}$$

The equation can be integrated through small, successive time steps to determine the relative positions and velocities of each atom [224, 274]. The initial starting structures for RMD calculations may be unconventional, although generally starting structures are built using template structures, molecular modelling and by means of distance geometry algorithms [241, 258, 273, 275, 276]. The result of a RMD calculation is expressed using a total potential energy term (E_{total}). E_{total} depends largely on the protocol and restraint inputs described and how well they can be used locate the global minimum on a potential energy surface. The total energy of a structure is made up of the following potential energy terms [224, 244, 275]:

$$E_{\text{total}} = E_{\text{bond}} + E_{\text{angle}} + E_{\text{dihedr}} + E_{\text{improper}} + E_{\text{vdW}} + E_{\text{coulomb}} + E_{\text{NOE}}$$

where the geometric energy terms E_{bond} , E_{angle} and E_{dihedr} correspond to bond lengths, bond angles and dihedral angles respectively, and E_{improper} is the term corresponding to planarity of aromatic rings, and chirality of stereocentres (see section 3.1.8.3). E_{vdW} and E_{coulomb} are the energy terms corresponding to Van der Waal forces and Coulombic forces respectively. The final term, E_{NOE} , corresponds to energies originating from NOE derived distance restraints [224, 275]. If any of the terms have high energies, this could indicate inconsistencies in the RMD protocol or NMR derived data. The selection of several possible minimised structures on the potential energy surface is accomplished by a random array of initial starting structures that incorporate the NMR derived restraints. The calculations run over many steps to ensure the global minimum can be determined [224, 241, 258, 264].

After RMD calculations, simulated annealing (SA) calculations are performed to further minimise the range of structures produced, to locate the global minimum [264]. SA works by simulating a molecule at a very high temperature (i.e. 2000 K), which drastically increases the kinetic energy of the system. The excess kinetic energy is removed from the system in a stepwise fashion, by coupling to a constant temperature ‘heat bath’ [258]. This effectively simulates the molecule cooling at a slow rate, until it reaches room temperature (unless other protocols are applied). This methodology is used to locate the global minima that may not be found using RMD alone. The overall outcome is improved representative peptide structures [221, 241, 264].

RMD and SA protocols can be adjusted prior to calculation, to improve the potential energy and quality of the final structures. In some cases, it proves advantageous to increase the theoretical temperature when performing RMD calculations, as it may result in less violations of NOE restraints in the final structures [244]. Additionally, starting SA calculations from higher temperatures and using a greater number of steps in the ‘cooling’ phase can improve the quality of the final structures [277].

3.1.9 Structure quality

Once the representative peptide structures have been produced, it is important to analyse the quality of the structures. This gives an indication of how consistent the NMR input is with regards to the final structures, and also provides insight into a peptide's secondary structure and flexibility. One of the first indications is the number and size of structural violations from NMR derived restraints. In an ideal calculation, all interproton distances should be less than or equal to 0.3 Å from the specified distance restraints [224]. Large violations pose a significant problem and tend to indicate an incorrect assignment of the NOESY spectrum [244]. In most cases the violations can be eliminated by reassigning the NOESY spectrum and running new RMD and SA calculations. In this way many RMD and SA calculations are repeated (with alterations to the NMR input) for the peptide, eventually producing structures with a minimal amount of structural violations.

The precision of the final structures is expressed statistically by a root-mean square standard deviation of the average structural geometry. For the final structures which are well converged and satisfy the NMR restraints, geometries generally have a RMSD of less than 2Å [224]. This indicates a high degree of precision for the final structures. The RMSD is generated by superimposing the centroids of all of the final structures and comparing the rotated structures with a standard average structure (idealised geometry). This is expressed by the following equation:

$$\text{RMSD} = \sqrt{\frac{1}{N} \sum_{i=1}^N (\mathbf{r}_i - \mathbf{r}'_i)^2}$$

where N is the number of atoms, \mathbf{r}_i and \mathbf{r}'_i represent the atomic coordinates of the candidate and reference structures respectively [224]. The family of resultant structures are rotated individually to best fit the standard structure. The standard structure is often the resultant structure that is the closest to the average geometry of all of the resultant structures. In cases where parts of the peptide have highly consistent geometry, those segments of the peptide structures are superimposed to provide a better representation. So, when analysing families of final structures, RMSD analysis is performed across the

entire length of the peptide, as well as selected segments. Large RMSD values often indicate errors in the NMR derived restraints or a lack of NOEs observed in the NOESY spectrum, as a result of highly disordered peptide structure [241, 278].

Structure quality is also examined by observing the dihedral angles of the resultant structures. This is quantified by calculating the angular order parameters for a family of structures, expressed by the equation;

$$S(\alpha_i) = \frac{1}{N} \left\| \left(\sum_{x=1}^N \alpha_i^x \right) \right\|$$

where $S(\alpha_i)$ is the order parameter of the dihedral angle α_i of residue i , and x corresponds to the individual structures, from 1 up to N [279]. These indicate the distribution of dihedral angles within a family of final structures. Angular order parameter (S) values range from 0 for randomly distributed dihedrals to 1 for those with no deviation from their idealised geometry. Angular order parameters are commonly used to assess the backbone dihedral angles ψ (ψ) and ϕ (ϕ), where ψ is defined by N_i , αC_i , C'_i and N_{i+1} and ϕ is defined by C'_{i-1} , N_i , αC_i and C'_i (figure 3.13). Backbone dihedral angles are considered to be well-defined where $S > 0.9$, corresponding to a standard deviation of 24° [279, 280].

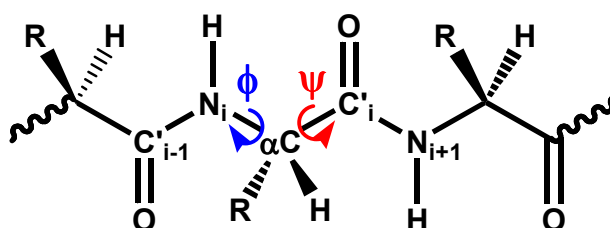


Figure 3.13 The dihedral angles ϕ (blue) and ψ (red). In this representation both ϕ and ψ are equal to 180° .

Only certain ψ and ϕ angles are structurally allowed. This is due to steric and torsional strain within the peptide structure [281]. The combinations of dihedral angles, when plotted against one another in a Ramachandran plot, provide an indication of the local secondary structure (figure 3.14). The Ramachandran plot categorises the dihedral angles

into density regions of defined secondary structure, from known protein and peptide structural data. Over 80% of the dihedral angle combinations will fall within the high density regions, termed favourable regions. The remaining densities are categorised into allowed, generous, and disallowed regions. Generally, the ψ and ϕ angles of Gly and Pro residues are excluded from Ramachandran plots due to their atypical dihedral angles [282].

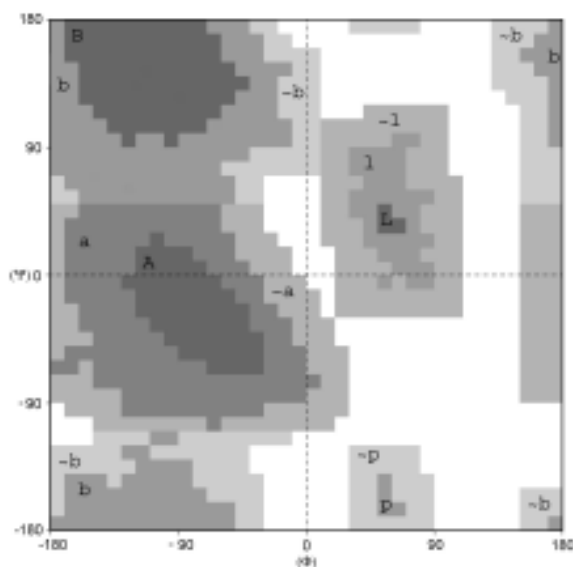


Figure 3.14 Ramachandran plot. Dihedral angle combinations for α -helices are labelled as favourable A, allowed a, and generous \sim a. A similar notation is used for β -sheets (B) and left handed α -helices (L). Disallowed regions are shown in white.

Typically, high quality structures will exhibit well-defined dihedral angles in the favourable and allowed regions of a Ramachandran plot. Generally Ramachandran plots are generated for an entire family of final structures, as well as the averaged dihedral angle combinations [282].

In conclusion, peptide structures of high quality will have geometries that are close to idealised geometries, low potential energies, and well defined regions of secondary structure [224].

3.1.10 Solvent selection

Many neuro- and antimicrobial peptides are active on a biological membrane surface [283-287]. In water, the carbonyl and amide groups of peptides tend to form hydrogen bonds with water molecules, disrupting secondary structure, and resulting in random peptide conformations. In contrast, NMR experiments of peptides in lipid bilayers or vesicles are often difficult to resolve, as the slow tumbling times cause significant line broadening [288]. So, when performing NMR experiments with biologically active peptides, it is important to select a practical solvent system that mimics the chemical environment at a membrane surface.

Membrane mimicking solvent systems are generally composed of a mixture of organic and aqueous solvents. Some commonly used solvent systems are deuterated trifluoroethanol (TFE) in water, and micelles of deuterated dodecylphosphotidylcholine (DPC) in water. These solvent systems have been shown to induce intermolecular hydrogen bonds, producing peptide structures that would be observed at a cellular membrane surface. Additionally, temperature and pH are important factors to consider when preparing a membrane mimicking solvent system [48, 289-291].

An artefact of using any aqueous solution (unless it is entirely deuterated) is a large proton signal in an NMR spectrum due to water. This signal is magnitudes larger than the peptide proton signals. Additional alterations to NMR pulse sequences, such as presaturation, can be used to suppress the water signal. This involves an additional low intensity continuous *rf* pulse during the relaxation delay at a frequency corresponding to water protons [224, 292-294]. Additional alterations to pulse sequences such as the WET and WATERGATE sequences also exist as an alternative method of suppressing the water signal [295-298].

Large alcohols with a low polarity and basicity such as TFE induce secondary structure of peptides by replacing water in the outer hydration shell. The produced effect involves the formation of intramolecular hydrogen bonds [290, 299]. TFE also has a much lower dielectric constant than water. This enhances intramolecular electrostatic interactions.

The bulky CF₃ substituent sterically hinders water molecules from reaching the peptide backbone. Relatively, a greater number of water molecules are displaced by TFE molecules in the outer hydration shell and released into the bulk solution. Hence the interaction is also entropically favoured [289].

Larger alcohols have a greater potential to stabilise secondary structure than small alcohols such as methanol and ethanol [300]. The tendency for fluorinated alcohols to form micelle-like aggregates in solution enhances this stabilising effect [301]. These aggregates form minute regions of low polarity that may further enhance secondary intramolecular interactions within a peptide.

Aqueous TFE is often recognised as a helix inducing solvent, though Sönnischen *et al.* demonstrated that this only occurred in peptides that had regions with the propensity to form helices [302]. In addition to these studies, aqueous TFE solutions have been shown to produce β -sheet and β -turn secondary structure in peptides [289, 303]. These factors suggest that aqueous TFE solutions do not force peptides to adopt secondary structure, but merely induce it where the propensity exists. Despite this, much debate still exists about the viability of aqueous TFE solvent systems. In some cases aqueous TFE has been shown to produce helical structures in peptide and protein regions that predominantly exist as β -sheets [299, 304, 305].

The use of fluorinated or large alcohols has been shown to disrupt the secondary, tertiary and quaternary structure of proteins in solution, by disrupting hydrophobic core regions. Peptides however, are generally too small to have hydrophobic cores within their structure. Hence fluorinated alcohols such as TFE in aqueous media still remain a practical membrane mimicking solvent system, for the study of peptides [300, 306].

3.2 Solid-state NMR spectroscopy

3.2.1 Chemical shift anisotropy

Solution state and solid-state NMR do not differ due to the specific phase of a sample, but the dynamics of the nuclei observed under an applied magnetic field. Solution state NMR involves rapidly tumbling molecules, with nuclei that do not have any specific orientation in three dimensions relative to an applied magnetic field. The resultant chemical shift is averaged to an isotropic value. In solid-state NMR, molecules are rigid or tumble at a reduced rate and the nuclei have an orientation dependent chemical shift. Nuclei in different orientations experience different degrees of electronic shielding relative to the applied magnetic field. The result is a range of chemical shift signals for a given nucleus, corresponding to each unique orientation, and anisotropic chemical shifts are observed. The extent of this ‘chemical shift anisotropy’ (CSA) observed is dependant on many factors, such as molecular motions, local molecular structure, and crystal packing [307].

The 3-dimensional nature of the electronic shielding experienced by a nucleus causing CSA is best described using an ellipsoid representation of the chemical shift tensor with principle tensor elements, σ_{11} , σ_{22} , and σ_{33} (figure 3.15). The observed chemical shift for a specific nuclear orientation is related to the length of a vector, from the centre of the ellipsoid to the outer edge, parallel to \mathbf{B}_0 [224]. The direction of the vector relative to the principle tensor elements is defined by the angles θ and ϕ using a spherical coordinate system. The orientation of the chemical shift tensor for a given nucleus relative to its local molecular structure has been defined for many systems [307]. If the values of the 3 principle tensor elements are defined, the orientations of molecules or molecular constituents can be determined with respect to the applied magnetic field [224, 307].

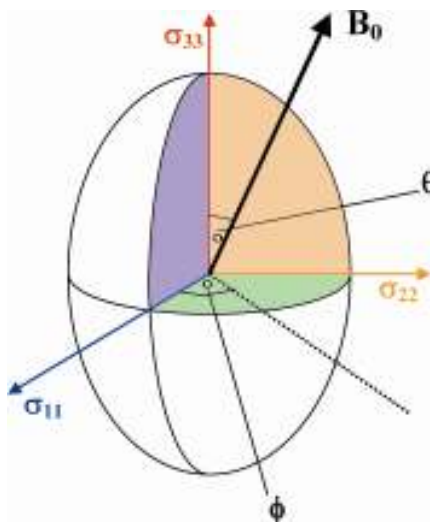


Figure 3.15 The ellipsoid representation of the chemical shift tensor and the principle tensor elements σ_{11} , σ_{22} , and σ_{33} . Different orientations of the tensor relative to the applied magnetic field \mathbf{B}_0 are described by the angles θ and ϕ and result in different chemical shifts values for the nucleus. Figure adapted from [224].

In solid-state NMR, the spectra observed are highly dependant on the nature of the crystalline phase. In a single crystal, a single chemical shift peak would appear for a small number of unique nuclear orientations. In a powdered sample, an overlay of many chemical shift signals is observed from a vast number of nuclear orientations. The result is a broad NMR signal with a characteristic line shape, recognised in solid state NMR as a ‘powder pattern’.

The nature of a powder pattern is related to the principle tensor elements for a given arrangement of nuclear orientations, and the CSA ($\Delta\sigma$) is measured such that:

$$\Delta\sigma = \sigma_{33} - \frac{1}{2} (\sigma_{11} + \sigma_{22})$$

where $\Delta\sigma$, σ_{11} , σ_{22} , and σ_{33} are in parts per million (ppm). Molecular motions, to an extent, cause of averaging of the CSA ($\Delta\sigma$). In the case of molecules in a liquid-crystalline phase, such as phospholipids in hydrated bilayers, rapid axial rotation of molecules can occur [307, 308]. The tensor elements orthogonal to the axis of rotation (σ_{11} and σ_{22}) are averaged and described by σ_{\perp} ; the remaining tensor element parallel to

the axis of rotation (σ_{33}) is described by σ_{\parallel} [307]. Figure 3.16 illustrates the theoretical powder patterns for nuclei with asymmetric CSA, and axially symmetric CSA.

NOTE:
This figure/table/image has been removed
to comply with copyright regulations.
It is included in the print copy of the thesis
held by the University of Adelaide Library.

Figure 3.16 Theoretical powder pattern for a nucleus with asymmetric chemical shift anisotropy (left), and with axially symmetric chemical shift anisotropy (right). Based on a figure from [307].

The isotropic chemical shift (δ_{iso}) can be calculated from the powder patterns, such that the CSA is averaged:

$$\delta_{\text{iso}} = \frac{1}{3} (\sigma_{11} + \sigma_{22} + \sigma_{33})$$

In some cases, the CSA lineshape can be narrowed to determine the isotropic chemical shift of a nucleus. This is achieved via spinning a sample at a rapid rate (1-70 kHz) at an angle of 54.44° (magic angle) relative to the applied magnetic field. This method of narrowing the CSA is known as magic angle spinning (MAS) [309].

3.2.2 Quadrupolar interactions

A nucleus with an asymmetric arrangement of nucleons has a spin $I > \frac{1}{2}$ and a non-spherical charge distribution. The result is a nucleus with a quadrupolar moment that is dependant on how much the nuclear charge distribution deviates from spherical symmetry. A quadrupolar nucleus is greatly affected by the local electrical field gradient generated from surrounding charges. A quadrupolar nucleus can orient itself 3 possible

orientations relative the surrounding electrical field gradient, resulting in spin states of differing energies, as illustrated in figure 3.17.

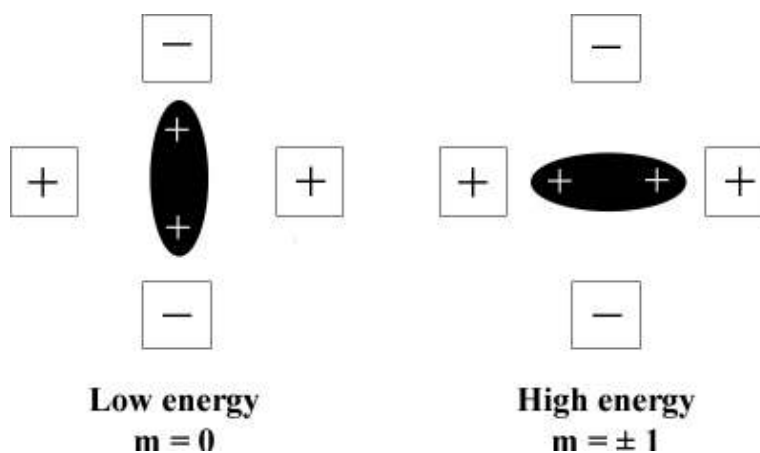


Figure 3.17 A quadrupolar nucleus (black), in high and low energy orientations relative to the local electrical field gradient (squares). Figure adapted from [251].

The extent of electronic shielding experienced by a quadrupolar nucleus in the presence of a magnetic field is dependent on the orientation relative to the direction of the magnetic field and the electrical field gradient. The electrical field gradient is represented by a tensor \mathbf{V} , that is included in the Hamiltonian (\hat{H}_Q) that describes the quadrupolar interaction:

$$\hat{H}_Q = \frac{eQ}{2I(2I-1)} h\mathbf{I} \cdot \mathbf{V} \cdot \mathbf{I}$$

where h is Planck's constant, eQ is the quadrupole moment for a single nucleus with spin I , and \mathbf{I} is the angular momentum operator [224].

When a magnetic field is applied, nuclei are oriented in $2I + 1$ state and the transition energies between states are degenerate in the absence of quadrupolar interactions. For a ^2H nucleus ($I = 1$), 3 states ($m = -1, 0, +1$) exist and 2 degenerate transition energies (ν_0) exist due solely to Zeeman interactions. When an axially symmetric electrical field

gradient is present, as for ^2H in a $^2\text{H-C}$ bond, the quadrupolar interactions alter the energy levels of the states equally and in the same direction. In most cases the Zeeman interactions are larger in magnitude than the quadrupolar interactions [224], as shown in figure 3.18.

NOTE:
 This figure/table/image has been removed
 to comply with copyright regulations.
 It is included in the print copy of the thesis
 held by the University of Adelaide Library.

Figure 3.18 The transitions energies (ν_0) between spin states (m), for a pair of nuclear spins ($I = 1$) due to Zeeman interactions alone, and the perturbation in energies ($\Delta\nu/2$) due to quadrupolar interactions. Figure adapted from [224].

In a single crystal, where $^2\text{H-C}$ bonds are aligned in one unique orientation, a doublet corresponding to the 2 transitions would be observed in the NMR spectrum. The splitting of energies between the transitions is

$$\Delta\nu = \frac{3}{4} \left(\frac{e^2qQ}{h} \right) (3\cos^2\theta - 1)$$

where e^2qQ is the quadrupolar coupling constant and θ is the Euler angle between the principle axis of the quadrupolar nucleus and the applied magnetic field. In a powdered sample, with quadrupolar nuclei in several orientations, the observed NMR spectrum is an overlap of two axially symmetric powder patterns, known as a 'Pake doublet' (figure 3.19) [224, 310].

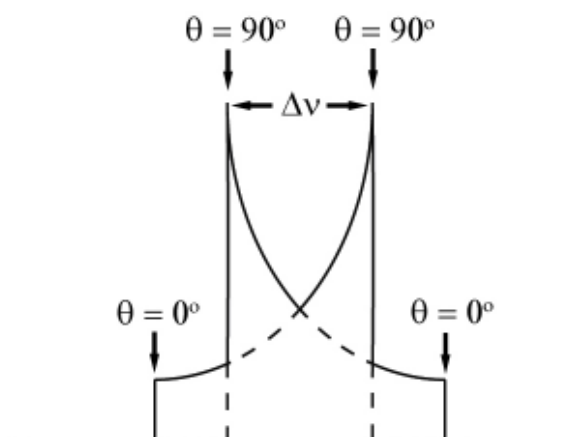


Figure 3.19 Characteristic Pake doublet from a powdered sample of a quadrupolar nucleus ($I=1$).

The quadrupolar splitting frequency is the spacing between the 2 maxima corresponding to where θ is 90° . For a rigid deuterium nucleus, the quadrupolar splitting ($\Delta\nu_{90}$) between the central peaks is

$$\Delta\nu_{90} = \frac{3}{4} \left(\frac{e^2 q Q}{h} \right)$$

and the splitting between the outermost steps ($\Delta\nu_0$) is

$$\Delta\nu_0 = \frac{3}{2} \left(\frac{e^2 q Q}{h} \right)$$

Molecular motions cause averaging of the quadrupolar splitting energies ($\Delta\nu$). This observed averaging of $\Delta\nu$ can indicate the mobility of a particular quadrupolar nucleus [224]. In most cases quadrupolar interactions are the most dominant interactions observed in the NMR spectra. They are used to indicate regions of flexibility and structural symmetry within a molecule of interest [311-313].

3.2.2 Dipolar interactions

Every nuclear spin possesses a dipole moment, generating a local magnetic field that in turn affects the spins of other nuclei. In a system where two unlike nuclei with a spin $I = \frac{1}{2}$ exist, dipolar interactions cause a change in the splitting of energies relative to what is observed due to Zeeman interactions alone (figure 3.20).

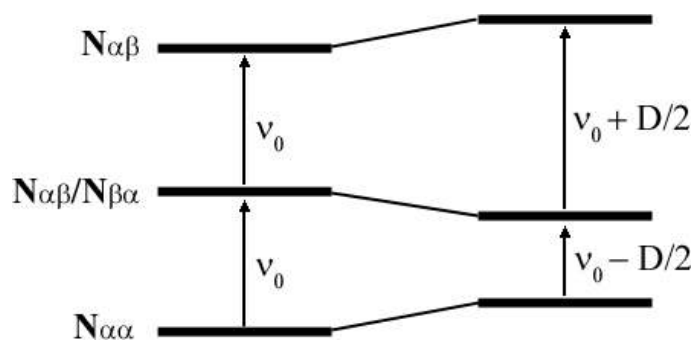


Figure 3.20 The transitions energies (ν_0) between spin states, for a pair of nuclear spins ($I = \frac{1}{2}$) due to Zeeman interactions, and perturbations ($D/2$) caused by dipolar interactions. Figure adapted from [310].

The dipolar coupling is a through-space interaction and the change in the transition energies is quantified by the dipolar coupling constant D

$$D = \frac{h\mu_0\gamma_i\gamma_j}{2\pi^2r^3}$$

where h is Planck's constant, μ_0 is the permeability of a vacuum, r is the internuclear distance, and γ denotes the gyromagnetic ratios of nuclei i and j . In systems abundant in nuclei with spins $I = \frac{1}{2}$, dipolar coupling is the strongest of the observed interactions. The extent of the dipolar interaction is very much dependant on the distance between nuclei. Hence, internuclear distances can be accurately determined from dipolar couplings using solid-state NMR [314].

In many experiments, the effects of dipolar couplings can cause unwanted line broadening, particularly in cases where a dilute half integer nucleus is analysed and the

sample is abundant in protons ($I = \frac{1}{2}$). These unwanted effects can be removed by proton decoupling methods, where a strong RF field is applied corresponding to all proton resonances prior to acquisition. In this way transitions between proton orientational states become rapid and are averaged to zero. The protons do not couple to the dilute spin of interest and only dipolar coupling interactions between the dilute spins are observed in the NMR spectrum [315, 316].

3.2.4 Solid-state NMR of phospholipid membranes

Biological membranes play an essential role at the cellular level for all living organisms. They act as a boundary, between the intracellular and extracellular matter and also can form sub-cellular compartments and organelles [317]. Many important cellular processes occur at the membrane that would otherwise not be feasible in purely aqueous media [318]. Additionally, ions, oxygen, water and other nutrients can flow across biological membranes via passive diffusion [9]. Biological membranes are largely comprised of proteins, steroidal compounds, and phospholipids [319]. The phospholipids in membranes are amphipathic in nature and self-assemble to form bilayers, where the phosphate headgroups face outward forming a hydrophilic surface, and the hydrophobic tails face inward forming a hydrophobic core [9, 317, 320]. In this way each polar face of the bilayer is exposed to aqueous media and the lipids remain soluble, as shown in figure 3.21.

NOTE:
This figure/table/image has been removed
to comply with copyright regulations.
It is included in the print copy of the thesis
held by the University of Adelaide Library.

Figure 3.21 Schematic diagram of a phospholipid bilayer. Based on a figure from [9].

In 1972, S. J. Singer and G. Nicolson devised the ‘fluid mosaic’ model for biological membranes, that describes them assembling themselves into a thin planar fluid [321].

Rather than phospholipids staying rigid in one place, they easily move laterally along the plane of the membrane. The model includes amphipathic transmembrane proteins within the membrane bilayer, with polar regions facing toward the outer surface of membranes, and the non-polar regions integrated into the hydrophobic core of membranes. The fluid mosaic model supersedes the Davson-Danielli model that describes globular proteins existing on the hydrophilic surfaces of biological membranes [322]. It is the most widely accepted model for biological membranes to this date [9, 317].

A common group of phospholipids that exist in eukaryotic membranes are glycerophospholipids; these are biosynthesised in the intracellular fluid adjacent to the endoplasmic reticulum from glycerol and fatty acids. Their general structure is composed of a glycerol backbone with a phosphate headgroup bound at the C3 position and two acyl chains bound at the C1 and C2 positions via ester bonds [9]. These lipids can self assemble to form bilayers under certain conditions and are used as models of biological membranes. Some common glycerophospholipids used are dimyristoyl phosphatidylcholine (DMPC) and dimyristoyl phosphatidylglycerole (DMPG). These phospholipids are zwitterionic and anionic respectively.

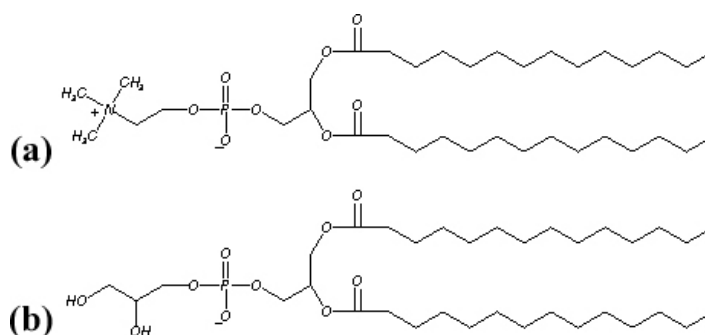


Figure 3.22 Glycerophospholipids used in model membranes. **(a)** DMPC (zwitterionic), and **(b)** DMPG (anionic).

The properties of model membranes have been studied using techniques such as X-ray diffraction, neutron scattering, solid-state NMR, surface plasmon resonance, dual

polarisation interferometry (DPI) and quartz crystal microbalance with dissipation monitoring (QCM-D) [323-326].

The nature of a phospholipid mixture varies depending on the concentration and charge of phospholipids, level of hydration, pH, temperature, and the presence of cations as well as other compounds or solvents. These factors in turn affect the phase and arrangement of the phospholipids within the sample and the NMR spectra observed. In some cases aligned bilayers are prepared between thin glass plates. Alternatively, lipid vesicle samples can also be prepared, as well as dry lipid samples [327, 328]. A novel method to observe phospholipid membranes by solid-state NMR is to use hydrated multi-lamellar vesicles (MLVs). MLVs are lipid vesicles containing many bilayers separated by hydrated inter-lamellar spaces arranged in an ‘onion like’ structure. In this case, the phospholipids are unoriented with respect to the applied magnetic field (figure 3.23) [329, 330]. When peptides are added to MLV samples, they interact with the hydrophobic interiors of bilayers, the outer hydrophilic surface, or both; depending on their size, conformation, and hydrophobicity. The nature of these peptide-membrane interactions are used to describe a peptides mode of action [112, 331, 332].

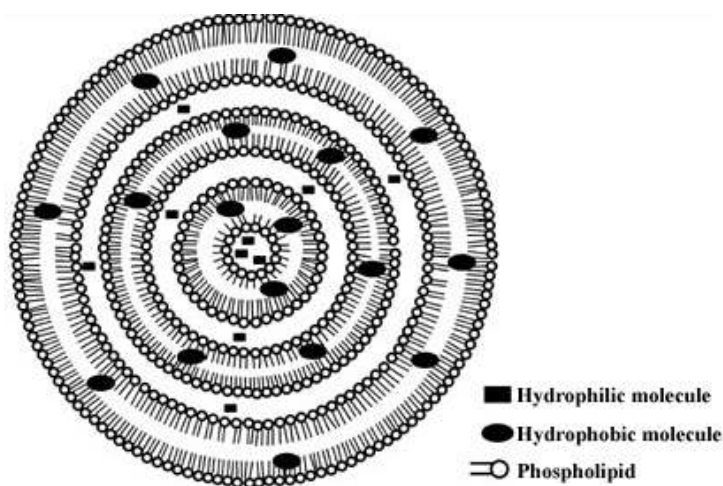


Figure 3.23 The ‘onion like’ structure of a multi-lamellar vesicle (MLV): hydrophilic molecules occupy the aqueous inter-lamellar spaces and hydrophobic molecules occupy the hydrophobic interiors of the bilayers.

3.2.4.1 ^{31}P NMR of phospholipid membranes

Phospholipid samples are abundant in ^{31}P nuclei (100% in natural abundance), thus ^{31}P NMR is employed to analyse both biological membrane and model membrane mixtures. The characteristic lineshapes of the ^{31}P NMR spectra are dependant on the nature of the phospholipid mixtures. Dried phospholipid samples show a broad characteristic lineshape with a CSA of approximately -190 ppm [333, 334] (figure 3.24a). Hydrated samples can spontaneously form phospholipid bilayers, with phospholipids that are more mobile and able to rotate about their principle axes (figure 3.24c). Consequently, the ^{31}P spectra of hydrated phospholipid samples have CSAs in the order of -50 ppm (figure 3.24b) [328, 333, 334].

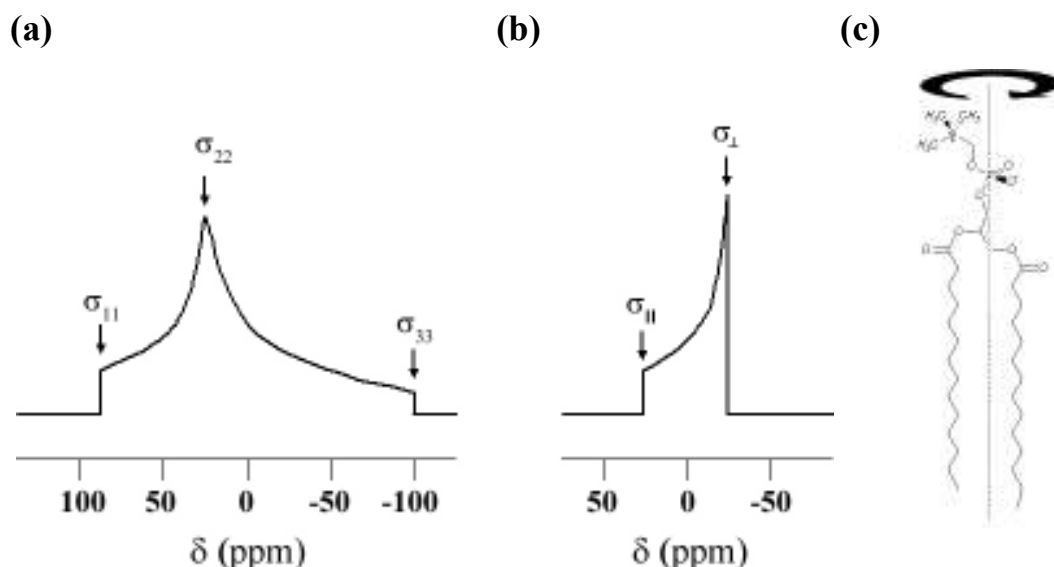


Figure 3.24 Theoretical ^{31}P powder patterns of (a) a dry phospholipid sample, (b) a hydrated phospholipid sample, and (c) the principle axis of rotation of DMPC.

Hydrated phospholipid samples show some degree of averaging of the CSA. The principle tensor elements approximately perpendicular to the axis of rotation, σ_{22} and σ_{33} are averaged and described by the element σ_{\perp} . The remaining tensor element σ_{11} is approximately parallel to axis of rotation, is averaged and described using the element σ_{\parallel} . The CSAs of the resultant ^{31}P spectra are greatly reduced relative to dry samples, and the CSA, $\Delta\sigma$, can be measured directly from the difference between the σ_{\perp} and σ_{\parallel} elements

of the axially symmetric powder pattern [333, 335]. The presence of peptides in lipid samples can perturb the phospholipid headgroup rotation and mobility and lead to changes in the ^{31}P spectra lineshape and the observed CSA [328, 336, 337]. In this way ^{31}P NMR is used to analyse of the mobility and ordering of phospholipid headgroups within bilayers.

The anisotropic ^{31}P NMR spectra of phospholipids can have line widths of up to ~ 190 ppm depending on the phase of the sample, yet each nucleus must be irradiated equally. For phospholipid samples, the spin-lattice decay times (T_1) are typically far greater than the very short spin-spin decay times (T_2). When acquiring a 1D NMR spectrum using a single 90° pulse, the NMR probe and receiver has a relatively long ring down time. The residual ring down appears in the FID signal, distorting the Fourier transformed NMR spectrum [333, 338]. To overcome this, anisotropic phospholipid samples are acquired using a Hahn spin-echo pulse sequence (figure 3.25).

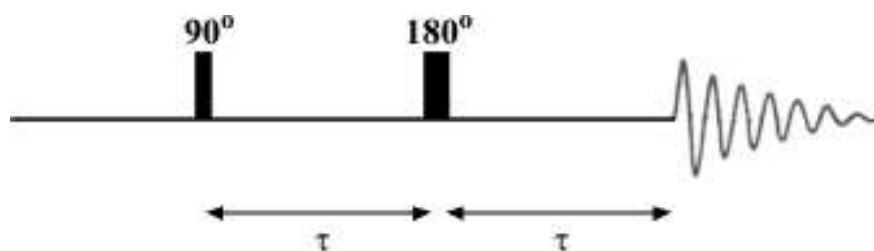


Figure 3.25 The general pulse sequence of a Hahn spin-echo experiment.

The Hahn spin-echo pulse sequence differs from a typical 1D NMR as an additional 180° pulse is inserted into the sequence, as well as two variable times τ , between pulses and the FID acquisition. The first 90° pulse pushes the net magnetisation into the xy -plane that decays in amplitude depending on T_2 , over a period τ . The following 180° pulse inverts the magnetisation and refocusses it within the xy plane, over a second period τ . The resultant FID signal is then acquired as the first ‘echo’ of the initial signal from the 90° pulse. In the absence of transverse relaxation, the signal after 2τ is the same magnitude as the first initial 90° pulse. Also, if the period τ is greater than the ring down time of the probe, then the residual ring down will not appear in the FID signal [333, 338-340]. Other complications in ^{31}P NMR spectra can arise from dipolar coupling between

phosphorous nuclei and protons, leading to additional line broadening [340, 341]. These dipolar couplings are typically larger than the CSA and can be removed via proton decoupling methods (see section 3.2.3).

3.2.4.2 ^2H NMR of phospholipid membranes

Deuterium has a very low natural abundance (0.015 %), hence deuterium labelled phospholipids are chemically (or biochemically) synthesised for the purposes of NMR analysis. In the case of solution-state ^1H NMR of peptides, entirely deuterated phospholipids are often used because ^2H resonances do not appear within the ^1H frequency range [291, 342]. Conversely, solid-state ^2H NMR experiments can be used to measure the dynamics and ordering of selected regions of the phospholipids, such as phosphate headgroups, glycerol backbones, and acyl chains.

Deuterium nuclei have a spin $I = 1$ and thus have a quadrupole moment. The magnitude of quadrupolar interactions are in the order of approximately 167 kHz. The ^2H NMR spectra of unoriented deuterium labelled compounds show a characteristic ‘Pake doublet’ for each unique type of deuterium nucleus in the sample (see section 3.2.2). In the case of phospholipids with deuterated acyl chains, a Pake doublet is observed for each unique CD_2/CD_3 group along the length of the acyl chain. In hydrated samples, the quadrupolar splitting values ($\Delta\nu$) become averaged to a degree, depending on the mobility of the CD_2/CD_3 groups. The CD_2 group closest to the phospholipid headgroup is generally the least mobile and produces a Pake doublet with a large $\Delta\nu$. The terminal CD_3 group generally is the most mobile and thus produces a Pake doublet with a much smaller $\Delta\nu$. It is generally assumed that the $\Delta\nu$ values decrease sequentially from the CD_2 closest to the phospholipid headgroup to the terminal CD_3 group, as a result of increasing acyl chain mobility [343, 344]. So the ^2H NMR spectra of phospholipids that are entirely deuterated along their acyl chains are effectively a superimposition of many Pake doublets. Each contributing Pake doublet has a quadrupolar splitting value, $\Delta\nu$, corresponding to each position on the acyl chain (figure 3.26).

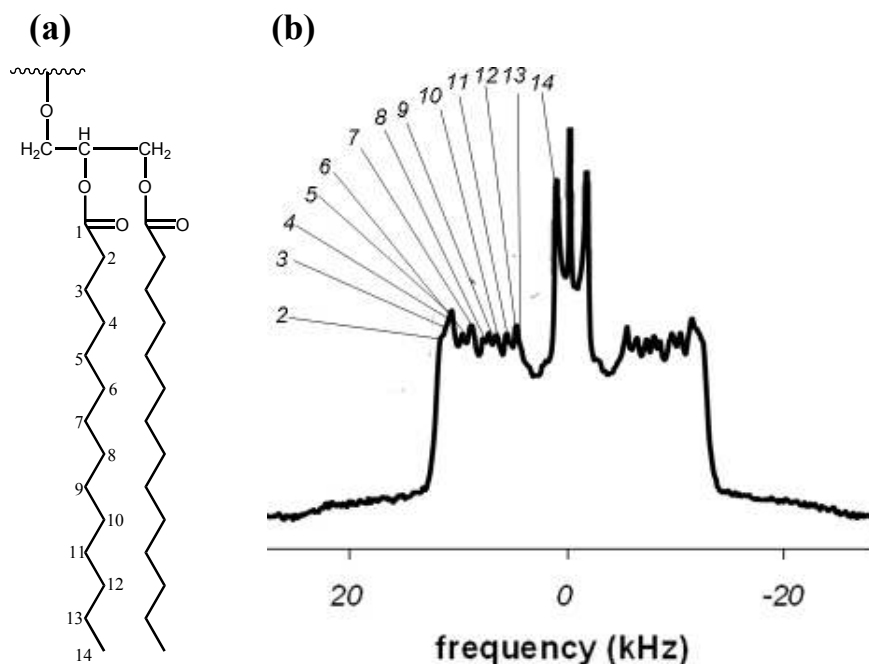


Figure 3.26 (a) The deuterated acyl chain region of DMPC (DMPC- d_{54}). **(b)** A ^2H spectrum of DMPC- d_{54} MLV adapted from [82]. The numbers on the spectrum indicate the maxima of each contributing Pake doublet corresponding to the acyl chain positions of the CD_2/CD_3 groups. The central maximum is due to residual deuterium from water.

The individual quadrupolar splittings from each carbon-deuterium bond of CD_2/CD_3 can be difficult to resolve, particularly when splitting values almost coincident. However, deconvolution of the overlaid Pake powder patterns can be achieved by ‘dePaking’ the ^2H NMR spectrum. The dePaking method involves fitting each spectrum to locate the splitting energies from each Pake doublet corresponding to the Euler angles (θ) of 0° and 90° ($\Delta\nu_0$ and $\Delta\nu_{90}$ respectively, see section 3.2.3.1) [313, 345, 346].

The averaging of quadrupolar splittings ($\Delta\nu$) from each carbon-deuterium bond of CD_2/CD_3 groups along the acyl chains is quantified by an order parameter S_{CD} as follows:

$$\Delta\nu = \frac{3}{4} \left(\frac{e^2 q Q}{h} \right) S_{\text{CD}} \quad \text{and}$$

$$S_{CD} = \frac{1}{2} \langle 3\cos^2\theta - 1 \rangle$$

where θ is the angle between the direction of the C-D bond and the applied magnetic field, the brackets represent a time-averaged function, and the quadrupolar coupling constant (e^2qQ) is 170kHz, as derived from deuterated paraffin hydrocarbons [347]. In hydrated bilayer samples, the S_{CD} values of deuterated acyl CD_2/CD_3 groups decrease sequentially from the headgroup toward the acyl chain termini, in proportion to the observed $\Delta\nu$ values. The S_{CD} values are plotted against the acyl chain CD_2/CD_3 positions in an S_{CD} order profile [312, 313].

The addition of peptides to deuterated phospholipid samples can alter the observed $\Delta\nu$ in 2H NMR spectra relative to those observed without the addition of peptides (control samples). If a peptide inserts itself perpendicular to the plane of the membrane, such as a pore forming antimicrobial peptide, then a decrease in the mobility of the acyl chains tends to occur. This causes greater observed $\Delta\nu$ in the 2H NMR spectra and greater S_{CD} values in the S_{CD} order profiles [348, 349]. If a peptide interacts largely with the phospholipid membrane surface, an increase in the lateral distance between phospholipid headgroups tends to occur. With the lipids further apart, there is a greater freedom for acyl chain movement and lower S_{CD} values are observed in the S_{CD} order profiles [350, 351]. A mixture of higher and lower observed $\Delta\nu$ values relative to the control may also occur in instances where peptides are partially inserted into the membrane [82].

The 2H NMR of acyl deuterated phospholipids have a broad line width. Spectral distortions can occur when acquiring spectra due to long ring down times and short spin-spin relaxation times, in a similar fashion to ^{31}P NMR experiments. In the case of 2H NMR experiments of anisotropic samples, a quadrupolar-echo pulse sequence is used (figure 3.27).

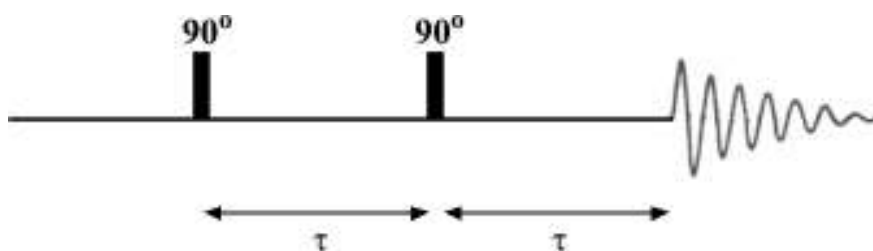


Figure 3.27 The general pulse sequence of a quadrupole-echo experiment [313, 352].

The pulse sequence is similar to that of a Hahn spin-echo pulse sequence. However, the second refocussing pulse is a 90° pulse rather than 180° . After 2τ periods the entire FID signal is measured, with the net magnetisation rotated 180° from its initial alignment in the z-axis [313]. There are some variations to the quadrupolar-echo pulse sequence: in some cases extra pulses and τ periods are added to the pulse sequences to avoid problems associated with dead time [352]. The pulse sequence is applied to remove any residual ring down from interfering with the resultant FID signal, in a similar manner to the Hahn spin-echo pulse sequence (see section 3.4.2.1).

Chapter 4

The Peptide profiles of the Australian brown tree frog *Litoria ewingii*

4.1 Introduction

4.1.1 The Australian brown tree frog *Litoria ewingii*

The Australian brown tree frog *Litoria ewingii*, also known as the ‘whistling frog’, is one of the most common frogs throughout southern Australia. The frog grows up to 45mm in body length, varies in colour from pale to dark brown (figure 4.1), and some found in regions of Victoria are partially or completely green. The frog inhabits creeks, marshes, wetlands, and residential areas. The frog is often recognised by its’ distinctive advertisement call and is also renowned for its’ swift ability to catch insects in mid flight [353]. Some closely related species are *Litoria paraewingii* and *Litoria verreauxii* [354, 355].



Figure 4.1 The Australian brown tree frog, *Litoria ewingii*.

The geographical distribution of *L. ewingii* extends in an arc from the southern tip of the Eyre Peninsula in South Australia, through Victoria and Tasmania to the south-east of coastal New South Wales [353] (figure 4.2). The species has been introduced into New Zealand, where it has established populations [356].



Figure 4.2 The geographical distribution of *Litoria ewingii*.

The varied morphology of *L. ewingii* populations found throughout southern Australia suggests that their taxonomic classification should be subject to review. Investigating the peptide profiles of geographically isolated populations may provide evidence to merit a reclassification of the species [54, 55, 92].

4.1.2 Peptide profiles of Australian frogs

Anuran skin peptide profiles appear to change rapidly with respect to changes in morphology [54, 92]. It may prove difficult to differentiate anuran species based on their morphology and/or behaviour alone. However, they may show significant differences in their peptide profiles. This could occur if populations of an anuran species become geographically isolated, their genes mutate and diverge over time, and they ultimately evolve into different species. This phenomenon by which populations of an organism become physically separated for a duration of time and evolve into different species, is known as allopatric speciation. For two different populations of an organism from a common ancestor to be classified as a different species, two separate individuals would need to mate and produce offspring that are unable to reproduce. Alternatively, a subspecies is generally defined as a population that may be geographically isolated and/or show morphological differences from another population, yet still able to produce fertile offspring when individuals from the separate populations interbreed [9].

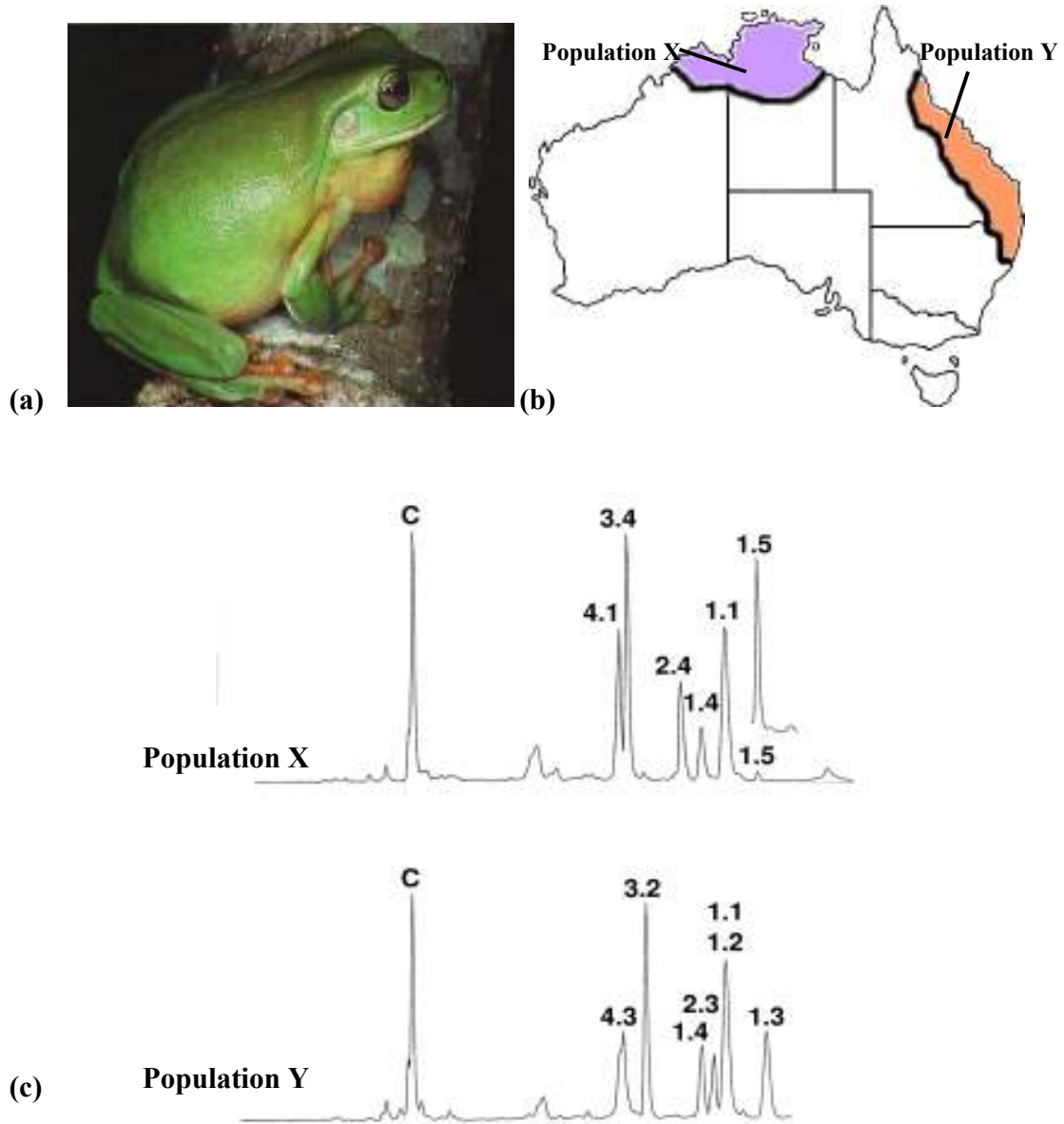


Figure 4.3 (a) The Australian green tree frog *Litoria caerulea*. (b) Geographical distribution of populations X (Northern Territory) and Y (coastal Queensland). (c) HPLC traces of populations of *Litoria caerulea* from different geographical regions [54, 92]. Each peptide isolated from the HPLC traces is depicted by a letter or number.

The peptide profile of a given anuran within the *Litoria* genus may be used to differentiate it from another geographical population, or species. This has been

demonstrated between the closely related species *L. aurea* and *L. raniformis* [71], and the more distantly related *L. xanthomera* and *L. splendida* [357, 358]. Peptide profiles of two major populations of the Australian green tree frog *L. caerulea* from Darwin and Coastal Queensland were shown to be unique, despite each population appearing to be morphologically identical (figure 4.3) [54, 92]. Additionally, subtle differences have been observed in the peptide profiles of *L. caerulea* from the Darwin area and offshore Melville Island, which was previously connected with the mainland less than 8000 years ago [359].

One extensive example of peptide profiling is that of the Red Tree Frog *L. rubella* from regions in central and northern Australia. The studies revealed unique profiles for at least six populations, some of which may eventually be reclassified as new species [60, 360].

4.1.3 Populations and taxonomy of *Litoria ewingii*

L. ewingii was first described in 1841 from Tasmanian specimens [361]. The species formerly of the *Hyla* genus [362] was later described as two species: *Hyla calliscelis* (1875) and *Hyla inguinalis* (1935) [363, 364]. The first adoption of a subspecies of *L. ewingii* was that of Boulenger in 1890 who regarded *calliscelis* as a subspecies: *Hyla ewingii calliscelis*. The specimens were, however, were from New South Wales, as far as the Blue Mountains and Sydney. This is well outside the typical locality of *L. ewingii*. Upon further studies into their morphology, the subspecies from New South Wales was later reclassified as *L. verreauxii* in 1961 [365].

An extensive review of the morphology of *L. ewingii* was conducted by Copeland in 1957; he identified six subspecies, and also considered *H. inguinalis* as a valid subspecies [366]. A recent change in the taxonomy of species closely related to *L. ewingii* has been the description of a new species from central and north-eastern Victoria: *L. paraewingii*; previously these frogs would have been identified as *L. ewingii* [354].

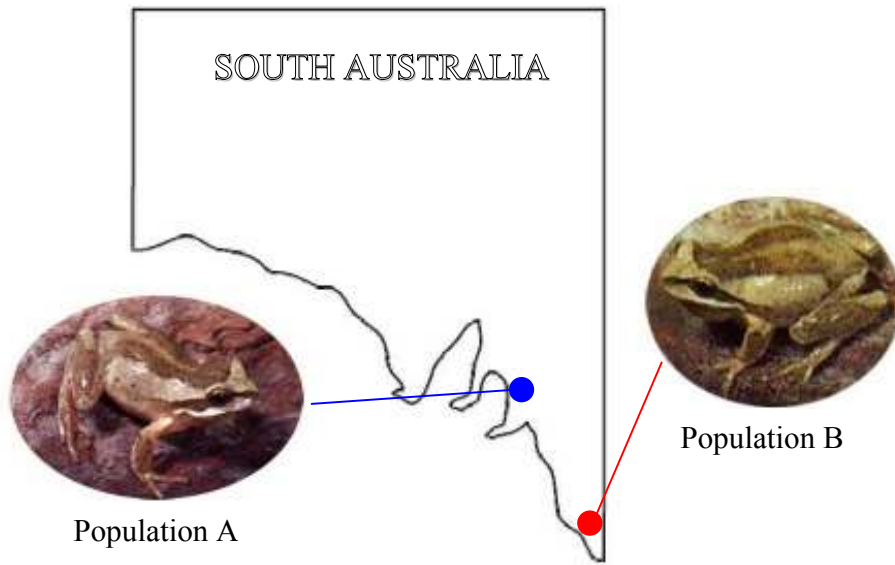


Figure 4.4 Geographical distribution populations of *Litoria ewingii*. Population A (left) from the Adelaide hills, and Population B (right) from Penola.

This study involves a comparison of the peptide profiles of *L. ewingii* taken from the Penola area of South Australia in 2007 [367], with that of a population from Adelaide, analysed in 1997 by Steinborner *et. al.* [368]. The population from Penola is approximately 400 km south east of Adelaide (figure 1.3). The purpose of this study is to compare the peptide profiles and morphology of these two populations and discuss their implications toward taxonomic classification. An additional part of this study is to isolate new peptides and determine their biological activity.

4.2 Results and Discussion

4.2.1 Isolation of *Litoria ewingii* skin peptides

Skin secretions of *L. ewingii* from the Penola based population (Population B) were collected on a monthly basis from March 2006 to February 2007. The secretions were purified by High Performance Liquid Chromatography (HPLC). From the HPLC trace of Population B, a total of six peptides were identified. The HPLC traces of skin secretions taken over different months of the year did not yield any significant variance in the peptides produced. The HPLC traces of Population B did, however, appear significantly different to that of Population A (figure 4.5).

NOTE:
This figure/table/image has been removed
to comply with copyright regulations.
It is included in the print copy of the thesis
held by the University of Adelaide Library.

Figure 4.5 The HPLC Traces of Population A [368], from the Adelaide Hills (upper) and Population B [367], from Penola (lower). Each different peptide is denoted by a numbers based on retention time. * not a peptide.

The sequences of the peptides from population B were determined from a mixture of both positive and negative ion electrospray mass spectrometry (ESMS) and automated Edman

sequencing. The sequences of the peptides, from both *L. ewingii* populations, are listed in table 4.1.

Table 4.1: Peptide sequences determined from *Litoria ewingii*. Peptides isolated from the Adelaide Hills and Penola populations are denoted as A and B respectively [367, 368]. Peptides are listed based on sequence homology.

Name	Population	Sequence ^a	MW	HPLC peak
Tryptophyllin 6.1 ^b	A	LFFWG-NH ₂	667	2
Tryptophyllin 6.2 ^b	A	IFFFP-NH ₂	668	5
Tryptophyllin 6.3 ^b	B	I V FFP-NH ₂	620	4
Ewingiin 1 ^c	A/B	GWFDVVKHIASAV-NH ₂	1426	3
Ewingiin 1.1 ^c	A/B	FDVVKHIASAV-NH ₂	1183	1
Ewingiin 2.1 ^d	A	GLLDMVTGLLG N L-NH ₂	1315	7
Ewingiin 2.2	B	GLLDMVTGLLG G L-NH ₂	1258	6
Ewingiin 2.3	B	GLLD V VT S LLG N L-NH ₂	1311	9
Ewingiin 2.4	B	GLLD V VT AV L G N L G L-NH ₂	1453	10
Caerin 1.1	A	GLLSVLG S VAKHVLP H V P VIAEHL-NH ₂	2583	8

^aDifferences in the amino acid sequences of population B peptides relative to the sequences of homologous peptides from population A, are highlighted in bold.

^bSo named because of their sequence similarity to the Tryptophyllin peptides isolated from *Litoria rubella* [369].

^cThis peptide was formerly named Uperin 7.1 because it was thought that there was a relationship to peptides from anurans of the genus *Uperoleia* [368]. This is no longer deemed appropriate, hence the peptide was renamed Ewingiin (derived from the name of this species).

^dFor similar reasons, the peptide initially called Caeridin 7.1 was renamed Ewingiin 2.1.

The only peptides present in the secretions of both *L. ewingii* populations are ewingiin 1 and the cleaved derivative ewingiin 1.1. A fascinating observation is the fact that different peptides are produced in each of the profiles, though the peptides show a high degree of sequence homology. There are two tryptophyllan pentapeptides (6.1, 6.2) present in the secretion of population A. Population B, instead only produces one pentapeptide, tryptophyllan 6.3; the major peptide of the secretion. Tryptophyllin 6.2 (population A) and tryptophyllan 6.3 (population B) only differ by the one amino acid in position 2 of the sequences. There are three ewingiin 2 peptides (2.2, 2.3, 2.4) isolated from population B that exhibit sequence homology (79-93 %) with ewingiin 2.1 from population A.

The most surprising observation from the peptide profile of population B is the lack of a caerin peptide; caerin peptides are potent, wide spectrum antibiotics commonly present in the granular secretions of several *Litoria* species [53-55, 67, 197, 358, 368, 369]. A lack of caerin peptides has, however, been previously observed in the peptide profiles of some *L. rubella* and *L. electrica* populations [60, 360].

4.2.2 Sequence determination of *Litoria ewingii* peptides

The first of the peptides isolated from population B of *L. ewingii* is tryptophyllin 6.3 (**4**), a small peptide named due to its similarity to tryptophyllin peptides isolated from species of the *Litoria* and *Phyllomedusa* genera [60, 360, 370]. A collision-induced (MS/MS) spectrum obtained in positive ion mode of the ESMS produced a (MH)⁺ ion of tryptophyllin 6.3 is illustrated in figure 4.6.

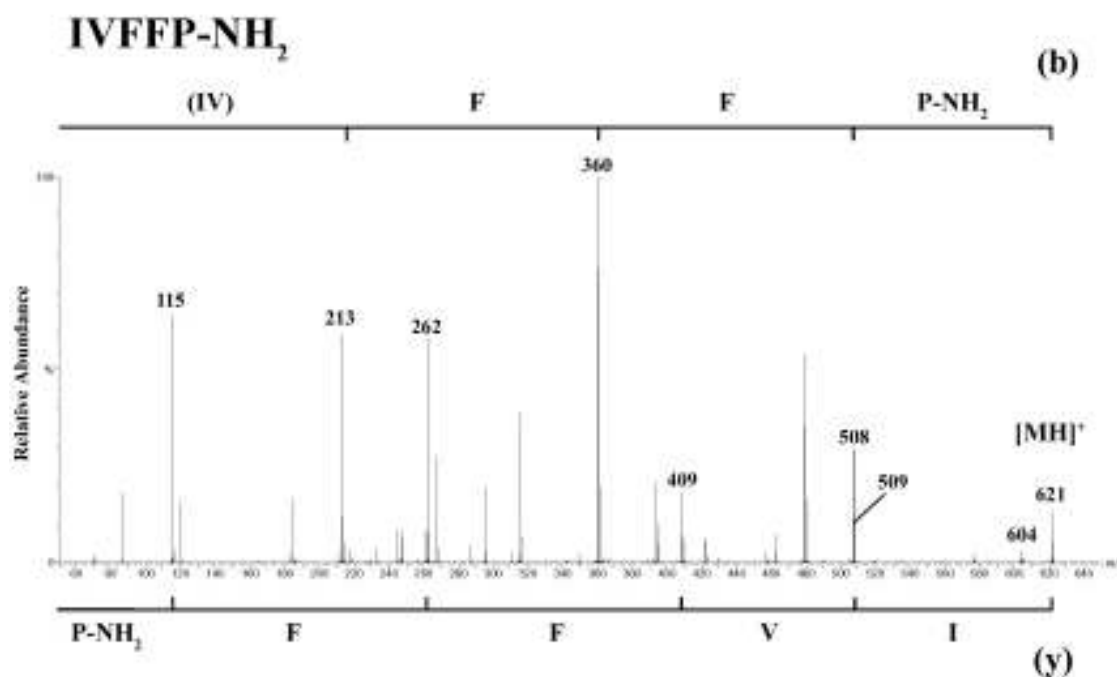


Figure 4.6 Collision induced (MS/MS) positive ion mass spectrum of tryptophyllin 6.3 (**4**), isolated from Population B of *Litoria ewingii*. Positive ion fragmentations of the (MH)⁺ species, (b) and (y) fragment ions are shown above and below the spectrum, respectively. No magnification.

The MS/MS data for the $(MH)^+$ ion of the tryptophyllin 6.3 (**4**) shown in Figure 4.6, illustrates (b) cleavage ions drawn above the spectrum and (y) cleavage ions below. Figure 4.6 contains three (b) cleavage ions and four (y) ions.

The MS/MS data derived from the $(M-H)^-$ ion of the tryptophyllin 6.3 (**4**) is shown in Figure 4.7.

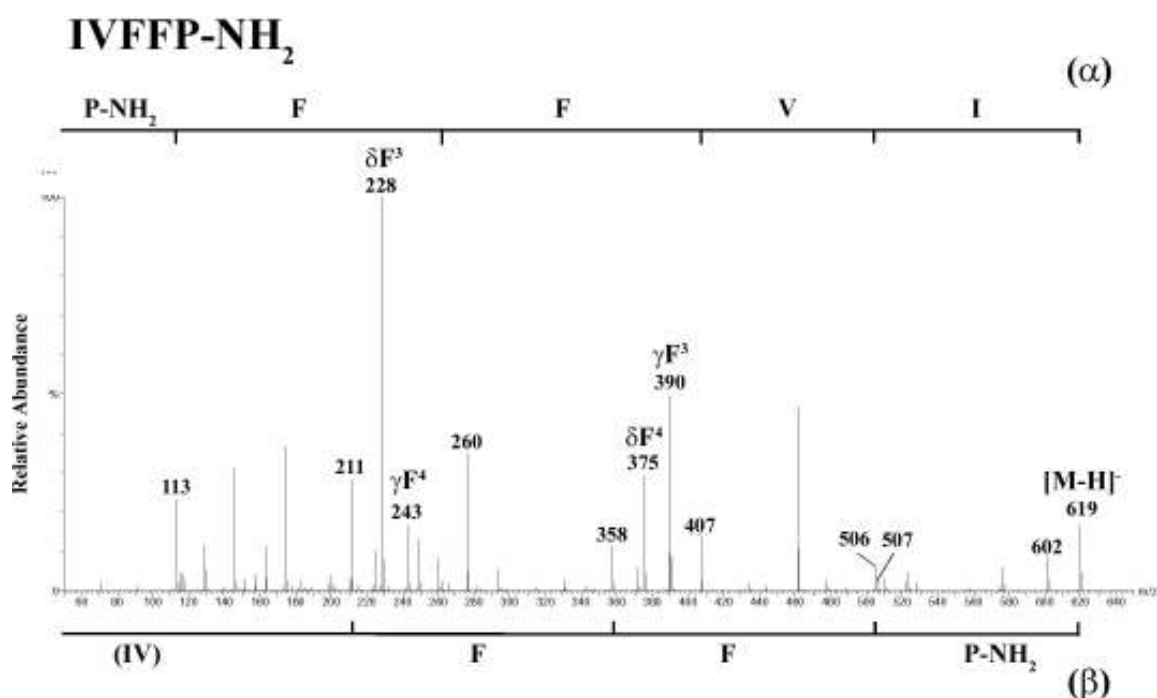


Figure 4.7 Collision induced (MS/MS) negative ion mass spectrum of tryptophyllin 6.3 (**4**) isolated from Population B of *Litoria ewingii*. Positive ion fragmentations of the $(M-H)^-$ species, (α) and (β) fragment ions are shown above and below the spectrum respectively. (γ) and (δ) ions produced from side chain induced backbone cleavages are also shown. Magnification: m/z 103-221 (x4); m/z 386-519 (x4).

Figure 4.7 illustrates (α) cleavage ions and (β) cleavage ions above and below the spectrum, respectively. The Figure 4.7 contains four (α) cleavage ions and three (β) ions. In addition, it contains the (δ) and (γ) ions produced from Phe3 and Phe4s' side chain induced backbone cleavages.

Collectively, the positive and negative ion backbone cleavages show the same sequence information. The isobaric leu1/Ile1 was assigned using Edman sequencing, completing the sequence.

The collision-induced (MS/MS) spectrum of the ESMS produced $(MH)^+$ ion of ewingiin 1 (**3**) obtained in the positive ion mode is illustrated in figure 4.8.

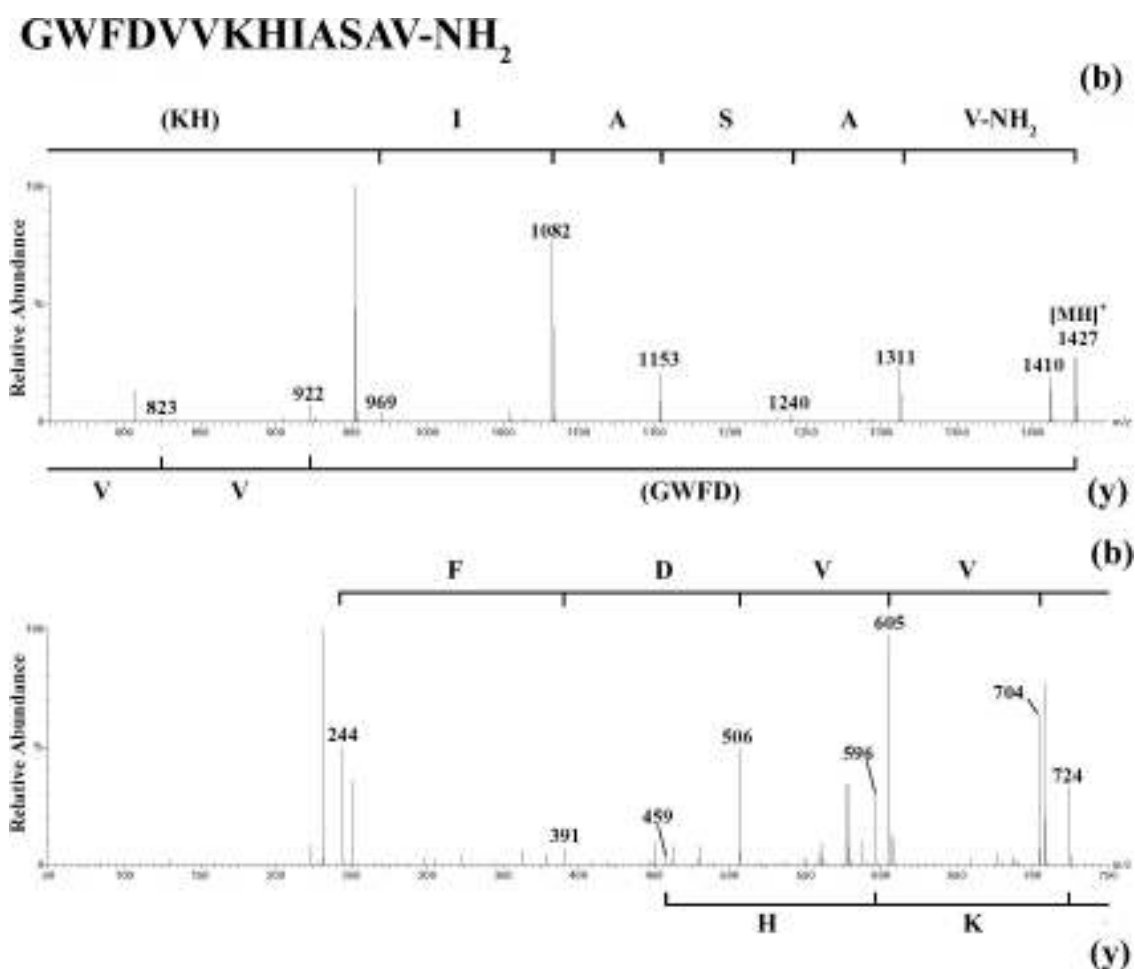


Figure 4.8 Collision induced (MS/MS) positive ion mass spectrum of the ewingiin 1 (**3**) isolated from Population B of *Litoria ewingii*. Positive ion fragmentations of the $[MH]^+$ species, (b) and (y) fragment ions are shown above and below the spectrum, respectively. Magnification: m/z 437-938 (x2).

The MS/MS data for the $[MH]^+$ ion of the ewingiin 1 (**3**) shown in figure 4.8, illustrates (b) cleavage ions drawn above the spectrum and (y) cleavage ions below. The ten (b)

The MS/MS data for the $[M-H]^-$ ion of the ewingiin 1 (**3**) shown in figure 4.9 illustrates (α) cleavage ions drawn above the spectrum. No (β) cleavages were observed in this spectrum. Sequencing of the peptide begins from 1377 due to facile characteristic side chain cleavages of Asp4 (releasing water) and Ser11 (releasing formaldehyde) [200, 201, 371]. The eight (α) cleavages allow assignment of six of the residues within the sequence and the (δ) and (γ) ions produced from the side chain induced cleavage confirms the position of Asp4 in the sequence [371]. Collectively the negative ion spectrum shows significantly less sequence information than the positive ion spectrum. The spectra collectively show the majority of the sequence, except for the first two residues (Gly1-Trp2). Edman sequencing was used to identify the isobaric Lys/Gln7, and the isomeric Leu/Ile9, and the first two residues, completing the sequencing.

The collision-induced (MS/MS) spectrum of the ESMS produced $(MH)^+$ ion of the ewingiin 1 derivative; ewingiin 1.1 (**1**) obtained in the positive ion mode is illustrated in figure 4.10.

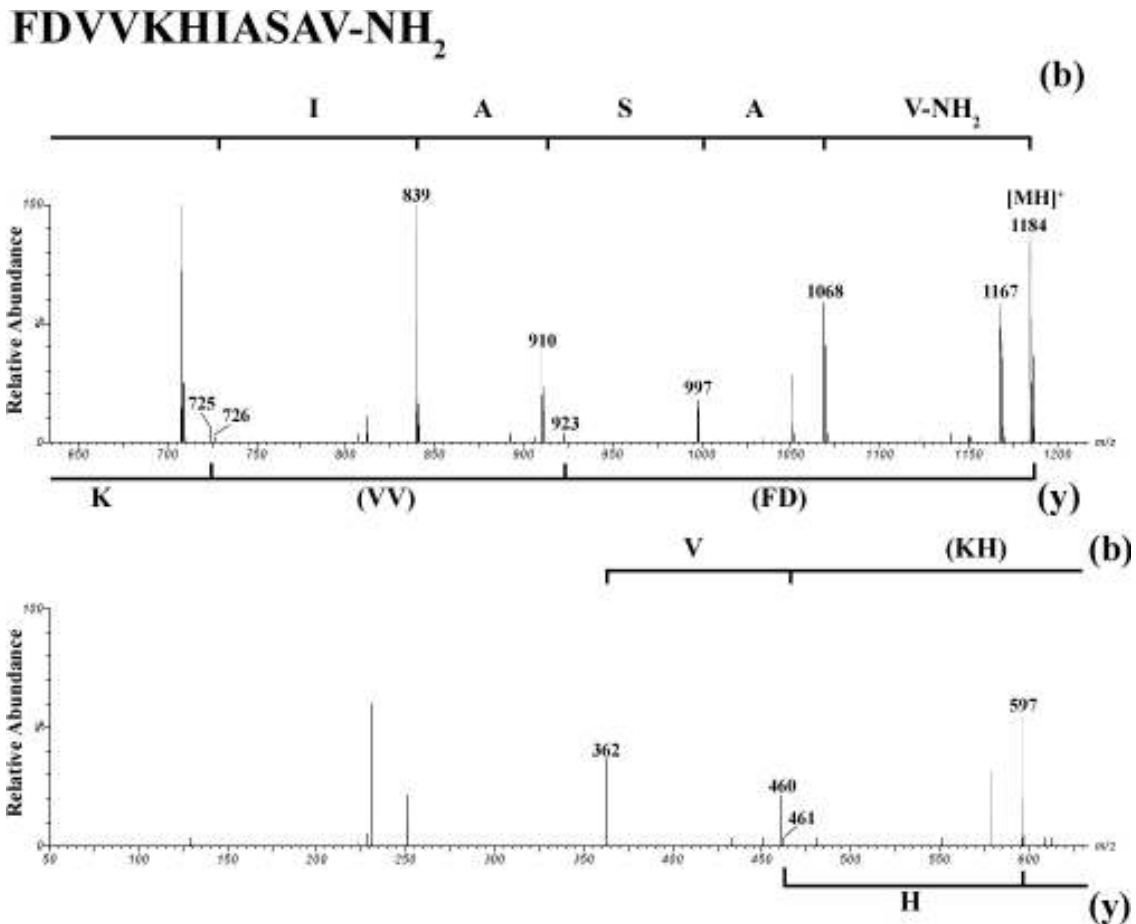


Figure 4.10 Collision induced (MS/MS) positive ion mass spectrum of ewingiin 1.1 (**1**) isolated from Population B of *Litoria ewingii*. Positive ion fragmentations of the [MH]⁺ species, (b) and (y) fragment ions are shown above and below the spectrum, respectively. Magnification: *m/z* 50-702 (x2); *m/z* 770-1130 (x2).

The spectrum of (**1**) illustrates seven (b) cleavage ions which can be used to identify nine of the residues, but not the orientation of the (Lys-His) residues. In addition, four (y) cleavage ions reveal the orientation of the Lys4 and His5 residues and an additional backbone cleavage after the first two residues. The spectrum shows the majority of the sequence, except for the first two residues (Phe1-Asp2). Edman sequencing was used to identify the isobaric Lys/Gln5, and the isomeric Leu/Ile7, and the first two residues, completing the sequencing.

The collision-induced (MS/MS) spectrum of the ESMS produced (MH)⁺ ion of ewingiin 2.2 (6) obtained in the positive ion mode is illustrated in figure 4.11.

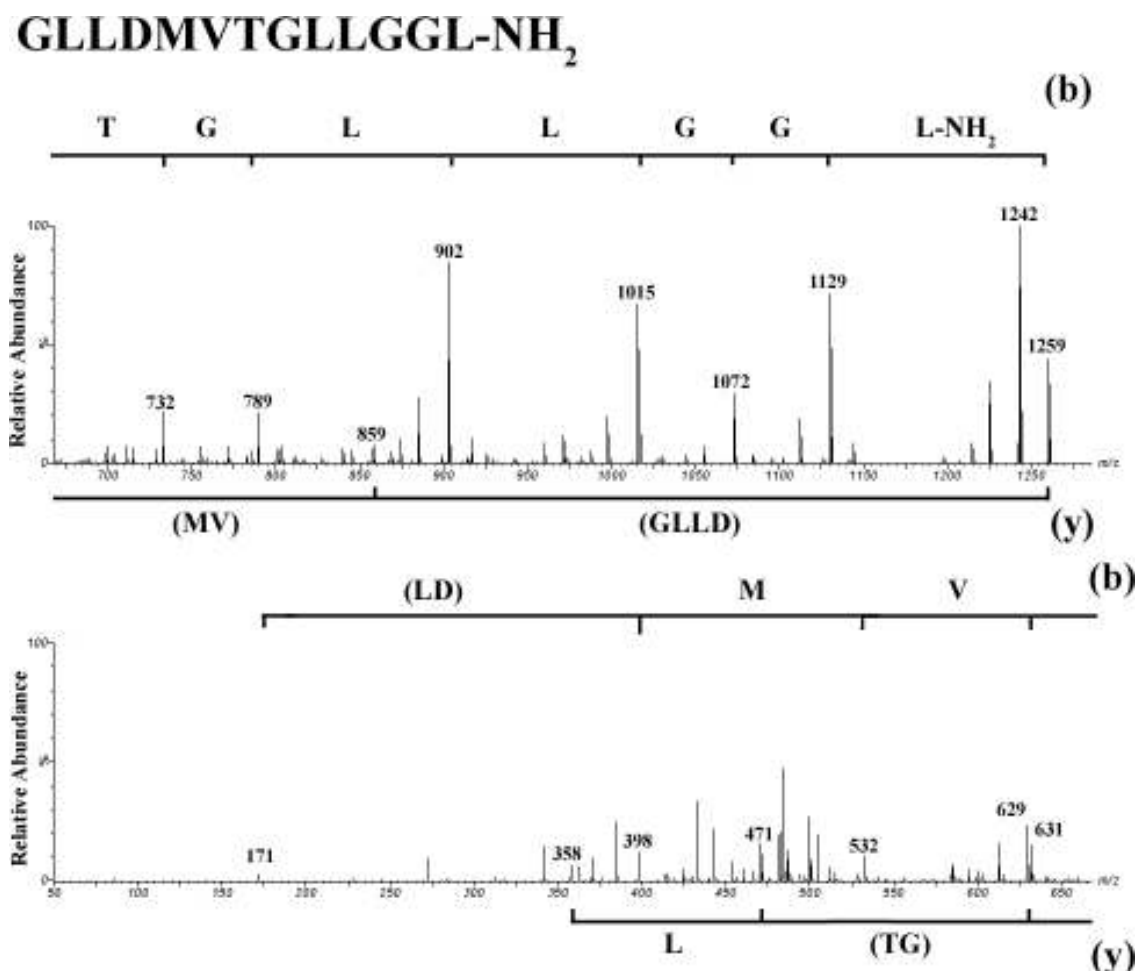


Figure 4.11 Collision induced (MS/MS) positive ion mass spectrum of ewingiin 2.2 (6) isolated from Population B of *Litoria ewingii*. Positive ion fragmentations of the [MH]⁺ species, (b) and (y) fragment ions are shown above and below the spectrum, respectively. Magnification: m/z 50-540 (x16).

The spectrum ewingiin 2.2 (6) illustrates ten (b) cleavage ions which can be used to identify the last nine of the residues, but not the orientation of the (Leu3-Asp4) residues. In addition, four (y) cleavage ions can be used to identify Leu9 and two pairs of residues, (Met-Val) and (Thr-Gly). Edman sequencing was used to identify the isomeric Leu/Ile throughout the sequence and the first four residues, completing the sequencing.

The collision-induced (MS/MS) spectra of the ESMS produced (MH)⁺ ion of ewingiin 2.3 (**9**) obtained in the positive ion mode is illustrated in figure 4.12.

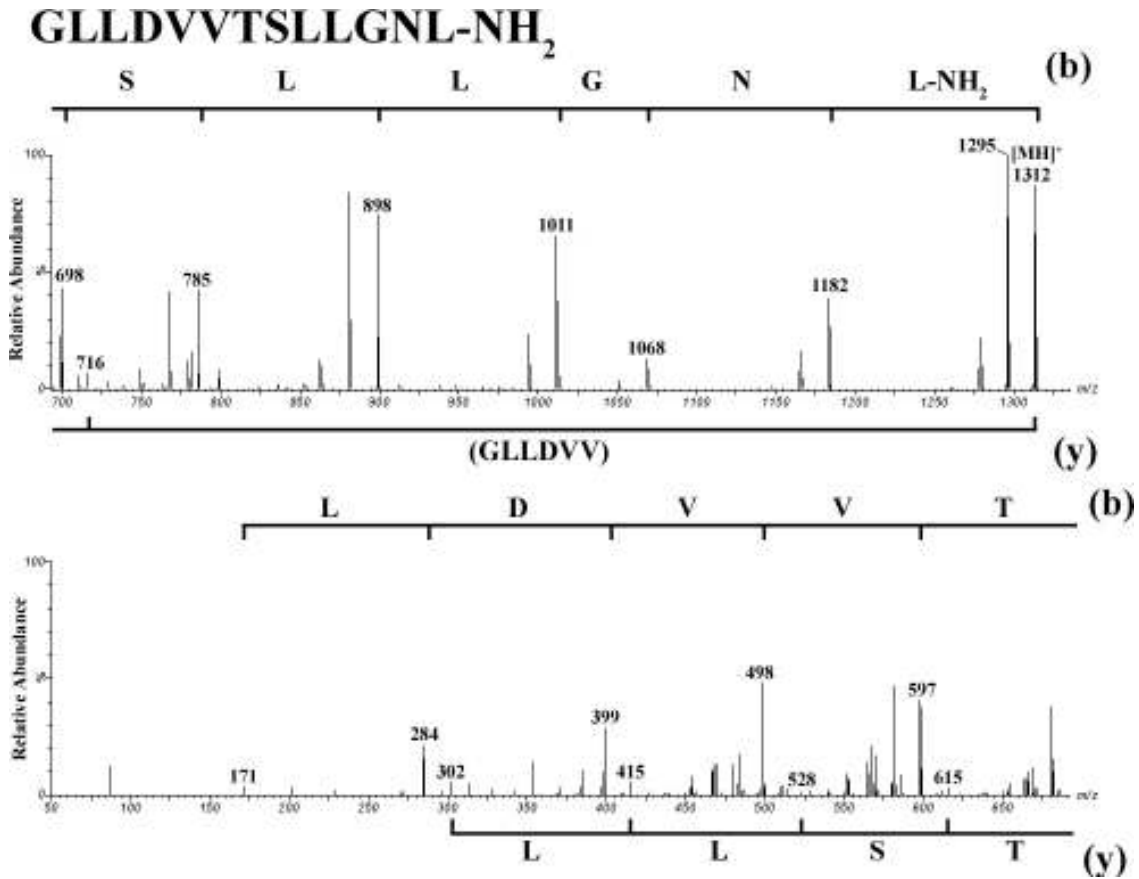


Figure 4.12 Collision induced (MS/MS) positive ion mass spectrum of the ewingiin 2.3 (**9**) isolated from Population B of *Litoria ewingii*. Positive ion fragmentations of the [MH]⁺ species, (b) and (y) fragment ions are shown above and below the spectrum, respectively. Magnification: *m/z* 50-346 (x10); *m/z* 350-1247 (x4).

The spectrum of ewingiin 2.3 (**10**) illustrates eleven (b) cleavage ions which can be used to identify residues three to eleven. In addition, five (y) cleavage ions can be used to identify residues seven to ten. Edman sequencing was used to identify the isomeric Leu/Ile throughout the sequence and the first two residues, completing the sequencing.

The collision-induced (MS/MS) spectra of the ESMS produced (MH)⁺ ion of ewingiin 2.4 (**10**) obtained in the positive ion mode is illustrated in figure 4.13.

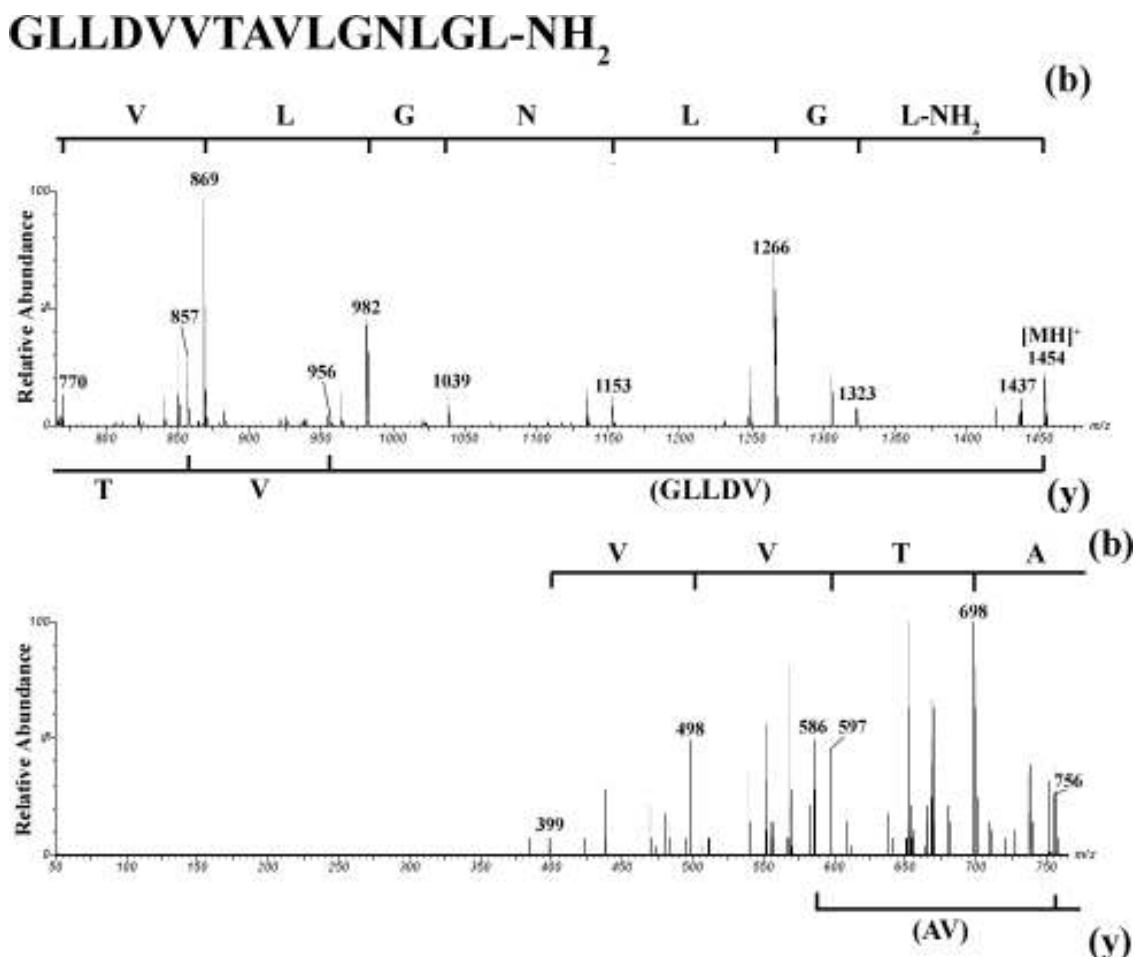


Figure 4.13 Collision induced (MS/MS) positive ion mass spectrum of ewingiin 2.4 **10** isolated from Population B of *Litoria ewingii*. Positive ion fragmentations of the (MH)⁺ species, (b) and (y) fragment ions are shown above and below the spectrum, respectively. Magnification: m/z 50-742 (x6); m/z 1273-1431 (x6).

The spectrum of ewingiin 2.4 (**10**) illustrates eleven (b) cleavage ions which can be used to identify residues five to thirteen. In addition, and four (y) cleavage ions can be used to identify residues six and seven. Edman sequencing was used to identify the isomeric Leu/Ile throughout the sequence and the first four residues, completing the sequencing.

A summary of the mass spectral data obtained for the peptides isolated from *L. ewingii* (Population B) is illustrated in table 4.2.

Table 4.2: Mass spectral data for *Litoria ewingii* peptides isolated from population B.

Tryptophyllin 6.3 IVFFP-NH₂

(MH)⁺ *m/z* 621

b ions *m/z* 621, 507, 360, 213 [FFP-NH₂]

y ions *m/z* 621, 508, 409, 262, 115 [IVFFP-NH₂]

(M-H)⁻ *m/z* 619

α ions *m/z* 619, 506, 407, 260, 113 [IVFFP-NH₂]

β ions *m/z* 619, 507, 358, 211 [FFP-NH₂]

γF³ *m/z* 390, **δF⁴** *m/z* 375, **γF⁴** *m/z* 243, **δF³** *m/z* 228

Sequence: IVFFP-NH₂

Ewingiin 1 GWFDVVKHIASAV-NH₂

(MH)⁺ *m/z* 1427

b ions *m/z* 1427, 1311, 1153, 1082, 969, 704, 605, 506, 391, 244 [FDVV(KH)IASAV-NH₂]

y ions *m/z* 1427, 922, 823, 724, 596, 459 [(GWFD)VVKH]

(M-H)⁻ *m/z* 1425

[(M-H)⁻ -CH₃O]⁻ *m/z* 1395

[(M-H)⁻ -CH₃O, -H₂O]⁻ *m/z* 1377

α ions from [(M-H)⁻ -CH₃O, -H₂O]⁻ *m/z* 1377, 1135, 988, 692, 564, 427, 406, 314, 243, 186

[(GW)F(D*VV)KHIAS*]

γD⁴ *m/z* 1018, **δD⁴** *m/z* 406

Sequence: (GW)FDVVKHIASAV-NH₂

Table 4.2: Continued.**Ewingiin 1.1 FDVVKHIASAV-NH₂**(MH)⁺ *m/z* 1184**b ions** *m/z* 1184, 1068, 997, 910, 839, 726, 461, 362 [V(KH)IASAV-NH₂]**y ions** *m/z* 1184, 923, 725, 597, 460, [(FD)(VV)KH]**Sequence:** (FD)VVKHIASAV-NH₂**Ewingiin 2.2 GLLDMVTGLLGGL-NH₂**(MH)⁺ *m/z* 1259**b ions** *m/z* 1259, 1129, 1072, 1015, 902, 789, 629, 532, [VTGLLGGL-NH₂]**y ions** *m/z* 1259, 732, 631, 529, 472, 358, 245 [(GLLDM)VTGLL]**Sequence:** (GLLD)VVTSLGGL-NH₂**Ewingiin 2.3 GLLDVVTSLLGNL-NH₂**(MH)⁺ *m/z* 1312**b ions** *m/z* 1312, 1182, 1068, 1011, 898, 785, 698, 597, 498, 399, 284, 171
[LDVVTSLLGNL-NH₂]**y ions** *m/z* 1312, 716, 615, 528, 415, 302 [(GLLDVV)TSLL]**Sequence:** (GL)LDVVTSLLGNL-NH₂**Ewingiin 2.4 GLLDMVTAVLGNLGL-NH₂**(MH)⁺ *m/z* 1454**b ions** *m/z* 1454, 1323, 1266, 1153, 1039, 982, 869, 770, 698, 597, 498, 399
[VVTAVLGNLGL-NH₂]**y ions** *m/z* 1453, 956, 857, 756, 586 [(GLLDV)VT(AV)]**Sequence:** (GLLD)VVTAVLGNLGL-NH₂

All of the peptides isolated from *L. ewingii* populations contain the post-translational modification C-terminal amide, confirmed by the loss of 17 Da from the [MH]⁺ ions. The negative ion ESMS spectra of the [M-H]⁻ species of ewingiins 2.2-2.4 were too complex to provide significant sequencing data. This is likely to be due to the competing facile side-chain cleavages of Asp, Asn, Ser, Thr and Met residues.

4.2.3 Biological activities of *Litoria ewingii* skin peptides

The peptides tryptophyllin 6.1-6.3 were tested for both smooth muscle (via CCK2 receptor activation) and opioid activities using guinea pig ileum [372, 373], as many other tryptophyllin peptides from the species *L. rubella* [68]. The peptides however, did not show any significant activities from either of the biological tests.

Ewingiin 1 (formerly Uperin 7.1) was tested in previous work and was shown to have moderate antibiotic activity (MIC ($\mu\text{g}/\text{mL}$)): *Leuconostoc lactis* (50); *Streptococcus uberis* (100) [368]. Ewingiin 2.1 (formerly caeridin 7.1) has been tested for antibiotic and nNOS inhibition activities in previous work, and showed no significant activities for either test [368]. Ewingiins 2.2-2.4 have yet to be tested. Caerin 1.1 is a documented wide spectrum antibiotic (MIC ($\mu\text{g}/\text{mL}^{-1}$)): *Bacillus cerues* (50), *Enterococcus faecalis* (25), *Leuconostoc lactis* (1.5), *Listeria innocua* (25), *Micrococcus luteus* (12), *Staphylococcus aureus* (3), *Staphylococcus epidermidis* (12), *Escherichia coli* (100), *Pasteurella multocida* (25)) and an nNOS inhibitor (IC₅₀ 36.6 μM) [369].

4.2.4 Morphological differences in *Litoria ewingii* populations

The population of *L. ewingii* from around regions of the Adelaide hills and Fleurieu peninsula (population A) show some subtle, but distinct differences relative to the population from south-eastern South Australia (population B).

Individuals from population A have three or four large, discrete, black spots on the posterior surfaces of the thighs upon a yellow background; these spots are not present on the thighs of individuals from population B (observations from a series of 30 specimens). Also an estimated one in twenty of *L. ewingii* from the Population B are green. These green individuals are absent in the Adelaide hills and Fleurieu peninsula. Green individuals are also known to be common throughout regions of Victoria, quite close in locality to population B. Elsewhere throughout the geographic distribution of *L. ewingii*, some individuals are a pale yellow, whereas others bear black markings, but these are small and irregularly shaped [353, 374].

4.3 Summary and Conclusions

The peptides profiles of populations of *Litoria ewingii* from Adelaide and south-eastern South Australia are distinctly different. The peptides from each population do, however, share a high degree of sequence homology. Geographical isolation of these populations and mutations in the DNA encoding the skin peptides, has lead to changes in the peptide profiles over time. The peptide profiling technique was successfully used to observe these changes. In this manner, peptide profiling could also be used to aid in mapping out the geographical migration pattern of frog species.

When the morphological features are combined with marked differences in peptide profiles it becomes evident that the populations merit taxonomic recognition. If it were further shown that individuals of *L. ewingii* from two separate populations were to have offspring that were infertile, then that would merit reclassification of the two anuran populations as being a separate species [9]. We lack evidence meriting specific status but note that the extent of divergence is comparable to the morphological distinction of the subspecies of *Litoria verreauxii*: *L. verreauxii verreauxii* and *L. verreauxii alpina*, though a comparison of their respective peptide profiles is not available. Accordingly we recognise the populations of *L. ewingii* as subspecies: *L. ewingii ewingii* and *L. ewingii calliscelis*.

Environmental factors may lead to the up regulation of some peptides. These factors arise in response to different environmental threats (microbial, fungal, plant etc.), which in turn would effect a given peptide profile. However, the SES technique largely depletes the granular glands upon activation (see Section 1.3.1), allowing for all detectable skin peptides to be analysed, using the highly sensitive HPLC and ESMS techniques [40, 44, 189, 375]. Also, the *L. ewingii* specimens were kept in isolation throughout this study, minimizing any environmental exposure.

Future studies include biologically testing the peptides isolated from population B, for analgesic, smooth muscle, hormonal, and antimicrobial activities. If some of these were found to be biologically active, the peptides could be used as lead compounds for the

development of pharmaceuticals. Studies into the 3-dimensional structure of the peptides using 2-dimensional NMR experiments may also follow. Future studies of the peptide profiles of *L. ewingii* populations from other regions may provide further insight into their migration pattern and taxonomic speciation.

4.4 Experimental

4.4.1 Collection and preparation of frog skin secretions

Seven specimens of *Litoria ewingii* were collected from near the River Murray at Renmark and maintained in captivity for the duration of this investigation. The frogs were held by the back legs, the skin moistened with deionised water, and the granular dorsal glands situated on the back were stimulated by means of a bipolar electrode of 21G platinum attached to a Palmer Student Model square wave electrical stimulator. The electrode was rubbed gently in a circular manner on the dorsal surface of the animal using 10 volts and a pulse duration of 3ms [44]. The liberated secretion was washed from the frog with deionised water (50cm³), the mixture filtered through a high volume (HV) filter unit (0.45 μ m), and reduced in volume to ca. 1cm³. This procedure does not injure the animal and was approved by the University of Adelaide Animal Ethics Committee.

4.4.2 HPLC separation of granular secretion

HPLC separation of the skin secretion was achieved using a VYDAC C18 HPLC column (5 μ , 200A, 4.6 x 250mm) (Separations Group, Hesperia, CA., USA) equilibrated with 10% acetonitrile/90% water/0.01% trifluoroacetic acid (TFA). The crude solution (150 μ L) was injected into the column. The elution profile was generated using a linear gradient produced by an ICI DP 800 Data Station controlling two LC1100 HPLC pumps, increasing from 10-75% acetonitrile over a period of 30 min. at a flow rate of 1mL/min. The eluant was monitored by ultraviolet absorbance at 214nm using ICI LC-1200 variable wavelength detector (ICI Australia, Melbourne, Australia). Fractions were collected, concentrated and dried *in vacuo* for MS and Edman Investigation. HPLC peptide profiles are shown in Figure 2.

4.4.3 Sequence determination of peptides by mass spectrometry

Electrospray mass spectra were obtained using a Micromass QTOF2 hybrid orthogonal acceleration time-of-flight mass spectrometer (Waters/Micromass, Manchester, UK) with a mass range to m/z 10,000. The QTOF2 is fitted with an electrospray (ES) source in an orthogonal configuration with a Z-spray interface. Samples were dissolved in

acetonitrile/water (1:1 v/v) and infused into the ES source at a flow rate of 5 $\mu\text{L}/\text{min}$. Experimental conditions were as follows: capillary voltage 50V. Tandem mass spectrometry (MS/MS) data were acquired using argon as the collision gas and collision energy was adjusted to give maximum fragmentation.

4.4.4 Automated Edman sequencing

Peptides were freeze dried from approximately 200 μl of solution and redissolved in 30 μl of 10% acetonitrile/90% water/0.01% TFA solutions. 15 μl of these samples were then N-terminally sequenced using a Procise® automated sequencer followed by a series of HPLC runs performed on a C18 reverse phase column using UV-absorbance detection. Automated Edman Sequencing was performed by Chris Cursaro, School of Molecular and Biomedical Science, The University of Adelaide.

4.4.5 Synthesis of peptides from *Litoria ewingii*

The ewingiin and tryptophyllan peptides were synthesized by Genscript Corp. (Scotch Plains, NJ, USA) using standard procedure [376].

4.4.6 Biological activity testing

Smooth muscle contraction testing and opioid activity studies of the peptides tryptophyllin 6.1-6.3 were carried out by Rebecca J. Jackway and Dr. Ian F. Musgrave in the Department of Clinical and Experimental Pharmacology; using standard procedures described previously [372, 373]. The biological activities of the peptides are summarised in section 4.2.3.

4.4.6.1 Smooth muscle activity testing

Male guinea pigs (~ 300 g) were used in these experiments. Immediately prior to the experiment, the guinea pigs were killed by stunning and subsequent decapitation. The ileum was extracted, mesenteric tissue was removed and the tissue cleaned by rinsing with physiological salt solution (Kreb's solution; comprising of in mM: KCl 2.7, CaCl_2 1.0, NaHCO_3 13.0, NaH_2PO_4 3.2, NaCl 137, glucose 5.5; pH 7.4). 2 cm segments were suspended in 10 mL organ baths containing Kreb's solution and gassed with 95 % O_2 and 5 % CO_2 . The ileum segments were connected to an isometric force-displacement

transducer and a tissue holder. The tension was recorded using MACLAB (version 3.0). The Krebs's solution was replaced several times to ensure that the ileum segments were washed thoroughly, and allowed to equilibrate for a period of 30 min under a resting tension of 2 g. Solution supply reservoirs and organ baths were maintained at 37 °C and gassed with O₂/CO₂ as described above.

Following the equilibration time, the bath solution was replaced several times until a stable tension baseline was reached. The tension was readjusted to 2 g. Acetylcholine (Ach) (10^{-8} – 10^{-6} M) was added to each organ bath to constrict the ileum tissue. This was washed out by replacing the Krebs's solution several times. A second addition of Ach (10^{-6} M) was added to ensure that the response was stable. The Ach was washed out and ileum tissue left for 5 min until a stable baseline was achieved. A cumulative concentration response curve to cholecystakinin octapeptide (CCK-8) (10^{-10} – 10^{-8} M) was then completed. Following a wash, the tissue was again left for 5 min until a stable baseline was achieved. The cumulative concentration response curve was repeated for CCK-8-NS (10^{-9} – 10^{-7} M) or peptide samples (10^{-10} – 10^{-5} M). In several experiments, following the wash, ileum tissues were pretreated with atropine (3×10^{-7} M), CCK-2 receptor antagonist YM022 (1×10^{-6} M) or L-N-nitroarginine (L-NNA) (2×10^{-4} M) and allowed to equilibrate for 15 min until a stable baseline was reached. Ach, CCK-8, CCK-8-NS and peptide samples were reapplied as outlined above.

To compare the potencies of different peptides and to measure the changes in potency produced by receptor antagonists, the contractions of the ileum were expressed as a percentage of Ach (10^{-6} M) contraction. Data are expressed as mean \pm SEM. Differences between data sets were evaluated by performing analysis of variance (ANOVA) followed by Dunnett's test. A level of $P < 0.05$ was considered to be significant.

4.4.6.2 Opioid activity studies

Male guinea pigs (~ 300 g) were used in these experiments. Immediately prior to the experiment, the guinea pigs were killed by stunning and subsequent decapitation. The ileum was extracted approximately 10 cm from the ileo-caecal junction and strips of

longitudinal muscle with attached myenteric plexus were removed and cleaned by rinsing with physiological salt solution (Kreb's solution). The tissue segments were prepared as per the smooth muscle contraction assay as described previously [50, 372].

Following the 30 min equilibration time, the bath solution was replaced several times until a stable baseline tension was obtained. The tension was readjusted to 2 g. Ach (10^{-8} – 10^{-6} M) was added to each organ bath to constrict the ileum tissue. This was washed out by replacing the Kreb's solution several times. To electrically stimulate neurons in the myenteric plexus, the tissue preparation was passed between a pair of platinum electrodes, which were connected to the output of a Grass stimulator (West Warwick, USA). The tissue was stimulated at 60 V, 0.1 Hz with pulses of 2 ms duration. L-NNA (2×10^{-4} M) was added and the tissue preparation equilibrated for a further 15 min until a stable contraction response was achieved. In each tissue preparation the concentration response curves for dynorphin A (1-13) (10^{-12} – 10^{-10} M) were constructed using serial application. Following a wash, the L-NNA (2×10^{-4} M) was reapplied and the tissue was again left for 5 min until a stable contraction was achieved. The cumulative concentration response curve was repeated for the peptide samples (10^{-10} – 10^{-5} M). In several experiments, following the wash, ileum tissues were pretreated with naloxone (1×10^{-7} M) in addition to L-NNA (2×10^{-4} M) and allowed to equilibrate for 15 min until a stable contraction was reached. Dynorphin A (1-13) and the peptides samples were reapplied as outlined above.

To compare the potencies of different peptides and to measure the changes in potency produced by naloxone, the concentrations of agonist which decrease the electrically stimulated contractions by 50 % (IC_{50}) were determined. The apparent dissociation constant K_d of naloxone was also calculated for each peptide using the equation $K_d = C/(DR-1)$ derived from the mass law for competitive antagonism, where C is the concentration of naloxone (1×10^{-7} M) and DR is the dose ratio of the agonist (the ratio of IC_{50} values in the presence and absence of the antagonist) [377]. Differences between data sets were evaluated by performing ANOVA, followed by Dunnett's test. A level of $P < 0.05$ was considered significant.

Chapter 5

Solution structures of two antimicrobial peptides from the scorpion *Mesobuthus eupeus mongolicus*

5.1 Introduction

5.1.1 *Mesobuthus eupeus mongolicus*

The scorpion commonly known as the ‘Lesser Asian Scorpion’, *Mesobuthus eupeus mongolicus* (formerly *Buthus eupeus mongolicus*), is a subspecies of *M. eupeus* first described by A. Birula in 1911 [378]. There are 23 recognised subspecies of *M. eupeus*, that are geographically distributed throughout regions of southern Europe (Turkey, Armenia, Georgia), southern Russia (Astrakahn region), the middle east (Israel, Iran, Iraq), and northern Asia (China, Mongolia, Kazakhstan, Korea) [379]. The subspecies *M. eupeus mongolicus* inhabits arid to semi-arid regions of the Gobi desert, ranging from northern China to southern Mongolia [380]. The species is quite small, as scorpion adults grow up to a total length of approximately 38 mm. The scorpions generally have yellow appendages (legs, claws, tail) and their cephalorax and abdomen (head and body) range from a yellow to dark grey, depending on the population (figure 5.1) [379].



NOTE:

This figure/table/image has been removed to comply with copyright regulations. It is included in the print copy of the thesis held by the University of Adelaide Library.

Figure 5.1: *Mesobuthus eupeus* (top) and the geographical distribution of the subspecies *M. eupeus mongolicus* (bottom) [380].

The venom of *M. eupeus mongolicus* has been used in Chinese medicine, as has the venom of a larger sympatric scorpion species, *M. martensii* (the ‘Chinese scorpion’) [380]. Unfortunately, in recent times *M. martensii* has been listed in the China Species Red list as a vulnerable species. Human overexploitation of the habitat of *M. eupeus mongolicus* may also threaten it as a species, though insufficient data exists to classify it as a threatened species [3, 4].

5.1.2 The venom composition of *Mesobuthus eupeus*

The venom of *M. eupeus*, like that of all scorpions, is composed of a mixture of mucopolysaccharides, hyaluronidase, phospholipase, low molecular weight histamine like

molecules, protease inhibitors, and biologically active peptides [6]. The majority of early research into the venom composition of *M. eupeus* was performed by Evgeny Grishin and co-workers from specimens in southern Russia [115, 381, 382]. It was found that a large portion of the venoms peptide content consists of disulfide-rich neurotoxic ion channel inhibitors, designed to subdue prey (such as insects and spiders) and for defence against predators. Many of the peptides, in particular the chloride channel inhibitors were named insectotoxins for their selectivity toward insect chloride channels [382-385].

With the aid of modern chromatographic methods and mass spectrometry, peptides that occur in much lower concentrations within the *M. eupeus* venom have been isolated and characterised. The activities and amino acid sequences of biologically active peptides isolated from *M. eupeus* venom are listed in table 5.1.

Table 5.1: Peptides isolated from the venom of *M. eupeus* specimens. Amino acid sequences may vary depending on the subspecies.

<i>Peptide</i>	<i>Amino acid sequence[#]</i>	<i>Disulfide motif</i>	<i>Activity*</i>	<i>Reference</i>
<i>Insectotoxin-11</i>	<u>M</u> <u>C</u> <u>M</u> <u>P</u> <u>C</u> <u>F</u> <u>T</u> <u>T</u> <u>R</u> <u>P</u> <u>D</u> <u>M</u> <u>A</u> <u>Q</u> <u>Q</u> <u>C</u> <u>R</u> <u>A</u> <u>C</u> <u>C</u> <u>K</u> <u>G</u> <u>R</u> <u>G</u> <u>K</u> <u>C</u> <u>F</u> <u>G</u> <u>P</u> <u>Q</u> <u>C</u> <u>L</u> <u>C</u> <u>G</u> <u>Y</u> D-NH ₂	2-19, 5-26, 16-31, 20-33	<i>a</i>	[385]
<i>Insectotoxin-12</i>	<u>A</u> <u>D</u> <u>G</u> <u>V</u> <u>K</u> <u>G</u> <u>K</u> <u>S</u> <u>G</u> <u>C</u> <u>K</u> <u>I</u> <u>S</u> <u>C</u> <u>F</u> <u>L</u> <u>D</u> <u>N</u> <u>D</u> <u>L</u> <u>C</u> <u>N</u> <u>A</u> <u>D</u> <u>C</u> <u>K</u> <u>Y</u> <u>G</u> <u>G</u> <u>K</u> <u>N</u> <u>L</u> <u>S</u> <u>W</u> <u>C</u> <u>I</u> <u>P</u> <u>D</u> <u>K</u> <u>S</u> <u>G</u> <u>Y</u> <u>C</u> <u>W</u> <u>C</u> <u>P</u> <u>N</u> <u>K</u> <u>G</u> <u>W</u> <u>N</u> <u>S</u> <u>I</u> <u>K</u> <u>S</u> <u>E</u> <u>T</u> <u>N</u> <u>T</u> <u>C</u> <u>-</u> <u>O</u> <u>H</u>	11-62, 15-37, 22-45, 26-47	<i>b</i>	[382]
<i>Insectotoxin-13</i>	<u>M</u> <u>C</u> <u>M</u> <u>P</u> <u>C</u> <u>F</u> <u>T</u> <u>T</u> <u>D</u> <u>H</u> <u>Q</u> <u>T</u> <u>A</u> <u>R</u> <u>R</u> <u>C</u> <u>R</u> <u>D</u> <u>C</u> <u>C</u> <u>G</u> <u>G</u> <u>R</u> <u>G</u> <u>R</u> <u>K</u> <u>C</u> <u>F</u> <u>G</u> <u>Q</u> <u>C</u> <u>L</u> <u>C</u> <u>G</u> <u>Y</u> D-OH	2-19, 5-27, 16-31, 20-33	<i>a</i>	[383]
<i>Insectotoxin-14</i>	<u>M</u> <u>C</u> <u>M</u> <u>P</u> <u>C</u> <u>F</u> <u>T</u> <u>T</u> <u>D</u> <u>H</u> <u>N</u> <u>M</u> <u>A</u> <u>K</u> <u>K</u> <u>C</u> <u>R</u> <u>D</u> <u>C</u> <u>C</u> <u>G</u> <u>N</u> <u>G</u> <u>K</u> <u>C</u> <u>F</u> <u>G</u> <u>P</u> <u>Q</u> <u>C</u> <u>L</u> <u>C</u> <u>N</u> <u>R</u> -OH	2-19, 5-26, 16-31, 20-33	<i>a</i>	[383]
<i>Insectotoxin-15</i>	<u>M</u> <u>C</u> <u>M</u> <u>P</u> <u>C</u> <u>F</u> <u>T</u> <u>T</u> <u>D</u> <u>P</u> <u>N</u> <u>M</u> <u>A</u> <u>N</u> <u>K</u> <u>C</u> <u>R</u> <u>D</u> <u>C</u> <u>C</u> <u>G</u> <u>G</u> <u>K</u> <u>K</u> <u>C</u> <u>F</u> <u>G</u> <u>P</u> <u>Q</u> <u>C</u> <u>L</u> <u>C</u> <u>N</u> <u>R</u> -OH	2-19, 5-26, 16-31, 20-33	<i>a</i>	[383]
<i>Insectotoxin-15A</i>	<u>M</u> <u>C</u> <u>M</u> <u>P</u> <u>C</u> <u>F</u> <u>T</u> <u>T</u> <u>D</u> <u>P</u> <u>N</u> <u>M</u> <u>A</u> <u>K</u> <u>K</u> <u>C</u> <u>R</u> <u>D</u> <u>C</u> <u>C</u> <u>G</u> <u>N</u> <u>G</u> <u>K</u> <u>C</u> <u>F</u> <u>G</u> <u>P</u> <u>Q</u> <u>C</u> <u>L</u> <u>C</u> <u>N</u> <u>R</u> -NH ₂	2-19, 5-26, 16-31, 20-33	<i>a</i>	[384]
<i>BeKm-1</i>	<u>R</u> <u>P</u> <u>T</u> <u>D</u> <u>I</u> <u>K</u> <u>C</u> <u>S</u> <u>E</u> <u>S</u> <u>Y</u> <u>Q</u> <u>C</u> <u>F</u> <u>P</u> <u>V</u> <u>C</u> <u>K</u> <u>S</u> <u>R</u> <u>F</u> <u>G</u> <u>K</u> <u>T</u> <u>N</u> <u>G</u> <u>R</u> <u>C</u> <u>V</u> <u>N</u> <u>G</u> <u>F</u> <u>C</u> <u>D</u> <u>C</u> F-OH	28-49, 34-54, 38-56	<i>c</i>	[386]
<i>BeM9</i>	<u>A</u> <u>R</u> <u>D</u> <u>A</u> <u>Y</u> <u>I</u> <u>A</u> <u>K</u> <u>P</u> <u>H</u> <u>N</u> <u>C</u> <u>V</u> <u>Y</u> <u>E</u> <u>C</u> <u>Y</u> <u>N</u> <u>P</u> <u>K</u> <u>G</u> <u>S</u> <u>Y</u> <u>C</u> <u>N</u> <u>D</u> <u>L</u> <u>C</u> <u>T</u> <u>E</u> <u>N</u> <u>G</u> <u>A</u> <u>E</u> <u>S</u> <u>G</u> <u>Y</u> <u>C</u> <u>Q</u> <u>I</u> <u>L</u> <u>G</u> <u>K</u> <u>Y</u> <u>G</u> <u>N</u> <u>A</u> <u>C</u> <u>W</u> <u>C</u> <u>I</u> <u>Q</u> <u>L</u> <u>P</u> <u>D</u> <u>N</u> <u>V</u> <u>P</u> <u>I</u> <u>R</u> <u>I</u> <u>P</u> <u>G</u> <u>K</u> <u>C</u> <u>H</u> <u>-</u> <u>O</u> <u>H</u>	12-65, 16-38, 24-48, 28-50	<i>b</i>	[381]
<i>BeM10</i>	<u>V</u> <u>R</u> <u>D</u> <u>G</u> <u>Y</u> <u>I</u> <u>A</u> <u>D</u> <u>D</u> <u>K</u> <u>D</u> <u>C</u> <u>A</u> <u>Y</u> <u>F</u> <u>C</u> <u>G</u> <u>R</u> <u>N</u> <u>A</u> <u>Y</u> <u>C</u> <u>D</u> <u>E</u> <u>E</u> <u>C</u> <u>K</u> <u>G</u> <u>A</u> <u>E</u> <u>S</u> <u>G</u> <u>K</u> <u>C</u> <u>W</u> <u>Y</u> <u>A</u> <u>G</u> <u>Q</u> <u>Y</u> <u>G</u> <u>N</u> <u>A</u> <u>C</u> <u>W</u> <u>C</u> <u>Y</u> <u>K</u> <u>L</u> <u>P</u> <u>D</u> <u>W</u> <u>V</u> <u>P</u> <u>I</u> <u>K</u> <u>Q</u> <u>K</u> <u>V</u> <u>S</u> <u>G</u> <u>K</u> <u>C</u> <u>N</u> <u>-</u> <u>O</u> <u>H</u>	12-64, 16-35, 22-45, 26-47	<i>b</i>	[381]
<i>BeM14</i>	<u>A</u> <u>R</u> <u>D</u> <u>A</u> <u>Y</u> <u>I</u> <u>A</u> <u>D</u> <u>D</u> <u>R</u> <u>N</u> <u>C</u> <u>V</u> <u>Y</u> <u>T</u> <u>C</u> <u>A</u> <u>L</u> <u>N</u> <u>P</u> <u>Y</u> <u>C</u> <u>D</u> <u>S</u> <u>E</u> <u>C</u> <u>K</u> <u>K</u> <u>N</u> <u>G</u> <u>A</u> <u>D</u> <u>S</u> <u>G</u> <u>Y</u> <u>C</u> <u>Q</u> <u>W</u> <u>L</u> <u>G</u> <u>R</u> <u>F</u> <u>G</u> <u>N</u> <u>A</u> <u>C</u> <u>W</u> <u>C</u> <u>K</u> <u>N</u> <u>L</u> <u>P</u> <u>D</u> <u>D</u> <u>V</u> <u>P</u> <u>I</u> <u>R</u> <u>K</u> <u>I</u> <u>P</u> <u>G</u> <u>K</u> <u>C</u> <u>H</u> <u>-</u> <u>N</u> <u>H</u> <u>2</u>	12-65, 16-36, 22-46, 26-48	<i>b</i>	[381]
<i>Meucin-13</i>	<u>I</u> <u>F</u> <u>G</u> <u>I</u> <u>A</u> <u>I</u> <u>G</u> <u>L</u> <u>L</u> <u>K</u> <u>N</u> <u>I</u> <u>F</u> <u>-</u> <u>N</u> <u>H</u> <u>2</u>	-	<i>d</i>	[113]
<i>Meucin-18</i>	<u>F</u> <u>F</u> <u>G</u> <u>H</u> <u>L</u> <u>F</u> <u>K</u> <u>L</u> <u>A</u> <u>T</u> <u>K</u> <u>I</u> <u>I</u> <u>P</u> <u>S</u> <u>L</u> <u>F</u> <u>Q</u> <u>-</u> <u>O</u> <u>H</u>	-	<i>d</i>	[113]
<i>Meucin-24</i>	<u>G</u> <u>R</u> <u>G</u> <u>R</u> <u>E</u> <u>F</u> <u>M</u> <u>S</u> <u>N</u> <u>L</u> <u>K</u> <u>E</u> <u>K</u> <u>L</u> <u>S</u> <u>G</u> <u>V</u> <u>K</u> <u>E</u> <u>K</u> <u>M</u> <u>K</u> <u>N</u> <u>S</u> <u>-</u> <u>O</u> <u>H</u>	-	<i>e</i>	[387]
<i>Meucin-25</i>	<u>V</u> <u>K</u> <u>L</u> <u>I</u> <u>Q</u> <u>I</u> <u>R</u> <u>I</u> <u>W</u> <u>I</u> <u>Q</u> <u>Y</u> <u>V</u> <u>T</u> <u>V</u> <u>L</u> <u>Q</u> <u>M</u> <u>F</u> <u>S</u> <u>M</u> <u>K</u> <u>T</u> <u>K</u> <u>-</u> <u>O</u> <u>H</u>	-	<i>e</i>	[387]
<i>MeuKTX</i>	<u>V</u> <u>G</u> <u>I</u> <u>N</u> <u>V</u> <u>K</u> <u>C</u> <u>K</u> <u>H</u> <u>S</u> <u>G</u> <u>Q</u> <u>C</u> <u>L</u> <u>K</u> <u>P</u> <u>C</u> <u>K</u> <u>D</u> <u>A</u> <u>G</u> <u>M</u> <u>R</u> <u>F</u> <u>G</u> <u>K</u> <u>C</u> <u>M</u> <u>N</u> <u>G</u> <u>K</u> <u>C</u> <u>D</u> <u>C</u> <u>T</u> PK-OH	7-27, 13-32, 17-34	<i>c</i>	[388]
<i>MeuKTXβ1</i>	<u>G</u> <u>F</u> <u>R</u> <u>E</u> <u>K</u> <u>H</u> <u>F</u> <u>Q</u> <u>R</u> <u>V</u> <u>K</u> <u>Y</u> <u>A</u> <u>V</u> <u>P</u> <u>E</u> <u>S</u> <u>T</u> <u>L</u> <u>R</u> <u>T</u> <u>V</u> <u>L</u> <u>Q</u> <u>T</u> <u>V</u> <u>V</u> <u>H</u> <u>K</u> <u>V</u> <u>G</u> <u>K</u> <u>T</u> <u>Q</u> <u>F</u> <u>G</u> <u>C</u> <u>P</u> <u>A</u> <u>Y</u> <u>Q</u> <u>G</u> <u>Y</u> <u>C</u> <u>D</u> <u>D</u> <u>H</u> <u>C</u> <u>Q</u> <u>D</u> <u>I</u> <u>E</u> <u>K</u> <u>K</u> <u>E</u> <u>G</u> <u>F</u> <u>C</u> <u>H</u> <u>G</u> <u>F</u> <u>K</u> <u>C</u> <u>K</u> <u>C</u> <u>G</u> <u>I</u> <u>P</u> <u>M</u> <u>G</u> F-OH	38-59, 45-64, 68-66	<i>c</i>	[389]
<i>MeuKTXβ2</i>	<u>G</u> <u>F</u> <u>R</u> <u>E</u> <u>K</u> <u>H</u> <u>F</u> <u>Q</u> <u>R</u> <u>V</u> <u>K</u> <u>Y</u> <u>A</u> <u>V</u> <u>P</u> <u>E</u> <u>S</u> <u>T</u> <u>L</u> <u>R</u> <u>T</u> <u>V</u> <u>L</u> <u>Q</u> <u>T</u> <u>V</u> <u>V</u> <u>H</u> <u>K</u> <u>V</u> <u>G</u> <u>K</u> <u>T</u> <u>Q</u> <u>F</u> <u>G</u> <u>C</u> <u>S</u> <u>A</u> <u>Y</u> <u>Q</u> <u>G</u> <u>Y</u> <u>C</u> <u>D</u> <u>D</u> <u>H</u> <u>C</u> <u>Q</u> <u>D</u> <u>I</u> <u>E</u> <u>K</u> <u>K</u> <u>E</u> <u>G</u> <u>F</u> <u>C</u> <u>H</u> <u>G</u> <u>F</u> <u>K</u> <u>C</u> <u>K</u> <u>C</u> <u>G</u> <u>I</u> <u>P</u> <u>M</u> <u>G</u> F-OH	38-59, 45-64, 68-66	<i>c</i>	[389]

[#] Disulfide bridging cystine residues are underlined, and the disulfide bridging motif defined.

***Biological activities:** *a.* chloride channel inhibitor; *b.* sodium channel inhibitor; *c.* potassium channel inhibitor; *d.* antimicrobial; *e.* antimalarial.

5.1.3 Antimicrobial meucin peptides

In recent years, Shunyi Zhu and his co-workers have isolated four non-disulfide bridged peptides from *M. eupeus mongolicus* venom, known as meucins (see Table 5.1). The peptides meucin-24 and meucin-25 inhibit the development of the malaria parasite *Plasmodium falciparum*, from infected erythrocytes (trophozoites). Amazingly, exposure of the trophozoites to 10 μ M of peptide (meucin-24 or meucin-25) for 72 hours completely clears all of the infected erythrocytes. In addition, viability tests show the peptides do not significantly affect mammalian gastric (GC-2) cells [387]. The shorter cationic peptides, meucin-13 and meucin-18 show a high degree of antimicrobial activity against a number of bacteria, fungi and yeast. Their lethal concentrations (99.9% reduction in the initial microbial density [390]) against a range of microbes are listed in table 5.2.

Table 5.2 Lethal concentrations (C_L) of meucin-13 and meucin-18 against microbes [113].

NOTE:

This figure/table/image has been removed to comply with copyright regulations. It is included in the print copy of the thesis held by the University of Adelaide Library.

Table 5.2 Continued

NOTE:
This figure/table/image has been removed
to comply with copyright regulations.
It is included in the print copy of the thesis
held by the University of Adelaide Library.

The lethal concentrations (C_L) show that in most cases meucin-18 is 2 to 14 fold more potent than meucin-13, with the exception of *B. megaterium* (both have a $C_L = 0.25\mu\text{M}$). Also, both antimicrobial peptides show greater potency against Gram-positive bacteria. This is quite common for membrane active antimicrobial peptides as Gram-negative cell walls contain both an inner and outer phospholipid bilayer. This suggests that meucin-13 and meucin-18 are likely to form pores within microbial membranes, similar to fallaxidin 4.1a (chapter 6), mellittin and aurein peptides [82, 391, 392]. The antimicrobial meucin peptides each have unique amino acid sequences and circular dichroism experiments indicate they form helical structures in membrane mimicking TFE/H₂O solution. Edmundson-Schiffer helical wheel projections based on the amino acid sequences also predict that meucin peptides are likely to adopt amphipathic α -helices on a membrane surface (figure 5.2) [393].

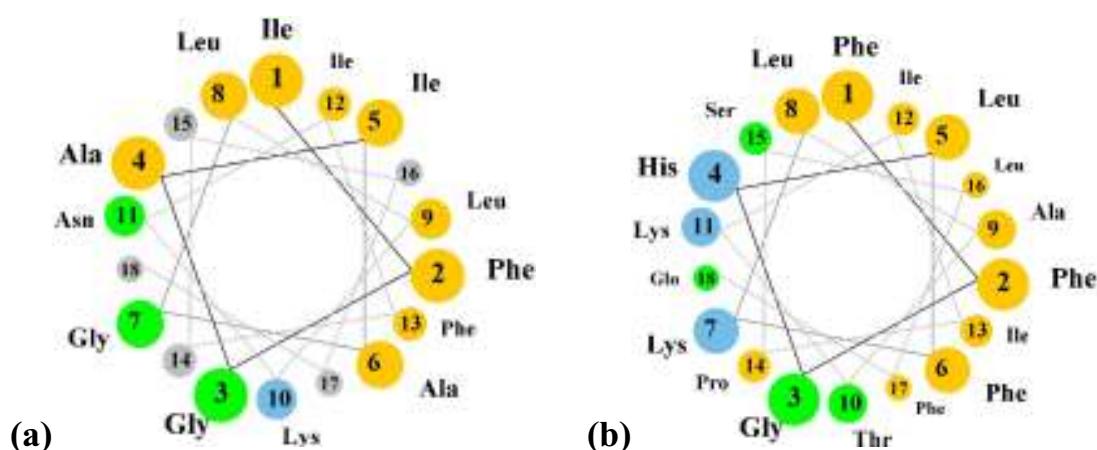


Fig 5.2 Edmundson-Schiffer helical wheel representation of meucin-13 (a) and meucin-18 (b). Non-polar, polar and basic amino acid residues are highlighted in yellow, green and blue, respectively.

Like many helical antibiotic peptides, cationic and polar sidechains are directed toward a hydrophilic face to enable electrostatic interactions with anionic microbial membranes.

The objective of this study is to verify the helical nature of meucin-13 and meucin-18 by investigating their solution structures in a membrane mimicking environment, using 2-dimensional NMR methods.

5.2 Results

Proton resonances were assigned using the sequential assignment method [394] described in section 3.1.4, using a combination of DQF-COSY, TOCSY and NOESY ^1H NMR spectra. In addition $^3J_{\text{NH}\alpha\text{H}}$ coupling constants from the 1-dimension ^1H NMR spectra and the DQF-COSY spectra were used to generate backbone dihedral restraints.

5.2.1 Chemical shift assignment

The TOCSY spectrum of meucin-13 showed coincident amide chemical shifts for Gly3 and Leu8, Ala6 and Leu9. Also, the amide chemical shifts of Ala4 and Phe13 were almost coincident. These amide chemical shifts were easily distinguished from one another upon assignment of the other regions of the TOCSY and COSY spectra. The majority of the amide region of the meucin-13 NOESY spectrum was well resolved, with sequential $\text{NH}_i\text{-NH}_{i+1}$ peaks observed from Gly3 to Phe13. The Phe2-Gly3 amide peak was not observed, so the Phe2 amide resonance was assigned from the $\text{NH}_i\text{-}\alpha\text{H}_{i+1}$ peak.

The TOCSY spectrum of meucin-18 showed a high degree of overlapping resonances in the amide region. Four coincident amide chemical shifts were observed for Ala9 and Ile13, Ile12 and Leu16, and three coincident amide chemical shifts were observed for Thr10, Ser15 and Phe17. These amide chemical shifts were distinguished from one another upon close examination of the NOESY spectrum, other regions of the TOCSY spectrum, and the COSY spectrum. The amide region of the meucin-18 NOESY spectrum was very well resolved with $\text{NH}_i\text{-NH}_{i+1}$ peaks observed from Phe2 to Gln18 with the exception of Pro14. In that case a medium $\text{NH}_i\text{-}\delta\text{H}_{i+1}$ peak was observed between Ile13 and Pro14, and medium $\delta\text{H}_i\text{-NH}_{i+1}$ peaks were observed between Pro14 and Ser15. The N-terminal residues in the NMR spectra of both meucin peptides were identified from the observed the $\alpha\text{H}_i\text{-NH}_{i+1}$ and $\alpha\text{H}_i\text{-}\beta\text{H}_{i+1}$ peaks, completing the sequences. The partial TOCSY and NOESY spectra for meucin-13 and meucin-18 are shown in figures 5.3 and 5.4, respectively.

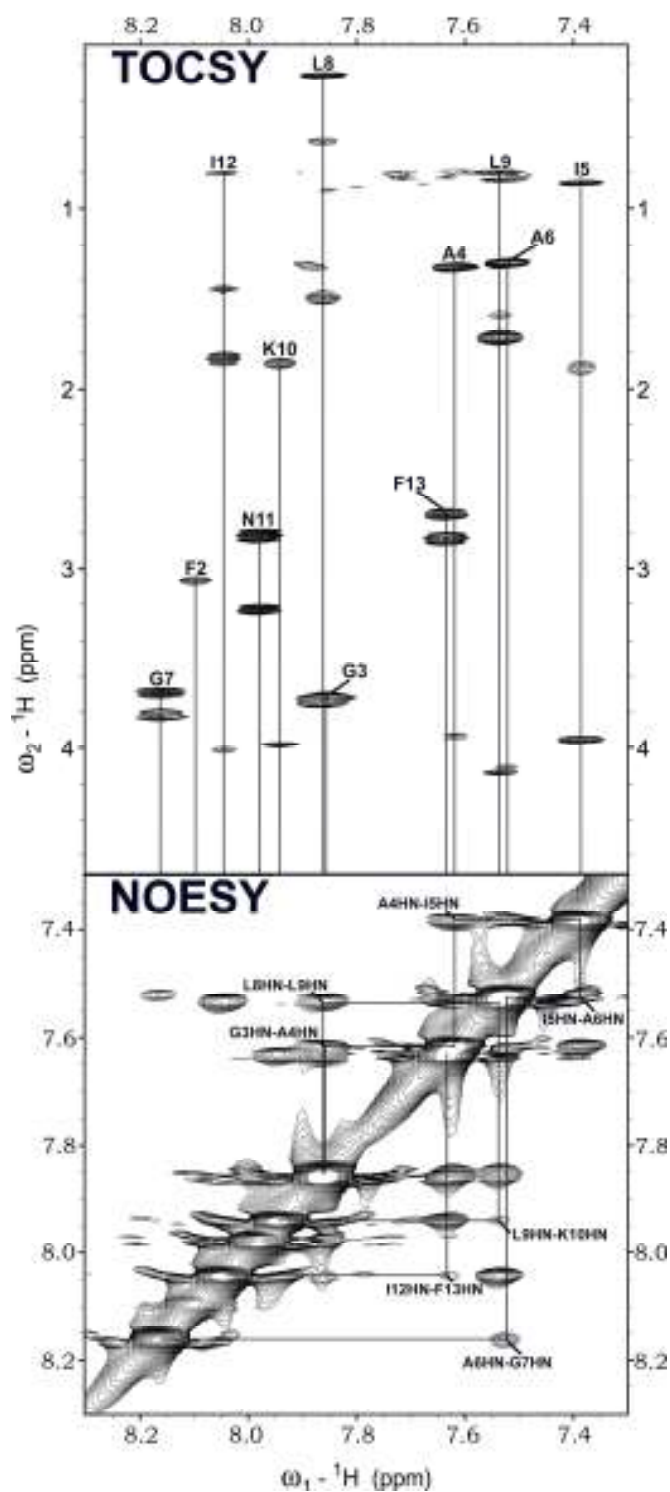


Figure 5.3 Partial NOESY (mixing time = 150 ms) and TOCSY spectra of meucin-13 in TFE/H₂O (1:1, v/v) at 25 °C. Vertical lines in the TOCSY spectrum connect the lines in each spin system. NOEs between sequential NH protons are indicated in the NOESY spectrum. Residues are labelled with the standard single-letter abbreviations for amino acids, and their position within the sequence.

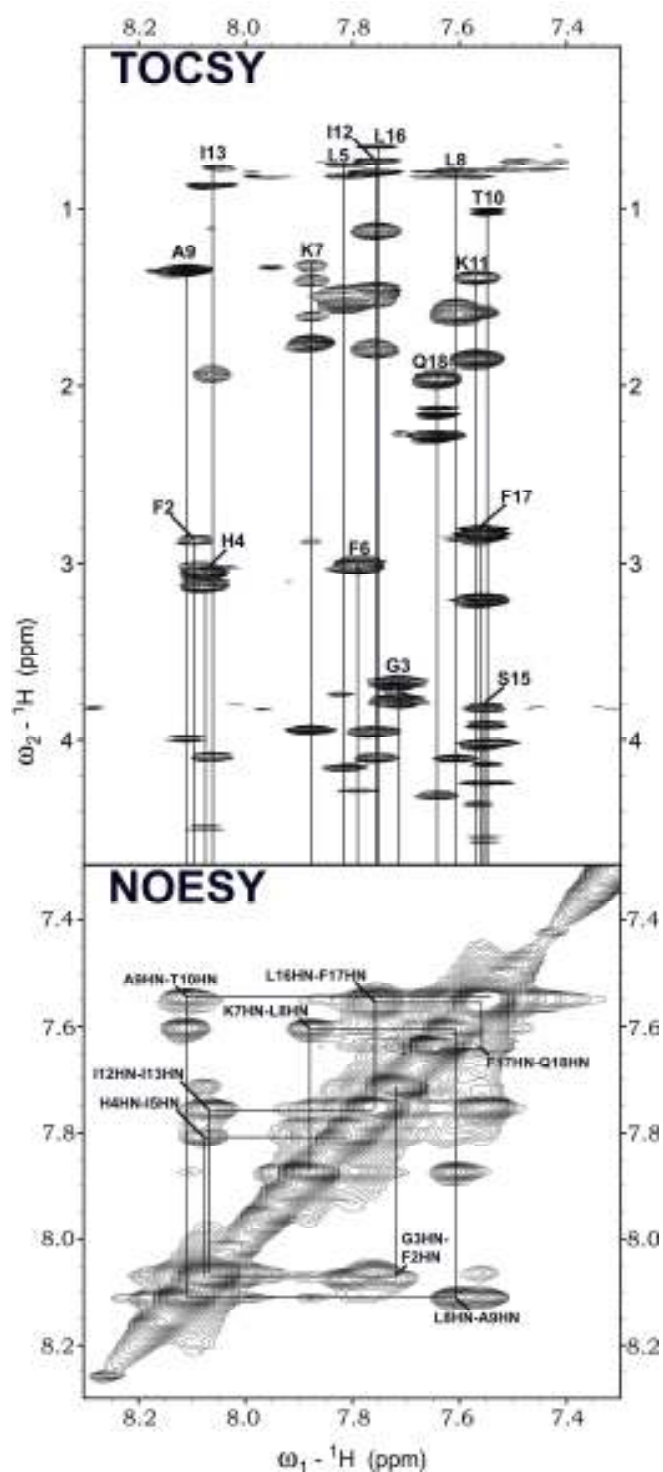


Figure 5.4 Partial NOESY (mixing time = 150 ms) and TOCSY spectra of meucin-18 in TFE/H₂O (1:1 v/v) at 25 °C. Vertical lines in the TOCSY spectrum connect the lines in each spin system. NOEs between sequential NH protons are indicated in the NOESY spectrum. Residues are labelled with the standard single-letter abbreviations for amino acids, and their position within the sequence.

A summary of all of the assigned ^1H resonances for meucinin-13 and meucinin-18 is listed in tables 5.3 and 5.4 respectively.

Table 5.3 ^1H -NMR Chemical shifts for meucinin-13 in TFE/ H_2O (1:1 by volume); n.o., not observed.

Residue	Chemical shift (ppm)				
	NH	α -CH	β -CH	Others	
Ile1	n.o.	3.74	1.82	γ -CH ₂	1.10, 1.39
				γ -CH ₃	0.88
				δ -CH ₃	0.82
Phe2	8.10	4.60	3.07, 3.07	H2,6	7.19
				H3,5	7.30
				H4	7.25
Gly3	7.86	3.73, 3.73			
Ala4	7.62	3.94	1.33, 1.33		
Ile5	7.39	3.96	1.89	γ -CH ₂	1.23, 1.47
				γ -CH ₃	0.86
				δ -CH ₃	0.83
Ala6	7.53	4.12	1.31, 1.31		
Gly7	8.16	3.71, 3.81			
Leu8	7.86	3.75	3.50, 1.39	γ -CH	0.91
				δ -CH ₃	0.63, 0.26
Leu9	7.53	4.14	3.72	γ -CH	1.60
				δ -CH ₃	0.80, 0.84
Lys10	7.94	3.98	1.86, 1.86	γ -CH ₂	1.43, 1.43
				δ -CH ₂	1.61, 1.61
				ϵ -CH ₂	2.90, 2.90
				ζ NH ₃ ⁺	7.48
Asn11	7.98	4.51	2.82, 3.23	δ -NH ₂	6.60, 7.15
Ile12	8.05	4.02	1.83	γ -CH ₂	1.83
				γ -CH ₃	1.46
				δ -CH ₃	0.81
Phe13	7.63	4.47	2.71, 2.84	H2,6	7.23
				H3,5	7.32
				H4	n. o.
				C(O)NH ₂	6.86, 6.90

Table 5.4 ¹H-NMR Chemical shifts for meucinin-18 in TFE/H₂O (1:1 by volume); n.o., not observed.

Residue	Chemical shift (ppm)			
	NH	α -CH	β -CH	Others
Phe1	n.o.	4.08	3.03, 3.03	2,6H 7.12 3,5H 7.23 4H n. o.
Phe2	8.09	4.49	2.88, 3.01	2,6H 7.06 3,5H 8.12 4H n. o.
Gly3	7.72	3.69, 3.78		
His4	8.08	4.50	3.06, 3.13	2H 8.44 4H 7.11
Leu5	7.81	4.16	1.54, 1.54	γ -CH 0.83 δ -CH ₃ 0.76, 0.76
Phe6	7.79	4.22	3.02, 3.02	H2,6 7.09 H3,5 7.18 4H n. o.
Lys7	7.88	3.95	1.77, 1.77	γ -CH ₂ 1.33, 1.32 δ -CH ₂ 1.61, 1.61 ϵ -CH ₂ 2.88, 2.88 ζ -NH ₃ ⁺ 7.53
Leu8	7.60	4.11	1.60, 1.60	γ -CH 0.83 δ -CH ₃ 0.79, 0.79
Ala9	8.10	4.00	1.35, 1.35	
Thr10	7.55	4.02	4.14	γ -CH ₃ 1.02
Lys11	7.56	4.36	1.86, 1.86	γ -CH ₂ 1.40, 1.40 δ -CH ₂ 1.59, 1.59 ϵ -CH ₂ 2.88, 2.88 ζ -NH ₃ ⁺ 7.49
Ile12	7.76	3.96	1.80	γ -CH ₂ 1.12, 1.12 γ -CH ₃ 0.80 δ -CH ₃ 0.74
Ile13	8.10	4.10	1.94	γ -CH ₂ 1.12, 1.58 γ -CH ₃ 0.88 δ -CH ₃ 0.79
Pro14		4.26	1.76, 2.30	γ -CH ₂ 1.84, 2.02 δ -CH ₂ 3.41, 3.66
Ser15	7.55	4.25	3.82, 3.93	
Leu16	7.76	4.57	1.13, 1.48	γ -CH 1.53 δ -CH ₃ 0.74, 0.80
Phe17	7.55	4.57	2.84, 3.22	2,6H 7.19 3,5H 7.32 4H n. o.
Gln18	7.64	4.22	1.97, 2.15	γ -CH ₂ 2.29, 2.29 ϵ -NH ₂ 6.47, 7.25 COOH n. o.

The majority of the proton resonances were assigned for each of the meucin peptides. The four proton resonances of some phenylalanine residues were unresolved in the TOCSY and NOESY spectra. Also the C-terminal carboxyl hydrogen was not observed for meucin-18, as it is likely the carboxylic acid group was deprotonated ($pK_a \sim 5$).

5.2.2 Secondary Chemical Shifts

The random coil chemical shifts for α -protons and amide protons in H_2O were obtained from Wishart *et. al.* [237], to indicate regions of secondary structure (see section 3.1.6). The difference in α -proton chemical shifts relative to the random coil chemical shifts (secondary chemical shifts), were smoothed over a window of $n \pm 2$ residues. The amide proton secondary chemical shifts were not smoothed.

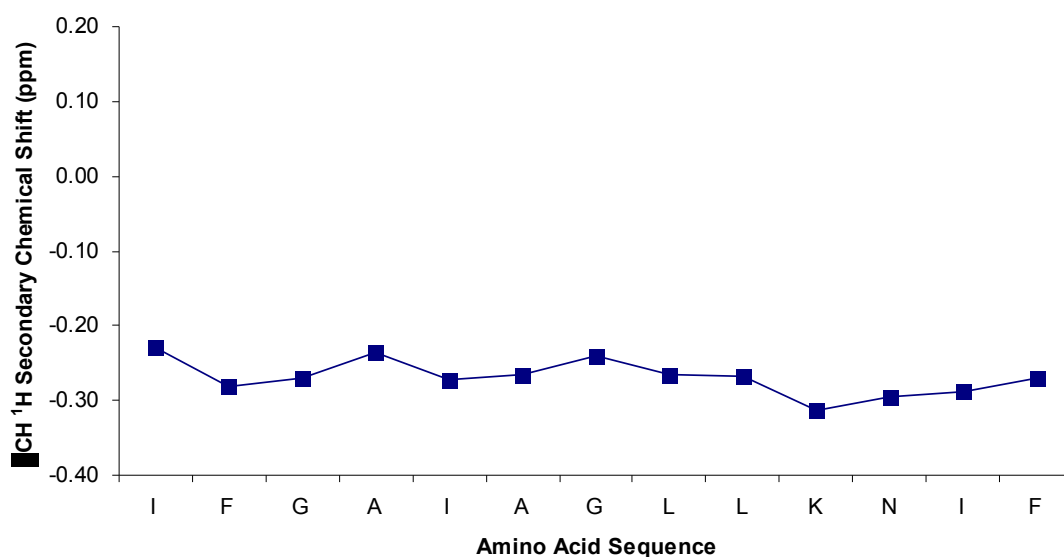


Figure 5.5 α -proton secondary shifts of meucin-13 in TFE/ H_2O , smoothed over a window of $n \pm 2$ residues.

Figure 5.5 illustrates the smoothed α -proton secondary chemical shifts for meucin-13. All secondary chemical shifts are below -0.20 ppm across the entire sequence. These upfield shifts are consistent with the peptide adopting a predominantly helical structure [395].

Figure 5.6 shows the unsmoothed amide secondary shifts for meucin-13. They show an unusual periodic change in chemical shift across the sequence. Generally, helical peptides periodically fluctuate in amide secondary chemical shift producing a ‘zig-zag’ plot that alternates every 3 to 4 residues. For residues Ala4 to Phe13, the amide secondary chemical shift deviates in a similar way from Gly7 to Phe 11, suggesting the peptide backbone does have helical structure. However, the amide secondary shift pattern is not as consistent as synthesised amphipathic α -helical peptides such as the GCN4 ‘leucine zipper’ peptide and LL9 [248, 395].

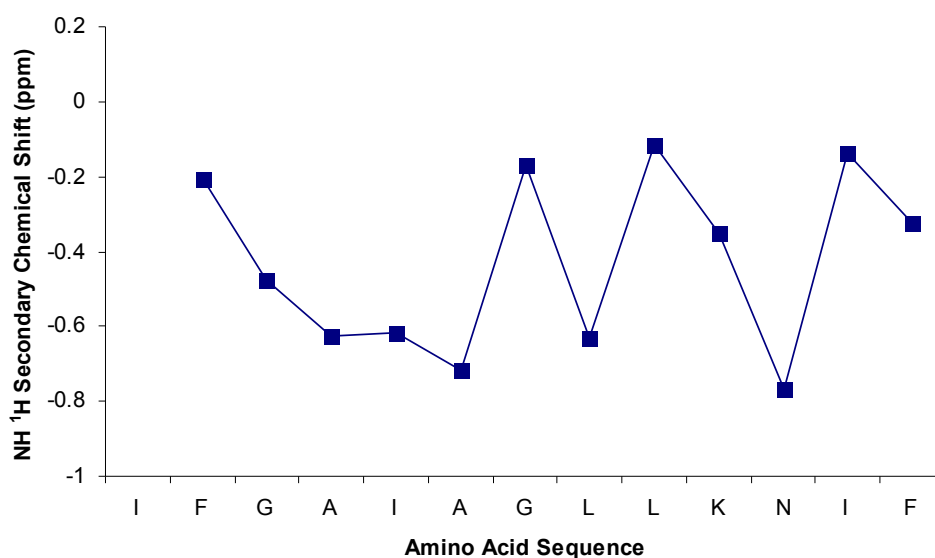


Figure 5.6 Amide proton secondary shifts of meucin-13 in TFE/H₂O.

Figure 5.7 illustrates the smoothed α -proton secondary chemical shifts for meucin-18. From the N-terminus up to Lys11, secondary chemical shifts are negative, consistent with predominantly helical structure. The remaining α -proton secondary chemical shifts suggest random coil structure across the 7 C-terminal amino acids, most likely due to the helix disrupting effect of the Pro14 residue.

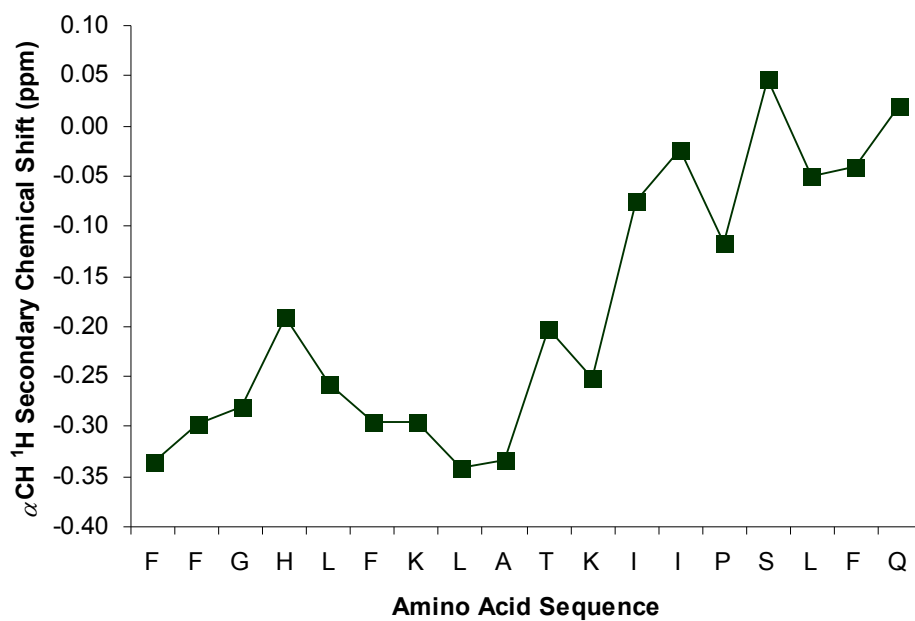


Figure 5.7 α -proton secondary shifts of meucin-18 in TFE/ H_2O , smoothed over a window of $n \pm 2$ residues.

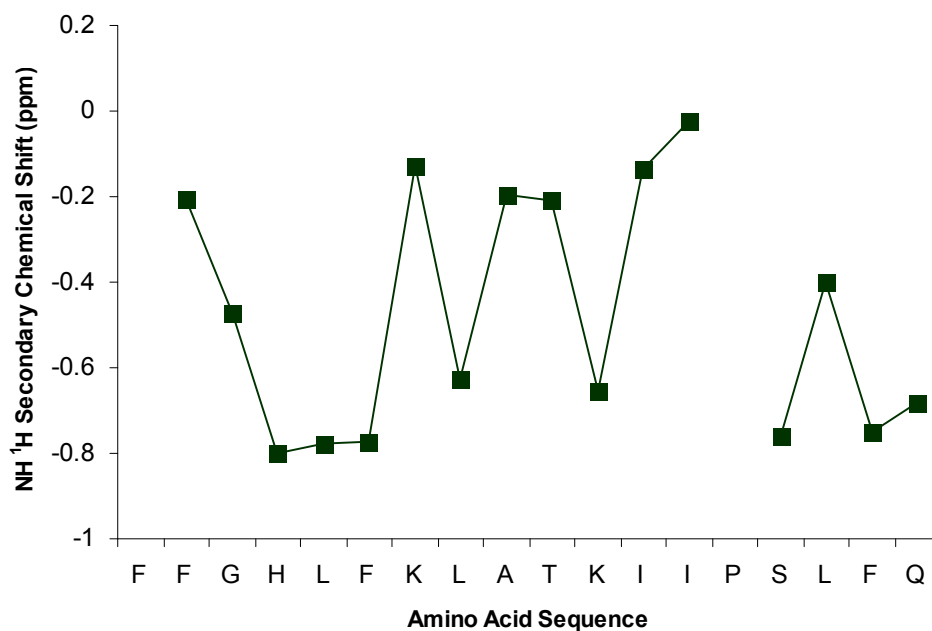


Figure 5.8 Amide proton secondary shifts of meucin-18 in TFE/ H_2O .

Figure 5.8 demonstrates the unsmoothed amide secondary shifts for meucinin-18. The N-terminal amide shifts up to Lys10 show a similar periodic trend to the first 10 residues of meucinin-13. The central residues clearly illustrate a periodic amide secondary chemical shift pattern of a predominantly helical structure. The amide secondary shifts of the last 4 residues deviate significantly from random coil values (-0.4 to -0.8 ppm), hence this region could also have a helical structure. However, the secondary structure in that region can not be clearly defined, due to the lack of an amide proton on the pro14 residue. The secondary shifts indicate that meucinin-18 may adopt a helix-hinge-helix structure, similar to the antimicrobial peptides cupiennin 1a and caerin 1 [396-398].

5.2.3 NOE Connectivities

The summaries of diagnostic NOE connectivities used in the structural calculations of meucinin-13 and meucinin-18 are shown in figures 5.9 and 5.10, respectively.

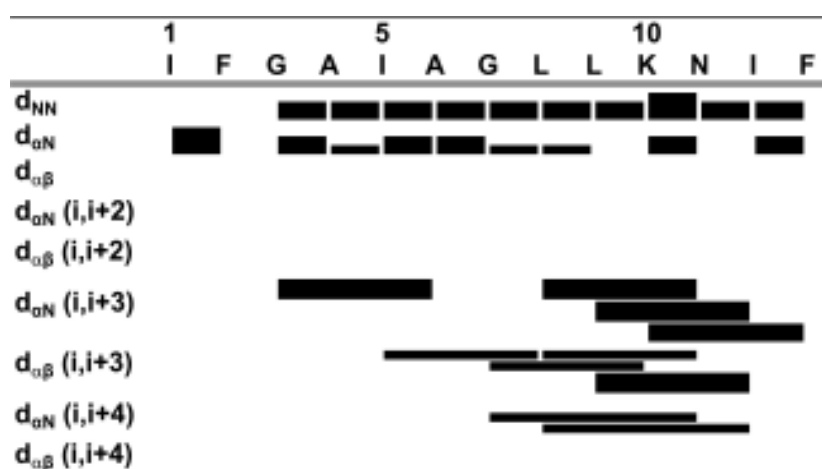


Figure 5.9 A summary of NOE connectivities used in structure calculations of meucinin-13 in TFE/H₂O (1:1 v/v). The thickness of the bars indicates the relative strength of NOEs (strong < 3.1 Å, medium 3.1–3.7 Å and weak > 3.7 Å).

The majority of meucinin-13 sequential d_{NN} and $d_{\alpha N}$ signals from Gly3 onward are medium in strength, with the exception of the strong $d_{\alpha N}$ signal between Ile1 and Phe2. A few medium-range signals are observed 2 residues apart, mainly consisting of medium $d_{\alpha N(i,i+2)}$ and weak $d_{\alpha\beta(i,i+2)}$ signals. A significant amount of medium-range signals are

observed 3 residues apart, namely weak to medium $d_{\alpha\text{N}(i,i+3)}$ and $d_{\alpha\beta(i,i+3)}$ signals. Also, 2 $d_{\alpha\beta(i,i+4)}$ signals are observed across the central amino acids in the sequence. Overall, the NOE connectivity pattern of meucin-13 is characteristic of α -helical structure across the majority of the sequence [399], with the exception of the first 5 N-terminal residues.

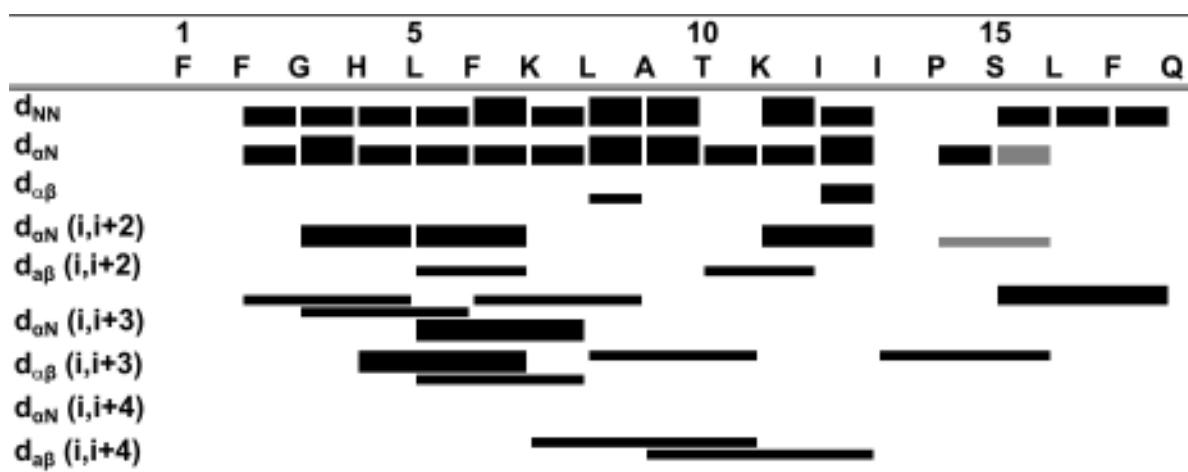


Figure 5.10 A summary of NOE connectivities used in structure calculations of meucin-18 in TFE/H₂O (1:1 v/v). The thickness of the bars indicates the relative strength of NOEs (strong < 3.1 Å, medium 3.1–3.7 Å and weak > 3.7 Å). Grey bars indicate ambiguous NOEs.

The sequential d_{NN} and $d_{\alpha\text{N}}$ signals of meucin-18 from Phe2 onward are medium to strong in intensity, with a gap in the sequential signals observed about the Pro14 residue. In a similar fashion to meucin-13, a few medium-range signals are observed 2 residues apart; namely medium $d_{\alpha\text{N}(i,i+2)}$ and weak $d_{\alpha\beta(i,i+2)}$ signals. A significant amount of medium-range signals are observed 3 residues apart. Mostly weak to medium $d_{\alpha\text{N}(i,i+3)}$ and $d_{\alpha\beta(i,i+3)}$ signals, spanning across Phe2 to Lys11. Additionally, weak $d_{\alpha\text{N}(i,i+3)}$ and $d_{\alpha\beta(i,i+3)}$ signals are observed across Ile13 to Gln18. Similar to meucin-13, 2 $d_{\alpha\beta(i,i+4)}$ signals are observed across the central amino acids in the sequence. There are less medium-range NOE connectivities in the N-terminal region indicating it could be either helical or random in structure. Also, a few ambiguous NOEs are observed in the C-terminal region. The NOE connectivity pattern of meucin-18 is characteristic of α -helical structure across most of the sequence, with less characteristic α -helical NOEs about the Pro14 residue and C-terminal region. This further emphasizes that meucin-18 is likely to adopt a helix-hinge-helix structure.

A few long-range NOE connectivities were observed for each peptide. 3 long-range NOE signals were observed across 5 residues for meucine-13: a $d_{\beta\text{HNH}(i,i+5)}$ (Phe2-Gly7), a $d_{\alpha\text{HNH}(i,i+6)}$ (Gly3-Leu9), and a $d_{\alpha\text{HNH}(i,i+5)}$ (Ala4-Leu9). 2 long-range NOE signals were observed across 5 residues for meucine-18: a $d_{\alpha\text{HNH}(i,i+5)}$ and a $d_{\beta\text{HNH}(i,i+5)}$ signal (both Lys11-Leu16). These interproton distances can exist within 6Å or less, in a helical structure. So, the few long-range NOEs observed are unlikely to be intermolecular interactions and the peptides appear to exist in their monomeric form under these conditions.

5.2.4 Coupling constants

The $^3J_{\text{NH}\alpha\text{H}}$ coupling constants were unable to be resolved from the splitting in the 1D ^1H NMR spectra for either of the meucine peptides. This was largely due to the overlap of amide proton signals. Upon close analysis of the spacing between antiphase multiplets in δ_2 of the DQF-COSY spectra as described by Kim and Prestegard [254], no $^3J_{\text{NH}\alpha\text{H}}$ coupling constants were observed below 6Hz, or above 8Hz. Hence, no backbone dihedral restraints were applied in the structural calculations.

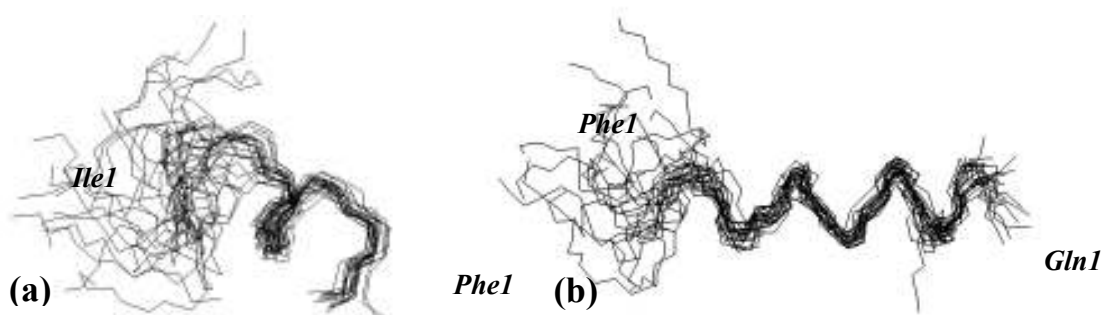
5.2.5 Structure calculations

After assigning and integrating cross-peaks from the NOESY spectrum, NOE cross-peak volumes were converted to distance restraints using ARIA as described by Nilges *et. al.* [400] (See Chapter 3). The total number of distance restraints generated for meucine-13 and meucine-18 were 127 and 289 respectively. No ambiguous restraints were generated from meucine-13 NOEs, and 15 were generated from meucine-18 NOEs. Summaries of grouped distance restraints generated after 8 iterations of ARIA structure calculations are listed in table 5.5.

Table 5.5 Summary of grouped NOE connectivities from the NOESY spectra for structure calculations of meucine-13 and meucine-18.

	Number of restraints	
	meucine-13	meucine-18
Sequential NOEs	36	71
Medium-range NOEs	26	52
Long-range NOEs	3	2
Intra-residue NOEs	62	149
Ambiguous NOEs	0	15
Total	127	289

The conjectures drawn from the NMR spectra of the meucine peptides corroborated well with the generated structures. Of the 60 final structures generated from RMD and SA calculations, the 20 with the lowest potential energy were fitted across selected backbone heavy atoms, where consistent geometry was observed. Figure 5.11 illustrates the overlays of the 20 lowest potential energy structures of meucine-13 and meucine-18, across residues Ala6-Phe13 and Ile5-Phe17, respectively.

**Figure 5.11** The 20 lowest energy structures of meucine-13 (a) and meucine-18 (b) in TFE/H₂O (1:1, v/v), superimposed best fits over the backbone atoms of Ala6-Phe13 and Ile5-Phe17 respectively.

It is evident in figure 5.11 that each meucine peptide adopts predominantly helical structures. The ‘fraying’ effect illustrates the propensity for conformational flexibility of the N-terminal residues. The RMSDs from the mean geometries of the backbone atoms across selected residues for meucine-13 and meucine-18 are 2.29 ± 0.40 Å and 0.744 ± 0.25 Å respectively. This shows that the overlaid meucine-18 structures exhibit a high degree of consistency across the selected backbone region, as illustrated in figure 5.11. The

structural and potential energy statistics generated from RMD and SA calculations for meucin-13 and meucin-18 are summarised in table 5.6.

Table 5.6 Structural statistics of meucin-13 and meucin-18 following RMD and SA calculations. The energies are derived from the mean of the 20 lowest energy structures. The RMSDs from the mean geometry were obtained by best-fitting selected residues of meucin-13 (6-13) and meucin-18 (5-16) that show congruent geometry about the backbone atoms (N, α C, C').

Energies (kcal.mol⁻¹)	meucin-13	meucin-18
E_{total}	6.54 ± 0.61	14.82 ± 0.94
E_{bond}	0.08 ± 0.02	0.46 ± 0.06
E_{angle}	3.58 ± 0.09	7.88 ± 0.41
E_{improper}	0.17 ± 0.02	0.24 ± 0.04
E_{vdW}	2.71 ± 0.51	6.23 ± 0.70
E_{NOE}	0.01 ± 0.02	0.01 ± 0.02
E_{cdih}	0.00	0.00
RMSD from mean geometry (Å)		
All heavy atoms	3.76 ± 0.62	3.35 ± 0.62
All backbone atoms	2.57 ± 0.53	2.57 ± 0.53
Heavy atoms of Selected backbone	3.63 ± 0.61	3.63 ± 0.61
Selected backbone atoms	2.29 ± 0.40	0.744 ± 0.25

The total potential energy of meucin-18 is ~2 fold that of meucin-13, and the largest contributing factors were the Van-der Waals (E_{vdW}) and angular (E_{angle}) potential energy terms. The resultant structures had angles that varied significantly from the predefined values in the parameters set for the RMD and SA calculations using ARIA [401], resulting in large E_{angle} terms. The hydrophobic faces of the amphipathic helices induce many Van-der Waals interactions between hydrophobic sidechains, as reflected by the large E_{vdW} potential energy terms. Statistical analysis of the final 20 NMR derived structures of another amphipathic helical peptide: cupiennin 1a, showed a similar trend in E_{vdW} and E_{angle} potential energies [112]. No violations from the idealised geometries (> 0.3 Å) were observed for either of the meucin peptides' structures, suggesting they adequately represent their respective NMR derived restraints.

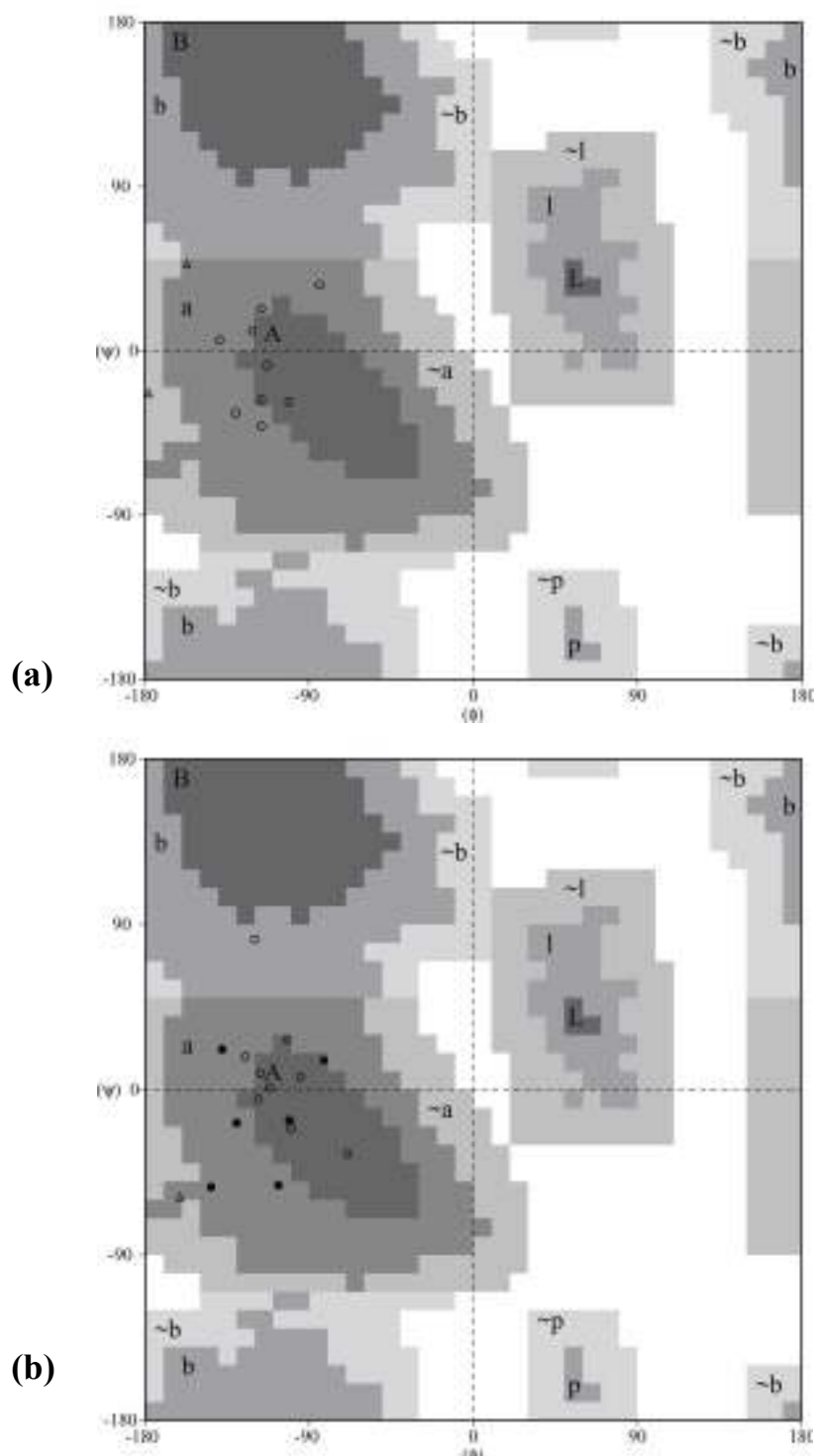


Figure 5.12 Ramachandran plot of average backbone ϕ and ψ angles for meucin-13 **(a)** and meucin-18 **(b)** in TFE/H₂O (1:1, v/v). Allowed regions for α -helices, are labelled A (most favoured), allowed 'a' and generic '~a'. The glycine and proline residues are indicated by Δ and \square , respectively, while the remaining residues are indicated by \circ . Well defined residues are indicated by the solid black markers.

Ramachandran plots of the average ϕ and ψ backbone dihedral angles of the final 20 structures meucic-13 and meucic-18 are displayed in figure 5.12. The Ramachandran plot of the meucic-13 structures showed a third of the residues (excluding glycines, C- and N-terminal residues) had angles in the favoured region for α -helices (A) and the remaining 2 thirds fall into the allowed region (a). No residues were considered to be well defined as all angle order parameters (S) were less than 0.9 (see Section 3.1.9). So, the structure of meucic-13 is predominantly helical across the peptide, with a moderate degree of flexibility or extended secondary structure.

The Ramachandran plot of meucic-18 showed 6 well defined residues (40%, excluding glycines, C- and N-terminal residues) at positions Lys7 and from Ile12-Leu16. This illustrates the consistent secondary structure about the central and C-terminal regions of the peptide. A total of 8 residues (53%, including Pro14) had backbone angles that fall into the favoured region for α -helices (A), and 5 residues (33%) that fall into the allowed region (a). Additionally the His4 residue showed a ϕ and ψ combination that falls into the allowed region for β -strands or β -turns. The ϕ and ψ combinations collectively show that meucic-18 has an α -helical structure across the majority of the peptide, excluding residues Phe1 to His4.

Figure 5.13 shows the energy minimised structures of meucin-13 and meucin-18, from the average of the final 20 structures generated. The amphipathic helical nature of each meucin peptides is demonstrated, as the charged and polar residues tend to point to the downward face and the hydrophobic residues the upward face. Additionally the Gly3 residue faces downward toward the hydrophilic face, exposing the polar amide and carbonyl groups of the peptide backbone.

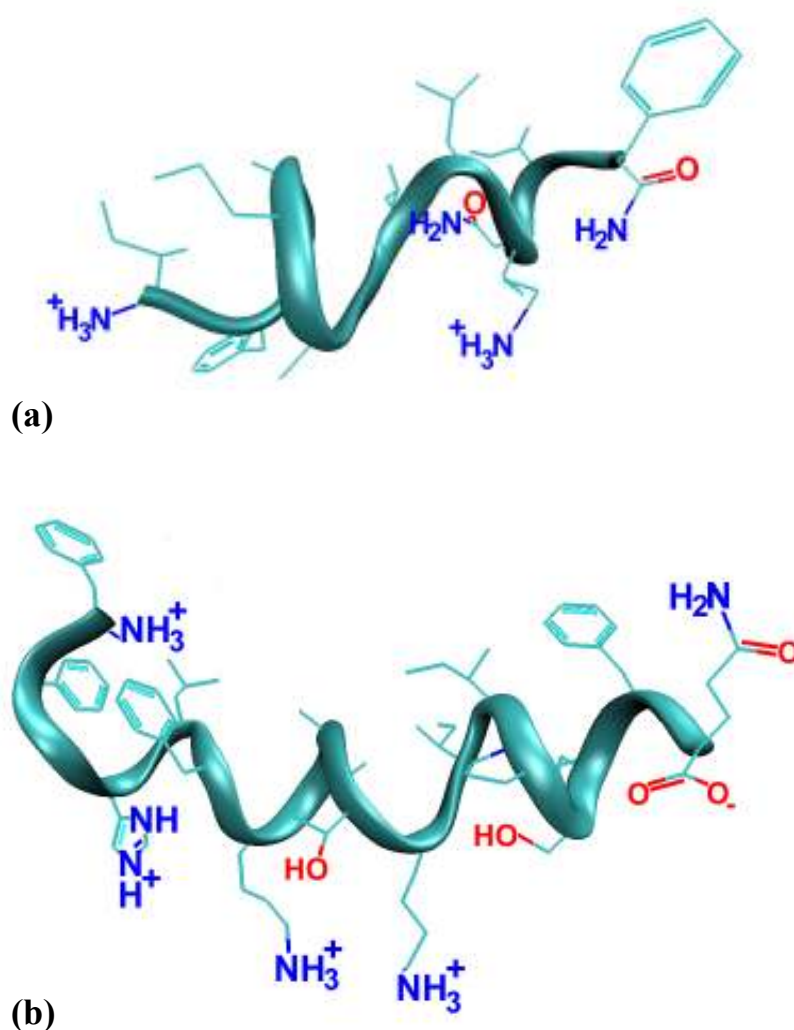


Figure 5.13 Ribbon representations of the minimised average structures of meucin-13 (a) and meucin-18 (b).

5.3 Discussion

The results in section 5.2 show that meucín-13 and meucín-18 adopt linear amphipathic helical structures in TFE/H₂O, as predicted from Edmundson-Schiffer helical wheel projections (See Section 5.1.3). This is further supported by previous circular dichroism experiments, that show the peptides adopt random structures in water and adopt helical structures in TFE/H₂O [113]. TFE/H₂O is a membrane mimicking solvent system, promoting the formation of intermolecular hydrogen bonds [289]. Hence, the structural conformations generated can be assumed to be a good representation of those adopted on a microbial membrane surface.

The meucín peptide structures show regions of flexibility, particularly about the N-termini. This is to a large extent is due to the glycine residues. Glycines only have a single proton as their side-chain, allowing for increased conformational freedom. They are known to disrupt helical structure and induce turns in protein structure [402]. Meucín-13 shows less consistency with typical α -helical structure, partly due to the glycine residues at positions 3 and 7 within the sequence. This is illustrated by the lack of medium range NOE connectivities across the N-terminal region (figure 5.9). Meucín-18 has a glycine residue at position 3, hence the NOE connectivity data also suggests flexibility or extended secondary structure within the N-terminal region. Additionally the Ramachandran plot for meucín-18 shows that His4 has backbone dihedral angles associated with β -strand or β -turn structure.

Proline residues are also known to disrupt helical structure and are often present in the hinge region of antimicrobial peptides that adopt a ‘helix-hinge-helix’ motif, such as caerin 1.1 [398]. Surprisingly the proline at position 14 within the sequence of meucín-18 only appears to disrupt the helical structure in 1 of the final 20 structures (figure 5.11). The NOE connectivity pattern also shows a lack of medium-range NOEs within the N-terminal region. The long-range NOE connectivities ($d_{\alpha\text{HNH}(i,i+5)}$ and $d_{\beta\text{HNH}(i,i+5)}$) between Lys11 and Leu16 suggest a β -turn may exist within the structure. However, the backbone dihedral angles of pro14 are synonymous with helical structure (figure 5.12) and the

residue is well defined. Also, the interproton distances associated with the long range NOEs ($\leq 6 \text{ \AA}$) can exist within the helical structure of meucin-18.

The cytolytic activities of the meucin peptides against numerous microbes, indicates their role in protecting the venom gland of *M. eupeus* from infection. In addition to antimicrobial activity, haemolysis assays showed that meucin peptides are cytolytic toward mammalian (rabbit) erythrocytes at low concentrations ($\leq 6.25 \mu\text{M}$). Additionally, meucin-13 and meucin-18 affected the membrane currents measured from rat dorsal root ganglion (DRG) cells at $20\mu\text{M}$ and $5\mu\text{M}$ concentrations, respectively [113]. It is likely that meucins lyse the eukaryotic cells within the haemolymph of other arthropods in a similar fashion. Hence, aid in the immobilisation and digestion of prey, by facilitating the access of toxins and digestive enzymes to their target tissues [403]. Other helical peptides with antimicrobial and haemolytic activities have been isolated from scorpion species, such as pandanin 2, isolated from the venom of *Pandinus Imperator* [139].

The differences in the activities of meucin-13 and meucin-18 are reflected by the lengths of their helical regions, and to some extent, their net charges. Meucin-18 has a net charge of +3 at pH 7 and has 2 cationic residues directed toward the hydrophilic face of the amphipathic helix: Lys7 and Lys11. In contrast, meucin-13 has a net charge of +2 at pH 7 and only one cationic residue: Lys10. These factors affect the peptides ability to bind to anionic membranes, penetrate the membrane surface, and form pores. The pore forming abilities of the peptides were observed by Gao *et. al.* upon microscopic examination of *M. luteas* (bacteria), *S. cerevisiase* (yeasts), and *G. candidum* (fungi) exposed to the peptides. The greater activity of meucin-18 is further shown in haemolytic assays of meucin-13 (37.7% haemolytic activity) and meucin-18 (74% haemolytic activity) with rabbit DRGs at $6.25 \mu\text{M}$. It is also important to note that in testing the toxicity of the peptides in mice (8 mice for each peptide), 1 in 8 died from injections of $20 \mu\text{g}$ and $10 \mu\text{g}$ of meucin-13 and meucin-18 (both dissolved in 0.9 % NaCl) respectively [113].

The antimicrobial meucin peptides represent a small percentage of linear antimicrobial peptides isolated from scorpion venoms. Though the peptides do show toxicity within

mice, adaptations to the sequences may retain the antimicrobial activity and significantly reduce the haemolytic and other toxic effects. The antimicrobial meucin peptides are significant candidates for the design of new pharmaceuticals, as an alternative to current therapeutic antibiotics.

5.4 Experimental

The 2-dimensional NMR spectra of meucin-13 and meucin-18 in TFE/H₂O (1:1) were acquired by members of Professor Shunyi Zhu's research group, State Key Laboratory of Integrated Management of Pest Insects and Rodents, Institute of Zoology, Chinese Academy of Sciences, Beijing, China. NMR spectra were acquired at 600 MHz on a Bruker DRX600 spectrometer (Bruker Optics, Billerica, MA, USA) with a ¹H frequency of 600 MHz, at 25 °C. 3 mg samples of peptides were dissolved in 0.5 ml d₃-TFE/H₂O (1:1, v/v), giving final concentrations of 4.2 mM (meucin-13) and 2.9 mM (meucin-18). The ¹H NMR resonances were referenced to the methylene protons of d₃-TFE (3.918 ppm). 2-Dimensional TOCSY, NOESY, DQF-COSY and 1D NMR experiments were conducted as described in Wong *et. al.* [110]. The NMR spectral data was sent to the Department of Chemistry, University of Adelaide for resonance assignment and peptide structure calculations.

5.4.1 Cross-peak assignment and structure calculations

The ¹H resonances in the 2D NMR spectra were assigned using Sparky software (version 3.106) via the standard sequential assignment procedure. For each symmetric pair of cross-peaks, the peak of larger volume was used in the conversion to a distance restraint [400]. Assignment of distance restraints of methylene and isopropyl groups was achieved using the floating chirality method [269].

Structures were generated from random starting conformations, using ARIA (version 1.2) [401] implemented with CNS (version 1.1) software [256]. The RMD refinement and SA cooling steps were doubled with respect to the standard protocol [401]. For each of the eight iterations, an initial 60 structures were generated. The 20 lowest calculated potential energy structures (from the final 60 of the eighth iteration) were selected for analysis. The program MOLMOL (version 2k.2) [404] was used to display the overlaid backbones of the 20 lowest energy structures and VMD software (version 1.8.2) [405] was used to display the energy minimised average structures.

Chapter 6

Solid-state NMR studies of the antimicrobial peptide, fallaxidin 4.1a

6.1 Introduction

6.1.1 Membrane active antimicrobial peptides

Antimicrobial peptides provide an essential line of defence against pathogens for many organisms, including plants, vertebrates, invertebrates, and microbes [406-408]. Many organisms produce an array of antimicrobial peptides to eliminate the vast range of pathogenic microbes they come in to contact with, even those with adaptive immune system such as humans [409]. Plants and invertebrates lack adaptive immunity; hence antimicrobial peptides are more imperative for survival. Thousands of antimicrobial peptides have been isolated and studied to date, which are a valuable alternative to traditional antibiotics currently used in therapeutic medicine [410].

Antimicrobial peptides generally range from 12-50 amino acids in length and are described by four sub-groups based on secondary structure: (i) α -helical peptides, (ii) extended peptides, (iii) disulfide bridged loop peptides, and (iv) β -stranded disulfide-rich peptides (with two or more disulfide bridges) [406, 411]. Another important factor to consider when classifying antimicrobial peptides is the presence of charged amino acid residues. Most antimicrobial peptides contain cationic side chains and a net positive charge at neutral pH, as this enhances electrostatic interactions between the peptides and the anionic microbial membranes. However, a small number of anionic antimicrobial peptides have been characterised, such as Maximin H5 isolated from *Bombina maxima* [412]. The peptide characterised in this study, fallaxidin 4.1a, is classified as a cationic α -helical peptide.

Many of the helical antimicrobial peptides isolated from amphibians are C-terminally amidated. An exception to this is magainin, which carries a C-terminal free acid [413]. It has been demonstrated that peptides that have C-terminal amides generally display

greater antimicrobial activity [414]. An increased positive charge usually results in an increase in antimicrobial activity but a large positive charge (e.g. greater than +9) can reduce potency [415]. This reduction in activity may be a consequence of the higher charge density affecting the propensity for helix formation [416].

The mechanisms of how amphipathic α -helical peptides interact with bacterial membranes are most widely described by two models: the “carpet” model [417] and the “barrel-stave” model [418] (see Section 1.3.2). In the case of the carpet model peptides assemble parallel to a membrane surface, acting in a detergent-like manner, straining the bilayer, resulting in the formation of transient defects in the membrane. The membrane then ultimately breaks up into small vesicles (mixed micelles) coated by the peptide, destroying the membrane, leading to cell death [78].

In the case of the barrel-stave model, the peptides insert themselves into the membrane and aggregate parallel to the membrane surface, forming transmembrane pores that disrupt the osmotic potential of the cell. The disruption leads to a breakdown of the transmembrane potential and ion gradients and leakage of the cellular contents occurs, resulting in cell death [418, 419]. Another similar transmembrane model that exists is the ‘toroidal’ pore, where both the peptides and the lipid head groups line the lumen of the pore [79, 420]. Mechanistic models of amphipathic helical peptides interacting with bacterial membranes are illustrated in Figure 6.3.

NOTE:

This figure/table/image has been removed to comply with copyright regulations. It is included in the print copy of the thesis held by the University of Adelaide Library.

Figure 6.1 The “carpet” mechanism (left) where the peptides coat the surface of the lipid bilayer until a threshold concentration is reached, mixed micelle formation occurs, and the membrane is destroyed. The “pore forming” mechanisms (right), where the peptides associate with the membrane surface, insert into the membrane, and form pores. In the “barrel-stave” model, peptides line the lumen of the pores, in the “toroidal pore” model both peptide and lipids line the lumen of the pores. Figure adapted from [421].

A minimum peptide length of 20 residues is required to span the membrane as an α -helix, although for smaller peptides a modified model has been proposed where the peptides dimerise end-to-end to effect complete penetration [422].

6.1.2 Bacterial and cytoplasmic membranes

The cell walls of Gram-positive and Gram-negative bacteria have a variety of differences in composition and structure, hence different chemical properties. The cellular walls of Gram-positive bacteria are generally comprised of a single plasma membrane, with a thick outer layer comprised peptidoglycan, teichoic acids, and lipoteichoic acids (Figure 6.2a). Conversely the cellular walls of Gram-negative bacteria are made up of an outer membrane rich in lipopolysaccharides on the outer leaflet, a periplasmic space (or periplasmic gel) that contains peptidoglycan, and an inner plasma membrane (Figure 6.2b) [9].

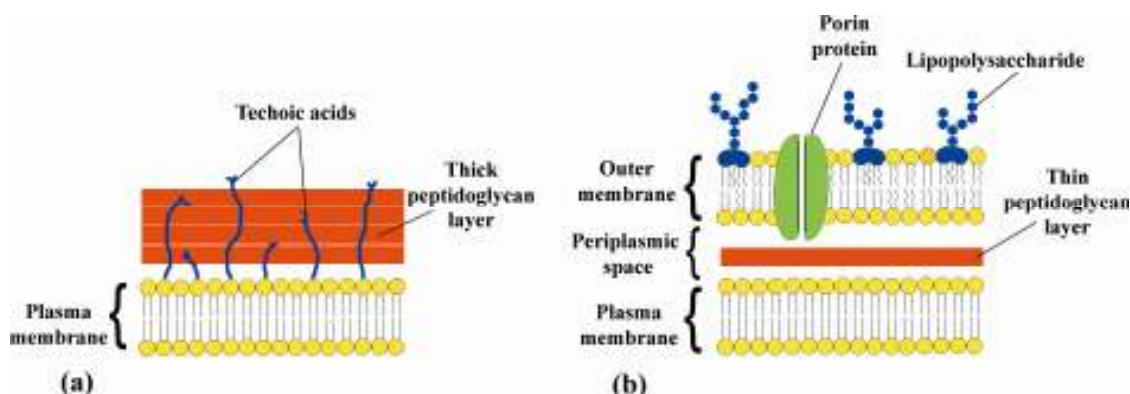


Figure 6.2 The general structure of the cellular walls of Gram-positive (a), and Gram-negative bacteria (b). Based on a figures from [9, 423]. Membrane proteins are not shown, with the exception of porin protein in the Gram-negative outer membrane.

The membranes of both Gram-positive and Gram-negative bacteria contain transmembrane proteins, and it is important to note that the outer membrane of Gram-negative bacteria contains porin proteins. These allow for the diffusion of electrolytes and small molecules across the outer membrane. Porin proteins are not common in Gram-positive bacteria, however do exist in the plasma membranes of a few species of *Mycobacteria* [424].

The presence of teichoic acids and lipopolysaccharides on the outer surfaces of bacterial walls result in a net negative surface charge and bacteria have average membrane potentials in the order of -70 mV. In contrast, the cytoplasmic membrane surfaces of animals are mostly comprised of zwitterionic phospholipid head groups, and have a net surface charge close to neutral, and very small membrane potentials of approximately -9 mV [425]. The membrane potential is a very important factor when considering binding affinity and specificity of cationic helical peptides. It has been known that membrane surface potentials induce pore formation of some antimicrobial peptides, most likely due to the effects on amphipathic helical formation, transmembrane peptide alignment, and depth of insertion into the bilayer [76, 426, 427].

6.1.3 Structure and biological activity of fallaxidin 4.1a

Recently members of the Bowie research group determined the skin peptide profile of *L. fallax* [428]. The peptide fallaxidin 4.1 isolated from the skin secretions shows modest antimicrobial activity. The sequence of fallaxidin 4.1 is unusual, in that it contains three Pro residues and has a C-terminal free acid group, features not typically present in antimicrobial peptides [409, 429].

Fallaxidin 4.1	GLLSFLPKVIGVIGHLIHPPS-OH
Fallaxidin 4.1a	GLLSFLPKVIGVIGHLIHPPS-NH ₂

In previous activity studies it was found that the C-terminal amide analogue of fallaxidin 4.1 (fallaxidin 4.1a) has considerably enhanced antimicrobial activity (up to 4 fold greater

than fallaxidin 4.1) against several Gram-positive bacteria [428, 430], as listed in Table 6.1.

Table 6.1 The antimicrobial activities of fallaxidin 4.1 and 4.1a [82].

Bacteria	Antimicrobial activity^a [MIC ($\mu\text{g}\cdot\text{mL}^{-1}$)]	
	Fallaxidin 4.1	Fallaxidin 4.1a
Gram-positive		
<i>Bacillus cereus</i> ^b	-	25
<i>Enterococcus faecalis</i> (ATCC29212)	-	50
<i>Leuconostoc lactis</i> ^b	12	3
<i>Listeria innocua</i> ^b	-	50
<i>Micrococcys luteus</i> (ATCC9341)	100	12
<i>Staphylococcus aureus</i> (ATCC29213)	-	25
<i>Staphylococcus epidermidis</i> (ATCC14990)	100	25
<i>Streptococcus uberis</i> ^b	50	12
Gram-negative		
<i>Enterobacter cloacae</i> (ATCC13047)	-	-
<i>Escherichia coli</i> (ATCC35218)	-	-

^a indicates that there is no activity $\leq 100 \mu\text{g}\cdot\text{mL}^{-1}$. ^b Wild strain.

An Edmundson-Schiff wheel projection of the first 18 amino acid residues of fallaxidin 4.1 predicts that the peptide is likely to adopt a helical structure on a biological membrane surface. 2D-NMR studies have shown that fallaxidin 4.1a adopts a partially helical structure in membrane mimicking DPC micelles (Figure 6.3).

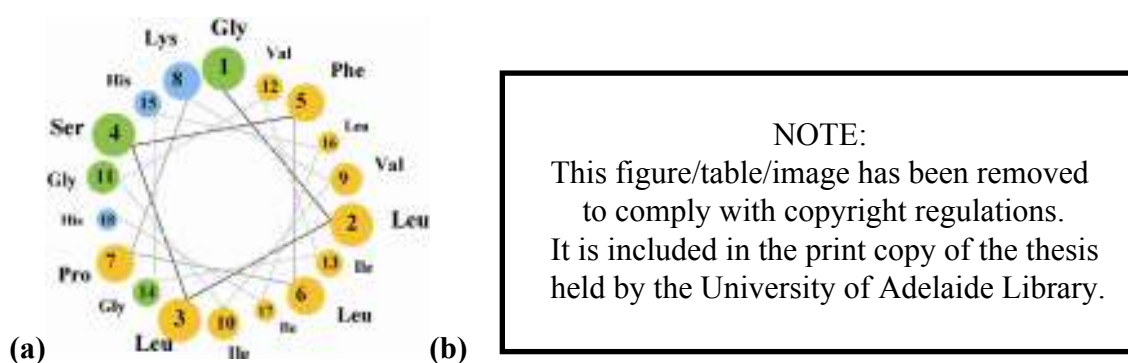


Figure 6.3 Helical wheel projections for the first 18 residues of fallaxidin 4.1a **(a)**, non-polar, polar and basic amino acid residues are highlighted in yellow, green and blue respectively. Ribbon representation of the minimised average solution structure of fallaxidin 4.1a in DPC micelles **(b)** [82].

Although the solution structure of fallaxidin 4.1a is important in understanding its antimicrobial activity, it is also essential to investigate the dynamics of its interactions with phospholipid membranes. Solid-state NMR spectroscopy has been widely used for this purpose and applied to model lipid membranes [308, 431, 432]. The lipids investigated have naturally abundant ^{31}P (100 %) in the phospholipid head groups and synthetically incorporated ^2H in the acyl chains. This allows the order and dynamics of the lipid molecules to be probed over a wide range of time scales [112, 431, 433-436]. The lipid mixtures used in this study are 1:1 d_{54} -DMPC/DMPC and 1:1:1 d_{54} -DMPC/DMPC/DMPG for neutral “mammalian” and anionic “bacterial” model membranes, respectively. Similar solid-state NMR studies with amphibian antimicrobial peptides have been conducted by Gehman *et al.* using the aurein 1.2, citropin 1.1, caerin 1.1, and maculatin 1.1 peptides [332].

In addition to solid-state NMR studies, members of the research group lead by Dr. Lisa Martin have performed real time analysis of fallaxidin 4.1a addition to supported lipid bilayers (SLBs) using Quartz Crystal Microbalance with dissipation monitoring (QCM). These experiments involve monitoring the change in frequency (Δf) and dissipation (ΔD) of a resonating quartz chip, coated with supported lipid bilayers (SLBs) [437-439]. QCM probes the immediate interaction between the peptide and the membrane prior to an

equilibrium state, thereby enabling some elucidation of the penetration pathway. In this study, solid-state NMR spectroscopy and QCM are used as complementary techniques for studying the interaction of fallaxidin 4.1a with phospholipid membranes.

The objective of this study is to obtain information about the interactions of fallaxidin 4.1a with mammalian (neutral) and bacterial (anionic) model membranes, using solid-state NMR and QCM. The results presented are used to study the peptides mechanism of antimicrobial activity and cell selectivity toward bacterial membranes.

6.2 Results

6.2.1 ^{31}P solid-state NMR spectroscopy

Solid-state ^{31}P NMR experiments were used to investigate the effect of fallaxidin 4.1a on the mobility of phospholipid head groups. Static ^{31}P NMR spectra were taken for unoriented lipid samples of 1:1 d_{54} -DMPC/DMPC and 1:1:1 d_{54} -DMPC/DMPC/DMPG mixtures alone and in the presence of fallaxidin 4.1a, at a 10:1 lipid/peptide ratio. The resultant spectra are shown in Figure 6.4.

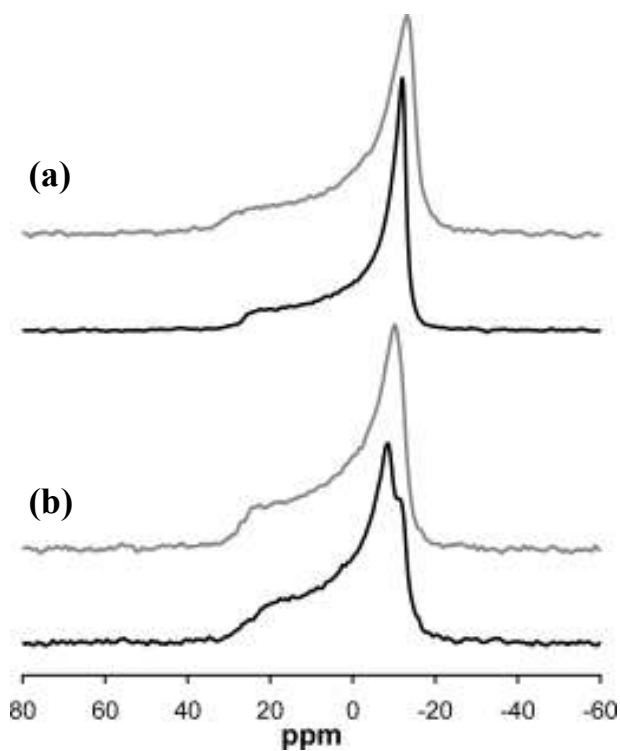


Figure 6.4 ^{31}P NMR spectra obtained for unoriented bilayers of (a) d_{54} -DMPC/DMPC and (b) d_{54} -DMPC/DMPC/DMPG alone (grey) in the presence of fallaxidin 4.1a (black) at a lipid/peptide ratio of 10:1 at 30 °C.

In all ^{31}P NMR spectra the unoriented line shapes show axially symmetric chemical shift anisotropy (CSA) properties, which indicates that the lipids are in the fluid or lamellar (L_α) phase [335]. The ^{31}P static NMR spectra of DMPC and DMPC/DMPG alone showed

CSAs of -43 and -38 ppm respectively. The singular powder patterns show that there is no degree of lateral phase separation of lipids in the control samples. In addition, the CSAs are typical for unoriented multilamellar vesicle (MLV) samples as shown in previous studies [285, 331, 332, 335].

The addition of fallaxidin 4.1a to neutral DMPC MLVs resulted in a reduction ^{31}P CSA of -38 ppm, similar to the CSAs observed for mixtures of maculatin 1.1 and caerin 1.1 with DMPC MLV in previous studies [332]. The 5 ppm reduction in CSA infers a decrease in ordering of phospholipid headgroups in the presence of fallaxidin 4.1a. This suggests that the peptide disrupts the packing of lipids within the bilayers, causing greater spacing between lipid molecules [333]. Only a singular lineshape is observed indicating no lateral phase separation of lipids and the bilayers are maintained within vesicle structures in the presence of the peptide.

The addition of fallaxidin 4.1a to anionic DMPC/DMPG MLVs resulted in two contributing ^{31}P powder patterns, indicating lateral phase separation of the lipids in the presence of peptide. Similar phase separations have been observed for the peptide cupiennin to DMPC/DMPG MLV suspensions [112]. Deconvolution of the two ^{31}P powder patterns using the DMFIT program [440] revealed two lipid lamellar component CSAs of -39 (60%) and -34 ppm (40 %). The approximated intensities of each contributing powder pattern are consistent with the molar fraction of PC (33%) and PG (66%) phosphate head groups as illustrated in Figure 6.5. The decrease in the minor CSA suggests an electrostatic interaction between the cationic functional groups of the peptide and the anionic head groups of DMPG, causing some degree of phase separation within the bilayers [112].

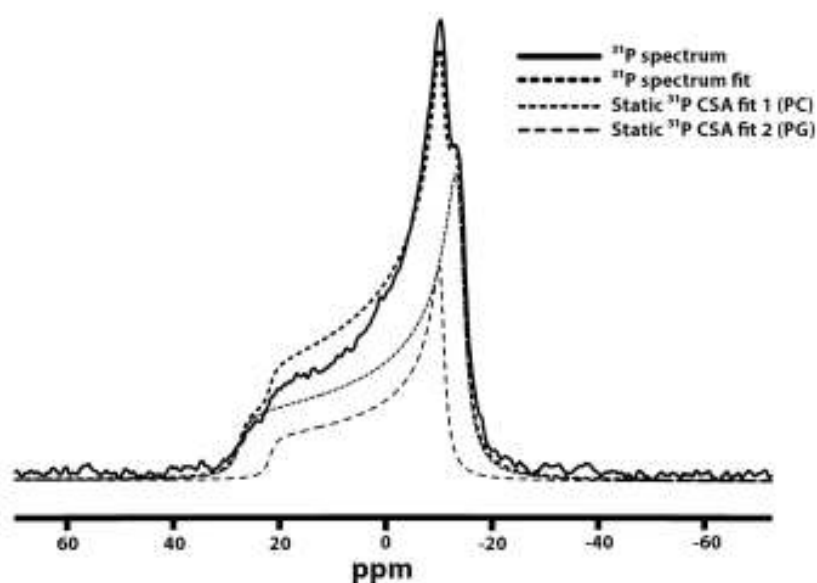


Figure 6.5: ^{31}P NMR spectra obtained for unoriented bilayers of d_{54} -DMPC/DMPC/DMPG in the presence of fallaxidin 4.1 at a lipid/peptide ratio of 10:1 at 30 °C. The ^{31}P spectrum fit^c is the resultant sum of Static ^{31}P CSA fits 1 (60%) and 2 (40%), from DMFIT.

A summary of the ^{31}P CSAs for each peptide-lipid mixture is given in Table 6.2.

Table 6.2 ^{31}P spectral data for DMPC and DMPC/DMPG MLV, alone (control) and with the addition of fallaxidin 4.1a.

Sample	^{31}P CSA (ppm) ^a	
	Control	+ fallaxidin 4.1a
DMPC MLV	-43	-38
DMPC/DMPG MLV	-38	-39 (60%) ^b
	-38	-34 (40%) ^b

^a CSA determined ± 0.5 ppm. ^b Contributing CSAs were fitted using the DMFIT program [440].

6.2.2 ^2H solid-state NMR spectroscopy

Deuterated DMPC was used in ^2H NMR experiments to investigate the effects of fallaxidin 4.1a on the mobility of acyl chains. Static ^2H NMR spectra were taken for unoriented lipid suspensions of 1:1 d_{54} -DMPC/DMPC and 1:1:1 d_{54} -DMPC/DMPC/DMPG mixtures alone and in the presence of fallaxidin 4.1a, at a 10:1

lipid/peptide ratio. The resultant spectra are an overlay of Pake doublets corresponding to CD_2 and CD_3 groups on the acyl chains of d_{54} -DMPC, as shown in Figure 6.6.

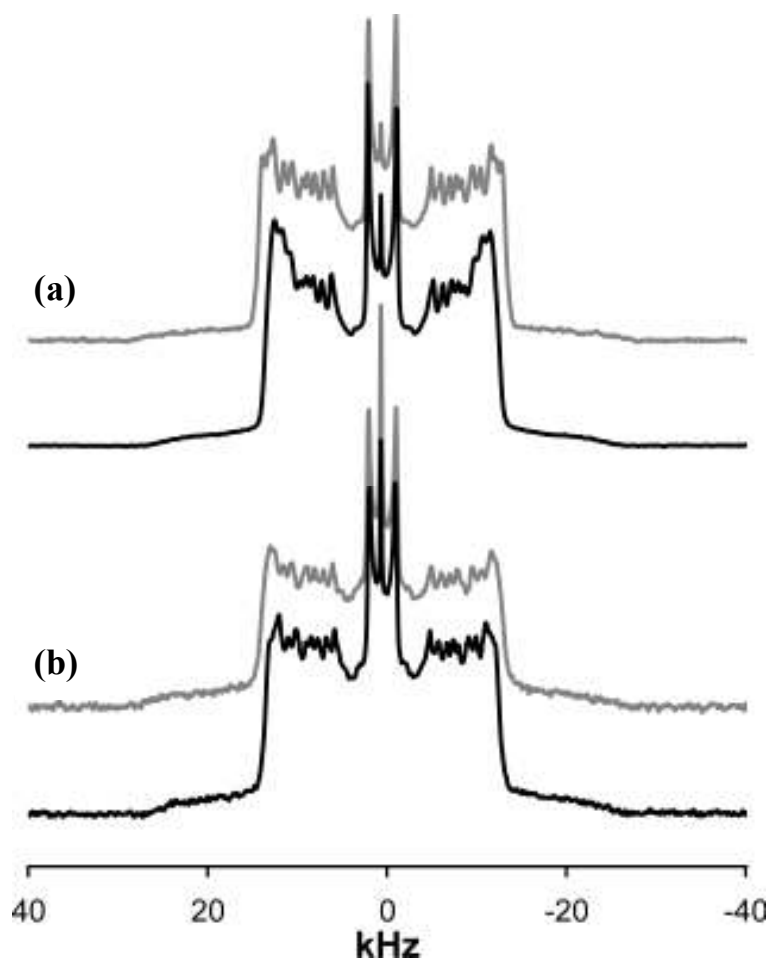


Figure 6.6 2H NMR spectra obtained for unoriented bilayers of (a) d_{54} -DMPC/DMPC and (b) d_{54} -DMPC/DMPC/DMPG alone (grey) in the presence of fallaxidin 4.1 (black) at a lipid/peptide ratio of 10:1 at 30 °C.

The static 2H NMR spectra are typical for hydrated d_{54} -DMPC/DMPC and 1:1:1 d_{54} -DMPC/DMPC/DMPG suspensions, with a small central isotropic peak due to residual deuterium in the buffer solution [344, 434, 441]. The 2H NMR spectrum of the DMPC MLV narrowed upon the addition fallaxidin 4.2, with a higher degree of superimposed Pake doublets on the outer edges of the powder pattern relative to the control sample. This indicates a decrease 2H quadrupolar splittings corresponding to CD_2 groups on the toward the head groups of the phospholipids. The 2H NMR spectrum of the

DMPC/DMPG MLV with fallaxidin 4.1a shows only a slight narrowing in the powder pattern relative to the control, indicating that the peptide has little influence on the acyl chain mobility of DMPC in the lipid mixture.

The overlapping ^2H quadrupolar splittings taken from static ^2H NMR spectra were ‘dePaked’ to further calculate the order parameters (S_{CD}) of the DMPC (see Section 3.2.4.2) [312, 344, 442]. The S_{CD} values indicate the degree of order of the CD_2/CD_3 groups in the deuterated acyl chains of DMPC, as shown in Figure 6.7 [307].

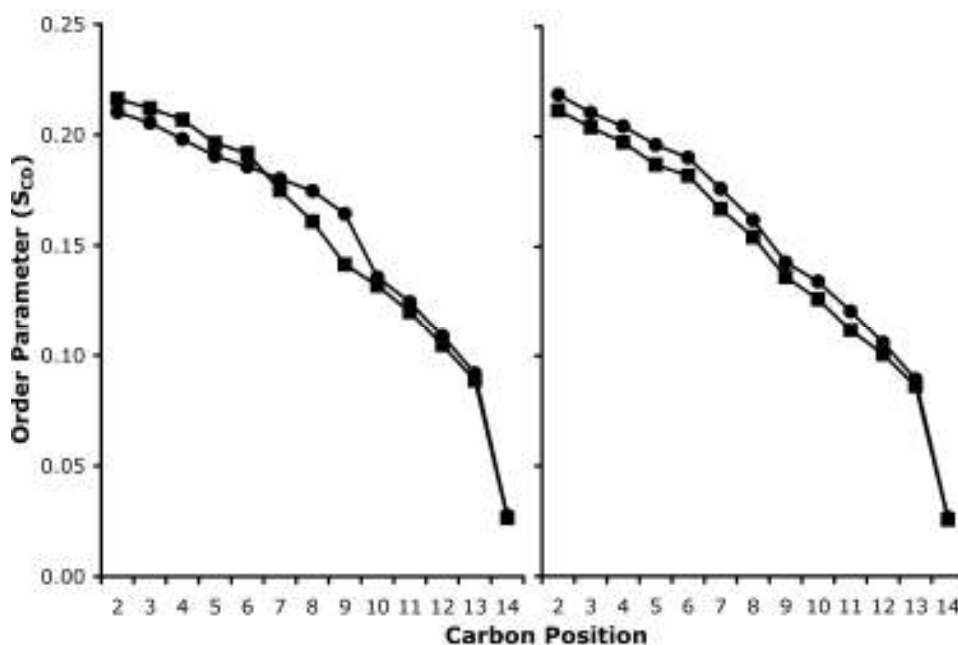


Figure 6.7 Plot of the carbon-deuterium bond order parameters (S_{CD}) against acyl chain carbon position for unoriented bilayers of d_{54} -DMPC/DMPC (left) and d_{54} -DMPC/DMPC/DMPG (right) alone (■) and in the presence of fallaxidin 4.1 (●) at a lipid/peptide ratio of 10:1 at 30 °C.

A decrease in the S_{CD} order profile of DMPC MLV was observed at the acyl chain positions 2 to 6 relative to the control, indicating increased motion and disorder of the upper part of the chain toward the head of the phospholipid. A significant increase in the S_{CD} order was observed at the central region of the acyl chain (3-16 %), a result of additional steric interactions and a reduction in space causing lower CD_2 mobility. The remaining S_{CD} values (10-14) are almost identical to those from the control, indicating little change in order toward the hydrophobic tail regions of the lipids. Collectively this

effect is the result of partial insertion of the peptide into the bilayer or a surface interaction. The S_{CD} order profile of DMPC/DMPG MLV showed a slight increase in quadrupolar splittings upon the addition of fallaxidin 4.1a, as reflected in the S_{CD} order profile. The peptide appears to order the neutral DMPC acyl chains in the mixed bilayer, suggesting the integrity of the bilayer is maintained with a slight reduction in space for acyl chain mobility.

A summary of the quadrupolar coupling constants taken from the 2H NMR spectra is given in Table 6.3.

Table 6.3 2H quadrupolar splittings (± 0.1 kHz) measured for d_{54} -DMPC/DMPC and d_{54} -DMPC/DMPC/DMPG unoriented bilayers, both alone and in the presence of fallaxidin 4.1a at a 10:1 lipid/peptide molar ratio and 30 °C.

Carbon position	2H Quadrupolar splittings (kHz)				% Change from lipid alone	
	DMPC	DMPC + Fall 1a	DMPC/PG	DMPC/PG + Fall 1a	DMPC + Fall 1a	DMPC/PG + Fall 1a
2	27.6	26.8	27.0	27.9	-3	+3
3	27.0	26.2	26.0	26.9	-3	+3
4	26.4	25.3	25.2	26.1	-4	+4
5	25.0	24.3	23.9	25.0	-3	+5
6	24.4	23.7	23.2	24.3	-3	+4
7	22.3	23.0	21.3	22.5	+3	+5
8	20.5	22.3	19.7	20.7	+9	+5
9	18.0	21.0	17.4	18.2	+16	+5
10	16.8	17.3	16.1	17.1	+3	+6
11	15.3	15.9	14.3	15.4	+4	+8
12	13.3	13.9	12.9	13.5	+4	+5
13	11.3	11.7	11.0	11.4	+4	+4
14	3.4	3.5	3.3	3.4	+4	+4

6.2.3 Quartz Crystal Microbalance

The concentration dependence of fallaxidin 4.1a was determined on neutral DMPC and on the anionic 2:1 DMPC/DMPG supported lipid bilayers. A decrease in frequency (Δf) correlates to an increase in mass on the QCM chip surface and vice versa. The frequency change versus time data for the 7th harmonic overtone is shown in Figure 6.8.

NOTE:

This figure/table/image has been removed to comply with copyright regulations. It is included in the print copy of the thesis held by the University of Adelaide Library.

Figure 6.8 QCM traces for the interaction of fallaxidin 4.1a with (a) DMPC, and (b) 2:1 DMPC/DMPG lipid bilayers as a function of peptide concentration (1-20 μM) and 19.1°C. The frequency change (Δf) of the 7th harmonic overtone versus time is shown. At time = 5 min the peptide was introduced onto the lipid surface and the peptide was incubated for 20 min [82].

The decrease in frequency obtained on the DMPC bilayer (Figure 6.8a) reveals an initial insertion of fallaxidin 4.1 into the lipid layer for all concentrations. However, at a peptide concentration of 5 μM , the increase in frequency is observed due to membrane disruption. Above this concentration threshold, the initial decrease in frequency followed by a large increase in frequency corresponds to peptide insertion into the bilayer followed by lipid removal.

In contrast, the addition of fallaxidin 4.1a on to 2:1 DMPC/DMPG bilayers (Figure 6.8b) shows an initial decrease in frequency followed by a plateau, consistent with insertion of

the peptide into the bilayer. The peptide insertion was notably more rapid at concentrations of 5 μM and above and more uniform plateau regions. These observations show the peptide inserts and remains incorporated into the bilayer, with minor removal of excess peptide from the surface above the threshold concentration.

QCM traces of frequency changes of four harmonic overtones upon depositing fallaxidin 4.1a (7 μM) on to 2:1 DMPC/DMPG bilayers, is shown in Figure 6.9.

NOTE:
This figure/table/image has been removed
to comply with copyright regulations.
It is included in the print copy of the thesis
held by the University of Adelaide Library.

Figure 6.9 The QCM traces for the frequency change (Δf) versus time for the interaction of fallaxidin 4.1a (7 μM) with 2:1 DMPC/DMPG bilayers. The responses for the 3rd, 5th, 7th and 9th harmonics are shown, at time = 5 min the peptide was introduced onto the lipid surface and the peptide was incubated for 20 min [82].

The recording of different frequency overtones provides a means of observing mass addition as a function of distance from the chip surface (9th closest and 3rd the furthest) [437, 443]. The decreases in frequency observed over all four overtones demonstrate that fallaxidin 4.1a causes an increase in mass across the entire depth of the membrane about the bilayer normal. This shows that the peptide is inserting in a transmembrane manner, in a similar fashion to the QCM trace of caerin 1.1 on DMPC bilayers [437]. The degree of frequency change decreases from the 3rd to the 9th harmonic, indicating that the mass increase is not uniform across the bilayer normal and that there is some excess accumulation of peptide on the interfacial region of the bilayer surface.

6.3 Discussion

Solution NMR studies show that the structure of fallaxidin 4.1a appears to be partially helical, yet disrupted about the central region of the peptide. Prolines and glycines, are known to disrupt α -helical structure [444, 445], as is reflected by the observed random coil characteristics about residues from Pro7 toward the C-terminal end of the peptide. However, the peptide's flexibility may enhance interactions with membranes in a similar manner to the central hinge regions of many amphipathic helical peptides [71, 112, 369]. The DPC and DMPC lipids each share the zwitterionic choline head group and DPC micelles mimic a membrane environment by promoting the formation of intramolecular hydrogen bonds. It could be assumed that fallaxidin 4.1a would adopt a similar structure in the DPC micelles as in DMPC MLVs, though the curvature on the membrane surface of DPC micelles may perturb the peptide's propensity to form a helical structure. The mixed DMPC/DMPG surface has a net negative surface charge on the membrane. The net charge of fallaxidin 4.1a is +2 under the experimental conditions used for this study (pH 6.9-7), given that the histidine residues ($pK_a \sim 6.5$) remain uncharged [9]. The additional electrostatic interactions with the cationic/polar side chains may induce a more helical secondary structure due to facial alignment of the cationic/polar side chains on one face of the helix, as anticipated from a Schiff-Edmundson helical wheel projection (see figure 6.3a).

Microscopy studies by Kim et. al. [446] with MLV suspensions (DOPC/cholesterol/DMPG 9:9:2) show that the average size of each MLV would be in the order of 4 μ M, given the lipid suspensions were hydrated and agitated mechanically via vortexing. The lipid to peptide ratio in the MLV suspensions used in the solid state NMR experiments is 10:1, and the concentration of peptide in the lipid suspension is ~ 100 mM (20 mg.mL^{-1}). This concentration is in great excess (~ 200 times) of what is used *in vivo* for antimicrobial activity assays. The high concentration of both peptide and lipids is necessary to observe the changes in lipid dynamics effectively by solid-state NMR. Arguably the peptide may interact with the phospholipid membranes purely as an artefact of the high concentrations used. However, the lipid part ($\sim 7 \text{ mg}/100 \mu\text{L}$) of the hydrated MLV suspensions still could allow sufficient space for a hydrophilic peptide to reside

within the aqueous component of the suspension, as is the case for rothein 1 peptide in DMPC MLV at a lipid/peptide ratio of 10:1 (see section 7.2.2). Additionally, the real time QCM experiments performed at much lower concentrations ($\sim 0.5\text{-}10\ \mu\text{g.mL}^{-1}$), show that fallaxidin 4.1a does interact with phospholipid membranes at concentrations similar to what is observed *in vivo* [82].

6.3.1 Solid-state NMR spectroscopy and QCM

The solid-state NMR and QCM of fallaxidin 4.1a with the DMPC and DMPC/DMPG lipid mixtures showed a high degree of differences between each lipid system. The solid-state NMR of DMPC MLV suggests a significant increase in the mobility and/or change in orientation of the phospholipid head groups upon addition of fallaxidin 4.1a. This is shown by the ^{31}P NMR powder pattern (CSA). Also, the S_{CD} order profiles determined from ^2H NMR showed an increase in order about the centre of the acyl chain (positions 7-9) and a decrease toward the head region of the chain. This difference in the acyl chain order may indicate incorporation of the peptide into the membrane surface (interfacial region), leading to increased spacing of the lipid head groups. This in turn would lead to a change in dynamics about the upper region of the acyl chains, as shown by the decreased S_{CD} order parameters and the decrease in the ^{31}P CSA. The insertion and subsequent rapid mass removal upon addition to DMPC SLBs at concentrations $\geq 5\ \mu\text{M}$ observed using QCM suggests the peptide destroys neutral bilayers via a surface (carpet) interaction.

The line shape or CSA of the static ^{31}P spectra gave an indication of the motion and alignment of the phosphate head groups, which infer changes in orientation and surface charge density. With the addition of fallaxidin 4.1a to the negatively charged DMPC/DMPG (2:1) MLV, the contributing ^{31}P CSA of the DMPG enriched component decreased, while the ^{31}P CSA of the DMPC component remained relatively unchanged. This decrease in ^{31}P CSA is typically associated with an alteration in head group conformation [447], suggesting an associative electrostatic interaction between the PG head groups and fallaxidin 4.1a. The deuterium NMR, however, revealed an increase in the acyl chain order of the DMPC phospholipids. Fallaxidin 4.1a may form toroidal or ‘barrel stave’ pores, where the anionic PG head groups orient themselves about the lumen

of the pores, as described in previous ^{31}P NMR studies of membranes with melittin [448] and cupiennin [112]. The additional membrane curvature about the toroidal pore would affect the averaging of the ^{31}P shielding tensor relative to a planar membrane surface; hence the observed reduction in ^{31}P CSA. This would explain the decrease in the ^{31}P CSA for the DMPG and an increase in order for the DMPC acyl chains. QCM data shows that fallaxidin 4.1a inserts into the membrane in a transmembrane fashion in negatively charged 2:1 DMPC/DMPG bilayers, similar to caerin 1.1 and maculatin 1.1 upon addition to 4:1 DMPC/DMPG bilayers [437]. The likely formation of transmembrane pores within anionic membranes was observed for all peptide concentrations (1-20 μM) in the QCM component of this study. Following saturation of the bilayer with pores, excess fallaxidin 4.1a aggregates on the surface of the membrane. These loosely associated peptide aggregates can be readily removed from the bilayer surface by rinsing with buffer solution [437].

6.3.2 Mechanism of antimicrobial activity

The peptides' ability to lyse bacteria via the carpet mechanism is dependant on its binding affinity and its effect on the membrane surface charge. Alternatively, once the peptide interacts with a membrane, its ability to insert into a bilayer and lyse bacteria via the barrel-stave or toroidal pore mechanism is essentially limited by the length of its amphipathic α -helical regions. Fallaxidin 4.1a is 24 amino acids in length, thus is easily able to span a bacterial membrane.

From the antimicrobial activity data, fallaxidin 4.1a appears to be cytolytic toward only the Gram-positive bacteria tested (Table 6.1), similar to many antimicrobial peptides such as citropin 1.1 and aurein 1.2 [46, 71]. The peptides may be able to form pores within the outer membranes of the Gram-negative bacteria while the inner membrane (and osmotic potential of the cell) remains intact. The presence of porin proteins within the outer membranes (for diffusion of ions further) suggests that transmembrane pores may have little influence on the integrity of Gram-negative cell membranes. Gram-negative bacteria may also destroy any peptide that traverses the outer membrane using proteolytic

enzymes present in the periplasmic space [9] (see Figure 6.2) and remain resistant to cell lysis via pore formation.

Castle *et al.* [449] reported a proposed mechanism of the linear non-helical apidaecin peptides via diffusion across a bacterial membrane and docking with a target molecule or receptor, leading to inhibition of the dnaK protein. Additional QCM studies by Piantavigna *et al.* [439] suggest that apidaecin peptides are easily able to traverse bacterial membranes. Fallaxidin 4.1a may interact with bacteria in a similar site-specific manner, in conjunction with non-specific membrane interactions. However, the QCM results are more consistent with the peptide interacting specifically with membranes.

Collectively, the solid state NMR and QCM results strongly suggest that fallaxidin 4.1a causes the formation of transmembrane pores at low peptide concentration ($\geq 1 \mu\text{M}$) in DMPC/DMPG (bacterial model) membranes and the disruption of DMPC (mammalian model) membranes only at higher peptide concentrations ($\geq 5 \mu\text{M}$). This highlights the concentration-dependent cell selective antimicrobial activity of fallaxidin 4.1a. Also, the antimicrobial activity tests show that fallaxidin 4.1a is selective toward Gram-positive bacteria.

To further prove that fallaxidin 4.1a does form pores within anionic membranes, additional membrane leakage experiments could be undertaken by adding fallaxidin 4.1a to solutions containing fluorescent dye encapsulated within giant unilamellar vesicles (GUVs). Experiments such as these were performed by Ambroggio *et al.* with the antimicrobial peptides citropin 1.1, aurein 1.2 and maculatin 1.1 [450]. Alternatively pore formation can be observed visually using cryo-electron microscopy, as done by Han *et al.* upon the addition of magainin 2 to DMPC/DPMC vesicles [451]. Further modifications to fallaxidin 4.1a may produce enhanced selectivity toward anionic membranes and greater antimicrobial potency. The evidence illustrated in this study clearly shows that fallaxidin 4.1a is an exceptional candidate for the future development of therapeutic antibiotics.

6.4 Experimental

6.4.1 Sample preparation

Fallaxidin 4.1a and its amide modification were synthesised with L-amino acids using the standard N- α -Fmoc method, by GenScript Corp. (Piscataway, NJ) [376] and shown to have greater than 90 % purity, as determined by HPLC and ESI-MS. Phospholipids were obtained from Avanti Polar Lipids (Alabaster, AL) and used without further purification. Fallaxidin 4.1a (2.1 mg, 1 μ mole) was co-dissolved with either a 1:1 molar mixture of *d*₅₄-DMPC/DMPC or a 1:1:1 molar mixture of *d*₅₄-DMPC/DMPC/DMPG using 1 ml of CHCl₃/MeOH (1:1 v/v); producing a lipid/peptide ratio of 10:1. The organic solvent was removed via rotary evaporation (250 mbar, 30 °C) to form a thin lipid/peptide film in a round bottom flask, and the samples lyophilised overnight. The dried samples were hydrated with 100 μ l of 50 mM MOPS (150 mM NaCl, pH 7) buffer, subjected to five freeze thaw/vortex cycles and centrifuged (1 minute, 4000 rpm). The resultant viscous translucent suspensions were transferred to 5 mm NMR tubes for NMR analysis. The ‘neutral DMPC’ and ‘anionic DMPC/DMPG’ controls were prepared in a similar manner, without the addition of fallaxidin 4.1a.

6.4.2 ³¹P solid-state NMR

All solid-state NMR experiments were performed on a Varian (Palo Alto, CA) Inova-300 spectrometer, using a 5 mm Doty (Columbia, SC) MAS probe at 30 °C. Static proton decoupled ³¹P NMR spectra were obtained at an operating frequency of 121.5 MHz using a Hahn spin-echo pulse sequence with a 5.8 μ s 90° pulse, 62 μ s interpulse delay and a 4 s recycle delay. ³¹P NMR spectra were averaged over 60,000 scans at a spectral width of 125 kHz with 100 Hz exponential line broadening upon processing. Overlapped ³¹P line shapes were deconvoluted using DMFIT software. Firstly, the baseline and the lineshapes of the contributing powder patterns were fitted by selecting the ‘CSA static’ model and a line broadening of 10Hz. Lorentzian integration functions were then employed to calculate the widths (CSAs) and relative intensities each contributing powder pattern [440].

6.4.3 ^2H solid-state NMR

^2H NMR spectra were obtained at an operating frequency of 46.1 MHz using a quadrupolar-echo pulse sequence with a 3.8 μs 90° pulse, 40 μs interpulse delay and a 0.5 s recycle delay. ^2H NMR spectra were averaged over 160,000 scans at a spectral width of 500 kHz with 100 Hz exponential line broadening. The overlapping Pake doublets from the unoriented deuterium spectra were ‘dePaked’ using single value decomposition [313, 346, 452], numerical calculations were administered by GNU Scientific library v.1.11 [453] and graphical outputs generated with gnuplot v4.2.4 [454].

6.4.4 Quartz Crystal Microbalance

QCM experiments were performed by members of Dr. Lisa Martin’s research group, School of Chemistry, Monash University, Clayton, Victoria, Australia. QCM measurements were performed using the Q-Sense E4 system (Q-Sense, Sweden). The sensor crystals used were 5 MHz, AT-cut, quartz discs (chips) with an evaporated gold surface (Q-Sense). The resonance frequency and energy dissipation were measured simultaneously at the fundamental frequency of the crystal (1st harmonic at 5 MHz) and four harmonics of the fundamental frequency (3rd, 5th, 7th and 9th harmonic at 15, 25, 35 and 45 MHz, respectively) [437]. Raw data were analysed by QTools (Q-Sense) and Origin 7.5 (OriginLab, USA) software.

Supported phospholipid bilayers were prepared using a liposome deposition procedure, whereby liposomes are allowed to spontaneously rupture and fuse together to form bilayers onto a 3-mercaptopropionic acid (MPA) modified chip. Liposome solutions of either neat DMPC or a heterogeneous 2:1 DMPC/DMPG composition were prepared as previously described [438]. Lipids were purchased from Avanti Polar Lipids (Alabaster, USA).

The liposome solutions (0.13 mM) were introduced into the QCM cells at a flow rate of 100 $\mu\text{L}/\text{min}$. Non-ruptured liposomes were rinsed off with buffer. After a baseline had

been established, the peptide solution (1, 2, 5, 7, 10 and 20 μM in buffer; total volume of 1 mL) was allowed to flow through the cells at 100 $\mu\text{L}/\text{min}$. The peptide was left to incubate with the lipid bilayer for at least 20 min and then the cells were rinsed with buffer. The buffer used throughout experiments was phosphate buffered saline (PBS), containing 0.1 M NaCl and 20 mM phosphate (pH 6.9). Sodium chloride (Ultra, $\geq 99.5\%$), potassium phosphate monobasic, and potassium phosphate dibasic (ACS reagent, $\geq 99\%$) were purchased from Sigma-Aldrich (Castle Hill, Australia). All experiments were performed at $19.10 \pm 0.05^\circ \text{C}$, as previously described [437, 439].

Chapter 7

NMR studies of CCK2 agonists

7.1 Introduction

7.1.1 Biological activities of amphibian neuropeptides

Recently the skin peptide profile of the Australian amphibian species *Litoria rothii* and two *Crinia* species, *C. signifera* and *C. riparia* have been investigated [66, 67, 69]. Their peptide profiles contain a range of antimicrobial peptides and neuropeptides. Biological tests of the skin peptides revealed that each species produced a unique neuropeptide that acted via CCK2 receptors, namely rothein 1 and from *L. rothii* [83], riparin 1 from *C. riparia* and signiferin 1 from *C. signifera* [50]. Additional tests were performed on a number of alanine substituted analogues of rothein 1, each with differing activities relative to the native peptide. The studies showed that each peptide would induce smooth muscle contraction and/or proliferation of splenocytes via CCK2 receptor activation [50, 83, 430], as summarised in Table 7.1.

Table 7.1 Smooth muscle and splenocyte proliferation activities of rothein 1 and *Crinia* peptides [50, 83, 430].

Peptide	Sequence	Smooth Muscle activity ^a	Splenocyte Proliferation activity ^b
		[Min. Conc. (M)]	[Min. Conc. (M)]
Rothein 1	SVSNIPESIGF-OH	Inactive	10 ⁻⁵
Rothein 1.1	A SVSNIPESIGF-OH	10 ⁻⁷	10 ⁻⁷
Rothein 1.2	SV A NIPESIGF-OH	Inactive	10 ⁻⁶
Rothein 1.3	SVSNIP A SIGF-OH	10 ⁻⁸	Inactive
Rothein 1.4	SVSNIP E AIGF-OH	10 ⁻⁸	Inactive
Rothein 1.5	SVSNIPESIG A -OH	Inactive	Inactive
Riparin 1	RLC <u>I</u> PV <u>I</u> F <u>P</u> C-OH	Inactive	10 ⁻⁷
Signiferin 1	RLC <u>I</u> P <u>Y</u> I <u>I</u> P <u>C</u> -OH	10 ⁻⁹	10 ⁻⁶

a. Determined using concentration-response curves of guinea pig ileum segment contraction. **b.** Determined using concentration-response curves of mouse splenocyte proliferation (Alamar blue test).

In the biological activity tests, the peptides bind to CCK2 receptors on cholinergic nerves surrounding the smooth muscle tissue (guinea pig ileum) causing the release of acetylcholine. The acetylcholine then binds to muscarinic receptors on smooth muscle, inducing a contraction. In the splenocyte proliferation assays, the peptides bind to CCK2 receptors on the outer membrane of selected splenocytes (specifically, Jurkat lymphoblasts and T-lymphocytes from the splenic tissue of mice) inducing cellular proliferation. The proliferation of splenocytes causes the reduction of alamar blue, which changes colour from blue to red, and the fluorescence of the reduced alamar blue measured (excitation 544 nm, emission 590 nm) [372, 455].

Tests performed using rothein 1 on guinea pig ileum reveal that the peptide does not show any significant smooth muscle contraction (below 1% of the standard acetylcholine). This is not surprising as the potent smooth muscle active peptides, caerulein 1.1 and 1.2, are also present in the *L. rothii* skin secretions [67]. The caerulein peptides induce smooth muscle contraction via binding to CCK2 receptor, and share a high degree of sequence homology with mammalian CCK peptides [67, 83]. Despite the lack of smooth muscle activity, Alamar blue tests have shown that rothein 1 induces splenocyte proliferation via binding to CCK2 receptors at a moderate concentration 10^{-5} M [83].

It is interesting that the analogues of rothein 1 show vastly different smooth muscle and splenocyte activities. Alanine substitution of the serine residues at the 1st and 3rd serine residues (rothein 1.1 and 1.2) enhances the splenocyte activity of the peptides (relative to rothein 1) and rothein 1.1 is also smooth muscle active. The most interesting of the findings is that rothein 1.3 (Glu7 to Ala7) and rothein 1.4 (Ser8 to Ala8) are smooth muscle active at low concentrations (10^{-8} M), yet show no significant splenocyte activity [83, 430]. The *Crinia* peptide riparin 1 causes splenocyte proliferation at the lowest detectable concentration (10^{-7} M), yet shows no smooth muscle activity. In contrast, signiferin 1 is the most potent smooth muscle active of the peptides (10^{-9} M) that also induces splenocyte proliferation at a moderate concentration (10^{-6} M) [50, 83].

The protein sequences of CCK2 receptors of guinea pigs (*Cavia porcellus*) and mice (*Mus musculus*) are 87% identical (see Appendix B) [456, 457]. So, alanine substituted rothein 1 peptide analogues and the selected *Crinia* neuropeptides show vastly different splenocyte and smooth muscle activities, though they bind to very similar mammalian receptors. This alludes to the question, why do these peptides appear to have such varied activities?

This study details: (i) the solution structure determination of rothein 1.3 and rothein 1.4, in aqueous TFE using 2-dimensional NMR techniques and a comparison of these structures with rothein 1, and (ii) an investigation of any key structural characteristics which may explain the varied activities of the rothein peptides. An additional objective of this study is to investigate the dynamic interactions between selected neuropeptides (rothein 1, riparin 1 and signiferin 1) and neutral membranes via solid-state NMR techniques, to determine what interactions may occur on cellular membrane surfaces prior to receptor binding.

7.1.2 Membrane mediated receptor binding of hormone peptides

The mechanistic pathways that mediate the binding of peptide hormones to transmembrane receptors has remained a controversial topic for many years. The simplest model of receptor binding involves a lock-and-key mechanism, where a peptide hormone binds directly to a transmembrane receptor from the extracellular fluid, triggering a cellular response via a secondary messenger pathway. Unlike small hormones such as adrenaline and melatonin, peptides are flexible and fold into specific conformations upon binding to a receptor site. The interaction of a randomly oriented peptide (from extracellular fluid) binding to a receptor can effect a significant change in free energy [85, 87, 458]. This one step ‘lock-and-key’ mechanism of hormone peptide to receptor binding may not reflect the biological activities (effective concentrations) of many hormone peptides.

Studies pioneered by Robert Schwyzler and co-workers detail the N-terminal fragments of hormone peptides ACTH(1-24) and dynorphin(1-13) interacting with bilayers within

artificial liposome suspensions, using a series of photolabelling, capacitance minimisation, and infrared attenuated total reflection spectroscopy experiments [458-464]. The objective of these studies was to observe the binding of peptide hormones with membranes and to see whether this reflects their activity. It was proposed that a peptide hormone may associate with the cellular membrane prior to binding to a receptor site. From this, a stepwise model for the binding of a hormone peptide to a transmembrane receptor was devised as follows: (i) the peptide in an extended (random) conformation transfers from the extracellular fluid on to the membrane surface, (ii) the peptide partially inserts into the membrane, (iii) the peptide orients itself into a conformation recognised by the receptor site and, (iv) the peptide binds to the receptor site and the hormone function is activated via a secondary messenger pathway. The membrane mediated binding of a hormone peptide to a transmembrane receptor is illustrated in Figure 7.1.

NOTE:
This figure/table/image has been removed
to comply with copyright regulations.
It is included in the print copy of the thesis
held by the University of Adelaide Library.

Figure 7.1 A schematic of the membrane mediated binding of amphipathic peptide hormones to transmembrane receptors. Based on a figure from [85].

This model of membrane mediated receptor binding can also apply to antagonist hormone peptides, where binding occurs with deactivation of the receptor. If this model is applicable, it may be important to design a peptide hormone based to have an affinity for the target cell membrane surface adjacent to the receptor site.

The phospholipid component of mammalian membranes generally contains a mixture of zwitterionic (neutral net charge) and anionic phospholipids, with 'fatty' acyl chains that

vary in length and degree of saturation [465]. Some common types of zwitterionic phospholipids present in mammalian membranes are phosphatidylcholine (PC), phosphatidylethanolamine (PE) and sphingomyelin (Sph). Some common types of anionic phospholipids include phosphatidylglycerine (PG), phosphatidylinositol (PI) and phosphatidylserine (PS) [465-468]. All of these are glycerophospholipids (glycerol backbone), with the one exception of sphingomyelin.

The arrangement of phospholipids within mammalian cellular membranes is asymmetric. The inner layer is enriched in both neutral and anionic aminophospholipids such as PS and PE and the outer layer almost exclusively made up of neutral PC and Sph lipids. This asymmetric distribution of phospholipids is regulated by a number of transporters which actively transport aminophospholipids from the outer layer to the inner layer [469]. Since the outer leaflet is largely made up of neutral lipids, zwitterionic lipids such as DMPC are commonly used as model membranes to represent the extracellular surface of eukaryotic cells.

7.1.3 Cholecystokinin receptor ligands

Human cholecystokinin and gastrin peptides are involved in the regulation of the gastrointestinal system in response to food intake, they also affect renal function and satiety [470]. The two families of peptide hormones contain a range of amino acid sequence lengths, derived from unique prepropeptide sequences. Additionally, each peptide family shares the same carboxy-terminal pentapeptide sequence (Table 7.2). The peptides have differing affinities for CCK receptors, depending on the length of the peptides, and the presence of sulphated tyrosine residues.

Table 7.2 Common human Cholecystokinin peptide ligands [84, 470, 471].

Peptide ^a	Sequence
CCK-33	RMSIVKLNQLDPSHRISDRDY(SO ₃)MGWMDF-NH ₂
CCK-8	DY(SO ₃)MGWMDF-NH ₂
CCK-4	WMDF-NH ₂
Gastrin-34	pEGPQGPPHLVADPSKKQGPWLEEEEEAY(SO ₃)GWMDF-NH ₂
Gastrin-17	pEGPWLEEEEEAY(SO ₃)GWMDF-NH ₂
Gastrin-14	WLEEEEEAY(SO ₃)GWMDF-NH ₂

^a CCK and Gastrin peptides exist in sulphated and non-sulphated forms.

CCK receptors exist as two subtypes; type I (CCK1) and type II (CCK2). CCK1 receptors are predominantly found throughout the gastrointestinal tract and specific parts of the central nervous system and show a high affinity for sulphated CCK and gastrin peptides. CCK2 receptors are predominantly located throughout the brain, CNS and in specific parts of the gastrointestinal tract. They show a high affinity for both sulphated and non-sulphated gastrin and CCK peptides. Throughout the gastrointestinal tract CCK2 receptors are found on many cell types, such as neurons, parietal cells, gastric epithelial cells and gastric chief cells [84]. They also are present on some lymphocytes such as monocytes, T-cells, and lymphoblasts [472-474]. Exploration into the use of radiolabelled CCK2 receptor ligands has been the focus of studies in recent years as CCK2 receptors are commonly over expressed in many types of cancerous tumours within the gastrointestinal tract [475].

CCK receptors are part of a large family of G-protein coupled receptors, located on the exterior membrane of cells. G-protein coupled receptors are hormone receptors involved in many biological processes; upon activation, they relay a response via a secondary signal-transduction pathway, triggering a cellular response. G-protein coupled receptors are large proteins, integrated into cellular membranes, with seven helical trans-membrane domains. The first high resolution 3D structure of a G-protein coupled receptor was that of rhodopsin, determined by Palczewski *et. al.* in 2000 (Figure 7.2) [476].

NOTE:
This figure/table/image has been removed
to comply with copyright regulations.
It is included in the print copy of the thesis
held by the University of Adelaide Library.

Figure 7.2 3-Dimensional X-ray crystal structure of the G-protein coupled receptor rhodopsin: α -helices are shown in purple, β -turns shown in dark blue. Adapted from [476], pdb code 1f88.

The amino acid sequences of the CCK receptors are known and molecular models have been reported based on the structural motif of rhodopsin [84, 477]. Further studies of the CCK2 receptor using site directed mutagenesis, affinity studies, and molecular modelling have been used to generate a model of the cholecystakinin nonapeptide (CCK-9) within the CCK2 receptor binding site [478, 479]. The studies show that a number of aromatic amino acid residues within the trans-membrane (TM) helices of the CCK2 receptor (Tyr189, Phe347 and Trp351) and other polar and charged residues (Arg57, His 207 and Asn358), are critical for the binding of CCK-9 within the CCK2 receptor site.

In addition to modelling studies, Mierke and co-workers performed NMR studies of the complex of non-sulphated CCK-8 (CCK-8ns) with the N-terminus of the CCK2 receptor [CCK2R(1-47)] and CCK-8ns with the third extracellular loop of the CCK2 receptor [CCK2R(352-379)]. Both NMR studies were performed using DPC micelles [480-482]. The NOE-derived distance restraints between the CCK-8ns and the selected segments of

CCK2 receptor were then integrated into a molecular model of the CCK2 receptor, based on the structural motif of rhodopsin [482]. The outcome was a refined model of the CCK-8ns/CCK2R complex for structure activity relationship studies; a model appropriate for structure-activity studies of CCK2 active amphibian peptides (see Figure 7.3).

NOTE:
This figure/table/image has been removed
to comply with copyright regulations.
It is included in the print copy of the thesis
held by the University of Adelaide Library.

Figure 7.3 Top (left) and side (right) views of the molecular model of CCK-8ns (grey) within the binding site of CCK2R (black). Ribbon representations of the extracellular (EC) and trans-membrane and N-terminal (NT) regions of the CCK2R protein backbone are shown, with stick representations of key amino acid residues, denoted by standard single letter abbreviations. CCK-8ns is illustrated with ribbon representations across the peptide backbone with ball and stick representation of the amino acid sidechains, key residues are denoted by standard three letter abbreviations. Figure adapted from [482].

Rothein 1, rothein 1.3, rothein 1.4 and the selected *Crinia* peptides may also bind within the CCK2 receptor site in a similar fashion to CCK-8ns. Hence, their 3-dimensional solution structures may provide the basis for further structure-activity relationship studies for modelling non-covalent interactions with the CCK2 receptor site. In addition to structural properties, the interactions of the peptides with phospholipid membrane surfaces can provide a further basis for exploring the membrane catalysed receptor binding model and explain their respective biological activities.

7.2 Results

7.2.1 Solution structures of rothein 1.3 and rothein 1.4

NMR spectra were acquired for rothein 1.3 and 1.4 in TFE/H₂O (1:1) and proton resonances assigned using the sequential assignment method [394] described in section 3.4, from a combination of COSY, TOCSY and NOESY ¹H NMR experiments. The NMR experiments, resonance assignment, and structural calculations to determine the solution structure of rothein 1, were performed previously by Emily Nicholson, School of Chemistry and Physics, the University of Adelaide [83]. For comparative reasons, the solution structure of rothein 1, as well as the NMR derived structural data are included in this chapter.

7.2.1.1 Chemical shift assignment

For rothein 1.3, a significant amount of overlap was observed in the amide proton region of the TOCSY spectrum, with coincident amide chemical shifts observed for residues Ile5, Ser8 and Gly10. However, these residues were unambiguously assigned upon examination of the COSY spectrum and the remaining TOCSY spectrum. Medium to weak sequential NH_i-NH_{i+1} peaks were observed from residues Ser2 to Phe11, with the exception of Pro6. In this case, a medium α H_i-NH_{i+1} peak was observed. The partial TOCSY and NOESY spectra for rothein 1.3 are shown in Figure 7.4.

For rothein 1.4, a moderate amount of overlap was observed in the amide proton region of the TOCSY spectrum, with a narrow variance in amide chemical shift observed for residues Ile5, Glu7, Ala8 and Gly 10. Unambiguous assignment of the chemical shifts were made upon examination of the COSY spectrum and the remaining TOCSY spectrum. No sequential NH_i-NH_{i+1} peaks were observed across residues Ser2 to Asn4, and the Glu7-Ala8 peak was obscured by the diagonal of the NOESY spectrum. However, medium α H_i-NH_{i+1} peak were observed for these residues, as well as for Pro6. Partial TOCSY and NOESY spectra for rothein 1.4 are shown in Figure 7.5.

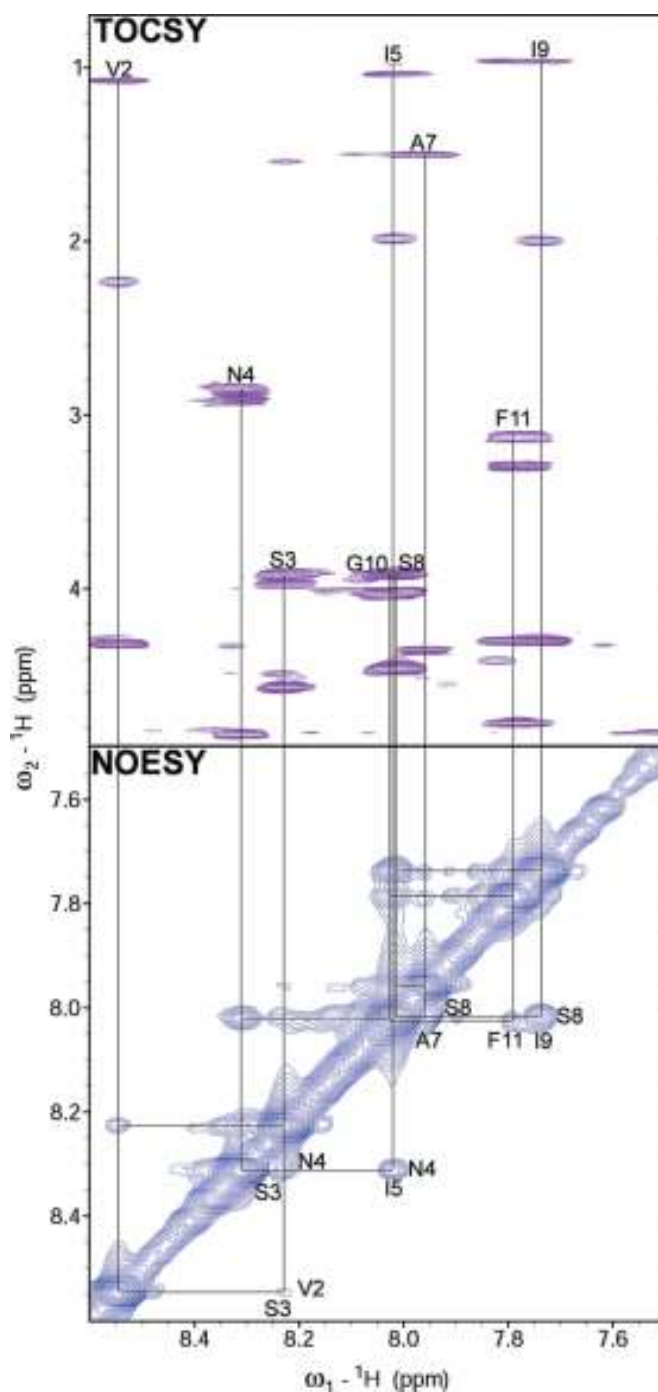


Figure 7.4 Partial NOESY (mixing time = 200 ms) and TOCSY spectra of rothein 1.3 in TFE/H₂O (1:1, v/v) at pH 1.52 and 25°C. NOEs between sequential NH protons are indicated in the NOESY spectrum. Vertical lines connect the resonances in each spin system. Residues are labelled with the standard single-letter abbreviations for amino acids, and their position within the sequence.

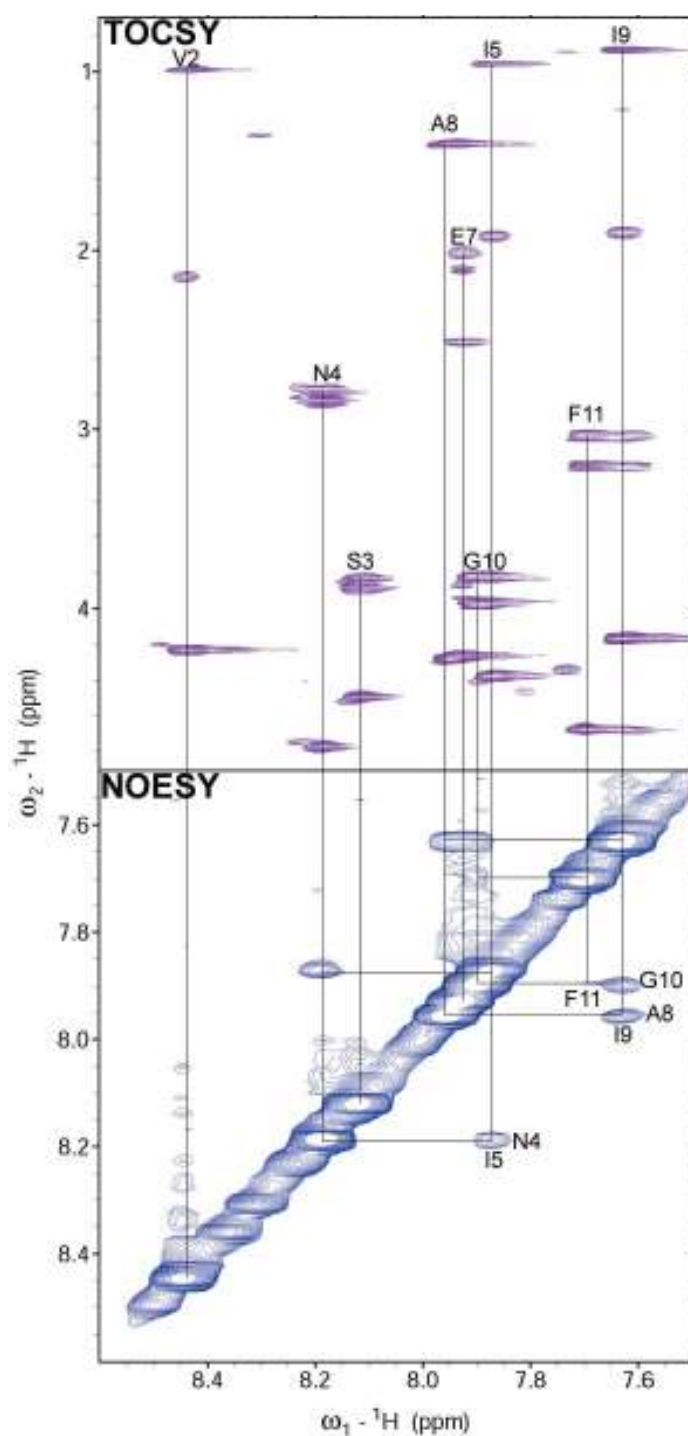


Figure 7.5 Partial NOESY (mixing time = 200 ms) and TOCSY spectra of rothein 1.4 in TFE/H₂O (1:1, v/v) at pH 2.40 and 25°C. NOEs between sequential NH protons are indicated in the NOESY spectrum. Vertical lines connect the resonances in each spin system. Residues are labelled with the standard single-letter abbreviations for amino acids, and their position within the sequence.

Additional low intensity peaks were observed in the COSY, TOCSY and NOESY spectra of rothein 1.3 and rothein 1.4. These series of peaks were likely to be the result of *cis-trans* isomerisation about the imide bond of the Pro6 residue (See section 3.5). These peaks were not assigned within any of the NMR spectra.

A summary of the assigned ^1H resonances for rothein 1.3 and rothein 1.4 are shown in Tables 7.3 and 7.4 respectively. Each spectrum was completely assigned, however N-terminal NH_3^+ resonances were not observed.

Table 7.3 ^1H NMR chemical shifts for rothein 1.3 in TFE/ H_2O (1:1,v/v) at pH 1.52 and 25°C. n.o. indicates resonance was not observed.

Residue	Chemical shift (ppm)			
	NH	α -CH	β -CH	Others
Ser1	n.o.	4.30	4.13	
Val2	8.55	4.32	2.24	γ -CH ₃ 1.08
Ser3	8.23	4.57	3.92, 3.98	
Asn4	8.31	4.83	2.86, 2.91	γ -NH ₂ 6.74, 7.50
Ile5	8.02	4.47	1.99	γ -CH ₂ 1.26, 1.64 γ -CH ₃ 1.04 δ -CH ₃ 0.98
Pro6	-	4.44	2.05, 2.35	γ -CH ₂ 2.05, 2.16 δ -CH ₂ 3.77, 3.95
Ala7	7.96	4.36	1.50	
Ser8	8.01	4.46	3.92, 4.03	
Ile9	7.74	4.30	2.00	γ -CH ₂ 0.97, 1.29 δ -CH ₃ 1.56
Gly10	8.02	3.92, 4.03		
Phe11	7.79	4.78	3.13, 3.29	H2,6 7.26 H3,5 7.31 H4 7.22

Table 7.4 ¹H NMR chemical shifts for rothein 1.4 in TFE/H₂O (1:1,v/v) at pH 2.40 and 25°C. n.o. indicates resonance was not observed.

Residue	Chemical shift (ppm)				
	NH	α -CH	β -CH	Others	
Ser1	n.o.	4.21	4.04		
Val2	8.45	4.23	2.15	γ -CH ₃	0.99
Ser3	8.12	4.49	3.83, 3.89		
Asn4	8.19	4.77	2.79, 2.84	γ -NH ₂	6.64, 7.38
Ile5	7.87	4.38	1.92	γ -CH ₂	1.17, 1.56
				γ -CH ₃	0.96
				δ -CH ₃	0.89
Pro6	-	4.33	1.90, 2.24	γ -CH ₂	1.96, 2.06
				δ -CH ₂	3.68, 3.83
Glu7	7.93	4.26	2.02, 2.11	δ -CH ₂	2.51
Ala8	7.96	4.28	1.41		
Ile9	7.63	4.16	1.90	γ -CH ₂	1.48
				γ -CH ₃	1.21
				δ -CH ₃	0.87
Gly10	7.90	3.83, 3.96			
Phe11	7.70	4.67	3.04, 3.20	H2,6	7.23
				H3,5	7.28
				H4	7.20

7.2.1.2 Secondary chemical shifts

The random coil chemical shifts for α -protons and amide protons were obtained from Wishart *et. al.* [237]. α -Proton chemical shifts for rothein 1 [83], rothein 1.3 and rothein 1.4 were plotted against the random coil chemical shifts, and smoothed over a window of $n \pm 2$ residues, the amide proton secondary chemical shifts of each peptide were not smoothed. The α -proton and amide proton secondary chemical shifts are illustrated in Figures 7.6 and 7.7 respectively.

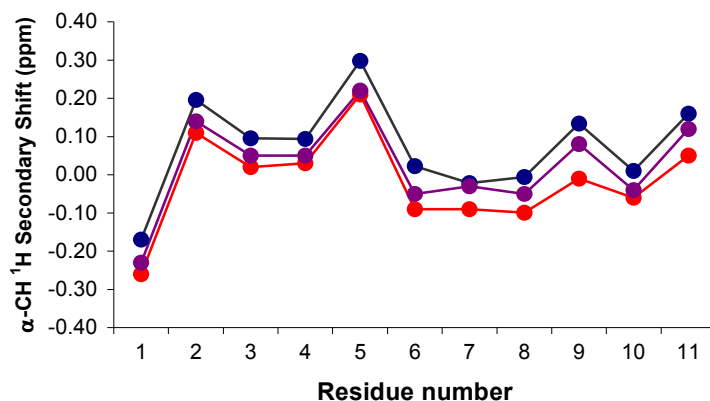


Figure 7.6 α -proton secondary shifts of rothein 1 (purple), rothein 1.3 (blue) and rothein 1.4 (red) in TFE/H₂O (1:1, v/v).

The α -proton secondary chemical shift trends of rothein 1, rothein 1.3 and rothein 1.4 are almost identical. The secondary shifts of the rothein peptides are within 0.4 ppm of the zero, and do not indicate any distinct regions of secondary structure. The plot indicates that the peptide conformations are likely to be random.

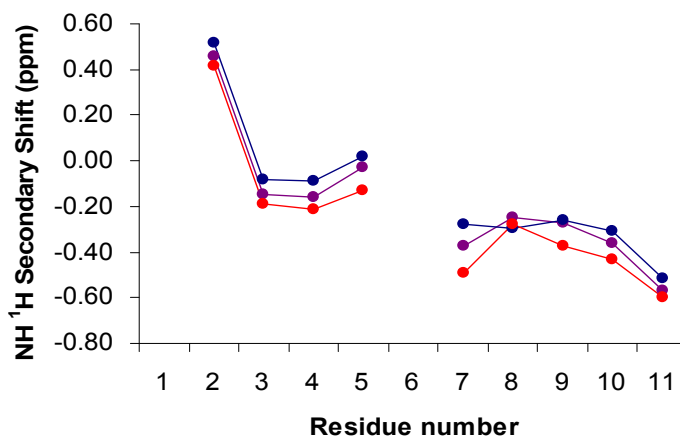


Figure 7.7 Amide proton secondary shifts of rothein 1 (purple), rothein 1.3 (blue) and rothein 1.4 (red) in TFE/H₂O (1:1, v/v). Positive values indicate a downfield shift from the random coil values, negative values indicate an upfield shift [237].

The amide proton secondary chemical shift trends of rothein 1, rothein 1.3 and rothein 1.4 are very similar. The amide secondary shifts for each peptide generally show a

decrease in the secondary shift values from the N-terminal to the C-terminal, with a gap due to the Pro6 amino acid residue. No defined regions of secondary structure can be determined from the amide proton secondary chemical shifts for rothein 1, rothein 1.3 and rothein 1.4.

7.2.1.3 NOE connectivities

The diagnostic NOE connectivity patterns of rothein 1, rothein 1.3 and rothein 1.4, based on ARIA assignments after eight iterations, are displayed in Figure 7.8. For rothein 1 very little sequential d_{NN} signals were observed across the length of the peptide, and medium to weak $d_{\alpha\text{N}}$ and $d_{\beta\text{N}}$ NOE connectivities exist across the majority of the peptide sequence. One medium range $d_{\alpha\text{N}(i,i+3)}$ is observed at the C-terminus of the peptide, characteristic of helical structure. However, the assignment of this medium range NOE is ambiguous. For rothein 1.3, medium sequential d_{NN} , and weak to medium $d_{\alpha\text{N}}$ and $d_{\beta\text{N}}$ NOE connectivities are observed across the majority of the peptide. Two medium $d_{\beta\text{N}(i,i+2)}$ NOEs are observed at the N-terminus and between the Pro6 and Ser8 amino acid residues. However, the latter NOE assignment is ambiguous. For rothein 1.4, four d_{NN} NOEs are observed toward the C-terminal end of the peptide, and medium to strong $d_{\alpha\text{N}}$ and $d_{\beta\text{N}}$ NOE connectivities are observed across the majority of the peptide. No diagnostic medium or long range signals were observed for rothein 1.4. Overall the diagnostic NOE connectivities are consistent with an extended structure for each peptide.

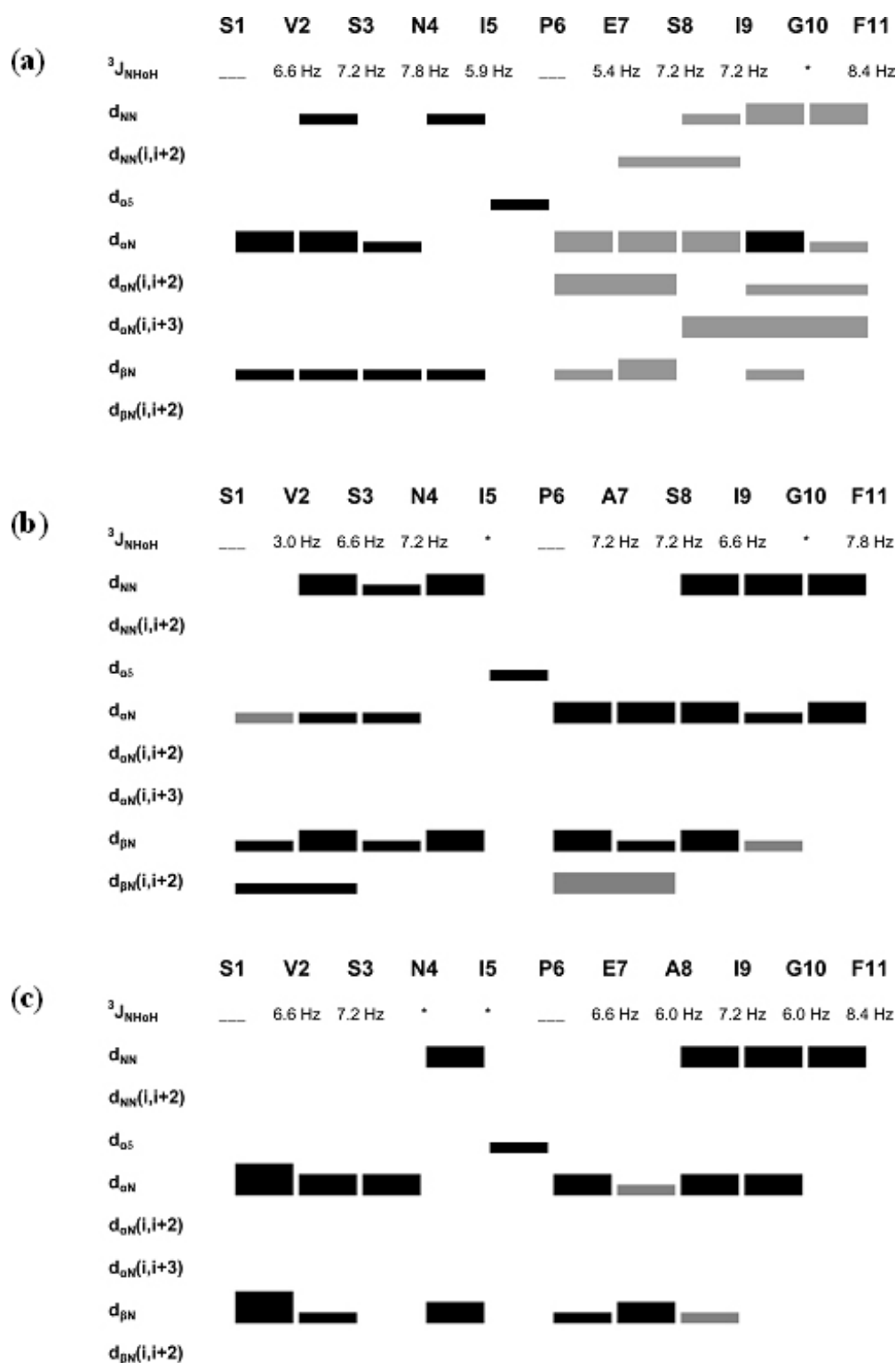


Figure 7.8 Summaries of NOE connectivities and $^3J_{\text{NH}\alpha\text{H}}$ coupling constants used in structure calculations of (a) rothein 1, (b) rothein 1.3 and (c) rothein 1.4 in TFE/H₂O (1:1 v/v). The thickness of the bars indicates the relative strength of NOEs (strong < 3.1 Å, medium 3.1–3.7 Å and weak > 3.7 Å).

7.2.1.4 Coupling constants

Figure 7.8 also shows the $^3J_{\text{NH}\alpha\text{H}}$ coupling constants for rothein 1, rothein 1.3 and rothein 1.4 determined directly from the amide region of the high resolution 1D NMR spectra. The majority of coupling constants fall within the range of 6-8 Hz, coupling constants that are consistent with random coil structure. One exception is the coupling constant of 3 Hz from Val2 amide proton of rothein 1.3, synonymous with helical structure. Another exception is the 8.4 Hz coupling constants from Phe11 of rothein 1 and rothein 1.4, that is consistent with β -strands or β -turns [229].

7.2.1.5 Structure calculations

The NOESY spectra of rothein 1.3 and rothein 1.4 were fully assigned and the cross-peak volumes converted to inter-proton distance restraints using a method described by Nilges *et. al.* [400]. A summary of the NOE derived distance restraints for rothein 1.3 and rothein 1.4 resulting after 8 iterations of ARIA structure calculations are shown in Table 7.5. A total of 87 non-redundant distance restraints were produced for rothein 1.3, 7 that were ambiguous. A total of 97 NOE restraints were derived from the NOESY spectrum of rothein 1.4, 2 that were ambiguous. In addition, one dihedral restraint was derived for rothein 1.3, and two for rothein 1.4 from the high resolution 1D NMR spectra.

Table 7.5 A summary of experimentally derived NOE distance restraints for rothein 1.3 and rothein 1.4.

Peptide	Number of Restraints	
	Rothein 1.3	Rothein 1.4
Sequence	SVSNIPASIGF-OH	SVSNIPEAIGF-OH
Sequential NOEs	29	26
Medium-range NOEs	2	0
Long-range NOEs	0	0
Intra-residue NOEs	49	69
Ambiguous NOEs	7	2
Total	87	97

The ARIA RMD and SA calculations produced 60 final structures for each peptide, the 20 structures with the lowest potential energy were chosen for analysis. The 20 lowest potential energy structures generated for rothein 1, rothein 1.3 and rothein 1.4 are illustrated in Figure 7.9, superimposed over residues Val2-Gly10.

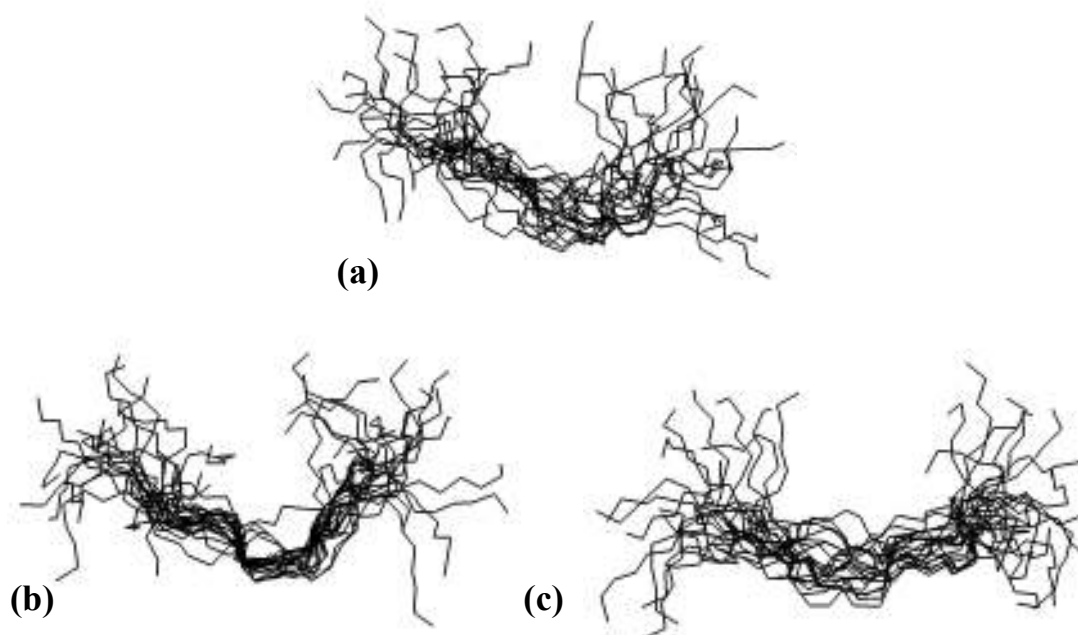


Figure 7.9 The 20 lowest energy structures of rothein 1 (a), rothein 1.3 (b) and rothein 1.4 (c) in TFE/H₂O (1:1, v/v), superimposed best fits over the backbone atoms of Val2-Gly10.

The backbone structures of rothein 1, rothein 1.3 and rothein 1.4 display little structural consistency across the central regions. The RMSDs from the mean geometries of the backbone atoms across residues Val2-Gly10 for rothein 1, rothein 1.3 and rothein 1.4 are $1.99 \pm 0.42 \text{ \AA}$, $1.83 \pm 0.44 \text{ \AA}$ and $1.84 \pm 0.27 \text{ \AA}$ respectively. This further indicates that the peptide structures are largely extended, with a high degree of conformational flexibility. The RMSDs from the mean geometries are even greater for all backbone atoms, indicating that the N and C-terminal amino acid residues have the greatest degree of flexibility. The statistics of the structures produced from RMD and SA calculations for rothein 1.3 and rothein 1.4 are summarised in Table 7.6.

Table 7.6 Structural statistics for rothein 1.3 and rothein 1.4 following RMD and SA calculations. The energies are derived from the mean of the 20 lowest energy structures. The RMSDs from the mean geometries were obtained by best-fitting the backbone atoms (N, α C, C') over the selected residues 2 to 10.

Energies (kcal.mol⁻¹)	rothein 1.3	rothein 1.4
E_{total}	5.01 ± 0.44	5.27 ± 0.15
E_{bond}	0.13 ± 0.03	0.15 ± 0.03
E_{angle}	1.41 ± 0.11	1.67 ± 0.12
E_{improper}	0.09 ± 0.01	0.10 ± 0.02
E_{vdW}	3.37 ± 0.39	3.34 ± 0.40
E_{NOE}	0.00 ± 0.00	0.00 ± 0.00
E_{cdih}	0.00 ± 0.00	0.00 ± 0.00
RMSD from mean geometry (Å)		
All heavy atoms	3.68 ± 0.56	3.66 ± 0.31
All backbone atoms	2.63 ± 0.56	2.45 ± 0.32
Heavy atoms of Selected backbone (residues 2-10)	2.64 ± 0.45	2.97 ± 0.26
Selected backbone atoms (residues 2-10)	1.83 ± 0.44	1.84 ± 0.27

The final structures for rothein 1.3 and rothein 1.4 analogues showed no NOE restraint violations. This suggests the resultant structures adequately represent the NMR data.

Analysis of the angular order parameters (ϕ and ψ dihedral angles, S values) for the final 20 structures of rothein 1.3 and rothein 1.4 showed no well defined residues. The average backbone ϕ and ψ dihedral angles of the final 20 structures for each peptide are plotted on Ramachandran plots in Figure 7.10. For rothein 1.3, 71 % of the average ϕ and ψ dihedral angles are distributed into favoured regions, and the remaining 29 % into allowed regions. The dihedral angles about the central region (Ser3-Ser8) suggest β -strand or β -turn structure with the exception of Pro6 (favoured α -helical region). For rothein 1.4, 43 % of the average ϕ and ψ dihedral angles are distributed into favoured regions, and the remaining 57 % into allowed regions, the dihedral angles about the central region (Asn4-Ala8) also suggest β -strand or β -turn structure, including Pro6.

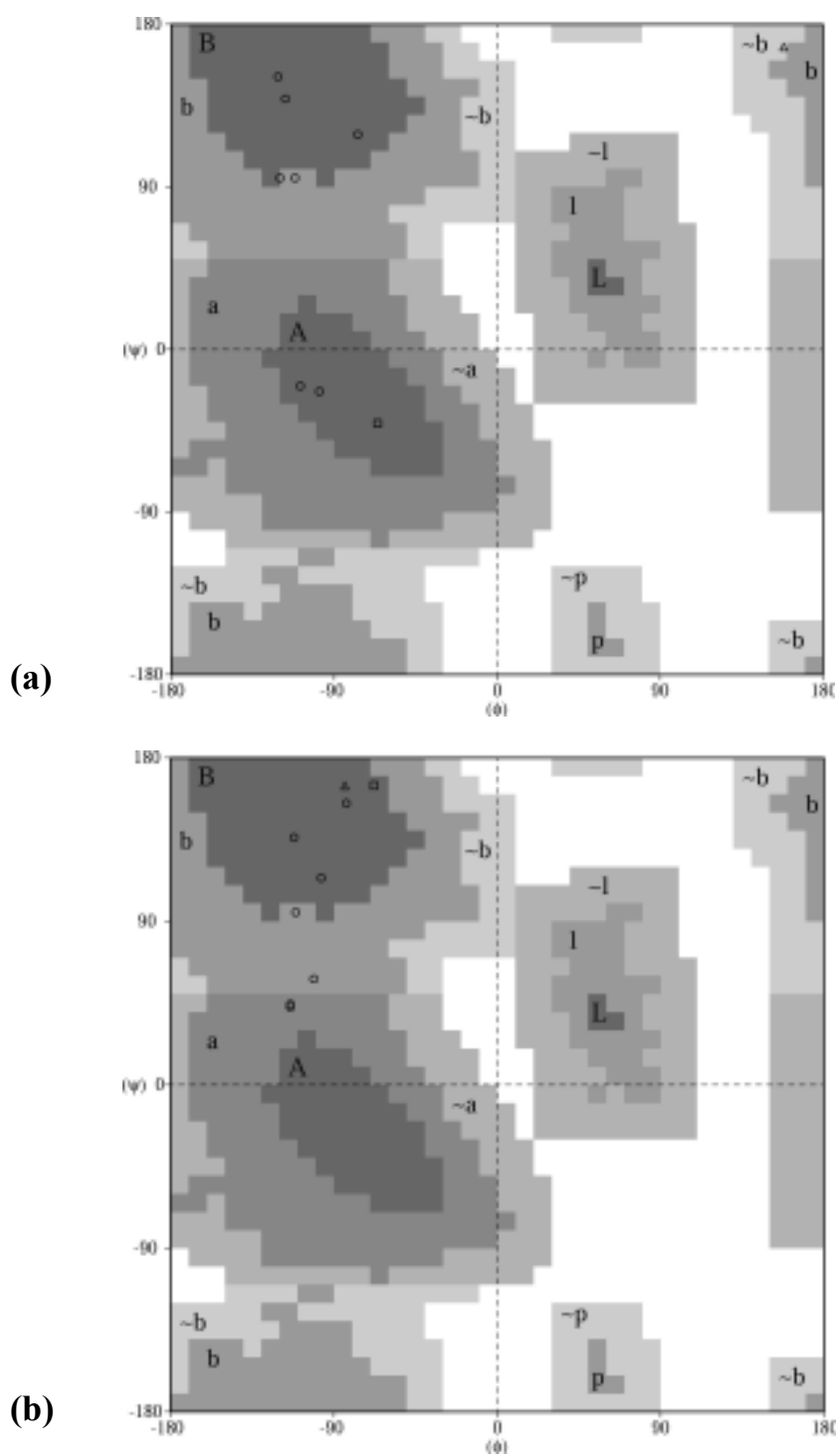


Figure 7.10 Ramachandran plot of average backbone ϕ and ψ angles for (a) rothein 1, (b) rothein 1.3 and (c) rothein 1.4 in TFE/H₂O (1:1, v/v). Favoured and allowed regions for α -helices are labelled A and a, respectively. Favoured and allowed regions for β -sheets labelled B and b, respectively. Glycine and proline residues are indicated by \triangle and \square , respectively; remaining amino acid residues are indicated by \circ .

The energy minimised average structures of rothein 1, rothein 1.3 and rothein 1.4 are illustrated in Figure 7.7. The structures of rothein 1 and rothein 1.3 show some folding within central regions, with sharp bends at the Pro6 backbone. Rothein 1 appears to be the most folded in terms of secondary structure, and rothein 1.4 appears to be the most extended. Considering the N and C-termini of each of the structures show a high degree of variance, only minor differences across the central regions of each rothein peptide structure can be defined.

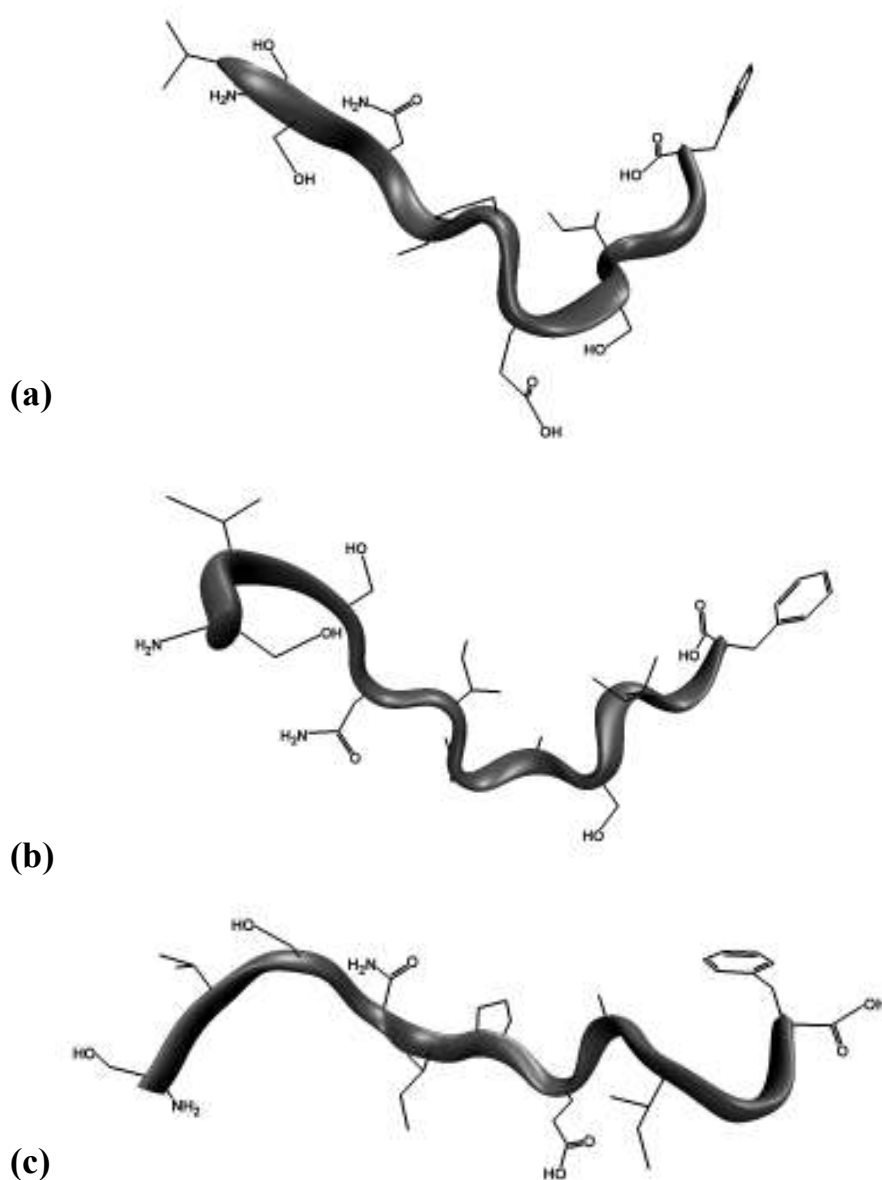


Figure 7.11 Ribbon representations of the energy minimised average structures of rothein 1 (a), rothein 1.3 (b) and rothein 1.4 (c).

7.2.2 Solid-state NMR of amphibian neuropeptides with membranes

7.2.2.1 ^{31}P solid-state NMR

Solid-state ^{31}P NMR experiments were used to investigate the effects of rothein 1, riparin 1 and signiferin 1 on the mobility and order of phospholipid head groups. Static ^{31}P NMR spectra were taken for unoriented lipid multilayers comprised of 1:1 d_{54} -DMPC/DMPC mixtures alone and in the presence of rothein 1, riparin 1 and signiferin 1, at a lipid/peptide ratio of 10:1. The resulting ^{31}P NMR spectra are shown in Figure 7.12.

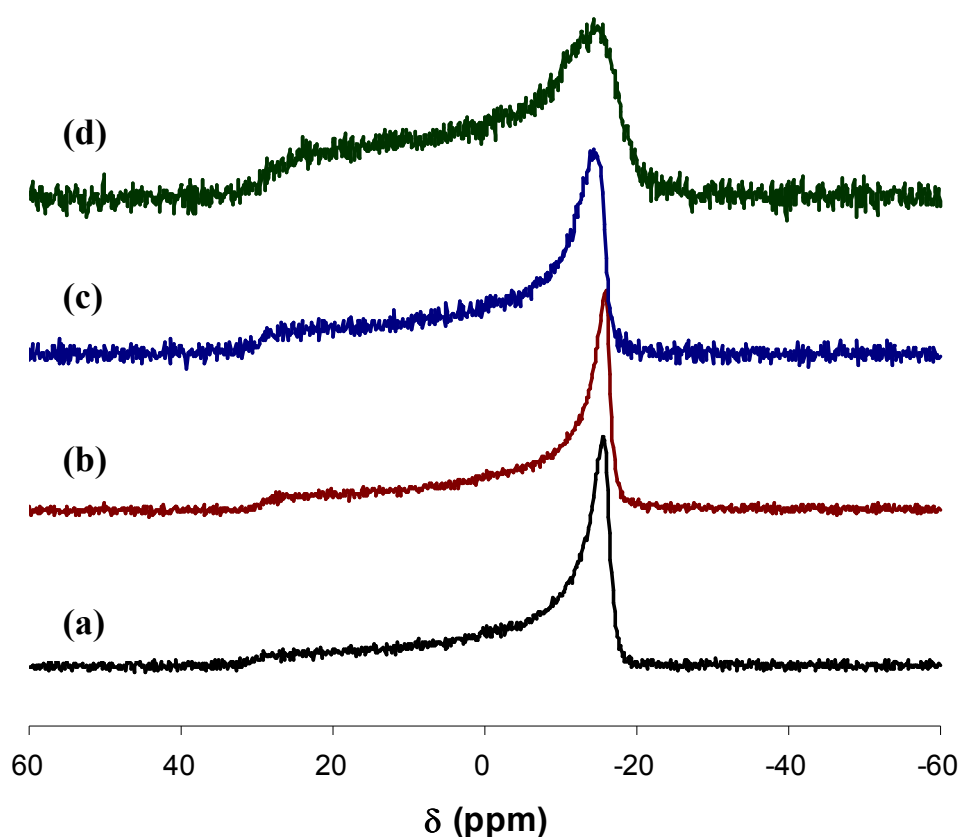


Figure 7.12 ^{31}P NMR spectra of d_{54} -DMPC/DMPC MLV (a) alone, and in the presence of (b) rothein 1, (c) riparin 1 and, (d) signiferin 1.

In all ^{31}P NMR spectra the unoriented line shapes show axially symmetric CSAs, indicating the lipids are in the fluid or lamellar (L_α) phase [335]. The ^{31}P static NMR

spectra of DMPC alone (control) showed a CSA of approximately -44 ppm, typical for unoriented MLV samples as shown in previous studies [285, 331, 332, 335]. The ^{31}P spectrum of DMPC MLV in the presence of rothein 1 showed an axially symmetric powder pattern, with a CSA of approximately -43 ppm, indicating that the peptide has little effect on the phospholipid head group orientation. The addition of riparin 1 to DMPC MLV caused a slightly reduced CSA of -41 ppm, indicating the peptide causes increased head group mobility or a change in orientation, possibly due to insertion of the peptide or a surface interaction. Interestingly, the addition of signiferin 1 to DMPC MLV resulted in a broadened ^{31}P spectral lineshape, with two major overlapping lineshapes; CSAs of approximately -41 and -38 ppm were observed. This indicates that signiferin 1 appears to cause some degree of lateral phase separation, or increased curvature of the membrane surface, as well as greater spacing between phospholipid head groups. This effect could be the result either an insertion of the peptide, or a surface interaction.

A summary of all of the ^{31}P spectral data of amphibian neuropeptides with DMPC MLVs is shown in Table 7.7.

Table 7.7 ^{31}P spectral data for DMPC and DMPC/DMPG MLV, alone (control) and with the addition of selected amphibian neuropeptides.

Sample	^{31}P CSA (ppm) ^a			
	Control	+ rothein 1	+ riparin 1	+ signiferin 1
DMPC CSA (ppm)	-44	-43	-41	-41 -38

^a CSA determined ± 0.5 ppm. ^b Contributing CSAs were fitted using the DMFIT program [440].

7.2.2.2 ^2H solid-state NMR

Deuterated DMPC was used in ^2H NMR experiments to investigate if rothein 1, riparin 1 and signiferin 1 disrupt phospholipid acyl chain mobility. Static ^2H NMR spectra were taken for unoriented lipid suspensions of 1:1 d_{54} -DMPC/DMPC and 2:2:1 d_{54} -DMPC/DMPC/DMPG mixtures alone and in the presence of peptide, at a 10:1 lipid/peptide ratio. The resultant spectra were an overlay of Pake doublets corresponding to deuterons on the acyl chains of d_{54} -DMPC. The ^2H spectra of 1:1 d_{54} -DMPC/DMPC

MLV alone (control) and in the presence of amphibian neuropeptides is shown in Figure 7.13.

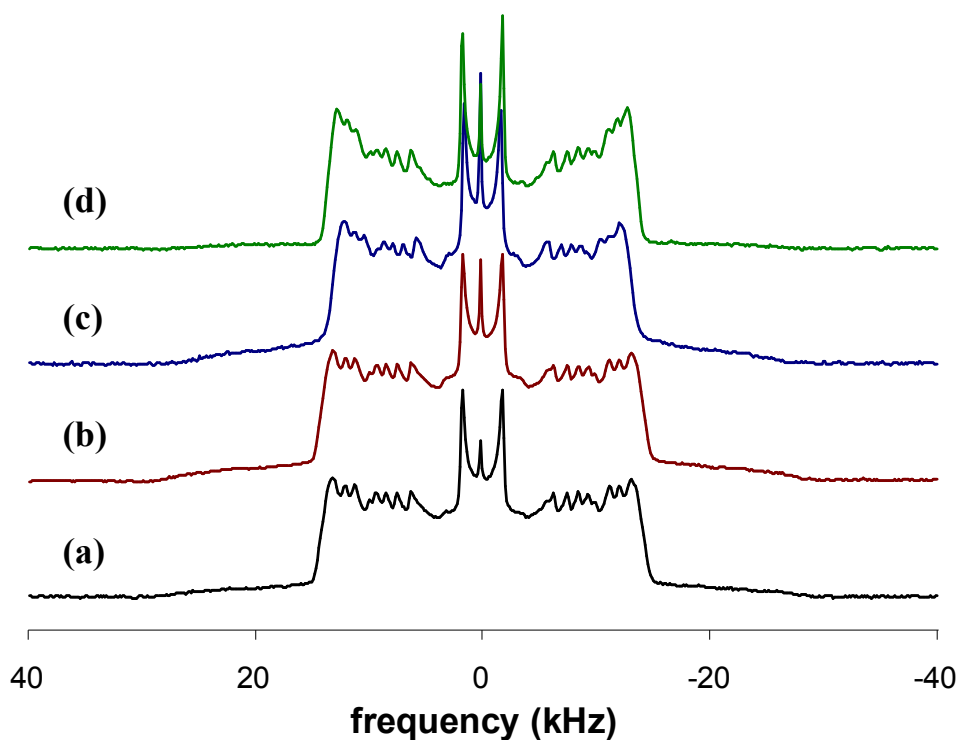


Figure 7.13 ^2H NMR spectra of d_{54} -DMPC/DMPC MLV (a) alone, and in the presence of (b) rothein 1, (c) riparin 1 and, (d) signiferin 1.

The static ^2H NMR spectra are typical for hydrated d_{54} -DMPC/DMPC MLV suspensions, with a small central isotropic peak due to residual deuterium in the buffer solution [344, 434, 441]. The addition of rothein 1 showed little change in the ^2H NMR spectrum relative to the control, showing the hydrophilic peptide has little effect on the hydrophobic core of the bilayer. The addition of signiferin 1 caused only minor narrowing in the ^2H NMR spectrum relative to the control, and a slight increase of overlaid Pake doublets on the outer edges of the spectrum. The ^2H NMR spectrum of DMPC MLV in the presence of riparin 1 shows a significant narrowing of the spectrum, indicating the peptide disrupts the hydrophobic core of the membrane leading to increased acyl chain mobility.

The ^2H quadrupolar splittings taken from static ^2H NMR spectra were ‘dePaked’ to calculate the order parameters (S_{CD}) (see Section 3.2.4.2) [312, 344, 442]. The S_{CD} values were used to determine the order of CD_2/CD_3 groups along acyl chains of d_{54} -DMPC [307]. The S_{CD} order profiles of 1:1 d_{54} -DMPC/DMPC MLV alone (control) and in the presence of rothein 1, riparin 1 and signiferin 1 is shown in Figure 7.14.

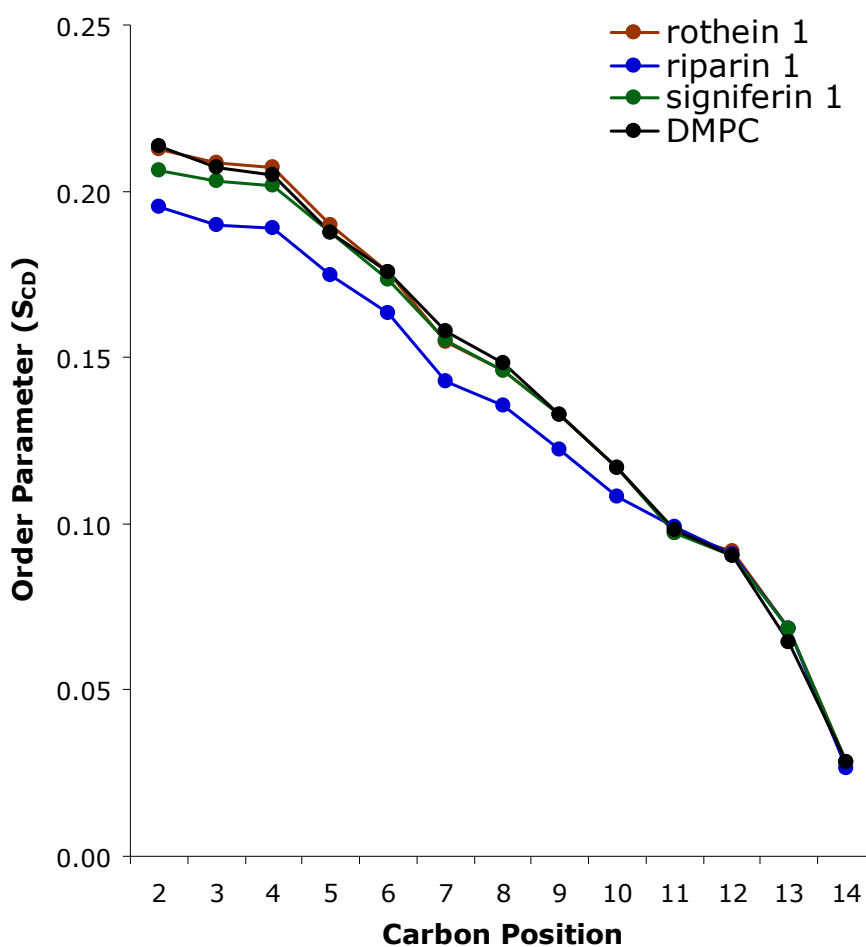


Figure 7.14 Plot of the carbon-deuterium bond order parameters (S_{CD}) against acyl chain carbon position for unoriented bilayers of 1:1 d_{54} -DMPC/DMPC alone (black), in the presence of rothein 1 (brown), riparin 1 (green), and signiferin 1 (blue), at a lipid/peptide ratio of 10:1 at 30 °C.

The S_{CD} order parameters do not significantly change at all in the presence of rothein 1, and only a minor decrease in order is observed in the presence of signiferin 1 across 2nd, 3rd, and 4th CD_2 positions. This indicates that signiferin 1 causes a minor decrease in

order about the hydrophilic surface of the DMPC bilayer. The order parameter profile of DMPC in the presence of riparin 1 shows a vast decrease in order across the majority of the length of the acyl chain. Indicating that riparin 1 interacts with the hydrophobic core of the bilayer, leading to disordering of the acyl chains.

A summary of the quadrupolar splittings of measured from the ^2H NMR spectra of 1:1 d_{54} -DMPC/DMPC MLV alone and in the presence of the selected amphibian neuropeptides is shown in Table 7.8.

Table 7.8 The ^2H quadrupolar splittings (± 0.1 kHz) measured for 1:1 d_{54} -DMPC/DMPC in the presence of rothein 1 (rot 1), riparin 1 (rip 1) and signiferin 1 (sig 1).

Carbon position	^2H Quadrupolar splittings (kHz)				% Change from lipid alone		
	DMPC	+ rot 1	+ rip 1	+ sig 1	+ rot 1	+ rip 1	+ sig 1
2	27.2	27.1	24.9	26.3	0	-8	-3
3	26.4	26.6	24.2	25.9	+1	-8	-2
4	26.1	26.4	24.1	25.7	+1	-8	-2
5	23.9	24.2	22.3	23.9	+1	-7	0
6	22.4	22.4	20.8	22.1	0	-7	-1
7	20.1	19.7	18.2	19.8	-2	-9	-1
8	18.9	18.6	17.3	18.6	-2	-8	-2
9	16.9	16.9	15.6	16.9	0	-8	0
10	14.9	14.9	13.8	14.9	0	-7	0
11	12.5	12.4	12.6	12.4	-1	+1	-1
12	11.5	11.7	11.6	11.5	+2	+1	0
13	8.2	8.7	8.7	8.7	+6	+6	+6
14	3.6	3.6	3.4	3.6	0	-6	0

7.3 Discussion

7.3.1 Structure analysis of rothein analogues

The 1:1 TFE/H₂O solution structures of the rothein 1.3 and rothein 1.4, derived from the NMR data, show extended structures (see Figure 7.7) [83]. Rothein 1.3 and rothein 1.4 show some differences in 3-dimensional structure relative to the structure of rothein 1, though the hydrophobic residues do appear to orientate themselves in similar directions within the central region of rothein 1.3 and rothein 1.4.

Turn structures such as β -turns often direct key residues toward the exterior of proteins and peptides, and are essential in the molecular recognition process by other biological molecules in the formation of complexes [483]. Rothein 1 does appear to have a ‘ β -turn like’ structure as the Pro6 α C to Ile9 α C distance is 7.16Å, and the generally expected structural feature of a β -turn is α C_i to α C_{i+3} distance of less than 7Å in a non-helical region [484]. Additionally, β -turns in peptide structure generally show hydrogen bonding of an amide proton (NH_i) to the carbonyl group on the third residue (CO_{i+3}) ahead in the peptide sequence [485]. However, rothein 1 lacks this hydrogen bonding as there is no amide proton on Pro6. The turn-like structure of rothein 1 directs the charged and polar residues Glu7 and Ser8 toward one face of the peptide (see Figure 7.7b), this feature may be involved in molecular recognition of the peptide by the CCK2 receptor. The solution structure of rothein 1.3 also appears to have a defined folding structure spanning from Ile5 to Ile10 (see Figures 7.4b, 7.5b), however to a lesser extent than the ‘ β -turn like’ structure of rothein 1. This structure directs the residues Pro6, Ala7 and Ser8 toward the exterior of the peptide, a region much less polar in nature relative to the turn like region of rothein 1. The structure of rothein 1.4 does not appear to have any turn like structure about the central region. This indicates the peptides may undergo additional folding within their central regions upon binding to the CCK2 receptor site.

Conformational structures of other known amphibian derived CCK2 receptor agonists such as riparin 1 and signiferin 1 peptides tend to show ‘bell’ shaped solution structures,

with β -turns stabilised by a disulfide bridge. Also an NMR derived model of non-sulphated CCK-8 (CCK-8ns) in complex with the CCK2 receptor from solution structures of CCK-8ns in complex with CCK2R(1-47), shows CCK-8ns adopting a pseudo-helical structure over the first four N-terminal residues of the peptide ligand, with a β -turn toward the C-terminus across the residues Gly4 to Glu7 (Figure 7.8) [481, 482].

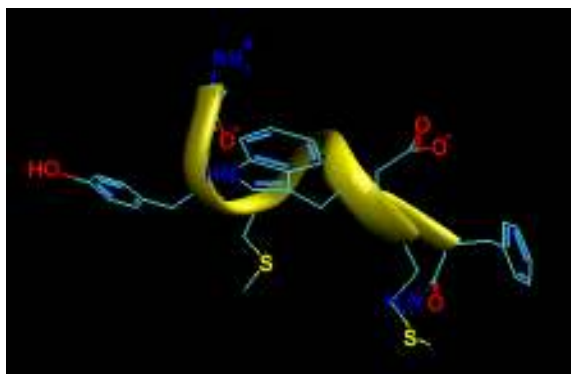


Figure 7.15 Ribbon representation of the solution structure of CCK-8ns in complex with CCK2R(1-47) in DPC micelles from NOE restraint MD and SA calculations, determined by Pellegrini *et al.* [481]. pdb code: 1d6g.

One key feature shared between CCK peptides and the rothein 1 peptides is the presence of a C-terminal phenylalanine residue. This must be essential for the binding of rothein 1 peptides as rothein 1.5 (Phe11 substituted with Ala11) shows no activity. The phenylalanine must be essential for hydrophobic interactions with residues such as Pro114, Ile121 and Ile126 of the first extracellular loop of CCK2, as well as establishing π - π stacking interactions with Phe120. The phenylalanine residues of the rothein 1 peptides do face different directions (see Figure 7.7). However, they may easily reorientate themselves upon binding to CCK2 receptor due to initial conformational flexibility about the C-terminus, particularly considering a glycine residue precedes phenylalanine (see Figure 7.5).

The notable Coulombic, hydrogen bonding and hydrophobic interactions between CCK-8ns and the CCK2 receptor are listed in Table 7.9 [482], as well as some possible

equivalent intermolecular interactions that may exist between the rothein 1 peptides and the CCK2 receptor.

Table 7.9 Notable intermolecular interactions of CCK8-ns with CCK2R as determined by Giragossian *et al.* [482].

NOTE:
This figure/table/image has been removed
to comply with copyright regulations.
It is included in the print copy of the thesis
held by the University of Adelaide Library.

The one notable Coulombic interaction between CCK-8ns complexed to CCK2 receptor is between the negatively charged Glu7 and His207. The substitution of Glu7 of rothein 1 with Ala7 in the sequence (rothein 1.3) does not eliminate the CCK2 activity of the peptide. Hence, a Coulombic interaction may exist between the C-terminal carboxylate anion of rothein 1 and His207 of the CCK2, as it is a negatively charged functional group in close proximity to the phenyl group (Phe11). However, CCK and gastrin peptides have C-terminal amidation, and their C-terminal carboxylate analogues are considered to be inactive [470]. The carboxylate side chain of the Glu7 residue of CCK-8ns also is considered to share a hydrogen bonding interaction with the amide sidechain of Asn115.

The hydroxyl oxygen of Ser8 (rothein 1, 1.3) or carboxyl oxygen of Glu7 (rothein 1, 1.4) may interact with Asn115 in a similar way.

It has been documented from both site directed mutagenesis and photoaffinity labelling studies that the sulphated Tyr2 of CCK8 and CCK-9 undergoes a Coulombic interaction with the guanidinium group of Arg57 residue within the N-terminal segment of the CCK2 receptor [478, 486]. In the proposed model by Giragossian *et al.* [482] the hydroxyl oxygen of Tyr2 (CCK-8ns) undergoes hydrogen bonding with the guanidinium hydrogens of Arg57, this weaker interaction may account for CCK8-ns being ~ 10 fold less active than sulphated CCK-8 [470]. Equivalent hydrogen bonding interactions are likely to exist between the hydroxyl oxygens of Ser1 or Ser3 of rothein 1 peptides, with Arg57 of the CCK2 receptor.

The non-covalent interactions of rothein 1 peptides with the CCK2 receptor are purely hypothetical. Further site-directed mutagenesis, photoaffinity labelling, NMR and modelling studies would be required to completely analyse the structure-activity relationship. However, it is clear that the rothein 1 analogues show differences in structure relative to rothein 1. With the aid of these studies, peptide structures can be generated to design peptidomimetic CCK2 receptor agonists, which retain the activities of the rothein 1 peptides.

7.3.2 Solid-state NMR

The addition of rothein 1 to DMPC MLV caused very little change in the ^{31}P CSA, ^2H NMR, and S_{CD} order profiles relative to the control sample. Rothein 1 is both hydrophilic in nature and has negative charge at a pH of 7, so it is unlikely that it inserts itself into the bilayer and essentially remains within the hydrophilic space between the DMPC bilayers.

The solid-state NMR of the addition of riparin 1 to DMPC MLV revealed a very pronounced effect. The ^{31}P CSA of -41 ppm was significantly reduced relative to the control (-44 ppm) indicating the peptide causes significant disorder within the surface region of the bilayer, most likely due to the positively charged arginine residue at the N-

terminus interacting with the negatively charged phosphate groups. In addition to the disordering within the hydrophilic surfaces of the bilayers, the ^2H NMR also revealed that riparin 1 caused a large decrease in quadrupolar splittings (and S_{CD} order parameters) relative to the control across the entire length of the acyl chains. This indicates that riparin 1 inserts itself into the hydrophobic core of the bilayer, increasing lateral spacing between phospholipids leading to more mobile and disordered phospholipids. Similar observations have been observed in the solid state NMR of some antimicrobial peptides believed to be pore forming within DMPC lipid suspensions, such as citropin and maculatin [331]. In other studies, such as those of fallaxidin 4.1a, suggest that pore forming antimicrobial peptides do not greatly affect the integrity of the core of the membrane and in fact increase the quadrupolar splittings of acyl CD_2/CD_3 groups [82] (See Chapter 6). However in the case of riparin 1 the insertion is only within one leaflet of the bilayer, rather than spanning the entire bilayer like pore forming peptides. A NMR study by Marcotte et. al. [487] of the opiate neuropeptide Methionine-enkephalin with bicellar systems using deuterated lipids showed that the introduction of the peptide caused a decrease in the ^2H quadrupolar splittings across all CD_2/CD_3 groups within the lipid acyl chains. These studies were performed with zwitterionic lipid bicelles and bicelles enriched with anionic lipids. The Methionine-enkephalin peptide showed differing effects on the quadrupolar splittings depending on the depth of peptide insertion into the bicellar membranes.

Collectively, the solid state NMR shows that riparin 1 is easily able to insert itself into the hydrophobic core of a phospholipid bilayer leading to a degree of disordering. The part of the peptide within the core is likely to be the 'hydrophobic loop' region of the peptide (amino acid residues 4-9). Additionally the polar/charged amino acid residues about the N- and C-termini of the peptide are able to interact with the zwitterionic lipid head groups, reinforcing the insertion of the peptide into the bilayer.

The addition of signiferin 1 to DMPC MLV showed very different effects on lipid dynamics and ordering relative to than riparin 1, despite the peptides sequence homology and similar secondary structures. The ^{31}P NMR revealed a very broad powder pattern, the

major contributing powder pattern had a CSA of approximately -41 ppm, and the remaining superimposed powder patterns had CSAs ranging from approximately -41 to -37 ppm. This indicates some degree of lateral phase separation within the lipid bilayer, and a range of altered head group ordering and/or orientation in the presence of signiferin 1. Interestingly, the ^2H NMR revealed only a major change in acyl chain order toward the head group region of the acyl chains. This effect has been observed in the solid state NMR of lipid suspensions with antimicrobial peptides that interact via a surface interaction (carpet mechanism), such as fallaxidin 4.1a in zwitterionic MLV suspensions (see chapter 6) [82].

These findings can be attributed to the fact that signiferin contains a polar amino acid Tyr6, that can participate in hydrogen bonding or ion dipole interactions with the zwitterionic PC head groups on the surface of the bilayer. This can increase the lateral spacing of the lipid headgroups and affect their mobility. However, complete insertion of the loop region of the peptide into the core of the bilayer may be inhibited under the conditions used. So, the solid state NMR of signiferin 1 in DMPC MLVs shows that signiferin 1 appears to accumulate on the surface of zwitterionic membranes.

An illustration of the interactions of rothein 1, riparin 1 and signiferin 1 with zwitterionic membranes based on the solid-state NMR evidence is shown in Figure 7.16.

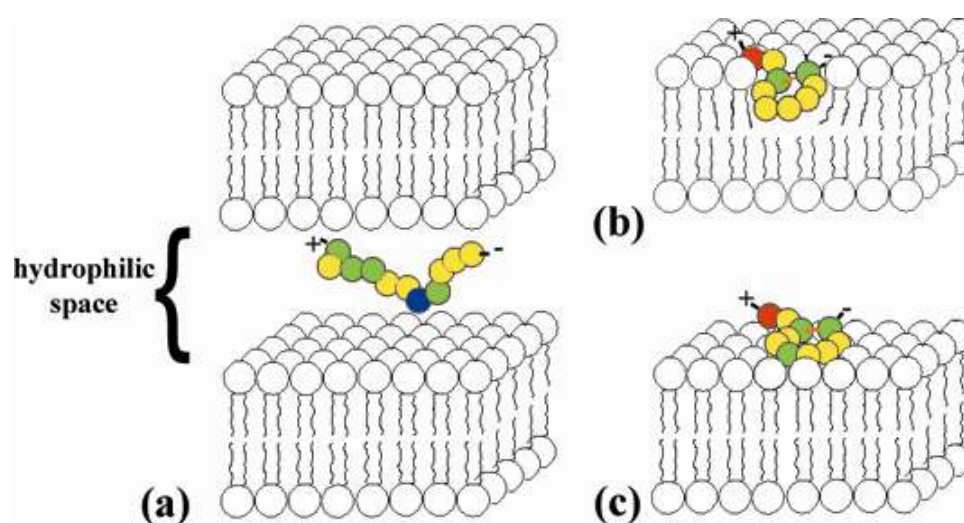


Figure 7.16 Static interactions from the addition of (a) rothein 1, (b) riparin 1 and (c) signiferin 1 to zwitterionic phospholipid bilayers.

The 3-dimensional conformations of the neuropeptides on a biological membrane surface are important determinants for investigating their interactions with bilayers. Rothein 1 has an extended structure with a small degree of fine structure throughout the central region of the peptide. In contrast, the 2 selected peptides from the *Crinia* species have ‘turn’ structures reinforced by a single disulfide bond. Each of the amphibian neuropeptides in this study has a unique secondary structure in membrane mimicking solvent systems, as previously determined using 2D NMR [50, 83].

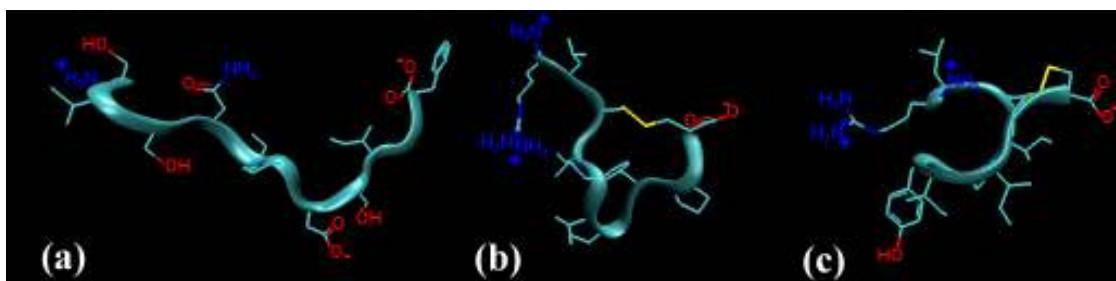


Figure 7.17 Ribbon representations of the energy minimised average structures of (a) rothein 1, (b) riparin 1 and (c) signiferin 1. Structures were determined previously using 2D NMR [50, 83].

The lack of defined structure of rothein 1 in TFE/H₂O reflects the marginal effects it has on lipid conformation and mobility as observed with solid state NMR. The structure of riparin 1 has defined polar/charged and non-polar regions across the termini and central regions loop regions, respectively. The flexibility of the hydrophobic loop region illustrates how it could easily insert into the hydrophobic core of the bilayer. In contrast to riparin 1, signiferin 1 clearly shows a bend in the loop region, that directs the polar hydroxyl group of the central tyrosine residue toward one face of the peptide (Figure 7.17c), and the remaining hydrophobic residues toward the other face. This bend in the hydrophobic region illustrates that signiferin 1 is less likely to insert the entire ‘loop’ region within the hydrophobic core, but remain on the surface with the hydrophobic residues directed toward the bilayer interior. So, the peptide partially inserts disrupting phospholipid headgroups the upper parts of the acyl chains at the bilayer surface.

The hydrophobicity, and net charge of the peptides are very important factors to consider when investigating the interactions with phospholipid bilayers prior to receptor binding. The sequences of the three selected amphibian neuropeptides are distinctly different, at physiological pH rothein 1 has a net charge of -1, and a large percentage of polar amino acid residues (55 %). In contrast, riparin 1 and signiferin 1 have a net charge of +1 at physiological pH, and a low percentage of polar amino acid residues (30 and 40 %, respectively). The net charge and hydrophobicities of rothein 1, riparin 1 and signiferin 1 are shown in Table 7.10.

Table 7.10 Smooth muscle and splenocyte proliferation activities of CCK2R active peptides.

NOTE:
This figure/table/image has been removed
to comply with copyright regulations.
It is included in the print copy of the thesis
held by the University of Adelaide Library.

7.3.3 Additional remarks

The varied activities of the selected amphibian neuropeptides and their analogues have been explained in part by their interactions with biological membranes, secondary structure, and key functional groups required for binding within the CCK2 receptor binding site. Rothein 1 appears to have very little interaction with neutral membranes, riparin 1 inserts itself into the interior of the membrane, and signiferin 1 accumulates on the surface. Signiferin 1 is the most potent of the peptides in terms of CCK2R activity. This may be reflected by the peptides ability to accumulate on the surface of a biological membrane, increasing the probability of signiferin 1 interacting with a CCK2 receptor site. Riparin 1 has only modest activity, perhaps due to: (i) to the peptide integrating into the membrane structure, and (ii) the lack of a tyrosine residue that has been shown to be important for CCK-8ns binding to the CCK2 receptor [480-482].

In addition to polar and hydrophobic interactions, the membrane potential of a cell is an important factor to consider with respect to membrane assisted binding of hormones to target receptors. Smooth muscle contraction via CCK2 activation occurs indirectly via CCK2 receptors on cholinergic nerves in the myenteric plexus, causing the release of acetylcholine followed by activation of muscarinic receptors on smooth muscle. Neurons are known to have a resting membrane potential of approximately -70 mV [9]. The activation of CCK2 receptors occurs directly on the cellular surfaces of Jurkat lymphoblasts and T-lymphocytes, causing splenocyte proliferation [489-491]. The membrane potentials of lymphoblasts and T-lymphocytes are in the order of -58 mV [492]. Riparin1 and signiferin 1 both contain a positive net charge at physiological pH, this may enhance their binding to both cholinergic neurons and splenocytes. In contrast, rothein 1 has a net negative charge at physiological pH. Hence the peptide may not bind as easily such cells, resulting in lower biological activities relative to riparin 1 and signiferin 1.

Clearly this collection of works with amphibian neuropeptides is a work in progress, and the theorised interactions of the peptides with biological membranes would need to be studied in real time to verify their mode of action upon approaching a membrane surface. Methods such as QCM-D, DPI and SPR could be utilised for this purpose using membrane bilayer films formed on solid surfaces, as performed previously in studies of antimicrobial peptides with membranes [325, 332, 437, 493].

7.4 Experimental

7.4.1 Preparation of synthetic rothein 1 peptides

The rothein 1 peptides were synthesised by Mimotopes (Clayton, Victoria, Australia) using L-amino acids via the standard *N*- α -Fmoc method [376]. The purity of the synthesised peptides was shown to be $\geq 95\%$ and $\geq 90\%$ for rothein 1.3 and rothein 1.4 respectively, as determined by HPLC and ESI-MS. Rothein 1.4 (10.0 mg, 8.6 μ mole) was dissolved in *d*₃-TFE and H₂O (700 μ l; 1:1, v/v), giving a final concentration of 12.4 mM, and a pH of 1.5. The same preparative procedure was used for the rothein 1.5 sample, giving a pH of 2.4. The pH was recorded using a Eutech Cyberscan pH 500 meter with a thin stem (183 x 4 mm) AEP 331 glass body pH probe. The pH was not corrected for either sample.

7.4.2 NMR Spectroscopy

NMR spectra were acquired using a Varian Inova-600 NMR spectrometer with a ¹H frequency of 600 MHz, at 25 °C. The ¹H NMR resonances were referenced to the methylene protons (3.918 ppm) of the residual unlabelled TFE. 2-Dimensional TOCSY, NOESY and DQF-COSY and ¹H NMR experiments were conducted for each rothein 1 peptide. Presaturation was used to suppress the water resonance by centering the transmitter frequency on the water resonance and applying a low power continuous *rf* pulse during the relaxation delay [294]. In the DQF-COSY experiment, gradient methods were used for water suppression [494].

Each 2D NMR experiment typically consisted of 256 *t*₁ increments with 32 time-averaged scans per increment. The FID in *t*₂ consisted of 2048 data points over a spectral width of 6154.3 Hz. The NOESY spectra were acquired with mixing times of 150 or 250 ms, and the TOCSY experiments with a spin-lock time of 70 ms. High resolution 1D ¹H NMR spectra were also acquired with 0.125 Hz per digital point resolution, to observe ³J_{NH α H} coupling constants.

All of the resulting 2D NMR spectra were processed on a Sun Microsystems Ultra Sparc 1/170 workstation using VNMR software (VNMRJ version 6.1A). The data matrices were multiplied by a Gaussian function in both dimensions and zero-filled to 2048 data points prior to Fourier transformation. The resulting processed 2D NMR matrices consisted of 2048 x 2048 real data points. The $^3J_{\text{NH}\alpha\text{H}}$ values were determined from the high resolution 1D ^1H NMR spectra.

7.4.3 Cross-peak assignment and structure calculations

The ^1H resonances in the 2D NMR spectra were assigned using Sparky software (version 3.106) via the standard sequential assignment procedure [229]. For each symmetric pair of cross-peaks, the peak of larger volume was used in the conversion to a distance restraint [400]. Assignment of distance restraints of methylene and isopropyl groups was achieved using the floating chirality method [269]. $^3J_{\text{NH}\alpha\text{H}}$ coupling constants were measured from the high resolution 1D NMR spectra and converted to backbone angle restraints as follows: $^3J_{\text{NH}\alpha\text{H}} < 5 \text{ Hz}$, $\phi = -60^\circ \pm 30^\circ$, $5 \text{ Hz} < ^3J_{\text{NH}\alpha\text{H}} < 6 \text{ Hz}$, $\phi = -60^\circ \pm 40^\circ$, $^3J_{\text{NH}\alpha\text{H}} > 8 \text{ Hz}$, $\phi = -120^\circ \pm 40^\circ$

Structures were generated from random starting conformations using the standard RMD and SA protocol of ARIA (version 1.2) [401] implemented with CNS (version 1.1) software [256]. For each of the 8 iterations, an initial 60 structures were generated. The 20 lowest potential energy structures (from the final 60 of the 8th iteration) were selected for analysis. The program MOLMOL (version 2k.2) [404] was used to display the overlaid backbone atoms of the 20 lowest energy structures and VMD software (version 1.8.2) [405] was used to display the energy minimised average structures.

7.4.4 Sample Preparation of MLV suspensions

The peptides rothein 1, riparin 1, and signiferin 1 were synthesised with L-amino acids using the standard N- α -Fmoc method, by GenScript Corp. (Piscataway, NJ) [376] and shown to have greater than 90 % purity, as determined by HPLC and ESI-MS. Phospholipids were obtained from Avanti Polar Lipids (Alabaster, AL) and used without further purification. Peptides (~2.5 mg, 1 μmole) were co-dissolved with either a 1:1

molar mixture of d_{54} -DMPC/DMPC or a 2:2:1 molar mixture of d_{54} -DMPC/DMPC/DMPG (~ 7 mg, 10 μ mole) in 700 μ L of $\text{CHCl}_3/\text{MeOH}$ (9:1 v/v); producing a lipid/peptide ratio of 10:1. The organic solvent was removed via rotary evaporation (250 mbar, 30 °C) to form a thin lipid/peptide film in a round bottom flask, and the samples lyophilised overnight. The dried samples were hydrated with 100 μ l of 50 mM MOPS (150 mM NaCl, pH 7) buffer, subjected to five freeze thaw/vortex cycles, and centrifuged (1 minute, 4000 rpm). The resultant viscous translucent suspensions were transferred to 5 mm NMR tubes for NMR analysis. The control samples were prepared in a similar manner, without the addition of peptide.

7.4.5 ^{31}P solid-state NMR

All solid-state NMR experiments were performed on a Varian (Palo Alto, CA) Inova-300 spectrometer, using a 5 mm Doty (Columbia, SC) MAS probe at 30 °C. Static proton decoupled ^{31}P NMR spectra were obtained at an operating frequency of 121.5 MHz using a Hahn spin-echo pulse sequence with a 5.8 μ s 90° pulse, 62 μ s interpulse delay and a 4 s recycle delay. ^{31}P NMR spectra were averaged over 60,000 scans at a spectral width of 125 kHz with 100 Hz exponential line broadening upon processing. Overlapped ^{31}P line shapes were deconvoluted using the DMFIT program, employing the ‘CSA static’ model [440].

7.4.6 ^2H solid-state NMR

^2H NMR spectra were obtained at an operating frequency of 46.1 MHz using a quadrupolar-echo pulse sequence with a 3.8 μ s 90° pulse, 40 μ s interpulse delay and a 0.5 s recycle delay. ^2H NMR spectra were averaged over 160,000 scans at a spectral width of 500 kHz with 100 Hz exponential line broadening. The overlapping Pake doublets from the unoriented deuterium spectra were ‘dePaked’ using single value decomposition [313, 346, 452], numerical calculations were administered by GNU Scientific library v.1.11 [453], and graphical outputs generated with gnuplot v4.2.4 [454].

Chapter 8

Summary

8.1 The peptide profiles of two *Litoria ewingii* populations

The peptide profiles of seven specimens of *Litoria ewingii* taken from Renmark, South Australia, were successfully analysed on a monthly basis using HPLC, ESMS and Edman sequencing. The peptide profile of the *L. ewingii* included a narrow spectrum antibiotic ewingiin 1.1, a unique pentapeptide tryptophyllin 6.3, and 3 unique peptides with unknown biological activity, ewingiins 2.2, 2.3 and 2.4. The peptide profiles of the *L. ewingii* population showed no significant seasonal variance throughout the duration of the study.

A comparison of the peptide profile of the Renmark *L. ewingii* population (population B) to a previously studied population from the Adelaide hills, South Australia (population A), revealed a significant difference in the peptides within the skin secretions. Each *L. ewingii* population contained 6 peptides within their peptide profiles, and only 2 were common to both species: ewingiin 1 and ewingiin 1.1. The peptide profile of population B showed one major pentapeptide, tryptophyllin 6.3. This peptide had 80% sequence homology (one amino acid residue difference) with tryptophyllin 6.2 isolated from population A. There were also 3 peptides: ewingiins 2.2, 2.3, and 2.4 isolated from population B that exhibit sequence homology (79-93 %) with the peptide ewingiin 2.1 from population A. The most interesting of the differences in peptide profiles between the populations, was a lack of the peptide caerin 1 in the peptide profile of population B. Ewingiins 2.2, 2.3 and 2.4 are yet to be tested for antimicrobial activity, though they do not contain any amino acid residues such as lysine, arginine and histidine that are commonly found in the sequences of antimicrobial amphibian peptides.

The results from this study show that geographical isolation of these 2 *L. ewingii* populations has lead to mutations in the DNA encoding the host-defence skin peptides over an extended period of time. In addition to the peptide profiles, close examination of

specimens from each *L. ewingii* population revealed slight differences in morphology between them, namely black spots on the posterior surfaces of the thighs only found on specimens within the Adelaide hills region. The collective evidence from this study suggests the populations require taxonomic reclassification, and further studies into the DNA of each population would be required to support this. This profiling technique can be applied as an indicator of evolutionary divergence for many amphibian species.

8.2 The solution structures meucin-13 and meucin-18

The solution structures of meucin-13 and meucin-18, antimicrobial peptides isolated from the venom of the ‘lesser Asian scorpion’ *Mesobuthus eupeus mongolicus* were determined, to classify them and elucidate their mechanism(s) of activity. Activity tests showed that meucin-18 was the more active of the two (~ 2 fold in most cases), and both peptides were cytolytic toward several Gram-positive and Gram-negative bacteria, as well as strains of yeasts and fungi. Using 2-dimensional NMR spectroscopy and RMD calculations, both peptides were found to adopt α -helical structures, in a d_3 -TFE/H₂O solvent system.

The solution structure of meucin-13 was helical about the central regions from residues 6-13, however the NMR also showed significant flexibility elsewhere, notably due to the presence of glycines within the amino acid sequence, and a lack of polar or charged side chains. The solution structure of meucin-18 was helical across residues 5-17, with flexibility about the N-terminal region of the peptide. The presence of cationic lysines in the amino acid sequences of the meucin peptides meant that each peptide could be classified as a cationic helical peptide. Hence, the meucin peptides are likely to form pores within anionic microbial membranes. The greater pore forming activity of meucin-18 can be attributed to the greater length of the helical region, a greater proportion of polar amino acid residues, and net positive charge at pH 7. The understanding of how these structural characteristics affect the antimicrobial activities of peptides provides the basis for designing peptide based antibiotics.

8.3 Membrane interactions of the antimicrobial peptide fallaxidin 4.1a

Recently, the amide modification of an antimicrobial peptide isolated from *Litoria fallax*, fallaxidin 4.1a, has been shown to have potent antimicrobial activity against a number of Gram-positive bacteria. Solid state NMR was used to determine the effects fallaxidin 4.1a on zwitterionic d_{54} -DMPC and anionic 2:1 d_{54} -DMPC/DMPG MLVs, as models for eukaryotic and prokaryotic membranes respectively. The objective of the study was to determine if fallaxidin 4.1a had a selective effect depending on the membrane surface charge, and to determine the mechanism of its antimicrobial activity. In d_{54} -DMPC alone, fallaxidin 4.1a caused a decrease in the ^{31}P CSA indicating some disordering of the phospholipid head groups, and the ^2H NMR data indicated that the peptide caused disorder toward the upper regions of the acyl chains. In d_{54} -DMPC/DMPG, two ^{31}P CSA line shapes were observed, the minor CSA due to the PG enriched component decreased relative to the control, indicating fallaxidin 4.1a had caused a degree of lateral phase separation, with a preference toward anionic DMPG head groups. In addition the ^2H NMR data revealed an increase in order across the entire acyl chains of the d_{54} -DMPC component, indicating less space for acyl chain movement as a result of transmembrane insertion and pore formation.

QCM-D experiments with DMPC and 2:1 DMPC/DMPG SLBs complemented the results of the solid state NMR experiments. It was found that fallaxidin 4.1a had a detergent like effect toward zwitterionic membranes, causing destruction of the SLBs at concentrations $\geq 5 \mu\text{M}$. In contrast, the peptide underwent transmembrane insertion within anionic SLBs at concentrations $\geq 1 \mu\text{M}$. Collectively the results show that fallaxidin 4.1a has great potential as an antibiotic peptide as it produces very different effects when interacting with zwitterionic and anionic membranes.

8.4 The solutions structures of two analogues of rothein 1 and the membrane interactions of CCK2 active amphibian neuropeptides

Recently, a number of analogues of rothein 1, have been shown to bind to CCK2 receptors, yet can have quite different biological activities. Activity tests showed that 2 of the analogues, rothein 1.3 and rothein 1.4 induce smooth muscle contractions at 10^{-8} M

concentrations, yet do not induce lymphocyte proliferation. In contrast rothein 1 has been shown to induce lymphocyte proliferation at 10^{-5} M, yet did not show any smooth muscle activity. The 3-D solution structures of alanine substituted rothein 1.3 (Glu7 to Ala7) and 1.4 (Ser8 to Ala8) were generated from 2-D NMR experiments, to determine whether any key structural features can provide reasoning for differences in their biological activities relative to the native peptide.

Each rothein peptide had a similar 3-D structure in TFE/H₂O, and the majority of the structures were largely extended with some fine structure across the central parts of the peptides. Analysis of the backbone dihedral angles of rothein 1.3 revealed an ‘open’ β -turn structure about residues 5-10, similar to the 3-D structure of rothein 1. The solution structure of rothein 1.4 was the most extended and random of the peptide structures, and the dihedral angles across residues 4-8 indicated an extended ‘ β -strand’ type structure. The difference in the biological activities of rothein 1 and its’ selected analogues, could not be defined directly from their flexible 3-D solution structures. Differences in hydrophobicity, net charge, and non-covalent interactions between the peptides and the CCK2 receptor site are additional contributing factors to consider. Further studies to investigate peptide interactions with cellular membranes prior docking to the receptor, and modelling of peptides docking the CCK2 receptor site, may provide further reasoning for the peptides biological activities.

Recently, the 3-D solution structures and biological activities of riparin 1 and signiferin 1 have been studied. In a similar way to the rothein 1 peptides, each peptide has been shown to bind to mammalian CCK2 receptors (on guinea pig ileum and mouse splenocytes), yet have different biological activities. Activity tests showed that riparin 1 induced splenocyte proliferation at $\leq 10^{-7}$ M, yet did not cause significant smooth muscle contraction of guinea pig ileum. Signiferin 1 caused smooth muscle contraction at a low concentration of 10^{-9} M, yet only caused lymphocyte proliferation at a concentration $\geq 10^{-5}$ M. The activities of the peptide were widely varied considering the high degree of sequence homology between mouse and guinea pig CCK2 receptors. It was proposed that membrane assisted binding of neuropeptides to receptors may reflect the differing

biological activities of the amphibian neuropeptides. The study involved using ^{31}P and ^2H solid-state NMR to analyse the membrane interactions of amphibian neuropeptides rothein 1, riparin 1, and signiferin 1 with phospholipid bilayers comprised of deuterated DMPC.

The solid-state NMR of the addition of rothein 1 to DMPC MLV revealed very little effect on the mobility of phospholipid headgroups, and the ordering of the deuterated acyl chains of d_{54} -DMPC. Rothein 1 is an anionic peptide (at pH 7) with many polar amino acid residues, the low lymphocyte activity and lack of smooth muscle activity is most likely due to a weak binding affinity for phospholipid membranes.

Solid-state NMR revealed the peptides riparin 1 and signiferin 1 showed a significant effect on the mobility of phospholipid membranes. Structural studies of the disulfide peptides show they are cationic at the N-terminal region, polar at the C-terminal region, with distinct β -turn structures directing hydrophobic residues toward the exterior of the peptide. The addition of signiferin 1 and riparin 1 to DMPC bilayers caused decreased CSAs in the ^{31}P spectra relative to the control. The ^2H spectra showed a decrease in order toward the upper part of the acyl chain for signiferin 1, and a large decrease across the majority of the acyl chain for riparin 1. This indicated that signiferin caused a high degree of disorder within the headgroups and upper acyl chains of DMPC bilayers, as a result of the peptide coating the surface and/or partially inserting into the bilayer, and riparin 1 appears to insert itself deep in to hydrophobic region of the DMPC bilayer causing significant lateral spacing between lipids, and disordering of acyl chains.

The results suggest that a combination of hydrophobic and electrostatic interactions drive the *Crinia* peptides toward cellular membrane surfaces, which may explain their greater biological activities relative to rothein 1. The conformations of the peptides and the presence of key residues, such as tyrosine in the sequence of signiferin 1, are also important factors to be considered. Membrane association is a significant step to be considered in the receptor binding of neuropeptides, and further studies using real time measurements could provide complementary evidence to support this. With further

development in this field, hormone peptides can be designed for specified cellular receptors based on both their structure and affinity for cellular membranes.

8.5 Conclusion

The collection of research presented in this thesis demonstrates how a range of biologically active peptides can be isolated and characterised using chromatography and mass spectrometry. A Variety if NMR based methods has been employed to probe the structure and membrane interactions of a number of peptides. The detailed studies assist in showing the mechanisms of how peptides interact at a molecular level, and provide innovative ways of understanding their biological activities.

References

1. Lee, N. P. & Arriola, E. R. (1999) Poison ivy, oak, and sumac dermatitis., *West. J. Med.* *171*, 354-355.
2. Sheumack, D., Howden, M., Spence, I. & Quinn, R. (1978) Maculotoxin: a neurotoxin from the venom glands of the octopus *Hapalochlaena maculosa* identified as tetrodotoxin, *Science*. *199*, 188-189.
3. Habermehl, G. G. (1981) *Venomous animals and their toxins*, Springer-Verlag, Berlin.
4. Markland, F. S. (1998) Snake venoms and the hemostatic system, *Toxicon*. *36*, 1749-1800.
5. Rash, L. D. & Hodgson, W. C. (2002) Pharmacology and biochemistry of spider venoms, *Toxicon*. *40*, 225-254.
6. Polis, G. A. (1990) *The Biology of Scorpions*, Stanford University Press, California.
7. Frokjaer, S. & Hovgaard, L. (2000) *Pharmaceutical Formulation Development of Peptides and Proteins*, Taylor and Francis, London.
8. Rang, H. P. & Lamb, P. (2003) *Pharmacology*, 5th edn, Churchill Livingstone, Edinburgh.
9. Campbell, N. A. (1999) *Biology*, 4th edn, Benjamin Cummings Pub. Co., California.
10. Sherwood, L. (2004) *Human Physiology. From Cells to Systems*, 5th edn, Thomson Learning Inc., Minneapolis.
11. Wold, F. & Moldave, K. (1984) *Post-Translational Modifications*, Academic Press, Orlando.
12. Mann, M. & Jensen, O. N. (2003) Proteomic analysis of post-translational modifications, *Nature Biotechnol.* *21*, 255-261.
13. Giovannini, M. G., Poulter, L., Gibson, B. W. & Williams, D. H. (1987) Biosynthesis and degradation of peptides derived from *Xenopus laevis* prohormones, *Biochem. J.* *243*, 113-120.
14. Alberts, B. (2008) *Molecular biology of the cell*, 5th edn, Garland Science, New York.
15. Zhou, M., Liu, Y., Chen, T., Fang, X., Walker, B. & Shaw, C. (2006) Components of the peptidome and transcriptome persist in *lin wa pi*: The dried skin of the Heilongjiang

- brown frog (*Rana amurensis*) as used in traditional Chinese medicine, *Peptides*. 27, 2688-2694.
16. Lee, H. M. & Chen, K. K. (1951) The occurrence of nor-epinephrine in chinese toad venom, *J. Pharmac. Exp. Ther.* 102, 286-290.
17. Lazarus, L. H. & Attila, M. (1993) The toad, ugly and venomous, wears yet a precious jewel in his skin, *Prog. Neurobiol.* 41, 473-507.
18. Mensah-Dwumah, M. & Daly, J. W. (1978) Pharmacological activity of alkaloids from poison-dart frogs (Dendrobatidae), *Toxicon*. 16, 189-194.
19. Erspamer, V., Erspamer, G. F., Severini, C., Potenza, R. L., Barra, D., Mignogna, G. & Bianchi, A. (1993) Pharmacological studies of 'sapo' from the frog *Phyllomedusa bicolor* skin: A drug used by the Peruvian Matses Indians in shamanic hunting practices, *Toxicon*. 31, 1099-1111.
20. Daly, J., Caceres, J., Moni, R., Gusovsky, F., Moos, M., Seamon, K., Milton, K. & Myers, C. (1992) Frog secretions and hunting magic in the upper Amazon: Identification of a peptide that interacts with an adenosine receptor, *Proc. Natl. Acad. Sci.* 89, 10960-10963.
21. Bick, R. J., Poindexter, B. J., Sweney, R. R. & Dasgupta, A. (2002) Effects of Chan Su, a traditional Chinese medicine, on the calcium transients of isolated cardiomyocytes: Cardiotoxicity due to more than Na, K-ATPase blocking, *Life Sci.* 72, 699-709.
22. Erspamer, V., Bertaccini, G. & Cei, J. M. (1962) Occurrence of an eledoisin-like polypeptide (physalaemin) in skin extracts of *Physalaemus fuscumaculatus*, *Experientia*. 18, 562-563.
23. Erspamer, V., Bertaccini, G. & Cei, J. M. (1962) Occurrence of bradykinin-like substances in the amphibian skin, *Experientia*. 18, 563-564.
24. Cei, J. M., Erspamer, V. & Rosechini, M. (1967) Taxonomic and evolutionary significance of biogenic amines and polypeptides occurring in amphibian skin. I. Neotropical *leptodactylid* frogs, *Syst. Zool.* 16, 328-342.
25. Cunha Filho, G. A., Schwartz, C. A., Resck, I. S., Murta, M. M., Lemos, S. S., Castro, M. S., Kyaw, C., Pires, J., Osmino R. & Leite, J. R. S. (2005) Antimicrobial activity of the bufadienolides marinobufagin and telocinobufagin isolated as major components from skin secretion of the toad *Bufo rubescens*, *Toxicon*. 45, 777-782.
26. Daly, J. W. (1998) Thirty years of discovering arthropod alkaloids in amphibian skin, *J. Nat. Prod.* 61, 162-172.

27. Erspamer, V. & Melchiorri, P. (1980) Active polypeptides: From amphibian skin to the gastrointestinal tract and brain of mammals, *Trends Pharmacol. Sci.* 1, 391-395.
28. Pukala, T. L., Bowie, J. H., Maselli, V. M., Musgrave, I. F. & Tyler, M. J. (2006) Host-defense peptides from the glandular secretions of amphibians: structure and activity, *Natural Product Reports.* 23, 368-393.
29. Jacob, L. S. & Zasloff, M. (1994) Potential therapeutic applications of magainins and other antimicrobial agents of animal origin. in *Antimicrobial Peptides. Ciba Foundations Symposium 186* (Marsh, J. & Goode, J. A., eds) pp. 197-223, John Wiley and Sons, London.
30. Grenard, S. (1994) Frogs and toads in *Medical Herpetology* pp. 2-127, Reptiles and Amphibian Magazine, Pottsville.
31. Baker, M. A., Maloy, W. L., Zasloff, M. & Jacob, L. S. (1993) Anticancer efficacy of magainin 2 and analogue peptides, *Cancer Res.* 53, 3052-3057.
32. Tyler, M. J. (1987) Frog and cane toad skin secretions in *Toxic Plants and Animals. A Guide for Australia.* (Covacevich, J., ed) pp. 329-339, Queensland Museum, Brisbane.
33. Anastasi, A., Erspamer, V. & Endean, R. (1968) Isolation and amino acid sequence of caerulein, the active decapeptide of the skin of *Hyla caerulea*, *Arch. Biochem. Biophys.* 125, 57-68.
34. Bannon, A. W., Decker, M. W., Holladay, M. W., Curzon, P., Donnelly-Roberts, D., Puttfarcken, P. S., Bitner, R. S., Diaz, A., Dickenson, A. H., Porsolt, R. D., Williams, M. & Arneric, S. P. (1998) Broad-spectrum, non-opioid analgesic activity by selective modulation of neuronal nicotinic acetylcholine receptors, *Science.* 279, 77-81.
35. Zasloff, M. (1987) Magainins, a class of antimicrobial peptides from *Xenopus* skin: Isolation, characterization of two active forms, and partial cDNA sequence of precursor, *Proc. Natl. Acad. Sci.* 84, 5449-5453.
36. Zasloff, M., Martin, B. & Chen, H. (1988) Antimicrobial activity of synthetic magainin peptides and several analogues, *Proc. Natl. Acad. Sci.* 85, 910-913.
37. Bowie, J. H., Chia, B. C. S. & Tyler, M. J. (1998) Host defence peptides from the skin glands of Australian amphibians: A powerful chemical arsenal, *Pharmacol. News.* 5, 16-21.
38. Pouny, Y., Rapaport, D., Mor, A., Nicolas, P. & Shai, Y. (1992) Interaction of antimicrobial dermaseptin and its fluorescently labeled analogues with phospholipid membranes, *Biochem.* 31, 12416-12423.

39. Boman, H. G. (1995) Peptide antibiotics and their role in innate immunity, *Ann. Rev. Immunol.* *13*, 91-92.
40. Dockray, G. & Hopkins, C. (1975) Caerulein secretion by dermal glands in *Xenopus laevis*, *J. Cell Biol.* *64*, 724-733.
41. Toledo, R. C. & Jared, C. (1995) Cutaneous granular glands and amphibian venoms, *Comp. Biochem. Physiol. A.* *111*, 1-29.
42. Carraway, R. E. & Cochrane, D. E. (1987) *J. Biol. Chem.* *261*, 15886-15889.
43. Erspamer, V., Erspamer, G. F., Mazzanti, G. & Endean, R. (1984) Active peptides in the skins of one hundred amphibian species from Australia and Papua New Guinea, *Comp. Biochem. Physiol. C.* *77*, 99-108.
44. Tyler, M. J., Stone, D. J. M. & Bowie, J. H. (1992) A novel method for the release and collection of dermal, glandular secretions from the skin of frogs, *J. Pharm. Toxicol. Methods.* *28*, 199-200.
45. Resnick, N. M., Maloy, W. L., Guy, H. R. & Zasloff, M. (1991) A novel endopeptidase from *Xenopus* that recognises α -helical secondary structure, *Cell.* *66*, 541-554.
46. Wegener, K. L., Wabnitz, P. A., Carver, J. A., Bowie, J. H., Chia, B. C. S., Wallace, J. C. & Tyler, M. J. (1999) Host defence peptides from the skin glands of the Australian Blue Mountains tree frog *Litoria citropa*. Solution structure of the antibacterial peptide citropin 1.1, *Eur. J. Biochem.* *265*, 627-637.
47. Frost, D. R. (2009) Amphibian Species of the World: an Online Reference. Version 5.3, American Museum of Natural History, New York.
<http://research.amnh.org/herpetology/amphibia/>
48. Apponyi, M. A., Pukala, T. L., Brinkworth, C. S., Maselli, V. M., Bowie, J. H., Tyler, M. J., Booker, G. W., Wallace, J. C., Carver, J. A., Separovic, F., Doyle, J. & Llewellyn, L. E. (2004) Host-defence peptides of Australian anurans: Structure, mechanism of action and evolutionary significance, *Peptides.* *25*, 1035-1054.
49. Pukala, T. L., Urathamakul, T., Watt, S. J., Beck, J. L., Jackway, R. J. & Bowie, J. H. (2008) Binding studies of nNOS-active amphibian peptides and Ca^{2+} calmodulin, using negative ion electrospray ionisation mass spectrometry, *Rapid Commun. Mass Spectrom.* *22*, 3501-3509.
50. Jackway, R. J., Pukala, T. L., Maselli, V. M., Musgrave, I. F., Bowie, J. H., Liu, Y., Surinya-Johnson, K. H., Donnellan, S. C., Doyle, J. R., Llewellyn, L. E. & Tyler, M. J. (2008) Disulfide-containing peptides from the glandular skin secretions of froglets of the genus *Crinia*: Structure, activity and evolutionary trends, *Regul. Pept.* *151*, 80-87.

51. Perriman, A. W., Apponyi, M. A., Buntine, M. A., Jackway, R. J., Rutland, M. W., White, J. W. & Bowie, J. H. (2008) Surface movement in water of splendipherin, the aquatic male sex pheromone of the tree frog *Litoria splendida*, *FEBS J.* 275, 3362-3374.
52. Rozek, T., Bowie, J. H., Wallace, J. C. & Tyler, M. J. (2000) The antibiotic and anticancer active aurein peptides from the Australian bell frogs *Litoria aurea* and *Litoria raniformis*. Part 2. Sequence determination using electrospray mass spectrometry, *Rapid Commun. Mass Spectrom.* 14, 2002-2011.
53. Wabnitz, P. A., Bowie, J. H., Tyler, M. J., Wallace, J. C. & Smith, B. P. (2000) Differences in the skin peptides of the male and female Australian tree frog *Litoria splendida* - the discovery of the aquatic male sex pheromone splendipherin, together with Phe8 caerulein and a new antibiotic peptide caerin 1.10, *Eur. J. Biochem.* 267, 269-275.
54. Stone, D. J. M., Waugh, R. J., Bowie, J. H., Wallace, J. C. & Tyler, M. J. (1993) Peptides from Australian frogs. The structures of the caerins from *Litoria caerulea*, *J. Chem. Res. (S)*. 138, (M) 910-936.
55. Waugh, R. J., Stone, D. J. M., Bowie, J. H., Wallace, J. C. & Tyler, M. J. (1993) Peptides from Australian frogs. The structures of the caerins and caeridins from *Litoria gilleni*, *J. Chem. Res. (S)*. 139, (M) 937-961.
56. Steinborner, S. T., Waugh, R. J., Bowie, J. H., Wallace, J. C., Tyler, M. J. & Ramsay, S. L. (1997) New caerin antibacterial peptides from the skin glands of the Australian tree frog *Litoria xanthomera*, *J. Pept. Sci.* 3, 181-5.
57. Steinborner, S. T., Currie, G. J., Bowie, J. H., Wallace, J. C. & Tyler, M. J. (1998) New antibiotic caerin 1 peptides from the skin secretion of the Australian tree frog *Litoria chloris*. Comparison of the activities of the caerin 1 peptides from the genus *Litoria*, *J. Pept. Res.* 51, 121-126.
58. Erspamer, V. (1994) Bioactive secretions in the amphibian integument in *Amphibian Biology: The Integument* (Heatwole, H. & Barthalmus, G. T., eds) pp. 178-350, Surrey, Beatty and Sons, Chipping Norton.
59. Wegener, K. L., Brinkworth, C. S., Bowie, J. H., Wallace, J. C. & Tyler, M. J. (2001) Bioactive dahlein peptides from the skin secretions of the Australian aquatic frog *Litoria dahlii*. Sequence determination by electrospray mass spectrometry, *Rapid Commun. Mass Spectrom.* 15, 1726-1734.
60. Wabnitz, P. A., Bowie, J. H., Wallace, J. C. & Tyler, M. J. (1999) Peptides from the skin glands of the Australian buzzing tree frog *Litoria electrica*. Comparison with the skin peptides of the red tree frog *Litoria rubella*, *Aust. J. Chem.* 52, 639-645.

61. Bradford, A. M., Raftery, M. J., Bowie, J. H., Wallace, J. C. & Tyler, M. J. (1993) Peptides from Australian frogs - the structures of the dynastins from *Limnodynastes salmini* and fletcherin from *Limnodynastes fletcheri*, *Aust. J. Chem.* **46**, 1235-1244.
62. Waugh, R. J., Raftery, M. J., Bowie, J. H., Wallace, J. C. & Tyler, M. J. (1996) The structures of the frenatin peptides from the skin secretions of the giant tree frog, *Litoria infrafrenata*, *J. Pept. Sci.* **2**, 117-124.
63. Doyle, J., Llewellyn, L. E., Brinkworth, C. S., Bowie, J. H., Wegener, K. L., Rozek, T., Wabnitz, P. A., Wallace, J. C. & Tyler, M. J. (2002) Amphibian peptides that inhibit neuronal nitric oxide synthase: The isolation of lesueurin from the skin secretion of the Australian stony creek frog *Litoria lesueuri*, *Eur. J. Biochem.* **269**, 100-109.
64. Rozek, T., Waugh, R. J., Steinborner, S. T., Bowie, J. H., Tyler, M. J. & Wallace, J. C. (1998) The maculatin peptides from the skin glands of the tree frog *Litoria genimaculata* - a comparison of the structures and antibacterial activities of maculatin 1.1 and caerin 1.1, *J. Peptide Sci.* **4**, 111-115.
65. Brinkworth, C. S., Bowie, J. H., Tyler, M. J. & Wallace, J. C. (2002) A comparison of the host defence skin peptides of the New Guinea tree frog (*Litoria genimaculata*) and the fringed tree frog (*Litoria eucnemis*). The link between the caerin and the maculatin antimicrobial peptides, *Aust. J. Chem.* **55**, 605-610.
66. Maselli, V. M., Bilusich, D., Bowie, J. H. & Tyler, M. J. (2006) Host-defence skin peptides of the Australian streambank froglet *Crinia riparia*: Isolation and sequence determination by positive and negative ion electrospray mass spectrometry, *Rapid Commun. Mass Spectrom.* **20**, 797-803.
67. Brinkworth, C. S., Bowie, J. H., Bilusich, D. & Tyler, M. J. (2005) The rothein peptides from the skin secretion of Roth's tree frog *Litoria rothii*. Sequence determination using positive and negative ion electrospray mass spectrometry, *Rapid Commun. Mass Spectrom.* **19**, 2716-2724.
68. Steinborner, S. T., Gao, C. W., Raftery, M. J., Waugh, R. J., Blumenthal, T., Bowie, J. H., Wallace, J. C. & Tyler, M. J. (1994) The structures of four tryptophyllin and three rubellidin peptides from the Australian red tree frog *Litoria rubella*, *Aust. J. Chem.* **47**, 2099-2108.
69. Maselli, V. M., Brinkworth, C. S., Bowie, J. H. & Tyler, M. J. (2004) Host-defence skin peptides of the Australian common froglet *Crinia signifera*: Sequence determination and negative ion electrospray mass spectra, *Rapid Commun. Mass Spectrom.* **18**, 2155-2161.
70. Bradford, A. M., Raftery, M. J., Bowie, J. H., Tyler, M. J., Wallace, J. C., Adams, G. W. & Severini, C. (1996) Novel uperin peptides from the dorsal glands of the Australian floodplain toadlet *Uperoleia inundata*, *Aust. J. Chem.* **49**, 475-484.

71. Rozek, T., Wegener, K. L., Bowie, J. H., Olver, I. N., Carver, J. A., Wallace, J. C. & Tyler, M. J. (2000) The antibiotic and anticancer active aurein peptides from the Australian bell frogs *Litoria aurea* and *Litoria raniformis*. The solution structure of aurein 1.2, *Eur. J. Biochem.* 267, 5330-5341.
72. Lamb, H. M., Wiseman, L. R. (1998) Pexiganan acetate, *Drugs.* 56, 1047-1052.
73. Hancock, R. E. W. (2000) Cationic antimicrobial peptides: towards clinical applications, *Expert Opin. Invest. Drugs.* 9, 1723-1729.
74. Andres, E., Dimarcq (2004) Cationic peptides: update of clinical development, *J. Int. Med.* 255, 519-520.
75. Epanand, R. M., Shai, Y., Segrest, J. P. & Anantharamaiah, G. M. (1995) Mechanisms for the modulation of membrane bilayer properties by amphipathic helical peptides, *Biopolymers.* 37, 319-38.
76. Sansom, M. S. P. (1991) The biophysics of peptide models of ion channels, *Prog. Biophys. Mol. Biol.* 55, 139-235.
77. Shai, Y. (1999) Mechanism of the binding, insertion and destabilization of phospholipid bilayer membranes by α -helical antimicrobial and cell non-selective membrane-lytic peptides, *Biochim. Biophys. Acta.* 1462, 55-70.
78. Shai, Y. & Oren, Z. (2001) From "carpet" mechanism to de-novo designed diastereomeric cell-selective antimicrobial peptides, *Peptides.* 22, 1629-1641.
79. Andreu, D., Ubach, J., Boman, A., Wahlin, B., Wade, D., Merrifield, R. B. & Boman, H. G. (1992) Shortened cecropin A-melittin hybrids - significant size reduction retains potent antibiotic activity, *FEBS Lett.* 296, 190-194.
80. Livermore, D. (2004) Can better prescribing turn the tide of resistance?, *Nat. Rev. Microbiol.* 2, 73-8.
81. Wegener, K. L. (2001) *Amphibian Peptides: Their Structures and Bioactivities*, Chemistry Ph.D. Thesis, The University of Adelaide, Adelaide.
82. Sherman, P. J., Jackway, R. J., Gehman, J. D., Praporski, S., McCubbin, G. A., Mechler, A., Martin, L. L., Separovic, F. & Bowie, J. H. (2009) Solution structure and membrane interactions of the antimicrobial peptide fallaxidin 4.1a: An NMR and QCM study, *Biochemistry.* 48, 11892-11901.
83. Sherman, P. J., Jackway, R. J., Nicholson, E., Musgrave, I. F., Boonthung, P. & Bowie, J. H. (2009) Activities of seasonably variable caerulein and rothein skin peptides from the tree frogs *Litoria splendida* and *Litoria rothii*, *Toxicon.* 54, 828-835.

84. Noble, F., Wank, S. A., Crawley, J. N., Bradwejn, J., Seroogy, K. B., Hamon, M. & Roques, B. P. (1999) Structure, distribution and functions of cholecystinin receptors, *Pharmacol. Rev.* *51*, 745-781.
85. Sargent, D. F. & Schwyzer, R. (1986) Membrane lipid phase as catalyst for peptide-receptor interactions, *Proc. Natl. Acad. Sci. USA.* *83*, 5774-5778.
86. Gremlich, H. U., Sargent, D. F. & Schwyzer, R. (1981) The adsorption of adrenocorticotropin-(1-24)-tetracosapeptide to lecithin bilayer membranes formed from liposomes, *Eur. Biophys. J.* *8*, 61-65.
87. Schwyzer, R. (1986) Molecular mechanism of opioid receptor selection, *Biochemistry.* *25*, 6335-6342.
88. Sargent, D. F., Bean, J. W., Kosterlitz, H. W. & Schwyzer, R. (1988) Cation dependence of opioid receptor binding supports theory on membrane-mediated receptor selectivity, *Biochemistry.* *27*, 4974-4977.
89. Deber, C. M. & Behnam, B. A. (1984) Role of membrane lipids in peptide hormone function: binding of enkephalins to micelles, *Proc. Natl. Acad. Sci. USA.* *81*, 61.
90. Kaiser, E. T. & Kezdy, F. J. (1983) Secondary structures of proteins and peptides in amphiphilic environments. (A review), *Proc. Natl. Acad. Sci. USA.* *80*, 1137.
91. Stone, D. J. M., Bowie, J. H., Tyler, M. J. & Wallace, J. C. (1992) The structure of caerin 1.1, a novel antibiotic peptide from Australian tree frogs., *J. Chem. Soc. Chem. Commun.*, 1224-1225.
92. Waugh, R. J., Stone, D. J. M., Bowie, J. H., Wallace, J. C. & Tyler, M. J. (1993) Peptides from Australian frogs. Structures of the caeridins from *Litoria caerulea*, *J. Chem. Soc. Perkin Trans. 1*, 573-576.
93. Fet, V. & Soleglad, M. V. (2005) Contributions to scorpion systematics. I. On recent changes in high-level taxonomy, *Euscorpius.* *31*, 1-13.
94. Braddy, S. J., Poschmann, M. & Tetlie, O. E. (2008) Giant claw reveals the largest ever arthropod, *Biology Letters.* *4*, 106-109.
95. Polis, G. A. & Brownell, P. (2001) *Scorpion biology and research*, Oxford University Press, New York.
96. Gao, B., Tian, C. & Zhu, S. (2007) Inducible antibacterial response of scorpion venom gland, *Peptides.* *28*, 2299-2305.

97. Miranda, F. & Lissitzky, S. (1961) Scorpamins: the Toxic Proteins of Scorpion Venoms, *Nature*. 190, 443-444.
98. Miranda, F., Rochat, H. & Lissitzky, S. (1964) Sur les neurotoxines de deux especes de scorpions nord-africains. I - Purification des neurotoxines (scorpamines) d'*Androctonus australis* (L.) et de *Buthus occitanus* (Am.), *Toxicon*. 2, 51-60.
99. Miranda, F., Rochat, H. & Lissitzky, S. (1964) Sur les neurotoxines de deux especes de scorpions nord-africains. III - Determinations preliminaires aux etudes de structure sur les neurotoxines (Scorpamines) d'*Androctonus australis* (L.) et de *Buthus occitanus* (Am.), *Toxicon*. 2, 123-138.
100. Miranda, F., Rochat, H. & Lissitzky, S. (1964) Sur les neurotoxines de deux especes de scorpions nord-africains. II- Proprietes des neurotoxines (Scorpamines) d'*Androctonus australis* (L.) et de *Buthus occitanus* (Am.), *Toxicon*. 2, 113-121.
101. Kopeyan, C., Martinez, G. & Rochat, H. (1979) Amino acid sequence of neurotoxin III of the scorpion *Androctonus australis Hector*, *Eur.J. Biochem.* 94, 609-615.
102. Rochat, H., Rochat, C., Miranda, F. & Lissitzki, S. (1984) The amino-acid sequence of neurotoxin I of *Androctonus australis Hector*, *Eur. J. Biochem.* 17, 262-266.
103. Rochat, H., Rochat, C., Sampieri, F., Miranda, F. & Lissitzky, S. (1972) The amino-acid sequence of neurotoxin II of *Androctonus australis Hector*, *Eur. J. Biochem.* 28, 381-388.
104. Gregoire, J. & Rochat, H. (1983) Covalent structure of toxins I and II from the scorpion *Buthus occitanus tunetanus*, *Toxicon*. 21, 153-162.
105. Zeng, X.-C., Li, W.-X., Wang, S.-X., Zhu, S.-Y. & Luo, F. (2001) Precursor of a Novel Scorpion Venom Peptide (BmKn1) with no Disulfide Bridge from *Buthus martensii* Karsch, *IUBMB Life*. 51, 117-120.
106. Bosmans, F. & Tytgat, J. (2007) Voltage-gated sodium channel modulation by scorpion α -toxins, *Toxicon*. 49, 142-158.
107. Zlotkin, E., Fishman, Y. & Elazar, M. (2000) AaIT: From neurotoxin to insecticide, *Biochimie*. 82, 869-881.
108. Zeng, X., Corzo, G. & Hahin, R. (2005) Scorpion venom peptides without disulfide bridges, *IUBMB Life*. 57, 13-21.
109. Habermann, E. & Zeuner, G. (1971) Comparative studies of native and synthetic melittins, *Naunyn-Schmiedeberg's Arch. Pharmacol.* 270, 1-9.

110. Wong, H., Bowie, J. H. & Carver, J. A. (1997) The solution structure and activity of caerin 1.1, an antimicrobial peptide from the Australian green tree frog, *Litoria splendida*, *Eur. J. Biochem.* *247*, 545-557.
111. Kuhn-Nentwig, L., Müller, J., Schaller, J., Walz, A., Dathe, M. & Nentwig, W. (2002) Cupiennin 1, a new family of highly basic antimicrobial peptides in the venom of the spider *Cupiennius salei* (Ctenidae), *J. Biol. Chem.* *277*, 11208-11216.
112. Pukala, T. L., Boland, M. P., Gehman, J. D., Kuhn-Nentwig, L., Separovic, F. & Bowie, J. H. (2007) Solution structure and interaction of cupiennin 1a, a spider venom peptide, with phospholipid bilayers, *Biochemistry.* *46*, 3576-3585.
113. Gao, B., Sherman, P., Luo, L., Bowie, J. & Zhu, S. (2009) Structural and functional characterization of two genetically related meucinin peptides highlights evolutionary divergence and convergence in antimicrobial peptides, *FASEB J.* *23*, 1230-1245.
114. Laraba-Djebari, F., Legros, C., Crest, M., Côtard, B., Romi, R., Mansuelle, P., Jacquet, G., van Rietschoten, J., Gola, M. & Rochat, H. (1994) The kaliotoxin family enlarged. Purification, characterization, and precursor nucleotide sequence of KTX2 from *Androctonus australis* venom, *J. Biol. Chem.* *269*, 32835-32843.
115. Grishin, E. V. (1981) Structure and function of *Buthus eupeus* scorpion neurotoxins, *J. Quant. Chem.* *20*, 291-298.
116. Ovchinnikov, Y. A. (1984) Bio-organic chemistry of polypeptide neurotoxins, *Pure Appl. Chem.* *56*, 1049-1068.
117. Yong Hua, J., Mansuelle, P., Terakawa, S., Kopeyan, C., Yanaihara, N., Ke, H. & Rochat, H. (1996) Two neurotoxins (BmK I and BmK II) from the venom of the scorpion *Buthus martensi Karsch*: purification, amino acid sequences and assessment of specific activity, *Toxicon.* *34*, 987-1001.
118. Srinivasan, K. N., Nirthanan, S., Sasaki, T., Sato, K., Cheng, B., Gwee, M. C. E., Kini, R. M. & Gopalakrishnakone, P. (2001) Functional site of bukatoxin, an α -type sodium channel neurotoxin from the Chinese scorpion (*Buthus martensi Karsch*) venom: probable role of the 52PDKVP56 loop, *FEBS Lett.* *494*, 145-149.
119. Zeng, X., Wang, S., Zhu, Y., Zhu, S. & Li, W. (2004) Identification and functional characterization of novel scorpion venom peptides with no disulfide bridge from *Buthus martensii Karsch*, *Peptides.* *25*, 143-150.
120. Romi-Lebrun, R., Lebrun, B., Martin-Eauclaire, M.-F., Ishiguro, M., Escoubas, P., Wu, F. Q., Hisada, M., Pongs, O. & Nakajima, T. (1997) Purification, Characterization, and Synthesis of Three Novel Toxins from the Chinese Scorpion *Buthus martensi*, which act on K^+ Channels, *Biochemistry.* *36*, 13473-13482.

121. Zhijian, C., Yun, X., Chao, D., Shunyi, Z., Shijin, Y., Yingliang, W. & Wenxin, L. (2006) Cloning and characterization of a novel calcium channel toxin-like gene BmCal from Chinese scorpion *Mesobuthus martensii* Karsch, *Peptides*. 27, 1235-1240.
122. Vargas, O., Martin, M. F. & Rochat, H. (1987) Characterization of six toxins from the venom of the Moroccan scorpion *Buthus occitanus mardochei*, *Eur. J. Biochem.* 162, 589-599.
123. Cestèle, S., Stankiewicz, M., Mansuelle, P., Waard, M. D., Dargent, B., Gilles, N., Pelhate, M., Rochat, H., Martin-Eauclaire, M.-F. & Gordon, D. (1999) Scorpion β -like toxins, toxic to both mammals and insects, differentially interact with receptor site 3 on voltage-gated sodium channels in mammals and insects, *Eur. J. Neurosci.* 11, 975-985.
124. Chuang, R. S. I., Jaffe, H., Cribbs, L., Perez-Reyes, E. & Swartz, K. J. (1998) Inhibition of T-type voltage-gated calcium channels by a new scorpion toxin, *Nature Neurosci.* 1, 668-674.
125. Sautière, P., Cestèle, S., Kopeyan, C., Martinage, A., Drobecq, H., Doljansky, Y. & Gordon, D. (1998) New toxins acting on sodium channels from the scorpion *Leiurus quinquestriatus hebraeus* suggest a clue to mammalian vs insect selectivity, *Toxicon.* 36, 1141-1154.
126. Garcia, M. L., Garcia-Calvo, M., Hidalgo, P., Lee, A. & MacKinnon, R. (1994) Purification and Characterization of Three Inhibitors of Voltage-Dependent K^+ Channels from *Leiurus Quinquestriatus Hebraeus* Venom, *Biochemistry.* 33, 6834-6839.
127. Ullrich, N., Gillespie, G. Yancey., Sontheimer, Harald. (1996) Human astrocytoma cells express a unique chloride current *Neuroreport.* 7, 1020-1024.
128. DeBin, J. A. & Strichartz, G. R. (1991) Chloride channel inhibition by the venom of the scorpion *Leiurus quinquestriatus*, *Toxicon.* 29, 1403-1408.
129. DeBin, J. A., Maggio, J. E. & Strichartz, G. R. (1993) Purification and characterization of chlorotoxin, a chloride channel ligand from the venom of the scorpion, *Am. J. Physiol. Cell Physiol.* 264, C361-369.
130. Bechis, G., Sampieri, F., Yuan, P. M., Brando, T., Martin, M. F., Diniz, C. R. & Rochat, H. (1984) Amino acid sequence of toxin VII, a β -toxin from the venom of the scorpion *Tityus serrulatus*, *Biochem. Biophys. Res. Commun.* 122, 1146-1153.
131. Possani, L. D., Martin, B.M., Fletcher, M.D., Fletcher, P.L. (1991) Discharge effects on pancreatic exocrine secretion produced by toxins purified from *Tityus serrulatus* scorpion venom, *J. Biol. Chem.* 266, 3178-3185.
132. Crest, M., Jacquet, G., Gola, M., Zerrouk, H., Benslimane, A., Rochat, H., Mansuelle, P. & Martin-Eauclaire, M. F. (1992) Kaliotoxin, a novel peptidyl inhibitor of

- neuronal BK-type Ca^{2+} -activated K^+ channels characterized from *Androctonus mauretanicus mauretanicus* venom, *J. Biol. Chem.* 267, 1640-1647.
133. Garcia-Calvo, M., Leonard, R. J., Novick, J., Stevens, S. P., Schmalhofer, W., Kaczorowski, G. J. & Garcia, M. L. (1993) Purification, characterization, and biosynthesis of margatoxin, a component of *Centruroides margaritatus* venom that selectively inhibits voltage-dependent potassium channels, *J. Biol. Chem.* 268, 18866-18874.
134. Sitges, M., Possani, L. & Bayon, A. (1986) Noxiustoxin, a short-chain toxin from the Mexican scorpion *Centruroides noxius*, induces transmitter release by blocking K^+ permeability, *J. Neurosci.* 6, 1570-1574.
135. Garcia-Valdes, J., Zamudio, F. Z., Toro, L. & Possani, L. D. (2001) Slotoxin, $\alpha\text{KTx1.11}$, a new scorpion peptide blocker of MaxiK channels that differentiates between α and $\alpha+\beta$ ($\beta 1$ or $\beta 4$) complexes, *FEBS Lett.* 505, 369-373.
136. Jaravine, V. A., Nolde, D. E., Reibarkh, M. J., Korolkova, Y. V., Kozlov, S. A., Pluzhnikov, K. A., Grishin, E. V. & Arseniev, A. S. (1997) Three-Dimensional Structure of Toxin OSK1 from *Orthochirus scrobiculosus* Scorpion Venom, *Biochemistry.* 36, 1223-1232.
137. Batista, C. V. F., Gómez-Lagunas, F., Lucas, S. & Possani, L. D. (2000) Tc1, from *Tityus cambridgei*, is the first member of a new subfamily of scorpion toxin that blocks K^+ -channels, *FEBS Lett.* 486, 117-120.
138. Batista, C. V. F., Gómez-Lagunas, F., Rodríguez de la Vega, R. C., Hajdu, P., Panyi, G., Gáspár, R. & Possani, L. D. (2002) Two novel toxins from the Amazonian scorpion *Tityus cambridgei* that block Kv1.3 and Shaker B K^+ -channels with distinctly different affinities, *BBA - Proteins Proteom.* 1601, 123-131.
139. Corzo, G., Escoubas, P., Villegas, E., Barnham, K. J., He, W., Norton, R. S. & Nakajima, T. (2001) Characterization of unique amphipathic antimicrobial peptides from venom of the scorpion *Pandinus imperator*, *Biochem. J.* 359, 35-45.
140. Valdivia, H. H., Kirby, M. S., Lederer, W. J. & Coronado, R. (1992) Scorpion toxins targeted against the sarcoplasmic reticulum Ca^{2+} -release channel of skeletal and cardiac muscle, *Proc. Natl. Acad. Sci.* 89, 12185-12189.
141. Fajloun, Z., Kharrat, R., Chen, L., Lecomte, C., Di Luccio, E., Bichet, D., El Ayeb, M., Rochat, H., Allen, P. D., Pessah, I. N., De Waard, M. & Sabatier, J. M. (2000) Chemical synthesis and characterization of maurocalcine, a scorpion toxin that activates Ca^{2+} release channel/ryanodine receptors, *FEBS Lett.* 469, 179-185.
142. Moerman, L., Bosteels, S., Noppe, W., Willems, J., Clynen, E., Schoofs, L., Thevissen, K., Tytgat, J., Eldere, J. V., Walt, J. v. d. & Verdonck, F. (2002) Antibacterial

and antifungal properties of α -helical, cationic peptides in the venom of scorpions from southern Africa, *Eur. J. Biochem.* 269, 4799-4810.

143. Zhu, S., Darbon, H., Dyason, K., Verdonck, F. & Tytgat, J. (2003) Evolutionary origin of inhibitor cystine knot peptides, *FASEB J.* 17, 1765-1767.

144. Dai, L., Corzo, G., Naoki, H., Andriantsiferana, M. & Nakajima, T. (2002) Purification, structure-function analysis, and molecular characterization of novel linear peptides from scorpion *Opisthacanthus madagascariensis*, *Biochem. Biophys. Res. Commun.* 293, 1514-1522.

145. Zhao, Z., Ma, Y., Dai, C., Zhao, R., Li, S., Wu, Y., Cao, Z. & Li, W. (2009) Imcroporin, a New Cationic Antimicrobial Peptide from the Venom of the Scorpion *Isometrus maculatus*, *Antimicrob. Agents Chemother.* 53, 3472-3477.

146. Torres-Larios, A., Gurrola, G. B., Zamudio, F. Z. & Possani, L. D. (2000) Hadrurin, a new antimicrobial peptide from the venom of the scorpion *Hadrurus aztecus*, *Eur. J. Biochem.* 267, 5023-5031.

147. Possani, L. D., Merino, E., Corona, M., Bolivar, F. & Becerril, B. (2000) Peptides and genes coding for scorpion toxins that affect ion-channels, *Biochimie.* 82, 861-868.

148. Thomson, J. J. (1913) *Rays of Positive Electricity and Their Application to Chemical Analyses*, Longmans, Green and Co., London.

149. Mattauch, J. & Herzog, R. (1934) About a new mass spectrograph, *Z. Physik.* 89, 786-795.

150. Dempster, A. J. (1918) A new method of positive ray analysis, *Phys. Rev.* 11, 316-325.

151. Beynon, J. H., Cooks, R. G., Amy, J. W., Baitinger, W. E. & Ridley, T. Y. (1973) Design and performance of a mass-analyzed ion kinetic energy (MIKE) spectrometer, *Anal. Chem.* 45, 1023A-1031A.

152. Stephens, W. E. (1946) A pulsed mass spectrometer with time dispersion, *Phys. Rev.* 69, 691.

153. Wiley, W. C. & McLaren, I. H. (1955) Time-of-Flight Mass Spectrometer with Improved Resolution, *Rev. Sci. Inst.* 26, 1150-1157.

154. Cotter, R. J. (1994) Time-of-flight mass spectrometry in *Time-of-Flight Mass Spectrometry* (Cotter, R. J., ed) pp. 16-48, American Chemical Society, Washington.

155. Paul, W. (1990) Electromagnetic traps for charged and neutral particles, *Angew. Chem. Int. Ed.* 29, 739-748.

156. Cooks, R. G. & Kaiser, R. E. (1990) Quadrupole ion trap mass spectrometry, *Acc. Chem. Res.* 23, 213-219.
157. Rose, M. E. (1982) *Mass Spectrometry for Chemists and Biochemists*, Cambridge University Press, Cambridge.
158. Harrison, A. G. & Cotter, R. J. (1990) Methods of ionization, *Methods Enzymol.* 193, 3-36.
159. Munson, M. S. B. & Field, F. H. (1966) Chemical ionization mass spectrometry. 1. General introduction, *J. Am. Chem. Soc.* 88, 2621-2630.
160. Harrison, A. G. (1983) *Chemical Ionization Mass Spectrometry*, CRC Press, Boca Raton.
161. Karas, M., Bachmann, D., Bahr, U. & Hillenkamp, F. (1987) Matrix-assisted ultraviolet laser desorption of non-volatile compounds, *Int. J. Mass Spectrom. Ion Processes.* 78, 53-68.
162. Karas, M. & Hillenkamp, F. (1988) Laser desorption ionization of proteins with molecular masses exceeding 10 000 daltons, *Anal. Chem.* 60, 2299A-2301A.
163. Tanaka, K., Waki, H., Ido, Y., Akita, S., Yoshida, Y., Yoshida, T. & Matsuo, T. (1988) Protein and polymer analyses up to m/z 100 000 by laser ionization time-of-flight mass spectrometry, *Rapid Commun. Mass Spectrom.* 2, 151-153.
164. Yamashita, M. & Fenn, J. B. (1984) Electrospray ion source. Another variation on the free-jet theme, *J. Phys. Chem.* 88, 4451-4459.
165. Griffiths, W. J., Jonsson, A. P., Liu, S., Rai, D. K. & Wang, Y. (2001) Electrospray and tandem mass spectrometry in biochemistry, *Biochem. J.* 355, 545-561.
166. Dole, M., Mach, L. L., Hines, R. L., Mobley, R. C., Ferguson, L. D. & Alice, M. B. (1968) Molecular beams of macroions, *J. Chem. Phys.* 49, 2210-2247.
167. Shukla, A. K. & Futrell, J. H. (1993) Collisional activation and dissociation of polyatomic ions, *Mass Spectrom. Rev.* 12, 211-255.
168. Cooks, R. G. (1978) *Collision Spectroscopy*, Plenum Press, New York.
169. Haynes, R. & Gross, M. L. (1990) Collision-induced dissociation, *Methods Enzymol.* 193, 237-263.

170. Syka, J. E. P., Coon, J. J., Schroeder, M. J., Shabanowitz, J. & Hunt, D. F. (2004) Peptide and protein sequence analysis by electron transfer dissociation mass spectrometry, *Proc. Natl. Acad. Sci. USA*. *101*, 9528-9533.
171. Mikesch, L. M., Ueberheide, B., Chi, A., Coon, J. J., Syka, J. E. P., Shabanowitz, J. & Hunt, D. F. (2006) The utility of ETD mass spectrometry in proteomic analysis, *BBA - Proteins Proteom.* *1764*, 1811-1822.
172. Little, D. P., Speir, J. P., Senko, M. W., O'Connor, P. B. & McLafferty, F. W. (2002) Infrared Multiphoton Dissociation of Large Multiply Charged Ions for Biomolecule Sequencing, *Anal. Chem.* *66*, 2809-2815.
173. Morris, H. R., Paxton, T., Dell, A., Langhorne, J., Berg, M., Bordoli, R. S., Hoyes, J. & Bateman, R. H. (1996) High sensitivity collisionally-activated decomposition tandem mass spectrometry on a novel quadrupole/orthogonal-acceleration time-of-flight mass spectrometer, *Rapid Commun. Mass Spectrom.* *10*, 889-896.
174. Wysocki, V. H., Resing, K. A., Zhang, Q. & Chen, G. (2005) Mass spectrometry of peptides and proteins, *Methods.* *35*, 211-222.
175. Dawson, P. H. (1976) *Quadrupole Mass Spectrometry and its Applications*, Elsevier, Amsterdam.
176. Steel, C. & Henchman, M. (1998) Understanding the quadrupole mass filter through computer simulation, *J. Chem. Ed.* *75*, 1049-1054.
177. Cooks, R. G., Beynon, J. H., Caprioli, R. M. & Lester, G. R. (1973) *Metastable Ions*, Elsevier, Amsterdam.
178. de Hoffmann, E. (1996) Tandem mass spectrometry: A primer, *J. Mass Spectrom.* *31*, 129-137.
179. Shukla, A. K. & Futrell, J. H. (2000) Tandem mass spectrometry: Dissociation of ions by collisional activation, *J. Mass Spectrom.* *35*, 1069-1090.
180. Cooks, R. G. (2005) Collision-induced dissociation: Readings and commentary, *J. Mass Spectrom.* *30*, 1215-1221.
181. Mamyurin, B. A., Krataev, V. I., Shmikk, D. V. & Zagulin, V. A. (1973) The mass-reflectron, a new nonmagnetic time-of-flight mass spectrometer with high resolution, *Sov. Phys. JETP.* *37*, 45-48.
182. Mamyurin, B. A. (1994) Laser assisted reflectron time-of-flight mass spectrometry, *Int. J. Mass Spectrom. Ion Proc.* *131*, 1-19.

183. Chernushevich, I. V., Loboda, A. V. & Thompson, B. A. (2001) An introduction to quadrupole-time-of-flight mass spectrometry, *J. Mass Spectrom.* *36*, 849-865.
184. Fenn, J. B., Mann, M., Meng, C. K., Wong, S. F. & Whitehouse, C. M. (1989) Electrospray ionization for mass spectrometry of large biomolecules, *Science.* *246*, 64-71.
185. Fenn, J. B., Mann, M., Meng, C. K., Wong, S. F. & Whitehouse, C. M. (1990) Electrospray ionization - principles and practice, *Mass Spectrom. Rev.* *9*, 37-70.
186. Taylor, G. I. (1964) Disintegration of water drops in an electric field, *Proc. Royal Soc. Lond. A.* *280*, 383-397.
187. Williams, D. H. & Fleming, I. (1995) *Spectroscopic Methods in Organic Chemistry*, McGraw-Hill Book Co., London.
188. Kebarle, P. (2000) A brief overview of the present status of the mechanisms involved in electrospray mass spectrometry, *J. Mass Spectrom.* *35*, 804-817.
189. Mant, C. T. & Hodges, R. S. (1991) *High Performance Liquid Chromatography of Peptides and Proteins. Separation, Analysis and Conformation*, CRC Press, Boca Raton.
190. García, M. C. (2005) The effect of the mobile phase additives on sensitivity in the analysis of peptides and proteins by high-performance liquid chromatography-electrospray mass spectrometry, *J. Chromatogr. B.* *825*, 111-123.
191. Yoshida, T. (2004) Peptide separation by hydrophilic-interaction chromatography: A review, *J. Biochem. Biophys. Methods.* *60*, 265-280.
192. Henschen, A., Hupe, K., Lottspeich, F. & Voelter, W. (1985) *High Performance Liquid Chromatography in Biochemistry*, VCH Publishers, Weinheim.
193. Yalcin, T., Khouw, C., Csizmadia, I. G., Peterson, M. R. & Harrison, A. G. (1995) Why Are B Ions Stable Species in Peptide Spectra?, *J. Am. Soc. Mass Spectrom.* *6*, 1165-1174.
194. Polce, M. J., Ren, D. & Wesdemiotis, C. (2000) Dissociation of the peptide bond in protonated peptides, *J. Mass Spectrom.* *35*, 1391-1398.
195. Paizs, B. & Suhai, S. (2004) Towards understanding the tandem mass spectra of protonated oligopeptides. 1: mechanism of amide bond cleavage, *J. Am. Soc. Mass Spec.* *15*, 103-113.
196. Paizs, B. & Sándor, S. (2005) Fragmentation pathways of protonated peptides, *Mass Spectrom. Rev.* *24*, 508-548.

197. Maclean, M. J., Brinkworth, C. S., Bilusich, D., Bowie, J. H., Doyle, J. R., Llewellyn, L. E. & Tyler, M. J. (2006) New caerin antibiotic peptides from the skin secretion of the Dainty Green Tree Frog *Litoria gracilentia*. Identification using positive and negative ion electrospray mass spectrometry, *Toxicon*. *47*, 664-675.
198. Bradford, A. M., Waugh, R. J. & Bowie, J. H. (1995) Characterization of underivatized tetrapeptides by negative-ion fast-atom bombardment mass spectrometry, *Rapid Commun. Mass Spectrom.* *9*, 677-685.
199. Biemann, K. & Martin, S. A. (1987) Mass spectrometric determination of the amino acid sequence of peptides and proteins, *Mass Spectrom. Rev.* *6*, 1-76.
200. Eckersley, M., Bowie, J. H. & Hayes, R. N. (1989) Collision-induced dissociations of deprotonated peptides, dipeptides and tripeptides with hydrogen and alkyl α -groups. An aid to structure determination., *Org. Mass Spectrom.* *24*, 597-602.
201. Waugh, R., Bowie, J. & Gross, M. (1993) Collision-Induced Dissociations of Deprotonated Peptides. Dipeptides Containing Asn, Arg and Lys, *Aust. J. Chem.* *46*, 693-702.
202. Bahr, U., Karas, M. & Kellner, R. (1998) Differentiation of lysine/glutamine in peptide sequence analysis by electrospray ionization sequential mass spectrometry coupled with a quadrupole ion trap, *Rapid Commun. Mass Spectrom.* *12*, 1382-1388.
203. Johnson, R. S., Martin, S. A., Biemann, K., Stults, J. T. & Watson, J. T. (2002) Novel fragmentation process of peptides by collision-induced decomposition in a tandem mass spectrometer: differentiation of leucine and isoleucine, *Anal. Chem.* *59*, 2621-2625.
204. Edman, P. & Begg, G. (1967) A protein sequenator, *Eur. J. Biochem.* *1*, 80-91.
205. Hunkapiller, M. W., Hewick, R. M., Dreyer, W. J. & Hood, L. E. (1983) High-sensitivity sequencing with a gas-phase sequenator, *Methods Enzymol.* *91*, 399-413.
206. Bodanszky, M. (1988) *Peptide Chemistry. A Practical Textbook*, Springer-Verlag, Berlin.
207. Gevaert, K. & Vandekerckhove, J. (2000) Protein identification methods in proteomics, *Electrophoresis.* *21*, 1145-1154.
208. Blundell, T. L. & Johnson, L. N. (1976) *Protein Crystallography*, Academic Press, New York.
209. Glusker, J. P. (1981) *Structural Crystallography in Chemistry and Biology*, Hutchinson Ross Pub. Co., Stroudsburg.

210. Rabi, I. I., Zacharias, J. R., Millman, S. & Kusch, P. (1938) A New Method of Measuring Nuclear Magnetic Moment, *Phys. Rev.* *53*, 318.
211. Bloch, F., Hansen, W. W. & Packard, M. (1946) Nuclear Induction, *Phys. Rev.* *69*, 127.
212. Purcell, E. M., Torrey, H. C. & Pound, R. V. (1946) Resonance Absorption by Nuclear Magnetic Moments in a Solid, *Phys. Rev.* *69*, 37.
213. Jacobson, B., Anderson, W. A. & Arnold, J. T. (1954) A proton magnetic resonance study of the hydration of deoxyribonucleic acid., *Nature.* *17*, 772-773.
214. Takeda, M. & Jardetzky, O. (1957) Proton Magnetic Resonance of Simple Amino Acids and Dipeptides in Aqueous Solution, *J. Chem. Phys.* *26*, 1346-1347.
215. Bovey, F. A. & Tiers, G. V. D. (1959) Proton N.S.R. Spectroscopy. V. Studies of Amino Acids and Peptides in Trifluoroacetic Acid, *J. Am. Chem. Soc.* *81*, 2870-2878.
216. Wüthrich, K. (1976) *NMR in Biological Research: Peptides and Proteins*, North-Holland Pub. Co., Amsterdam.
217. Freeman, R. (1995) A short history of NMR, *Chem. Heterocycl. Comp.* *31*, 1004-1005.
218. Nelson, F. A. & Weaver, H. E. (1964) Nuclear Magnetic Resonance Spectroscopy in Superconducting Magnetic Fields, *Science.* *146*, 223-232.
219. Aue, W. P., Bartholdi, E. & Ernst, R. R. (1976) Two dimensional spectroscopy. Application to nuclear magnetic resonance., *J. Chem. Phys.* *64*, 2229-2246.
220. Ernst, R. R. & Anderson, W. A. (1966) Application of Fourier transform spectroscopy to magnetic resonance, *Rev. Sci. Inst.* *37*, 93-102.
221. Wider, G. (2000) Structure determination of biological macromolecules in solution using nuclear magnetic resonance spectroscopy, *Biotechniques.* *29*, 1278-1294.
222. Sanders, C. R. & Hunter, B. K. (1993) *Modern NMR Spectroscopy: A Guide for Chemists*, Oxford University Press, New York.
223. Gunther, H. (1994) *NMR spectroscopy: basic principles, concepts, and applications in chemistry*, Wiley, New York.
224. Evans, J. N. S. (1995) *Biomolecular NMR Spectroscopy*, Oxford University Press, Oxford.

225. Silverstein, R. M. & Webster, F. X. (1998) *Spectrometric Identification of Organic Compounds*, 6th edn, John Wiley and Sons, New York.
226. Lambert, J. B. & Mazzola, E. P. (2004) *Nuclear Magnetic Resonance: An Introduction to Principles, Applications and Experimental Methods*, Pearson Education, New Jersey.
227. Friebolin, H. (1991) *Basic One- and Two-Dimensional NMR Spectroscopy*, VCH Publishers, Weinheim.
228. Braun, S., Kalinoski, H.-O. & Berger, S. (1998) *150 and More Basic NMR Experiments*, Wiley-VCH, Weinheim, Germany.
229. Wüthrich, K. (1986) *NMR of Proteins and Nucleic Acids*, John Wiley and Sons, New York.
230. Bax, A. (1981) An improved method for heteronuclear chemical shift correlation by two-dimensional NMR, *J. Magn. Res.* 42, 501-505.
231. Sørensen, O. W., Eich, G. W., Levitt, M. H., Bodenhausen, G. & Ernst, R. R. (1983) Product operator formalism for the description of NMR pulse experiments, *Prog. Nucl. Magn. Reson. Spectrosc.* 16, 163-192.
232. Kriwacki, R. W. & Pitner, T. P. (1989) Current aspects of practical two-dimensional (2D) nuclear magnetic resonance (NMR) spectroscopy: Applications to structure elucidation., *Pharm. Res.* 6, 531-554.
233. Rance, M., Sørensen, O. W., Bodenhausen, G., Wagner, G., Ernst, R. R. & Wüthrich, K. (1983) Improved spectral resolution in COSY ^1H NMR spectra of proteins via double quantum filtering, *Biochem. Biophys. Res. Commun.* 117, 479-485.
234. Keeler, J. (2010) *Understanding NMR spectroscopy*, 2nd edn, John Wiley and Sons, Chichester, U.K.
235. Davis, D. G. & Bax, A. (1985) Assignment of complex ^1H NMR spectra via two-dimensional homonuclear Hartmann-Hahn spectroscopy, *J. Am. Chem. Soc.* 107, 2820-2821.
236. Bax, A. (1989) Homonuclear Hartmann-Hahn experiments, *Methods Enzymol.* 176, 151-168.
237. Wishart, D. S., Bigam, C. G., Holm, A., Hodges, R. S. & Sykes, B. D. (1995) ^1H , ^{13}C and ^{15}N random coil NMR chemical shifts of the common amino acids. I. Investigations of nearest-neighbor effects, *J. Biomol. NMR.* 5, 67-81.

238. Wüthrich, K. (1989) Protein structure determination in solution by nuclear magnetic resonance spectroscopy, *Science*. 243, 45-50.
239. Jeener, J. (1979) Investigation of exchange processes by two-dimensional NMR spectroscopy, *J. Chem. Phys.* 71, 4546-4553.
240. Clore, G. M. & Gronenborn, A. M. (1998) New methods of structure refinement for macromolecular structure determination by NMR, *Proc. Natl. Acad. Sci.* 95, 5891-5898.
241. Clore, G. M. & Gronenborn, A. M. (1989) Determination of three-dimensional structures of proteins and nucleic acids in solution by nuclear magnetic resonance spectroscopy, *Crit. Rev. Biochem. Mol. Biol.* 24, 479-564.
242. Neuhaus, D. & Williamson, M. P. (1989) *The Nuclear Overhauser Effect in Structural and Conformational Analysis*, VCH Publishers, New York.
243. Gronenborn, A. M. & Clore, G. M. (1990) Protein structure determination in solution by two-dimensional and three-dimensional nuclear magnetic resonance spectroscopy, *Anal. Chem.* 62, 2-15.
244. Sutcliffe, M. J. (1993) Structure determination from NMR data II. Computational approaches in *NMR of Macromolecules: A Practical Approach* (Roberts, G. C. K., ed) pp. 359-390, Oxford University Press, New York.
245. Wüthrich, K., Billeter, M. & Braun, W. (1984) Polypeptide secondary structure determination by nuclear magnetic resonance observation of short proton-proton distances, *J. Mol. Biol.* 180, 715-740.
246. Dalgarno, D. C., Levine, B. A. & Williams, R. J. P. (1983) Structural information from NMR secondary chemical shifts of peptide α C-H protons in proteins, *Biosci. Rep.* 3, 443-452.
247. Wishart, D. S., Sykes, B. D. & Richards, F. M. (1991) Relationship between nuclear magnetic resonance chemical shift and protein secondary structure, *J. Mol. Biol.* 222, 311-333.
248. Kuntz, I. D., Kosen, P. A. & Craig, E. C. (1991) Amide chemical shifts in many helices in peptides and proteins are periodic, *J. Am. Chem. Soc.* 113, 1406-1408.
249. Hol, W. G. J. (1985) The role of the α -helix dipole in protein function and structure, *Prog. Biophys. Mol. Biol.* 45, 149-195.
250. Blundell, T., Barlow, D., Borkakoti, N. & Thornton, J. (1983) Solvent-induced distortions and the curvature of α -helices, *Nature*. 306, 281-283.

251. Macomber, R. S. (1998) *A Complete Introduction to Modern NMR Spectroscopy*, John Wiley and Sons, New York.
252. Pardi, A., Billeter, M. & Wüthrich, K. (1984) Calibration of the angular dependence of the amide proton-C α coupling constants, $^3J_{\text{HN}\alpha}$, in a globular protein, *J. Mol. Biol.* **180**, 741-751.
253. Bystrov, V. F., Ivanov, V. T., Portnova, S. L., Balashova, T. A. & Ovchinnikov, Y. A. (1973) Refinement of the angular dependence of the peptide vicinal NH-C $^{\alpha}$ H coupling constant, *Tetrahedron.* **29**, 873-877.
254. Kim, Y. & Prestegard, J. H. (1989) Measurement of vicinal couplings from cross peaks in COSY spectra, *J. Magn. Res.* **84**, 9-13.
255. Nilges, M. & O'Donoghue, S. I. (1998) Ambiguous NOEs and automated NOE assignment, *Prog. Nucl. Magn. Reson. Spectrosc.* **32**, 107-139.
256. Brünger, A. T., Adams, P. D., Clore, G. M., DeLano, W. L., Gros, P., Grosse-Kunstleve, R. W., Jiang, J.-S., Kuszewski, J., Nilges, M., Pannu, N. S., Read, R. J., Rice, L. M., Simonson, T. & Warren, G. L. (1998) Crystallography & NMR System: a new software suite for macromolecular structure determination, *Acta Cryst. D.* **D54**, 905-921.
257. Barsukov, I. L. & Lian, L. (1993) Structure determination from NMR data. I. Analysis of NMR data in *NMR of Macromolecules: A Practical Approach* (Roberts, G. C. K., ed) pp. 315-357, Oxford University Press, New York.
258. Kaptein, R., Boelens, R., Scheek, R. M. & van Gunsteren, W. F. (1988) Protein structures from NMR, *Biochem.* **27**, 5389-5395.
259. Habeck, M., Rieping, W., Linge, J. P. & Nilges, M. (2004) NOE assignment with ARIA 2.0 - the nuts and bolts in *Protein NMR Techniques* (Downing, A. K., ed) pp. 379-402, Humana Press, Totowa.
260. Linge, J. P., Habeck, M., Rieping, W. & Nilges, M. (2003) ARIA: Automated NOE assignment and NMR structure calculation, *Bioinformatics.* **19**, 315-316.
261. Havel, T. F. (1991) An evaluation of computational strategies for use in the determination of protein structure from distance constraints obtained by nuclear magnetic resonance, *Prog. Biophys. Mol. Biol.* **56**, 43-78.
262. Nilges, M. (1995) Calculation of protein structures with ambiguous distance restraints. Automated assignment of ambiguous NOE crosspeaks and disulphide connectivities, *J. Mol. Biol.* **245**, 645-660.

263. Güntert, P., Berndt, K. D. & Wüthrich, K. (1993) The program ASNO for computer-supported collection of NOE upper distance constraints as input for protein structure determination, *J. Biomol. NMR.* 3, 601-606.
264. Nilges, M., Clore, G. M. & Gronenborn, A. M. (1988) Determination of three-dimensional structures of proteins from interproton distance data by dynamical simulated annealing from a random array of atoms - circumventing problems associated with folding, *FEBS Lett.* 239, 129-136.
265. Fletcher, C. M., Jones, D. N. M., Diamond, R. & Neuhaus, D. (1996) Treatment of NOE constraints involving equivalent or nonstereoassigned protons in calculations of biomacromolecular structures, *J. Biomol. NMR.* 8, 292-310.
266. Güntert, P., Werner, B., Gillet, M. & Wüthrich, K. (1989) Automated stereospecific proton NMR assignments and their impact on the precision of protein structure determinations in solution, *J. Am. Chem. Soc.* 111, 3997-4004.
267. Driscoll, P. C., Gronenborn, A. M. & Clore, G. M. (1989) The influence of stereospecific assignments on the determination of three-dimensional structures of proteins by nuclear magnetic resonance spectroscopy: Application to the sea anemone protein BDS-I, *FEBS Lett.* 243, 223-233.
268. Zuiderweg, E. R. P., Boelens, R. & Kaptein, R. (1985) Stereospecific assignments of ¹H-NMR methyl lines and conformation of valyl residues in the *lac* repressor headpiece, *Biopolymers.* 24, 601-611.
269. Folmer, R. H. A., Hilbers, C. W., Konings, R. N. H. & Nilges, M. (1997) Floating stereospecific assignment revisited - application to an 18 kDa protein and comparison with J-coupling data, *J. Biomol. NMR.* 9, 245-258.
270. Weber, P. L., Morrison, R. & Hare, D. (1988) Determining stereo-specific ¹H nuclear magnetic resonance assignments from distance geometry calculations, *J. Mol. Biol.* 204, 483-487.
271. Clore, G. M., Gronenborn, A. M., Brünger, A. T. & Karplus, M. (1985) Solution conformation of a heptadecapeptide comprising the DNA binding helix F of the cyclic AMP receptor protein of *Escherichia coli*: Combined use of ¹H nuclear magnetic resonance and restrained molecular dynamics, *J. Mol. Biol.* 186, 435-455.
272. Brünger, A. T., Clore, G. M., Gronenborn, A. M. & Karplus, M. (1986) Three-dimensional structure of proteins determined by molecular dynamics with interproton distance restraints: Application to crambin, *Proc. Natl. Acad. Sci.* 83, 3801-3805.
273. Kaptein, R., Zuiderweg, E. R. P., Scheek, R. M., Boelens, R. & van Gunsteren, W. F. (1985) A protein structure from nuclear magnetic resonance data: *lac* repressor headpiece, *J. Mol. Biol.* 182, 179-182.

274. Karplus, M. & Petsko, G. A. (1990) Molecular dynamics simulations in biology, *Nature*. 347, 631-639.
275. Bax, A. (1989) Two-dimensional NMR and protein structure, *Annu. Rev. Biochem.* 58, 223-56.
276. Nilges, M., Gronenborn, A. M., Brünger, A. T. & Clore, G. M. (1988) Determination of the three-dimensional structures proteins by simulated annealing with interproton distance restraints, *Protein Eng.* 2, 27-38.
277. Kang, R. S., Daniels, C. M., Francis, S. A., Shih, S. C., Salerno, W. J., Hicke, L. & Radhakrishnan, I. (2003) Solution structure of a CUE-ubiquitin complex reveals a conserved mode of ubiquitin binding, *Cell*. 113, 621-630.
278. Nabburs, S. B., Spronk, C. A. E. M., Vriend, G. & Vuister, G. W. (2004) Concepts and tools for NMR restraint analysis and validation, *Concepts Mag. Reson. A*. 22, 90-105.
279. Hyberts, S. G., Goldberg, M. S., Havel, T. F. & Wagner, G. (1992) The solution structure of eglin C based on measurements of many NOEs and coupling constants and its comparison with X-ray structures, *Protein Sci.* 1, 736-751.
280. Pallaghy, P. K., Duggan, B. M., Pennington, M. W. & Norton, R. S. (1993) Three-dimensional structure in solution of the calcium channel blocker ω -conotoxin, *J. Mol. Biol.* 234, 405-420.
281. Ramachandran, G. N., Ramakrishnan, C. & Sasisekharan, V. (1963) Stereochemistry of polypeptide chain configurations, *J. Mol. Biol.* 7, 95-99.
282. Morris, A. L., MacArthur, M. W., Hutchinson, E. G. & Thornton, J. M. (1992) Stereochemical quality of protein structure coordinates, *Protein. Struct. Funct. Genet.* 12, 345-364.
283. Epanand, R. M. & Vogel, H. J. (1999) Diversity of antimicrobial peptides and their mechanisms of action, *BBA - Biomembranes*. 1462, 11-28.
284. Bechinger, B. (2000) Understanding peptide interactions with the lipid bilayer: A guide to membrane protein engineering, *Curr. Opin. Chem. Biol.* 4, 639-644.
285. Bonev, B., Watts, A., Bokvist, M. & Grobner, G. (2001) Electrostatic peptide-lipid interactions of amyloid- β peptide and pentyllysine with membrane surfaces monitored by ^{31}P MAS NMR, *Phys. Chem. Chem. Phys.* 3, 2904-2910.
286. Inooka, H., Ohtaki, T., Kitahara, O., Ikegami, T., Endo, S., Kitada, C., Ogi, K., Onda, H., Fujino, M. & Shirakawa, M. (2001) Conformation of a peptide ligand bound to its G-protein coupled receptor, *Nat. Struct. Biol.* 8, 161-165.

287. Moroder, L. & Romano, R. (1994) Synthesis, conformational and biological properties of lipophilic derivatives of gastrin and cholecystokinin peptides, *Pure Appl. Chem.* *66*, 2111-2114.
288. Lauterwein, J., Bosch, C., Brown, L. R. & Wüthrich, K. (1979) Physicochemical studies of the protein-lipid interactions in melittin-containing micelles, *Biochim. Biophys. Acta.* *556*, 244-264.
289. Rajan, R. & Balaram, P. (1996) A model for the interaction of trifluoroethanol with peptides and proteins, *Int. J. Pept. Protein Res.* *48*, 328-336.
290. Nelson, J. W. & Kallenbach, N. R. (1986) Stabilisation of the ribonuclease S-peptide α -helix by trifluoroethanol, *Protein. Struct. Funct. Genet.* *1*, 211-217.
291. Mendz, G. L., Moore, W. J., Brown, L. R. & Martenson, R. E. (1984) Interaction of myelin basic protein with micelles of dodecylphosphocholine, *Biochem.* *23*, 6041-6046.
292. Jesson, J. P., Meakin, P. & Kneissel, G. (1973) Homonuclear decoupling and peak elimination in Fourier transform nuclear magnetic resonance, *J. Am. Chem. Soc.* *95*, 618-620.
293. Wider, G., Hosur, R. J. & Wüthrich, K. (1983) Suppression of the solvent resonance in 2D NMR spectra of proteins in H₂O solution., *J. Magn. Res.* *52*, 130-135.
294. Gueron, M., Plateau, P. & Decorps, M. (1991) Solvent signal suppression in NMR, *Prog. Nucl. Magn. Reson. Spectrosc.* *23*, 135-209.
295. Smallcombe, S. H., Patt, S. L. & Kiefer, P. A. (1995) WET solvent suppression and its application to LC NMR and high-resolution NMR spectroscopy, *J. Magn. Res.* *117*, 295-303.
296. Ogg, R. J., Kingsley, P. B. & Taylor, J. S. (1994) WET, a T1- and B1-insensitive water-suppression method for in vivo localised ¹H NMR spectroscopy, *J. Magn. Res. B.* *104*, 1-10.
297. Piotto, M., Saudek, V. & Sklenár, V. (1992) Gradient-tailored excitation for single-quantum NMR spectroscopy of aqueous solutions, *J. Biomol. NMR.* *2*, 661-665.
298. Liu, M., Mao, X., Ye, C., Huang, H., Nicholson, J. K. & Lindon, J. C. (1998) Improved WATERGATE pulse sequences for solvent suppression in NMR spectroscopy, *J. Magn. Res.* *132*, 125-129.
299. Reiersen, H. & Rees, A. R. (2000) Trifluoroethanol may form a solvent matrix for assisted hydrophobic interactions between peptide side chains, *Protein Eng.* *13*, 739-743.

300. Hong, D. P., Hoshino, M., Kuboi, R. & Goto, Y. (1999) Clustering of fluorine-substituted alcohols as a factor responsible for their marked effects on proteins and peptides, *J. Am. Chem. Soc.* *121*, 8427-8433.
301. Hirota, N., Mizuno, K. & Goto, Y. (1998) Group additive contributions to the alcohol-induced alpha-helix formation of melittin - implication for the mechanism of the alcohol effects on proteins, *J. Mol. Biol.* *275*, 365-378.
302. Sönnichsen, F. D., Van Eyk, J. A., Hodges, R. S. & Sykes, B. D. (1992) Effect of trifluoroethanol on protein secondary structure: An NMR and CD study using a synthetic actin peptide, *Biochem.* *31*, 8790-8798.
303. Santiveri, C. M., Pantoja-Uceda, D., Rico, M. & Jiménez, M. A. (2005) β -Hairpin formation in aqueous solution and in the presence of trifluoroethanol: A ^1H and ^{13}C NMR conformational study of designed peptides, *Biopolymers.* *79*, 150-62.
304. Kuwata, K., Hoshino, M., Era, S., Batt, C. A. & Goto, Y. (1998) α - β transition of α -lactoglobulin as evidenced by heteronuclear NMR., *J. Mol. Biol.* *283*, 731-739.
305. Narhi, L. O., Philo, J. S., Li, T., Zhang, M., Samal, B. & Arakawa, T. (1996) Induction of α -helix in the β -sheet protein tumor necrosis factor- α : Thermal- and trifluoroethanol-induced denaturation at neutral pH, *Biochemistry.* *35*, 11447-11453.
306. Dong, A., Matsuura, J., Manning, M. C. & Carpenter, J. F. (1998) Intermolecular β -sheet results from trifluoroethanol-induced nonnative α -helical structure in β -sheet predominant proteins - infrared and circular dichroism spectroscopic study, *Arch. Biochem. Biophys.* *355*, 275-281.
307. Fyfe, C. A. (1983) *Solid State NMR for Chemists*, CFC Press, Ontario.
308. Bechinger, B. (1999) The structure, dynamics and orientation of antimicrobial peptides in membranes by multidimensional solid-state NMR spectroscopy, *BBA - Biomembranes.* *1462*, 157-183.
309. Hennel, J. & Klinowski, J. (2005) Magic angle spinning: A historical perspective in *New techniques in solid-state NMR* (Klinowski, J., ed) pp. 1-14, Springer-Verlag, Berlin.
310. Pake, G. E. (1948) Nuclear resonance absorption in hydrated crystals: Fine structure of the proton line., *J. Chem. Phys.* *16*, 327-336.
311. Kentgens, A. P. M. (1997) A practical guide to solid-state NMR of half-integer quadrupolar nuclei with some applications to disordered systems, *Geoderma.* *80*, 271-306.
312. Davis, J. H. (1983) The description of membrane lipid conformation, order and dynamics by ^2H -NMR, *BBA - Rev. Biomembranes.* *737*, 117-171.

313. Davis, J. H., Jeffrey, K. R., Bloom, M., Valic, M. I. & Higgs, T. P. (1976) Quadrupolar echo deuteron magnetic resonance spectroscopy in ordered hydrocarbon chains, *Chem. Phys. Lett.* *42*, 390-394.
314. Hodgkinson, P. & Emsley, L. (1999) The accuracy of distance measurements in solid-state NMR, *J. Magn. Res.* *139*, 46-56.
315. Pines, A., Gibby, M. G. & Waugh, J. S. (1973) Proton enhanced nuclear magnetic resonance of dilute spins in solids, *J. Chem. Phys.* *59*, 569-590.
316. Pines, A., Gibby, M. G. & Waugh, J. S. (1972) Proton-enhanced nuclear induction spectroscopy. A method for high resolution NMR of dilute spins in solids, *J. Chem. Phys.* *56*, 1776-1777.
317. Finean, J. B. & Michell, R. H. (1981) Isolation, composition and general structure of membranes. in *Membrane Structure* (Finean, J. B. & Michell, R. H., eds) pp. 1-36, Elsevier, Amsterdam.
318. Dowhan, W. & Bogdanov, M. (2002) Functional role of lipids in membranes in *Biochemistry of Lipids, Lipoproteins and Membranes* (Vance, D. E. & Vance, J. E., eds) pp. 1-35, Elsevier Science, Amsterdam.
319. Rouser, G., Nelson, G. J., Fleischer, S. & Simon, G. (1968) Lipid composition of animal cell membranes, organelles and organs in *Biological Membranes: Physical Fact and Function* (Chapman, D., ed) pp. 5-69, Academic Press, London.
320. Bocian, D. F. & Chan, S. I. (1978) NMR studies of membrane structure and dynamics, *Ann. Rev. Phys. Chem.* *29*, 307-335.
321. Singer, S. G. & Nicolson, G. L. (1972) The fluid mosaic model of the structure of cell membranes, *Science.* *175*, 720-731.
322. Danielli, J. F. & Davson, H. (1935) A contribution to the theory of permeability of thin films, *J. Cell. Comp. Phys.* *5*, 495.
323. Tristram-Nagle, S., Liu, Y., Legleiter, J. & Nagle, J. F. (2002) Structure of gel phase DMPC determined by X-Ray diffraction, *Biophys. J.* *83*, 3324-3335.
324. Nagle, J. F. & Tristram-Nagle, S. (2000) Structure of lipid bilayers, *BBA - Rev. Biomembranes.* *1469*, 159-195.
325. Lee, T.-H., Heng, C., Swann, M. J., Gehman, J. D., Separovic, F. & Aguilar, M.-I. (2010) Real-time quantitative analysis of lipid disordering by aurein 1.2 during membrane adsorption, destabilisation and lysis, *BBA - Biomembranes.* *1798*, 1977-1986.

326. Mashaghi, A., Swann, M., Popplewell, J., Textor, M. & Reimhult, E. (2008) Optical Anisotropy of Supported Lipid Structures Probed by Waveguide Spectroscopy and Its Application to Study of Supported Lipid Bilayer Formation Kinetics, *Anal. Chem.* *80*, 5276-5276.
327. Burnell, E. E., Cullis, P. R. & de Kruijff, B. (1980) Effects of tumbling and lateral diffusion on phosphatidylcholine model membrane ^{31}P -NMR lineshapes, *BBA - Biomembranes.* *603*, 63-69.
328. Bechinger, B., Aisenbrey, C. & Bertani, P. (2004) The alignment, structure and dynamics of membrane-associated polypeptides by solid-state NMR spectroscopy, *BBA - Biomembranes.* *1666*, 190-204.
329. Auguste, F., Douliez, J.-P., Bellocq, A.-M., Dufourc, E. J. & Gulik-Krzywicki, T. (1997) Evidence for multilamellar vesicles in the lamellar phase of an electrostatic lyotropic ternary system. A solid state ^2H -NMR and freeze fracture electron microscopy study, *Langmuir.* *13*, 666-672.
330. Diat, O. & Roux, D. (1993) Preparation of monodisperse multilayer vesicles of controlled size and high encapsulation ratio, *J. Phys. II.* *3*, 9-14.
331. Balla, M. S., Bowie, J. H. & Separovic, F. (2004) Solid-state NMR study of antimicrobial peptides from Australian frogs in phospholipid membranes, *Eur. Biophys. J.* *33*, 109-116.
332. Gehman, J. D., Luc, F., Hall, K., Lee, T.-H., Boland, M. P., Pukala, T. L., Bowie, J. H., Aguilar, M.-I. & Separovic, F. (2008) Effect of antimicrobial peptides from Australian tree frogs on anionic phospholipid membranes, *Biochemistry.* *47*, 8557-8565.
333. Smith, I. C. P. & Ekiel, I. H. (1984) Phosphorus-31 NMR of phospholipids in membranes in *Phosphorus-31 NMR. Principles and Applications* (Garenstein, D. G., ed) pp. 447-475, Academic Press Inc., London.
334. Yeagle, P. L. (1987) ^{31}P NMR and the phospholipid headgroups of membranes in *Phosphorus NMR in Biology* (Burt, C. T., ed) pp. 95-113, CRC Press, Florida.
335. Seelig, J. (1978) ^{31}P nuclear magnetic resonance and the head group structure of phospholipids in membranes, *Biochim. Biophys. Acta.* *515*, 105-140.
336. Balla, M. S., Bowie, J. H. & Separovic, F. (2004) Solid-state NMR study of antimicrobial peptides from Australian frogs in phospholipid membranes, *Eur. Biophys. J.* *33*, 109-16.
337. Wieprecht, T., Dathe, M., Beyermann, M., Krause, E., Maloy, W. L., MacDonald, D. L. & Bienert, M. (1997) Peptide hydrophobicity controls the activity and selectivity of magainin 2 amide in interaction with membranes, *Biochem.* *36*, 6133-6140.

338. Carr, H. Y. & Purcell, E. (1954) Effects of diffusion on free precession in nuclear magnetic resonance experiments, *Phys. Rev.* *94*, 630-638.
339. Hahn, E. (1950) Spin echos, *Phys. Rev.* *80*, 580-594.
340. Rance, M. & Byrd, R. A. (1983) Obtaining high-fidelity spin-1/2 powder spectra in anisotropic media: phase-cycled Hahn echo spectroscopy, *J. Magn. Reson.*
341. Niederberger, W. & Seelig, J. (1976) Phosphorus-31 chemical shift anisotropy in unsonicated phospholipid bilayers, *J. Am. Chem. Soc.* *98*, 3704-3706.
342. Lee, K. H., Fitton, J. E. & Wüthrich, K. (1987) Nuclear magnetic resonance investigation of the conformation of δ -haemolysin bound to dodecylphosphocholine micelles, *Biochim. Biophys. Acta.* *911*, 144-153.
343. Lafleur, M., Cullis, P. R., Fine, B. & Bloom, M. (1990) Comparison of the orientational order of lipid chains in the L_{α} and H_{II} Phases, *Biochemistry.* *29*, 8325-8333.
344. Lafleur, M., Fine, B., Sternin, E., Cullis, P. R. & Bloom, M. (1989) Smoothed orientational order profile of lipid bilayers by ^2H -nuclear magnetic resonance, *Biophys. J.* *56*, 1037-41.
345. Bloom, M., Davis, J. H. & MacKay, A. L. (1981) Direct determination of the oriented sample NMR spectrum from the powder spectrum for systems with local axial symmetry, *Chem. Phys. Lett.* *80*, 198-202.
346. Sternin, E., Bloom, M. & MacKay, A. L. (1983) De-Pake-ing of NMR spectra, *J. Magn. Reson.* *55*, 274-282.
347. Burnett, L. J. & Muller, B. H. (1971) Deuteron quadrupole coupling constants in three solid deuterated paraffin hydrocarbons: C_2D_6 , C_4D_{10} , C_6D_{14} , *J. Chem. Phys.* *55*, 5829-5831.
348. Bechinger, B., Zasloff, M. & Opella, S. J. (1992) Structure and interactions of magainin antibiotic peptides in lipid bilayers: A solid-state nuclear magnetic resonance investigation, *Biophys. J.* *62*, 12-14.
349. Yamaguchi, S., Huster, D., Waring, A., Lehrer, R. I., Kearney, W., Tack, B. F. & Hong, M. (2001) Orientation and dynamics of an antimicrobial peptide in the lipid bilayer by solid-state NMR spectroscopy., *Biophys. J.* *81*, 2203-2214.
350. de Planque, M. R. R., Greathouse, D. V., Koeppe, R. E., Schafer, H., Marsh, D. & Killian, J. A. (1998) Influence of lipid/peptide hydrophobic mismatch on the thickness of diacylphosphatidylcholine bilayers. A ^2H NMR and ESR study using designed transmembrane α -helical peptides and gramicidin A., *Biochem.* *37*, 9333-9345.

351. Banerjee, U., Zidovetzki, R., Birge, R. R. & Chan, S. I. (1985) Interaction of alamethicin with lecithin bilayers: A ^{31}P and ^2H NMR study, *Biochem.* 24, 7621-7627.
352. Duer, M. J. (2002) Essential Techniques for Spin-1/2 Nuclei in *Solid-state NMR spectroscopy: principles and applications* (Duer, M. J., ed) pp. 73-110, Blackwell Science Ltd., London.
353. Tyler, M. J. & Knight, F. (2009) *Field Guide to The Frogs of Australia*, CSIRO, Melbourne.
354. Watson, G. F., Loftus-Hills, J. J. & Littlejohn, M. J. (1971) The *Litoria ewingii* complex (Anura: Hylidae) in south-eastern Australia. 1. A new species from Victoria, *Aust. J. Zool.* 901, 401-416.
355. Anstis, M. (1974) Australian frogs. Part 2. The behaviour and life history of *Litoria verreauxi* (Hylidae), *Bull. Herpet.* 1, 19-21.
356. McCann, C. (1961) The introduced frogs of New Zealand, *Tuatara.* 8, 107-120.
357. Steinborner, S. T., Waugh, R. J., Bowie, J. H., Wallace, J. C., Tyler, M. J. & Ramsay, S. L. (1997) New caerin antibacterial peptides from the skin glands of the Australian tree frog *Litoria xanthomera*, *J. Pept. Sci.* 3, 181-185.
358. Stone, D. J. M., Waugh, R. J., Bowie, J. H., Wallace, J. C. & Tyler, M. J. (1992) Peptides from Australian frogs. Structures of the caerins and caeridin 1 from *Litoria splendida*, *J. Chem. Soc. Perkin Trans. 1*, 3173-3178.
359. Nix, H. A. & Kalma, J. D. (1972) Climate as a dominant control in the biogeography of northern Australia and New Guinea in *Bridge and barrier : the natural and cultural history of Torres Strait* (Walker, D., ed) pp. 66-91, Research School of Pacific Studies. Australian National University Publication BG/3.
360. Steinborner, S. T., Wabnitz, P. A., Waugh, R. J., Bowie, J. H., Gao, C. W., Tyler, M. J. & Wallace, J. C. (1996) The structures of new peptides from the Australian red tree frog *Litoria rubella* - the skin peptide profile as a probe for the study of evolutionary trends of amphibians, *Aust. J. Chem.* 49, 955-963.
361. Duméril, A. M. C. & Bibron, G. (1841) *Érpetologie générale ou histoire naturelle complete des reptiles.*, Roret, Paris.
362. Tyler, M. J. (1971) The phylogenetic significance of vocal sac structure in hylid frogs, *Univ. Kansas Publ. Mus. Nat. Hist.* 19, 319-360.
363. Peters, W. C. H. (1875) Las uber neue amphibien., *MbBA.* 1874, 616-624.

364. Ahl, E. (1935) Beschreibung eines neuen Laubfrosches aus Sudastralien, *Zoologische Anzeiger*. 109, 252-253.
365. Moore, J. A. (1961) The frogs of eastern New South Wales, *Bull. Am. Mus. Nat. His.* 121, 149-386.
366. Copeland, S. J. (1957) Australian frogs of the genus *Hyla*, *Proc. Linnean Soc. NSW.* 82, 9-108.
367. Jackway, R. J., Pukala, T. L., Donnellan, S. C., Sherman, P. J., Tyler, M. J. & Bowie, J. H. (2011) Skin peptide and cDNA profiling of Australian anurans: Genus and species identification and evolutionary trends, *Peptides*. 32, 161-172.
368. Steinborner, S. T., Bowie, J. H., Tyler, M. J. & Wallace, J. C. (1997) An unusual combination of peptides from the skin glands of Ewings tree frog, *Litoria ewingi* - sequence determination and antimicrobial activity, *Aust. J. Chem.* 50, 889-894.
369. Pukala, T. L., Bowie, J. H., Maselli, V. M., Musgrave, I. F. & Tyler, M. J. (2006) Host-defence peptides from the glandular secretions of amphibians: Structure and activity, *Nat. Prod. Rep.* 23, 368-393.
370. Montecucchi, P. C. (1985) Isolation and primary structure determination of amphibian skin tryptophyllins, *Peptides*. 6, 187-195.
371. Brinkworth, C. S., Dua, S., McAnoy, A. M. & Bowie, J. H. (2001) Negative ion fragmentations of deprotonated peptides: backbone cleavages directed through both Asp and Glu., *Rapid Commun. Mass Spectrom.* 15, 1965-1973.
372. Baudinette, R. V., Boontheung, P., Musgrave, I. F., Wabnitz, P. A., Maselli, V. M., Skinner, J., Alewood, P. A., Brinkworth, C. S. & Bowie, J. H. (2005) Eugenin: an immunomodulator used to protect young in the pouch of the tammar wallaby *Macropus eugenii*, *FEBS J.* 272, 433-439.
373. Jackway, R. J., Maselli, V. M., Musgrave, I. F., Maclean, M., Tyler, M. J. & Bowie, J. H. (2009) Skin peptides from anurans of the *Litoria rubella* Group: sequence determination using electrospray mass spectrometry. Opioid activity of two major peptides, *Rapid Commun. Mass Spectrom.* 23, 1189-1195.
374. Tyler, M. J. Unpublished observations.
375. Mirgorodskaya, O. A., Shevchenko, A. A., Chernushevich, I. V., Dodonov, A. F. & Miroshnikov, A. I. (1994) Electrospray ionization time-of-flight mass spectrometry in protein chemistry, *Analyt. Chem.* 66, 99-107.
376. Maeji, N. J., Bray, A. M., Valerio, R. M. & Wang, W. (1995) Larger scale multipin peptide synthesis, *J. Pept. Res.* 8, 33-38.

377. Kosterlitz, H. W. & Watt, A. J. (1968) Kinetic parameters of narcotic agonists and antagonist, with particular reference to N-allylnoroxymorphone (naloxone), *Br. J. Pharmacol.* 33, 266-276.
378. Birula, A. A. (1911) Arachnologische Beiträge. I. Zur Scorpionen- und Solifugen-Fauna des Chinesischen Reiches, *Revue Russe d'Entomologie.* 11, 195-199.
379. Teruel, R. (2002) First record of *Mesobuthus eupeus* (Koch, 1839) from western Turkey (Scorpions: Buthidae), *Rev. Iber. Aracnol.* 5, 75-76.
380. Shi, C.-M., Huang, Z.-S., Wang, L., He, L.-J. & Hua, Y.-P. (2007) Geographical distribution of two species of *Methobuthus* (scorpiones, buthidae) in China: Insights from systematic field surveys and predictive models, *J. Aracnol.* 35, 215-226.
381. Volkova T.M., G. A. F., Telezhinskaia I.N., Potapenko N.A., Grishin E.V. (1985) Neurotoxins from the venom of the Central Asian scorpion *Buthus eupeus*, *Bioorg. Khim.* 11, 1445-1456.
382. Grishin E.V., S. L. N., Soldatov N.M., Kostetsky P.V., Ovchinnikov Y.A. (1979) Amino acid sequence of insectotoxin I2 from central Asia scorpion *Buthus eupeus* venom., *Bioorg. Khim.* 5.
383. Tytgat, J., Debont, T., Rostoll, K., Müller, G. J., Verdonck, F., Daenens, P., van der Walt, J. J. & Possani, L. D. (1998) Purification and partial characterization of a 'short' insectotoxin-like peptide from the venom of the scorpion *Parabuthus schlechteri*, *FEBS Lett.* 441, 387-391.
384. Lomize, A. L., Maïorov V. N., Arseniev A.S. (1991) Determination of the spatial structure of insectotoxin I5A from *Buthus erpeus* by ¹H-NMR spectroscopy data, *Bioorg. Khim.* 17, 1613-1632.
385. Adamovich T.B., N. I. V., Grishin E.V., Ovchinnikov Y.A. (1977) Amino acid sequence of insectotoxin I1 from the venom of middle-asian scorpion *Buthus eupeus*, *Bioorg. Khim.* 3, 485-493.
386. Korolkova, Y. V., Kozlov, S. A., Lipkin, A. V., Pluzhnikov, K. A., Hadley, J. K., Filippov, A. K., Brown, D. A., Angelo, K., Strøbaek, D., Jespersen, T., Olesen, S. P., Jensen, B. S. & Grishin, E. V. (2001) An ERG channel inhibitor from the scorpion *Buthus eupeus*, *J. Biol. Chem.* 276, 9868-9876.
387. Gao, B., Xu, J., del Carmen Rodriguez, M., Lanz-Mendoza, H., Hernández-Rivas, R., Du, W. & Zhu, S. (2010) Characterization of two linear cationic antimalarial peptides in the scorpion *Mesobuthus eupeus*, *Biochimie.* 92, 350-359.

388. Gao, B., Peigneur, S., Tytgat, J. & Zhu, S. (2010) A potent potassium channel blocker from *Mesobuthus eupeus* scorpion venom, *Biochimie. In Press, Corrected Proof*.
389. Zhu S., G. B., Aumelas A., Del Carmen Rodriguez M., Lanz-Mendoza H., Peigneur S., Diego-Garcia E., Martin-Eauclaire M.-F., Tytgat J., Possani L.D. (2010) MeuTXKbeta1, a scorpion venom-derived two-domain potassium channel toxin-like peptide with cytolytic activity, *Biochim. Biophys. Acta. 1804*, 872-883.
390. Hultmark, D. (1998) Quantification of antimicrobial activity, using the inhibition-zone assay in *Techniques in Insect Immunology* (Wiesner, A., Dumphy, A. G., Marmaras, V. J., Morishima, I., Sugumaran, M., Yamakawa, M., ed) pp. 103-107, SOS Publications, New Jersey.
391. Dempsey, C. E. (1990) The actions of melittin on membranes, *BBA - Rev. Biomembranes. 1031*, 143-161.
392. Smith, R., Separovic, F., Milne, T. J., Whittaker, A., Bennett, F. M., Cornell, B. A. & Makriyannis, A. (1994) Structure and orientation of the pore-forming peptide, melittin, in lipid bilayers, *J. Mol. Biol. 241*, 456-66.
393. Schiffer, M. & Edmundson, A. B. (1967) Use of helical wheels to represent the structures of proteins and to identify segments with helical potential, *Biophys. J. 7*, 121-135.
394. Wüthrich, K. & Wider, G. (1982) Sequential resonance assignments as a basis for determination of spatial protein structures by high resolution proton nuclear magnetic resonance, *J. Mol. Biol. 155*, 311-319.
395. Zhou, N. E., Zhu, B., Sykes, B. D. & Hodges, R. S. (1992) Relationship between amide proton chemical shifts and hydrogen bonding in amphipathic α -helical peptides, *J. Am. Chem. Soc. 114*, 4320-4326.
396. Pukala, T. L., Doyle, J. R., Llewellyn, L. E., Kuhn-Nentwig, L., Apponyi, M. A., Separovic, F. & Bowie, J. H. (2007) Cupiennin 1a, an antimicrobial peptide from the venom of the neotropical wandering spider *Cupiennius salei*, also inhibits the formation of nitric oxide by neuronal nitric oxide synthase, *FEBS J. 274*, 1778-1784.
397. Wegener, K. L., Carver, J. A. & Bowie, J. H. (2003) The solution structures and activity of caerin 1.1 and caerin 1.4 in aqueous trifluoroethanol and dodecylphosphocholine micelles, *Biopolymers. 69*, 42-59.
398. Pukala, T. L., Brinkworth, C. S., Carver, J. A. & Bowie, J. H. (2004) Investigating the importance of the flexible hinge in caerin 1.1: Solution structures and activity of two synthetically modified caerin peptides, *Biochemistry. 43*, 937-944.

399. Wuthrich, K. (1986) *NMR of Proteins and nucleic acids.*, John Wiley and Sons, New York.
400. Nilges, M., Macias, M. J., Odonoghue, S. I. & Oschkinat, H. (1997) Automated NOESY interpretation with ambiguous distance restraints - the refined NMR solution structure of the pleckstrin homology domain from β -spectrin, *J. Mol. Biol.* **269**, 408-422.
401. Nilges, M. & O'Donoghue, S. I. (1998) Ambiguous NOEs and automated NOE assignment, *Prog. Nucl. Magn. Reson. Spectrosc.* **32**, 107-139.
402. Monne, M., Nilsson, I., Elofsson, A. & von Heijne, G. (1999) Turns in transmembrane helices: Determination of the minimal length of a 'helical hairpin' and derivation of a fine-grained turn propensity scale, *J. Mol. Biol.* **293**, 807-814.
403. Kuhn-Nentwig, L. (2003) Antimicrobial and cytolytic peptides of venomous arthropods, *Cell. Mol. Life Sci.* **60**, 2651-2668.
404. Koradi, R., Billeter, M. & Wüthrich, K. (1996) MOLMOL - a program for display and analysis of macromolecular structures, *J. Mol. Graphics.* **14**, 51-55.
405. Humphrey, W., Dalke, A. & Schulten, K. (1996) VMD - visual molecular dynamics, *J. Mol. Graphics.* **14**, 33-38.
406. Boman, H. G. (2003) Antibacterial peptides: Basic facts and emerging concepts, *J. Int. Med.* **254**, 197-215.
407. Putsep, K., Branden, C., Boman, H. G. & Normark, S. (1999) Antibacterial peptides from *H. pylori*, *Nature.* **398**, 671-672.
408. Mor, A., Hani, K. & Nicolas, P. (1994) The vertebrate peptide antibiotics dermaseptins have overlapping structural features but target specific microorganisms, *J. Biol. Chem.* **269**, 31635-31641.
409. Smet, K. & Contreras, R. (2005) Human antimicrobial peptides: Defensins, cathelicidins and histatins, *Biotechnol. Lett.* **27**, 1337-1347.
410. Sitaram, N. & Nagaraj, R. (2002) The therapeutic potential of host-defense antimicrobial peptides, *Curr. Drug Targets.* **3**, 259-267.
411. Giuliani, A., Pirri, G. & Nicoletto, S. (2007) Antimicrobial peptides: an overview of a promising class of therapeutics, *Cent. Eur. J. Biol.* **2**, 1-33.
412. Lai, R., Liu, H., Hui Lee, W. & Zhang, Y. (2002) An anionic antimicrobial peptide from toad *Bombina maxima*, *Biochem. Biophys. Res. Commun.* **295**, 796-799.

413. Zasloff, M. (1987) Magainins, a class of antimicrobial peptides from *Xenopus* skin: Isolation, characterization of two active forms, and partial cDNA sequence of a precursor, *Proc. Natl. Acad. Sci.* *84*, 5449-5453.
414. Strandberg, E., Tiltak, D., Ieronimo, M., Kanithasen, M., Wadhvani, P. & Ulrich, A. S. (2007) Influence of C-terminal amidation on the antimicrobial and haemolytic activities of cationic α -helical peptides, *Pure Appl. Chem.* *79*, 717-728.
415. Giangaspero, A., Sandri, L. & Tossi, A. (2001) Amphipathic alpha helical antimicrobial peptides, *Eur. J. Biochem.* *268*, 5589-5600.
416. Zelezetsky, I. & Tossi, A. (2006) Alpha-helical antimicrobial peptides - using a sequence template to guide structure-activity relationship studies, *BBA - Biomembranes.* *1758*, 1436-1449.
417. Shai, Y. (1995) Molecular recognition between membrane-spanning polypeptides, *Trends Biochem. Sci.* *20*, 460-464.
418. Epand, R. M., Shai, Y. C., Segrest, J. P. & Anantharamaiah, G. M. (1995) Mechanisms for the modulation of membrane bilayer properties by amphipathic helical peptides, *Biopolymers.* *37*, 319-338.
419. Huang, H. W. (2000) Action of antimicrobial peptides: Two-state model, *Biochemistry.* *39*, 8347-8352.
420. Ludtke, S. J., He, K., Heller, W. T., Harroun, T. A., Yang, L. & Huang, H. W. (1996) Membrane pores induced by magainin, *Biochemistry.* *35*, 13723-13728.
421. Brogden, K. A. (2005) Antimicrobial peptides: pore formers or metabolic inhibitors in bacteria?, *Nat. Rev. Micro.* *3*, 238-250.
422. Cornell, B. A., Separovic, F., Baldassi, A. J. & Smith, R. (1988) Conformation and orientation of gramicidin A in oriented phospholipid bilayers measured by solid state carbon-13 NMR, *Biophys. J.* *53*, 67-76.
423. DiRienzo, J. M., Nakamura, K. & Inouye, M. (1978) The outer membrane proteins of Gram-negative bacteria: biosynthesis assembly and functions, *Ann. Rev. Biochem.* *47*, 481-532.
424. Niederweis, M. (2003) Mycobacterial porins – new channel proteins in unique outer membranes, *Mol. Microbiol.* *49*, 1167-1177.
425. Matsuzaki, K., Sugishita, K., Fujii, N. & Miyajima, K. (1995) Molecular basis for membrane selectivity of an antimicrobial peptide, magainin 2, *Biochemistry.* *34*, 3423-3429.

426. Stankowski, S., Schwartz, U. D. & Schwartz, G. (1988) Voltage-dependent pore activity of the peptide alamethicin correlated with incorporation in the membrane: Salt and cholesterol effects, *BBA - Biomembranes*. 941, 11-18.
427. Mattila, K., Kinder, R. & Bechinger, B. (1999) The alignment of a voltage-sensing peptide in dodecylphosphocholine micelles and in oriented lipid bilayers by nuclear magnetic resonance and molecular modeling, *Biophys. J.* 77, 2102-2113.
428. Jackway, R. J., Bowie, J. H., Bilusich, D., Musgrave, I. F., Surinya-Johnson, K. H., Tyler, M. J. & Eichinger, P. C. (2008) The fallaxidin peptides from the skin secretion of the Eastern Dwarf Tree Frog *Litoria fallax*. Sequence determination by positive and negative ion electrospray mass spectrometry: antimicrobial activity and cDNA cloning of the fallaxidins, *Rapid Commun. Mass Spectrom.* 22, 3211-3519.
429. Wang, Z. & Wang, G. (2004) APD: The antimicrobial peptide database, *Nucleic Acids Res.* 32, D590-D592.
430. Jackway, R. J. (2008) *Biologically Active Peptides from Australian Amphibians*, Chemistry Ph. D. Thesis, The University of Adelaide.
431. Bechinger, B. (2005) Detergent-like properties of magainin antibiotic peptides: a ^{31}P solid-state NMR spectroscopy study, *BBA - Biomembranes*. 1712, 101-108.
432. Lu, J., Damodaran, K., Blazyk, J. & Lorigan, G. A. (2005) Solid-state nuclear magnetic resonance relaxation studies of the interaction mechanism of antimicrobial peptides with phospholipid bilayer systems, *Biochemistry*. 44, 10208-10217.
433. Spooner, P. J. R. & Watts, A. (1991) Reversible unfolding of cytochrome C upon interaction with cardiolipin bilayers. II. Evidence from phosphorus-31 NMR measurements, *Biochemistry*. 30, 3880-3885.
434. Lu, D., Vavasour, I. & Morrow, M. R. (1995) Smoothed acyl chain orientational order parameter profiles in dimyristoylphosphatidylcholine-distearoylphosphatidylcholine mixtures: a ^2H -NMR study, *Biophys. J.* 68, 574-83.
435. Watts, A. (1998) Solid-state NMR approaches for studying the interaction of peptides and proteins with membranes, *BBA - Rev. Biomembranes*. 1376, 297-318.
436. Tiburu, E. K., Karp, E. S., Birrane, G., Struppe, J. O., Chu, S., Lorigan, G. A., Avraham, S. & Avraham, H. K. (2006) ^{31}P and ^2H relaxation studies of helix VII and the cytoplasmic helix of the human cannabinoid receptors utilizing solid-state NMR techniques, *Biochemistry*. 45, 7356-7365.
437. Mechler, A., Praporski, S., Atmuri, K., Boland, M., Separovic, F. & Martin, L. L. (2007) Specific and selective peptide-membrane interactions revealed using Quartz Crystal Microbalance, *Biophys. J.* 93, 3907-3916.

438. Mechler, A., Praporski, S., Piantavigna, S., Heaton, S. M., Hall, K. N., Aguilar, M.-I. & Martin, L. L. (2009) Structure and homogeneity of pseudo-physiological phospholipid bilayers and their deposition characteristics on carboxylic acid terminated self-assembled monolayers, *Biomaterials*. *30*, 682-689.
439. Piantavigna, S., Czihal, P., Mechler, A., Richter, M., Hoffmann, R. & Martin, L. (2009) Cell penetrating apidaecin peptide interactions with biomimetic phospholipid membranes, *Int. J. Pept. Res. Therapeut.* *15*, 139-146.
440. Massiot, D., Fayon, F., Capron, M., King, I., Calvé, S. L., Alonso, B., Durand, J.-O., Bujoli, B., Gan, Z. & Hoatson, G. (2002) Modelling one- and two-dimensional solid-state NMR spectra, *Magn. Reson. Chem.* *40*, 70-76.
441. Otten, D., Brown, M. F. & Beyer, K. (2000) Softening of membrane bilayers by detergents elucidated by deuterium NMR spectroscopy, *J. Phys. Chem. B*. *104*, 12119-12129.
442. Boden, N., Jones, S. A. & Sixl, F. (1991) On the use of deuterium nuclear magnetic resonance as a probe of chain packing in lipid bilayers, *Biochemistry*. *30*, 2146-55.
443. Du, B. Y. & Johansson, D. (2004) Operation of the quartz crystal microbalance in liquids: derivation of the elastic compliance of a film from the ratio of bandwidth shift and frequency shift, *Langmuir*. *20*, 2809-2812.
444. Gunasekaran, K., Nagarajaram, H. A., Ramakrishnan, C. & Balaram, P. (1998) Stereochemical punctuation marks in protein structures: glycine and proline containing helix stop signals, *J. Mol. Biol.* *275*, 917-932.
445. Woolfson, D. N. & Williams, D. H. (1990) The influence of proline residues on α -helical structure, *FEBS Lett.* *277*, 185-188.
446. Kim, S., Jacobs, R. E. & White, S. H. (1985) Preparation of multilamellar vesicles of defined size-distribution by solvent-spherule evaporation, *BBA - Biomembranes*. *812*, 793-801.
447. Kohler, S. J. & Klein, M. P. (1977) Orientation and dynamics of phospholipid head groups in bilayers and membranes determined from ^{31}P nuclear magnetic resonance chemical shielding tensors, *Biochemistry*. *16*, 519-26.
448. Yang, L., Harroun, T. A., Weiss, T. M., Dong, L. & Huang, H. W. (2001) Barrel-stave model or toroidal model? A case study on melittin pores, *Biophys. J.* *81*, 1475-1485.

449. Castle, M., Nazarian, A., Yi, S. S. & Tempst, P. (1999) Lethal effects of apidaecin on *Escherichia coli* involve sequential molecular interactions with diverse targets, *J. Biol. Chem.* 274, 32555-32564.
450. Ambroggio, E. E., Separovic, F., Bowie, J. H., Fidelio, G. D. & Bagatolli, L. A. (2005) Direct Visualization of Membrane Leakage Induced by the Antibiotic Peptides: Maculatin, Citropin, and Aurein, *Biophys. J.* 89, 1874-1881.
451. Han, M., Mei, Y., Khant, H. & Ludtke, S. J. (2008) Pore Formation by Antimicrobial Peptide, Magainin 2, in Phospholipid Vesicles Detected and Visualized by Cryo-Electron Microscopy, *Microsc. Microanal.* 14, 1610-1611.
452. Whittall, K. P., Sternin, E., Bloom, M. & Mackay, A. L. (1989) Time- and frequency-domain "dePakeing" using inverse theory, *J. Mag. Reson.* 84, 64-71.
453. Galassi, M., Davies, J., Theiler, J., Gough, B., Jungman, G., Booth, M. & Rossi, F. (2008) *GNU Scientific Library*, 1.11 edn.
454. Williams, T., Kelley, C., Campbell, J., Kotz, D. & Lang, R. (2007) *gnuplot, An Interactive Plotting Program*, The Free Software Foundation.
455. Ahmed, S. A., Gogal, R. M. & Walsh, J. E. (1994) A new rapid and simple non-radioactive assay to monitor and determine the proliferation of lymphocytes: An alternative to [³H]thymidine incorporation assay, *J. Immunol. Methods.* 170, 211-224.
456. Wank, S. A., Pisegna, J. R. & De Weerth, A. (1994) Cholecystokinin receptor family: molecular cloning, structure, and functional expression in rat, guinea pig and human, *Ann. N. Y. Acad. Sci.* 713, 49-66.
457. Lay, J. M., Jenkins, C., Friis-Hansen, L. & Samuelson, L. C. (2000) Structure and developmental expression of the mouse CCK-B receptor gene, *Biochem. Biophys. Res. Commun.* 272, 837-842.
458. Gysin, B. & Schwyzer, R. (1983) Liposome-mediated labeling of adrenocorticotropin fragments parallels their biological activity, *FEBS Lett.* 158, 12-16.
459. Schoch, P., Sargent, D. F. & Schwyzer, R. (1979) Hormone-receptor interactions: Corticotropin-(1-24)-tetracosapeptide spans artificial lipid bilayer membranes, *Biochem. Soc. Trans.* 7, 846-849.
460. Gremlich, H. U., Sargent, D. F. & Schwyzer, R. (1981) The adsorption of adrenocorticotropin-(1-24)-tetracosapeptide to lecithin bilayer membranes formed from liposomes, *Eur. Biophys. J.* 8, 61-65.

461. Gysin, B. & Schwyzer, R. (1983) Head group and structure specific interactions of enkephalins and dynorphin with liposomes: Investigation by hydrophobic photolabeling, *Arch. Biochem. Biophys.* 225, 467-474.
462. Gremlich, H. U., Fringeli, U. P. & Schwyzer, R. (1983) Conformational changes of adrenocorticotropin peptides upon interaction with lipid membranes revealed by infrared attenuated total reflection spectroscopy, *Biochemistry.* 22, 4257-4264.
463. Gremlich, H. U., Fringeli, U. P. & Schwyzer, R. (1984) Interaction of adrenocorticotropin-(11-24)-tetradecapeptide with neutral lipid membranes revealed by infrared attenuated total reflection spectroscopy, *Biochemistry.* 23, 1808-1810.
464. Erne, D., Sargent, D. F. & Schwyzer, R. (1985) Preferred conformation, orientation, and accumulation of dynorphin A-(1-13)-tridecapeptide on the surface of neutral lipid membranes, *Biochemistry.* 24, 4261-4263.
465. Spector, A. A. & Yorek, M. A. (1985) Membrane lipid composition and cellular function, *J. Lipid Res.* 26, 1015-35.
466. Hiramatsu, K. & Arimori, S. (1982) Rapid determination of lipids in healthy human lymphocytes, *J. Chromatogr. B.* 227, 423-431.
467. Mitchell, T. W., Ekroos, K., Blanksby, S. J., Hulbert, A. J. & Else, P. L. (2007) Differences in membrane acyl phospholipid composition between an endothermic mammal and an ectothermic reptile are not limited to any phospholipid class, *J. Exp. Biol.* 210, 3440-3450.
468. Seelig, A., Seelig, J. & Robert, A. M. (2001) Membrane structure in *Encyclopedia of physical science and technology* pp. 355-367, Academic Press, New York.
469. Daleke, D. L. (2003) Regulation of transbilayer plasma membrane phospholipid asymmetry, *J. Lipid Res.* 44, 233-242.
470. Wank, S. A. (1998) G Protein-Coupled receptors in gastrointestinal physiology I. CCK receptors: an exemplary family, *Am. J. Physiol. Gastrointest. Liver Physiol.* 274, G607-613.
471. Noble, F. & Roques, B. P. (1999) CCK-B receptor: Chemistry, molecular biology, biochemistry and pharmacology, *Prog. Neurobiol.* 58, 349-379.
472. Lignon, M.-F., Bernad, N. & Martinez, J. (1991) Pharmacological characterisation of type B cholecystokinin binding sites on the human JURKAT T lymphocyte cell line, *Mol. Pharmacol.* 39, 615-620.
473. Lignon, M.-F., Bernad, N. & Martinez, J. (1994) Cholecystokinin receptors in cells of the immune system, *Ann. N. Y. Acad. Sci.* 713, 334-336.

474. Sacerdote, P., Wiedermann, C. J., Wahl, L. M., Pert, C. B. & Ruff, M. R. (1991) Visualization of cholecystokinin receptors on a subset of human monocytes and in rat spleen, *Peptides*. *12*, 167-176.
475. Roosenburg, S., Laverman, P., van Delft, F. & Boerman, O. (2011) Radiolabeled CCK/gastrin peptides for imaging and therapy of CCK2 receptor-expressing tumors, *Amino Acids*. *41*, 1049-1058.
476. Palczewski, K., Kumasaka, T., Hori, T., Behnke, C. A., Motoshima, H., Fox, B. A., Trong, I. L., Teller, D. C., Okada, T., Stenkamp, R. E., Yamamoto, M. & Miyano, M. (2000) Crystal structure of rhodopsin: A G protein-coupled receptor, *Science*. *289*, 739-745.
477. Wank, S. A. (1995) Cholecystokinin receptors, *Am. J. Physiol. Gastrointest. Liver Physiol*. *269*, G628-646.
478. Galés, C., Poirot, M., Taillefer, J., Maigret, B., Martinez, J., Moroder, L., Escrieut, C., Pradayrol, L., Fourmy, D. & Silvente-Poirot, S. (2003) Identification of tyrosine 189 and asparagine 358 of the cholecystokinin 2 receptor in direct interaction with the crucial C-terminal amide of cholecystokinin by molecular modeling, site-directed mutagenesis, and structure/affinity studies, *Mol. Pharmacol*. *63*, 973-982.
479. Jagerschmidt, A., Guillaume, N., Roques, B. P. & Noble, F. (1998) Binding sites and transduction process of the cholecystokinin B receptor: Involvement of highly conserved aromatic residues of the transmembrane domains evidenced by site-directed mutagenesis, *Mol. Pharmacol*. *53*, 878-885.
480. Stone, S. R., Giragossian, C., Mierke, D. F. & Jackson, G. E. (2007) Further evidence for a C-terminal structural motif in CCK2 receptor active peptide hormones, *Peptides*. *28*, 2211-2222.
481. Pellegrini, M. & Mierke, D. F. (1999) Molecular complex of cholecystokinin-8 and N-terminus of the cholecystokinin A receptor by NMR Spectroscopy, *Biochemistry*. *38*, 14775-14783.
482. Giragossian, C. & Mierke, D. F. (2002) Intermolecular interactions between cholecystokinin-8 and the third extracellular loop of the choleocystokinin-2 receptor, *Biochemistry*. *41*, 4560-4566.
483. Rose, G. D., Gierasch, L. M. & Smith, J. S. (1985) Turns in peptides and proteins, *Adv. Protein Chem*. *37*, 1-109.
484. Richardson, J. S. (1981) The anatomy and taxonomy of protein structure, *Adv. Protein Chem*. *34*, 167-339.

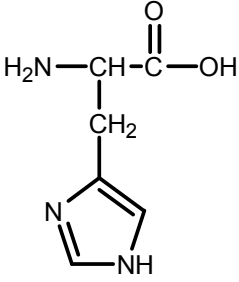
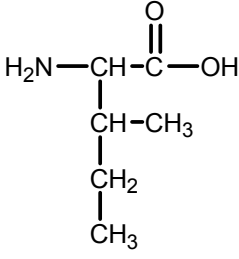
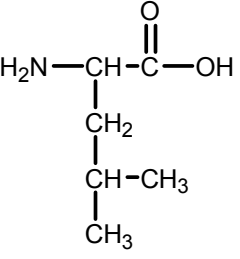
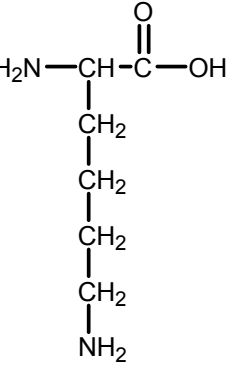
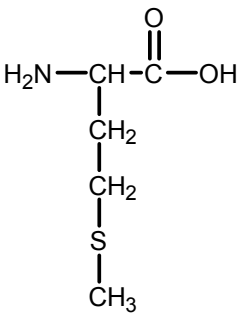
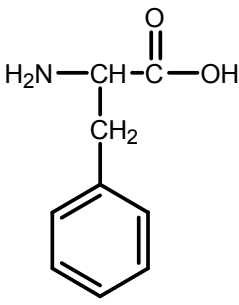
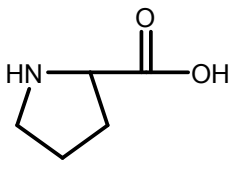
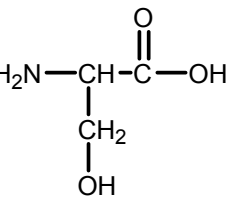
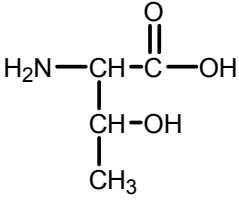
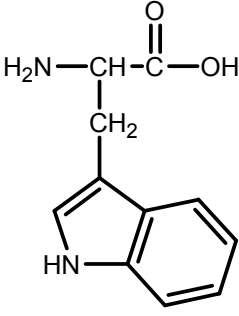
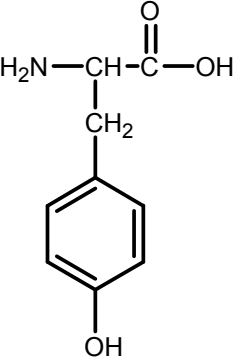
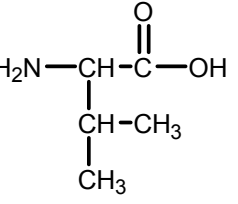
485. Panasik, N., Fleming, P. J. & Rose, G. D. (2005) Hydrogen-bonded turns in proteins: The case for a recount, *Protein Sci.* *14*, 2910-2914.
486. Silvente-Poirot, S., Escrieut, C., Galés, C., Fehrentz, J. A., Escherich, A., Wank, S. A., Martinez, J., Moroder, L., Maigret, B., Bouisson, M., Vaysse, N. & Fourmy, D. (1999) Evidence for a direct interaction between the penultimate C-terminal aspartic acid of cholecystinin and histidine 207 located in the second extracellular loop of the cholecystinin B receptor, *J. Biol. Chem.* *274*, 23191-23197.
487. Marcotte, I., Dufourc, E. J., Ouellet, M. & Auger, M. (2003) Interaction of the neuropeptide met-enkephalin with Zwitterionic and negatively charged bicelles as viewed by ^{31}P and ^2H solid-state NMR, *Biophys. J.* *85*, 328-339.
488. Eisenberg, D. (1984) Three-dimensional structure of membrane and surface proteins, *Annu. Rev. Biochem.* *53*, 595-623.
489. Cuq, P., Gross, A., Terraza, A., Fourmy, D., Clerc, P., Donand, J. & Magous, R. (1997) mRNAs encoding CCK_B but not CCK_A receptors are expressed in human T lymphocytes and Jurkat lymphoblastoid cells, *Life Sci.* *61*, 543-555.
490. Dornard, J., Roche, S., Michel, T., Bali, J. P. & Magous, R. (1995) Gastrin CCKB type receptors on human T lymphoblastoid Jurkat cells, *Am. J. Physiol.* *268*, G552-G529.
491. Iwara, N., Marayama, T., Matsumori, Y., Ito, M., Nagata, A., Taniguchi, T., Chikara, K., Matsuo, Y., Minowada, J. & Matsui, T. (1996) Autocrine loop through CCKB/gastrin receptors involved in the growth of human leukemia cells, *Blood.* *88*, 2683-2689.
492. Sarkadi, B., Tordai, A. & Gárdos, G. (1990) Membrane depolarization selectively inhibits receptor-operated calcium channels in human T (Jurkat) lymphoblasts, *BBA - Biomembranes.* *1027*, 130-140.
493. Mozsolits, H., Wirth, H.-J., Werkmeister, J. & Aguilar, M.-I. (2001) Analysis of antimicrobial peptide interactions with hybrid bilayer membrane systems using surface plasmon resonance, *BBA - Biomembranes.* *1512*, 64-76.
494. John, B. K., Plant, D., Webb, P. & Hurd, R. E. (1992) Effective combination of gradients and crafted RF pulses for water suppression in biological samples, *J. Magn. Res.* *98*, 200-206.

Appendices

Appendix A

The 20 common amino acids, abbreviations and nominal masses.

<p>Alanine</p> $\begin{array}{c} \text{O} \\ \parallel \\ \text{H}_2\text{N}-\text{CH}-\text{C}-\text{OH} \\ \\ \text{CH}_3 \end{array}$ <p>Ala (A) 71 Da</p>	<p>Arginine</p> $\begin{array}{c} \text{O} \\ \parallel \\ \text{H}_2\text{N}-\text{CH}-\text{C}-\text{OH} \\ \\ \text{CH}_2 \\ \\ \text{CH}_2 \\ \\ \text{CH}_2 \\ \\ \text{NH} \\ \\ \text{C}=\text{NH} \\ \\ \text{NH}_2 \end{array}$ <p>Arg (R) 156 Da</p>	<p>Asparagine</p> $\begin{array}{c} \text{O} \\ \parallel \\ \text{H}_2\text{N}-\text{CH}-\text{C}-\text{OH} \\ \\ \text{CH}_2 \\ \\ \text{C}=\text{O} \\ \\ \text{NH}_2 \end{array}$ <p>Asn (N) 114 Da</p>	<p>Aspartic acid</p> $\begin{array}{c} \text{O} \\ \parallel \\ \text{H}_2\text{N}-\text{CH}-\text{C}-\text{OH} \\ \\ \text{CH}_2 \\ \\ \text{C}=\text{O} \\ \\ \text{OH} \end{array}$ <p>Asp (D) 115 Da</p>
<p>Cystine</p> $\begin{array}{c} \text{O} \\ \parallel \\ \text{H}_2\text{N}-\text{CH}-\text{C}-\text{OH} \\ \\ \text{CH}_2 \\ \\ \text{SH} \end{array}$ <p>Cys (C) 103 Da</p>	<p>Glutamic acid</p> $\begin{array}{c} \text{O} \\ \parallel \\ \text{H}_2\text{N}-\text{CH}-\text{C}-\text{OH} \\ \\ \text{CH}_2 \\ \\ \text{CH}_2 \\ \\ \text{C}=\text{O} \\ \\ \text{OH} \end{array}$ <p>Glu (E) 129 Da</p>	<p>Glutamine</p> $\begin{array}{c} \text{O} \\ \parallel \\ \text{H}_2\text{N}-\text{CH}-\text{C}-\text{OH} \\ \\ \text{CH}_2 \\ \\ \text{CH}_2 \\ \\ \text{C}=\text{O} \\ \\ \text{NH}_2 \end{array}$ <p>Gln (Q) 128 Da</p>	<p>Glycine</p> $\begin{array}{c} \text{O} \\ \parallel \\ \text{H}_2\text{N}-\text{CH}-\text{C}-\text{OH} \\ \\ \text{H} \end{array}$ <p>Gly (G) 57 Da</p>

<p>Histidine</p>  <p>His (H) 147 Da</p>	<p>Isoleucine</p>  <p>Ile (I) 113 Da</p>	<p>Leucine</p>  <p>Leu (L) 113 Da</p>	<p>Lysine</p>  <p>Lys (K) 128 Da</p>
<p>Methionine</p>  <p>Met (M) 131 Da</p>	<p>Phenylalanine</p>  <p>Phe (F) 147 Da</p>	<p>Proline</p>  <p>Pro (P) 97 Da</p>	<p>Serine</p>  <p>Ser (S) 71 Da</p>
<p>Threonine</p>  <p>Thr (T) 101 Da</p>	<p>Tryptophane</p>  <p>Trp (W) 186 Da</p>	<p>Tyrosine</p>  <p>Tyr (Y) 163 Da</p>	<p>Valine</p>  <p>Val (V) 99 Da</p>

Appendix B

Amino acid sequence alignment of human (CCKBR), mouse (MUCCKBR) and guinea pig (GPCCKRB) type II cholecystokinin receptors.

>Protein alignment 2 Alignment of 2 sequences: GPCCKRB, MCKCKBR

Score = 2061.0, Identities = 398/455 (87%), Positives = 420/455 (92%), Gaps = 4/455 (0%)

```

GPCCKRB      1 MELLKLNRSLSQGP GPGAPICRPAGPLLNSSGAGNLSCE TPRI RAGT RELELAIRITL  60
M+LLKLNRSLSQGP GPG G+ LCRP LLNSS AGNLSCE TPRI RGTRELEL IRITL
MCKCKBR      1 MDLLKLNRSLSQGP GPGSSSLCRPGVSLLNSSSAGNLSCE TPRI RGTRELELTIRITL  60

GPCCKRB     61 YAVIFLMSVGGNMLIIVVLGLSRRLRTVTNAFLLSLAVSDLLLAVACMPFTLLPNLMGTF 120
YAVIFLMSVGGN+LIIVVLGLSRRLRTVTNAFLLSLAVSDLLLAVACMPFTLLPNLMGTF
MCKCKBR     61 YAVIFLMSVGGNVLIIIVVLGLSRRLRTVTNAFLLSLAVSDLLLAVACMPFTLLPNLMGTF 120

GPCCKRB    121 IFGTVICKAVSYLMGVSVSVSTLSLVAIALERYSAICRPLQARVWQTRSHAARVIVATWL 180
IFGTVICKAVSYLMGVSVSVSTL+L AIALERYSAICRPLQARVWQTRSHAARVI+ATWL
MCKCKBR    121 IFGTVICKAVSYLMGVSVSVSTLNLA AIALERYSAICRPLQARVWQTRSHAARVILATWL 180

GPCCKRB    181 LSGLLMVPYPVYTVVQPVGPRVLQCVHRWPSARVRQTWSVLLLLLLLFFVPGVVMVAVAYGL 240
LSGLLMVPYPVYTVVQPVGPR+LQC+H WPS RV+Q WSVLLL+LLFF+PGVVMVAVAYGL
MCKCKBR    181 LSGLLMVPYPVYTVVQPVGPRILQCMHLWPSERVQQMWSVLLLLLLLFFIPGVVMVAVAYGL 240

GPCCKRB    241 ISRELYLGLRFDGDADSESQSRVRGRGGLSG--SAPGPAHQNGRCRPESGLSGEDSDGCV 298
ISRELYLGLRFDGD DSE+QSRVR +GGL G +APGP HQNG CR + L+GEDSDGCV
MCKCKBR    241 ISRELYLGLRFDGDNDSETQSRVRNQGG LPGA AAPGPVHQNGGCRHVTSLTGEDSDGCV 300

GPCCKRB    299 VQLPRSRPALELSALAASTPAPGPGSRPTQAKLLAKKRVRMMLLVIVLFFFLCWLVPVYSA 358
VQLPRSR LE++ L T PGP RP QAKLLAKKRVRMMLLVIV+LFF+CWLVPVYSA
MCKCKBR    301 VQLPRSR--LEMTLTTPTTGP GPGPRPNQAKLLAKKRVRMMLLVIVLFFVVCWLVPVYSA 358

GPCCKRB    359 NTWRAFDGPGAHRALSGAPISFIHLLSYASACVNPLVYCFMHRRFRQACLET CARCCPRP 418
NTWRAFDGPGA RAL+GAPISFIHLLSY SAC NPLVYCFMHRRFRQACL+TCARCCPRP
MCKCKBR    359 NTWRAFDGPGARRALAGAPISFIHLLSYTSACANPLVYCFMHRRFRQACLDTCARCCPRP 418

GPCCKRB    419 PRARPRPLPEEDPPTPSIASLSRSLSYTTISTLGP 453
PRARPRPLP+EDPPTPSIASLSRSLSYTTISTLGP
MCKCKBR    419 PRARPRPLPEEDPPTPSIASLSRSLSYTTISTLGP 453

```


Appendices

>Protein alignment 3 Alignment of 2 sequences: GPCCKRB, HUCCKBR

Score = 2162.0, Identities = 423/453 (93%), Positives = 431/453 (95%), Gaps = 6/453 (1%)

```

GPCCKRB      1 MELLKLNRS LQGP GPGAP LCRPAG PLLNSSGAGNLS CETPRIRGAGT RELELAIRITL 60
                MELLKLNRS+QG GPGPGA LCRP  PLLNSS  GNLSCE PRIRGAGT RELELAIRITL
HUCCKBR      1 MELLKLNRSVQGTGPGPGAS LCRPAG PLLNSSSVGNLSCEP PRIRGAGT RELELAIRITL 60

GPCCKRB     61 YAVIFLMSVGGNMLIIIVVLG LSRRLRTVTNAFLLSLAVSDLLLAVACMPFTLLPNLMGTF 120
                YAVIFLMSVGGNMLIIIVVLG LSRRLRTVTNAFLLSLAVSDLLLAVACMPFTLLPNLMGTF
HUCCKBR     61 YAVIFLMSVGGNMLIIIVVLG LSRRLRTVTNAFLLSLAVSDLLLAVACMPFTLLPNLMGTF 120

GPCCKRB    121 IFGTVICKAVSYLMGVSVSVSTLSLVAIALERYSAICRPLQARVWQTRSHAARVIVATWL 180
                IFGTVICKAVSYLMGVSVSVSTLSLVAIALERYSAICRPLQARVWQTRSHAARVIVATWL
HUCCKBR    121 IFGTVICKAVSYLMGVSVSVSTLSLVAIALERYSAICRPLQARVWQTRSHAARVIVATWL 180

GPCCKRB    181 LSGLLMVPYPVYTVVQPVGPRVLQCVHRWPSARVRQTWSVLLLLLLLLFFVPGVVMAYAYGL 240
                LSGLLMVPYPVYTVVQPVGPRVLQCVHRWPSARVRQTWSVLLLLLLLLFF+PGVVMAYAYGL
HUCCKBR    181 LSGLLMVPYPVYTVVQPVGPRVLQCVHRWPSARVRQTWSVLLLLLLLLFFIPGVVMAYAYGL 240

GPCCKRB    241 ISRELYLGLRFDGDADSESQSRVRGRGGLSGSAPGPAHQNGRCRPE SGLSGEDSDGCYVQ 300
                ISRELYLGLRFDGD+DS+SQSRVR +GGL  PG  HQNGRCRPE+G  GEDSDGCYVQ
HUCCKBR    241 ISRELYLGLRFDGSDSDSQSRVRNQGGL----PGAVHQNGRCRPE TGAVGEDSDGCYVQ 296

GPCCKRB    301 LPRSRPALELSALAASTPAPGPGSRPTQAKLLAKKRVRMLLVIVVLF FLCWLPVYSANT 360
                LPRSRPALEL+AL A  P PG GSRPTQAKLLAKKRVRMLLVIVVLF FLCWLPVYSANT
HUCCKBR    297 LPRSRPALELTALTA--PGPGSGSRPTQAKLLAKKRVRMLLVIVVLF FLCWLPVYSANT 354

GPCCKRB    361 WRAFDGPGAHRALSGAPISFIHLLSYASACVNPLVYCFMHRFRQACLET CARCCPRPPR 420
                WRAFDGPGAHRALSGAPISFIHLLSYASACVNPLVYCFMHRFRQACLET CARCCPRPPR
HUCCKBR    355 WRAFDGPGAHRALSGAPISFIHLLSYASACVNPLVYCFMHRFRQACLET CARCCPRPPR 414

GPCCKRB    421 ARPRLP EEDPPTPSIASLSRSLSYTTISTLGPG 453
                ARPR LP+EDPPTPSIASLSRSLSYTTISTLGPG
HUCCKBR    415 ARPRALPDEDPPTPSIASLSRSLSYTTISTLGPG 447

```

>Protein alignment 4 Alignment of 2 sequences: HUCCKBR, MCCKBR

Score = 2034.0, Identities = 399/455 (87%), Positives = 417/455 (91%), Gaps = 10/455 (2%)

```

HUCCKBR      1 MELLKLNRSVQGTGPGPGASLCRPGAPLLNSSSVGNLSCEPPRIRGAGTRELELAIRITL  60
M+LLKLNRS+QG GPG G+SLCRPG LLNSSS GNLSCE PRIRG GTRELEL IRITL
MCCKBR       1 MDLLKLNRSLQGPGPSGSSLCRPGVSLNSSSAGNLSCEPPIRIRGTGTRELELTIRITL  60

HUCCKBR     61 YAVIFLMSVGGNMLIIVVLGLSRRLRTVTNAFLLSLAVSDLLLAVACMPFTLLPNLMGTF 120
YAVIFLMSVGGN+LIIVVLGLSRRLRTVTNAFLLSLAVSDLLLAVACMPFTLLPNLMGTF
MCCKBR      61 YAVIFLMSVGGNMLIIVVLGLSRRLRTVTNAFLLSLAVSDLLLAVACMPFTLLPNLMGTF 120

HUCCKBR    121 IFGTVICKAVSYLMGVSVSVSTLSLVAIALERYSAICRPLQARVWQTRSHAARVIVATWL 180
IFGTVICKAVSYLMGVSVSVSTL+L AIALERYSAICRPLQARVWQTRSHAARVI+ATWL
MCCKBR     121 IFGTVICKAVSYLMGVSVSVSTLNLAIALERYSAICRPLQARVWQTRSHAARVILATWL 180

HUCCKBR    181 LSGLLMVPYPVYTVVQPVGPRVLCVHRWPSARVRQTWSVLLLLLLFFIPGVVMAVAYGL 240
LSGLLMVPYPVYTVVQPVGPR+LQC+H WPS RV+Q WSVLLL+LLFFIPGVVMAVAYGL
MCCKBR     181 LSGLLMVPYPVYTVVQPVGPRILQCMHLWPSERVQQMWSVLLLILLFFIPGVVMAVAYGL 240

HUCCKBR    241 ISRELYLGLRFDGSDSDSQSRVRNQGLPGA-----VHQNGRCRPETGAVGEDSDGCV 294
ISRELYLGLRFDGD+DS++QSRVRNQGLPG          VHQNG CR T  GEDSDGCV
MCCKBR     241 ISRELYLGLRFDGDNDSETQSRVRNQGLPGAAAPGPVHQNGGCRHVTSLTGEDSDGCV 300

HUCCKBR    295 VQLPRSRPALELTALTAP--GPGSGSRPTQAKLLAKKRVRMMLLVIVLFFLCWLPVYSA 352
VQLPRSR  LE+T LT P  GPG G RP QAKLLAKKRVRMMLLVIV+LFF+CWLPVYSA
MCCKBR     301 VQLPRSR--LEMTTLTPTTGPVGPVPRNQAKLLAKKRVRMMLLVIVLFFVLCWLPVYSA 358

HUCCKBR    353 NTWRAFDGPGAHRALSGAPISFIHLLSYASACVNPLVYCFMHRFRQACLETTCARCCPRP 412
NTWRAFDGPGA RAL+GAPISFIHLLSY SAC NPLVYCFMHRFRQACL+TCARCCPRP
MCCKBR     359 NTWRAFDGPGARRALAGAPISFIHLLSYTSACANPLVYCFMHRFRQACLDTCARCCPRP 418

HUCCKBR    413 PRARPRALPDEDPTPSIASLSRSLYTTISTLGPG 447
PRARPR LPDEDPTPSIASLSRSLYTTISTLGPG
MCCKBR     419 PRARPRPLPDEDPTPSIASLSRSLYTTISTLGPG 453

```

Publications

Publications relevant to this thesis

Gao, B., Sherman, P., Luo, L., Bowie, J. & Zhu, S. (2009) Structural and functional characterization of two genetically related meucin peptides highlights evolutionary divergence and convergence in antimicrobial peptides, *FASEB J.* 23, 1230-1245.

Sherman, P. J., Jackway, R. J., Gehman, J. D., Praporski, S., McCubbin, G. A., Mechler, A., Martin, L. L., Separovic, F. & Bowie, J. H. (2009) Solution structure and membrane interactions of the antimicrobial peptide fallaxidin 4.1a: An NMR and QCM study, *Biochemistry.* 48, 11892-11901.

Sherman, P. J., Jackway, R. J., Nicholson, E., Musgrave, I. F., Boonthung, P. & Bowie, J. H. (2009) Activities of seasonably variable caerulein and rothein skin peptides from the tree frogs *Litoria splendida* and *Litoria rothii*, *Toxicon.* 54, 828-835.

Jackway, R. J., Pukala, T. L., Donnellan, S. C., Sherman, P. J., Tyler, M. J. & Bowie, J. H. (2011) Skin peptide and cDNA profiling of Australian anurans: Genus and species identification and evolutionary trends, *Peptides.* 32, 161-172.

Other publications

Maclea, M. J., Walker, S., Wang, T., Eichinger, P. C. H., Sherman, P. J. & Bowie, J. H. (2009) Diagnostic fragmentations of adducts formed between carbanions and carbon disulfide in the gas phase. A joint experimental and theoretical study, *Org. Biomol. Chem.* 8, 371-377.

Wang, T., Andreatza, H. J., Pukala, T. L., Sherman, P. J., Calabrese, A. N. & Bowie, J. H. (2011) Histidine-containing host-defence skin peptides of anurans bind Cu²⁺. An electrospray ionisation mass spectrometry and computational modelling study, *Rapid Commun. Mass Spectrom.* 25, 1209-1221.

Gao, B., Sherman, P., Luo, L., Bowie, J. & Zhu, S. (2009) Structural and functional characterization of two genetically related meucin peptides highlights evolutionary divergence and convergence in antimicrobial peptides.

The FASEB Journal, v. 23(4), pp. 1230-1245

NOTE:

This publication is included on pages 243-258 in the print copy of the thesis held in the University of Adelaide Library.

It is also available online to authorised users at:

<http://dx.doi.org/10.1096/fj.08-122317>

Sherman, P.J., Jackway, R.J., Gehman, J.D., Praporski, S., McCubbin, G.A., Mechler, A., Martin, L.L., Separovic, F. & Bowie, J.H. (2009) Solution structure and membrane interactions of the antimicrobial peptide Fallaxidin 4.1a: an NMR and QCM study.
Biochemistry, v. 48(50), pp. 11892-11901

NOTE:

This publication is included on pages 259-268 in the print copy of the thesis held in the University of Adelaide Library.

It is also available online to authorised users at:

<http://dx.doi.org/10.1021/bi901668y>

Sherman, P.J., Jackway, R.J., Nicholson, E., Musgrave, I.F., Boontheung, P. & Bowie, J.H. (2009)
Activities of seasonably variable caerulein and rothein skin peptides from the tree frogs *Litoria
splendida* and *Litoria rothii*.
Toxicon, v. 54(6), pp. 828-835

NOTE:

This publication is included on pages 269-276 in the print copy
of the thesis held in the University of Adelaide Library.

It is also available online to authorised users at:

<http://dx.doi.org/10.1016/j.toxicon.2009.06.009>

Jackway, R.J., Pukala, T.L., Donellan, S.C., Sherman, P.J., Tyler, M.J. & Bowie, J.H. (2011) Skin peptide and cDNA profiling of Australian anurans: genus and species identification and evolutionary trends.

Peptides, v. 32(1), pp. 161-172

NOTE:

This publication is included on pages 277-288 in the print copy of the thesis held in the University of Adelaide Library.

It is also available online to authorised users at:

<http://dx.doi.org/10.1016/j.peptides.2010.09.019>